ISSN 1880-8468

Technical Report of
International Development Engineering
国際開発工学報告

TRIDE-2009-01 February 13, 2009

# Abstracts of Master Theses
## Presented in February 2009

Department of International Development Engineering,
Graduate School of Science and Engineering,
Tokyo Institute of Technology
**http://www.ide.titech.ac.jp/TR**

# Preface

Master theses of Department of International Development Engineering, Tokyo Institute of Technology were presented successfully on August 1, 2008 and February 13, 2009. This technical report consists of the abstracts of those theses.

# Technical Report of International Development Engineering
# TRIDE-2009-01

## Table of Contents

# Practical Detection Issues of Spectrum Sensing for Cognitive Radio Systems

Student Number: 06M51349 Name: Sabita Maharjan Khadka Supervisor: Jun-ichi TAKADA

## 1 Introduction

The radio frequency spectrum is a precious natural resource. With the increasing bandwidth requirements of the current and emerging wireless services, the effective and efficient management of spectrum has been realized as a serious issue. However many current systems do not seem to utilize the allocated spectrum fully and efficiently. So, dynamic access and utilization of spectrum is necessary. Cognitive radio has been proposed as the means to promote efficient use of spectrum by exploring the existence of spectrum holes. The strategy is that the cognitive radio system should opportunistically use a channel which is allocated to a primary user only when the channel is identified as vacant by spectrum sensing. This approach has the advantage of minimal coordination with primary systems. The opportunistic approach is also fair in the sense that the responsibility is on the secondary system to sense the signal from the primary system if it wants to use the spectrum. The key challenge of spectrum sensing is the detection of weak signals in presence of noise and interference with a very small probability of misdetection.

The first application of spectrum sensing was studied by IEEE 802.22 Standard Working Group. The IEEE 802.22 WG proposed to standardize a fixed wireless access system based on cognitive radio technology to enable spectrum access and sharing by the secondary system. This standard is called IEEE 802.22 Wireless Regional Area Network (WRAN). The IEEE 802.22 WRAN aims to provide the wireless broadband access to rural areas as well as to sub-urban areas where the spectrum utilization rate is quite low.

Energy detector is the simplest detector proposed for cognitive radio so far. Even though the number of literatures are increasing on the analysis of various detectors for cognitive radio, there has been relatively less work in the analysis of practical aspects of the system. The effect of crucial signal processing blocks such as analog to digital converter and crucial elements of system modeling such as noise uncertainty etc. have not yet been explored much. Therefore, there is a crucial need of detailed analysis of signal processing for energy detector as a cognitive radio receiver.

The rest of the paper is organized as following. Firstly an economic energy detector prototype using off-the-shelf instruments has been proposed for cognitive radio system in section 2. The detection performance has been investigated with and without considering the effect of quantization in section 3. The effect of noise uncertainty in the detector performance has been explored in section 4. Finally, section 5 concludes the paper.

## 2 Spectrum Sensing Technique

### 2.1 Neyman-Pearson Detection

Let us assume that a known deterministic signal $s[n]$ is corrupted by additive white Gaussian noise (receiver noise) $w[n]$ with zero mean and variance $\sigma_w^2$[2]. Then, the received signal x[n] will have either of the following two forms:

$$H_0 : x[n] = w[n] \quad \text{signal is absent,} \tag{1}$$

$$H_1 : x[n] = h[n]s[n] + w[n] \quad \text{signal is present,} \tag{2}$$

where $n = 1, 2, ...., N$ is the discrete time index, $N$ is the number of samples considered and $h[n]$ is the linear time varying characteristic of the propagation channel. Assuming that the distribution of signal samples $s[n]$ is a Gaussian random process with zero mean and variance $\sigma_s^2$, the decision statistic of Neyman-Pearson (NP) approach is to determine between the hypotheses $H_0$ and $H_1$ based on the observations of $X = [x[1]x[2]...x[N]]^T$. The decision statistic of NP detecctor is given by[1]

$$T = \Re[\sum_{n=1}^{N} x[n]s^*[n]] \tag{3}$$

If the signal is absent, the decision statistic follows a central chi-square distribution with $N$ degrees of freedom. If the signal is present, it follows a non-central chi-square distribution. Under either hypothesis, as long as $N$ is large enough, since $x[n]$ is Gaussian and since $T$ is a linear combination of Gaussian random variables, $T$ is also Gaussian. So, based on the central limit theorem, the distribution of $T$ can be approximated as Gaussian i.e.

$$\begin{cases} H_0 : T \sim \mathcal{N}(\mu_0, \sigma_0^2) \\ H_1 : T \sim \mathcal{N}(\mu_1, \sigma_1^2) \end{cases} \tag{4}$$

where the received signal $x[n]$ can be both real (passband) or complex valued (baseband) with the same power.

[1] in this case the considered detector is the matched filter for which the incoming signal structure is known beforehand.

## 2.2 Energy Detector

Energy detection is a signal detection mechanism based on NP approach [2] [3]. The NP detector computes the energy of the received signal and compares it to the threshold in order to determine whether or not the signal from the primary system is present. The decision value of the energy detector is given by,

$$T = \sum_{n=1}^{N} |x[n]|^2. \tag{5}$$

The probability of false alarm ($P_{\mathrm{FA}}$) and the probability of detection ($P_{\mathrm{D}}$) of energy detector are given by

$$P_{\mathrm{FA}} = Q(\frac{\gamma - N\sigma_w^2}{\sqrt{N\sigma_w^4}}), \tag{6}$$

$$P_{\mathrm{D}} = Q(\frac{\gamma - N(\sigma_w^2 + \sigma_s^2)}{\sqrt{N(\sigma_w^2 + \sigma_s^2)^2}}). \tag{7}$$

for complex valued signal. The energy detector can meet any desired $P_{\mathrm{D}}$ and $P_{\mathrm{FA}}$ simultaneously if the number of samples $N$ is not limited provided that $w[n]$, $s[n]$ as well as $h[n]$ are modelled as stationary and ergodic random processes. In reality however, these processes are neither stationary nor ergodic. So, for a practical system, the robustness of the system towards various issues and errors should be carefully investigated in order to ensure that the detector performance is acceptable.

## 2.3 Energy Detector Prototype

Though the number of literatures regarding the performance evaluation of detectors for cognitive radio system is increasing, the crucial need of the experimental study still persists to explore the feasibility and the practical performance limits of the detectors under real noise and interference conditions in wireless channels. So, it is our motivation to propose a detector prototype for cognitive radio receiver feasible to work in practical environment. Our proposed detector model is shown in Figure 1. It comprises of off-the-shelf instruments which make it versatile, economic as well as frequency agile.

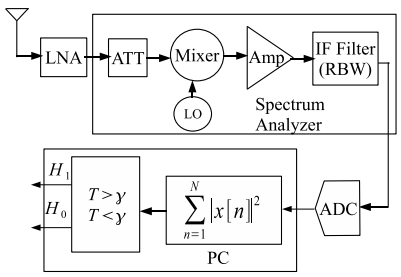


Figure 1: Block diagram of the prototype to implement energy detector

The low noise amplifier is used to decrease the overall noise figure of the system. The attenuator is used in order to prevent overloading in case of strong signals. If the RF signal be directly fed to the ADC, the sampling frequency is supposed to be very high. So, the mixer in spectrum analyzer is used to down-convert the RF signal. The output of spectrum analyzer is the intermediate frequency (IF) signal. Once the RF signal is converted to IF signal, all the signal processing can be done in IF range. The signal is then fed to the analog to digital converter (ADC) which performs sampling and quantization of the IF signal in order to use the data for analysis in the data acquisition system. In this prototype, PC is the data acquisition system in which the energy of the quantized samples is computed, the threshold is determined and the hypotheses are compared to determine the presence/absence of the primary signal.

# 3 Effect of Quantization on Detection Performance

## 3.1 Background

Most of the literatures about the analysis of detection performance of cognitive radio receiver consider the detection performance based on actual samples. In reality however, the performance depends on the quantized samples, not on the actual samples. So, it is our motivation to explore the effect of quantization on the performance of energy detector.

## 3.2 System Model

Figure 2 shows the low pass model of cognitive radio receiver. All blocks of the receiver except ADCs are assumed to be linear [4] and the sampling time is assumed to have no jitter. So, the signal at the filter output is given by

$$x(t) = s(t) + n(t) \tag{8}$$

where $s(t)$ and $n(t)$ are the signal and noise component respectively.

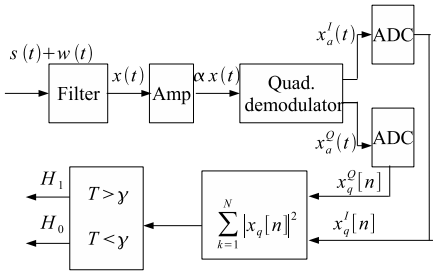


Figure 2: Model of the Receiver

Though the amplifier gain $\alpha$ can be automatically controlled in practical systems, in this study, it is assumed to be fixed to analyze its effect [4]. Let us assume that the input to the ADC is normalized and that the full scale range (FSR) of the ADC is $\pm 1$. If the amplitude of the input to the ADC is within the FSR, the error is given by

Table 1: Parameters of the ISDB-T signal used for simulation

| Parameters | Values |
|---|---|
| Effective symbol length ($T_u$) | 252 $\mu$s |
| Guard interval ($T_g$) | $\frac{T_u}{4} = 63$ $\mu$s |
| Symbol duration ($T_s$) | 315 $\mu$s |
| Number of symbols | 20 |
| Total duration | 6.3 ms |
| Number of carriers | 1405 |
| Total bandwidth | 5.575 MHz |
| Sampling frequency | 16.254 MHz |

$$|e_q[k]| < \frac{\Delta_q}{2}, \tag{9}$$

where $\Delta_q$ is the stepsize of quantization given by

$$\Delta_q = \frac{2}{2^M - 1}, \tag{10}$$

where $M$ is the number of bits used for quantization. If the amplifier gain is too large such that the input does no more fit within the FSR, clipping occurs hence increasing the error beyond what is given by (9).

### 3.3 Simulation Results

The ISDB-T signal was generated following the description given in [5] to analyze the effect of quantization assuming Mode 1. The spectrum of the generated ISDB-T signal is shown in Figure 3. The parameters of the generated signal are given in Table 1.

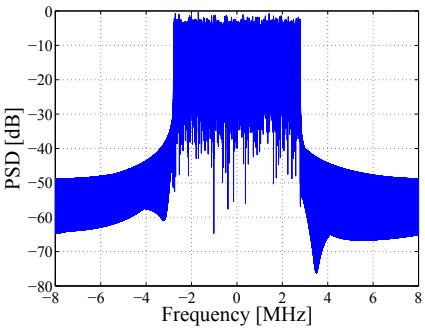


Figure 3: Spectrum of the generated ISDB-T signal

Figure 4 shows the effect of quantization noise and clipping. The performance is optimum within certain range of $\alpha$. For lower values of $\alpha$, the probability of detection can be drastically improved by increasing the number of bits of ADC because in this case quantization error is dominant. On the other hand, for higher values of $\alpha$, increasing the number of bits does not help because the clipping noise becomes dominant in this case. Therefore, the trade-off should be made so that the detection performance is least affected.

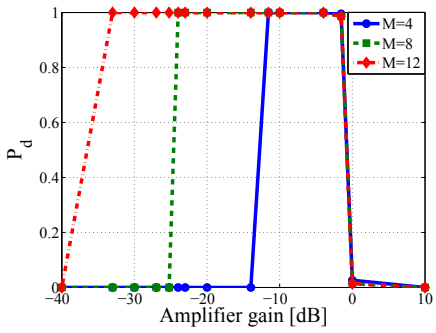


Figure 4: Effect of Quantization and Clipping Errors ($N = 1024$, $SNR = -9$ dB, $P_{\mathrm{FA}} = 1\%$)

## 4 Noise Uncertainty

### 4.1 Background

Most of the literatures about cognitive radio detectors assume that the background noise is additive white Gaussian and that the variance is exactly known, which is most of the time not the case in real environment. So, it is our motivaion to explore the effect of noise uncertainty in the detection performance of energy detector.

### 4.2 Evaluation

Let $s(t)$ denote a band-limited primary signal with a total bandwidth of $B$. Let $h$ be the fading process, and let $w(t)$ be the additive noise process. Let us assume that the reeived signal (with additive noise) is sampled ideally at Nyquist rate. A stationary white Gaussian assumption for background noise is only an approximation. So, Let us model the noise process $w[n]$ to have any distribution $W$ from a set of possible distributions $\mathcal{W}$. This set is called the noise uncertainty set. Fading is modeled in similar manner. The fading process $H \in \mathcal{H}_f$ is considered a possibly random linear time-varying filter response. Similarly, let us denote the set of distributions for $S$ as $\mathcal{S}_p$. Although the actual noise variance might vary over distributions in the set $\mathcal{W}$, let us assume that there is a single nominal noise variance $\sigma_n^2$ associated with the noise uncertainty set $\mathcal{W}$. By convention, we consider all the $S \in \mathcal{S}_p$ to share the same average variance $\sigma_s^2$.

Because the energy detector evaluates the detection performance based on energy of the incoming signal, the distributional uncertainty of noise can be summarized in a single interval $\sigma_w^2 \in [(\sigma_n^2 - \rho)\mathrm{dB}, (\sigma_n^2 + \rho)\mathrm{dB}]$ where $\rho > 0$ dB is a parameter that quantifies the size of the noise uncertainty.

Now including the effect of noise uncertainty as described in [6], $P_{\mathrm{FA}}$ and $P_{\mathrm{D}}$ are given by

$$P_{FA} = Q\left(\frac{\gamma - N\rho\sigma_n^2}{\sqrt{N\rho^2\sigma_n^4}}\right) \tag{11}$$

$$P_D = Q\left(\frac{\gamma - N(\frac{1}{\rho}\sigma_n^2 + \sigma_s^2)}{\sqrt{N(\frac{1}{\rho}\sigma_n^2 + \sigma_s^2)^2}}\right) \quad (12)$$

for baseband signal where $\rho$ is considered in linear scale.

### 4.3 Simulation Results

For the simulation results that follow, the ISDB-T signal as described in section 3 was used.

Figure 5 shows the performance of energy detector for different values of noise uncertainty $\rho$. As the value of $\rho$ increases, the performance degrades. For example, when the noise uncertainty is 1 dB, the detector does not work below an SNR of $-8$ dB. For $\rho = 5$ dB, the detector does not work even for higher values of SNR.

Figure 6 shows the variation of the probability of detection with sensing time for different values of the noise uncertainty $\rho$. From this figure, it can be seen that the detection performance improves as sensing time increases. However when the noise uncertainty is as big as 1 dB, the detector performance is rendered by the uncertainty and hence it does not work.

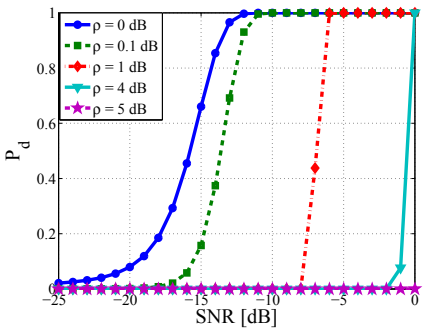


Figure 5: Detection Performance for different values of $\rho$ ($N = 1024, P_{\mathrm{FA}} = 1\%$,)

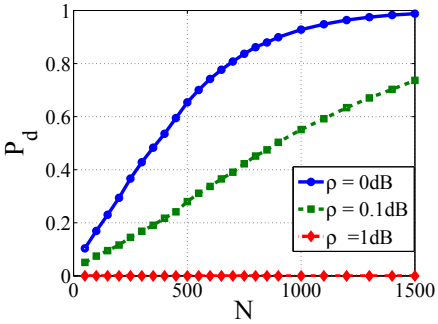


Figure 6: Detection Performance for different values of $\rho$ ($SNR = -9\ dB, P_{\mathrm{FA}} = 1\%$)

## 5 Conclusion

In this paper, an energy detector prototype using off-the-shelf instruments was proposed for cognitive radio system. As ADC is one of the most important signal processing units in cognitive radio receiver, the performance of energy detector was explored counsidering the effect of quantization and clipping. The effect of quantization was clearly pronounced in the detection performance of energy detector. Although the effect of quantization is unavoidable in any practical detector, there are ways to tackle its effect by proper modelling and design of the instruments. For example, if the dynamic range required for the detector is too high, using sufficient number of bits for quantization will increase the resolution of the system and hence minimize the quantization error. Though increasing the number of bits does not help much in reducing the clipping error, it might not be severe as long as the system can maintain fairly high dynamic range with sufficient number of bits. On the other hand, if the expected signal level input to the receiver has moderate dynamic range, using relatively less number of bits may be enough for fair performance which is saving in terms of hardware requirement.

As real noise is neither white nor its variance is exactly known in actual systems, the effect of noise uncertainty was also investigated in the detection performance of energy detector. The simulation results reflected that the detector becomes nonrobust below certain values of SNR depending on the noise uncertainty of the system.

## References

[1] C. Cordeiro, K. Birru and S. Shanker, "IEEE 802.22: The first worldwide wireless standard based on cognitive radios ," In proc. of DySPAN'05, November 2005.

[2] S. Kay, "Statistical decision theory I (Ch. 3)" and "Deterministic signals (Ch. 4)," in Fundamentals of Statistical Signal Processing, Detection Theory, pp.60-140, Prentice Hall, 1998.

[3] H. Tang, "Some Physical Layer Issues of Wide-band Cognitive Radio Systems," 2005 First IEEE International Sympo- sium on New Frontiers in Dynamic Spectrum Access Networks (DySPAN 2005), pp. 151-159, Nov. 2005.

[4] M. Sawada, H. Okada, T. Yamazato and M. Katayama "Influence of ADC nonlinearity on the performance of an OFDM receiver," IEICE Trans. Commun., Vol.E89-B, No.12, Dec. 2006.

[5] "Transmission System for Digital Terrestrial Television Broadcasting," ARIB Standard, ARIB STD-B31 Version 1.5, Association of Radio Industries and Businesses, 2003.

[6] R. Tandra and A. Sahai, "SNR Walls for Signal Detection," IEEE Journal of Selected Topics in Signal Processing, Vol. 2, No. 1, Feb. 2008.

# SEMI MACHINE TRANSLATION SYSTEM BASED ON COLLECTIVE INTELLIGENCE

Student Number:06M18033 Name:Takuya Ishibashi Supervisor: Yukihiko Yamasita

集合知に基づく 高精度半機械翻訳システム

石橋 卓也

インターネット における Wikipedia に代表される Wiki システムは，世界中の数多く の人々が参加し，学術· 生活など の広範囲で有益な情報を持続的に提供し ている。し かし，現状の Wiki システムには，言語ごと に文書ファ イルを用意する 必要があるとい う 言語の壁が存在する。こ の壁を越え，一つの文書ファ イルから 世界中の人々が情報を取得できるよう にするためには，機械翻訳が必要不可欠と なるが，既存の機械翻訳には，構文解析や意味選択における 誤認識が生じ るとい う 問題が残されている。

本研究では，文法や意味など の情報を 付加し た XML 文書 (Adam, Auxiliary Description to Attach Meaning) を 提案する。さら に，多数の人々が Adam 文書の記述を 可能にする 支援ツールを 開発し，持続可能な情報提供システムの構築を 目指す。

## 1 INTRODUCTION

A lot of people in the world participate in the Wiki system project. Wiki system, such as Wikipedia, provides sustainedly useful information in various fields such as study and life. However, the present Wiki system has a problem that it is necessary to prepare at least one document for each language. For solving this problem and getting information in many languages from one document, machine translation is necessary. But, the present machine translation is not free from errors in structural analysis and mean analysis. For the reason, even if it can be used as a support tool, the system is not practiced.
In this research, I propose an XML document called ADAM (Auxiliary Description to Attach Meaning) which has the information of grammar and meaning. I developed a supporting tool to describe an ADAM document aiming sustainable production of ADAM document based on collective intelligence.

## 2 BACKGROUNDS

### 2.1 Collective Intelligence

Collective Intelligence is often used as the word stands for sets of intelligence by many people. But, it means essentially the notion of the wisdom of crowds. [1]
By the birth of Internet, it is easy for a lot of people to deliver contents using the Collective Intelligence and participate in that contents. Now Wiki system and Blog provide various and useful information using the Collective Intelligence.

#### 2.1.1 Wiki

Wiki [2] is a kind of system rewriting a hyper text document on a web server by using web browser. The software which is used by this system and all documents made by using this system are called Wiki. The followings are the features of Wiki.

1. It is able to change and save documents for anyone and at anytime and anywhere on Internet.
2. The tool needed to change a document is only a web browser.
3. The rule to make-up a document at Wiki is easier than HTML.
4. It is easy to link between documents in same Wiki system. Therefore, we can make a complex set of documents easily.
5. Various documents can be seen and changed without registering, user account or an advance permission if a person can access the Wiki server.

Wikipedia is the most famous Wiki system. Document in 229 languages exist in Wikipedia. English project is the biggest project and has about 1.4 billion word. Japanese project has 260 thousand word. But, it has problem that the substances of content and the quantities of information are different among languages. One of solutions to overcome the problem is machine translation. It may improve the quality and quantity of Wikipedia as Collective Intelligence.

## 2.2 Machine Translation

Machine translation is to translate a text in a language into one in another language automatically. As a practical service, there are the translation software for computer and translation service on Internet. But it is very difficult to translate a sentence precisely, because natural language is used by missing words and has many synonym.

### 2.2.1 Problem of Machine Translation

A computer is not able to understand the meaning of words different from a human. For this reason, a computer translates a sentence only by processing information of construction of a sentence. Then, following problems occur in machine translation. Figure 1 is an example of mistake in machine translation.

- In the analysis process of construction of a sentence
  - Error in the analysis process of structure
    Relationship between a subjective and a predicate is wrong.
  - Error in the analysis process of meaning
    Analysis of the meaning of each word is wrong.
  - Error in the analysis process of context
    Analysis of context is wrong or context is neglected.
- In the transformation and generation process
  - Error in the generation process
    The order of words in translation is wrong.
  - Error in the transformation process
    Expression of a word in translation is not appropriate.

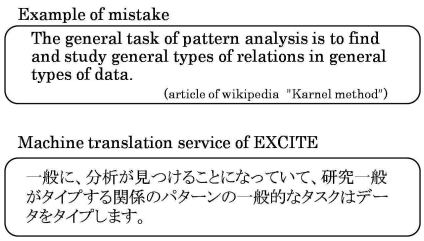


Figure 1: Example of mistake

# 3 Semi Machine Translation System with Adam Document

I propose the ADAM (Auxiliary Description to Attach Meaning) document that is an XML document and has additional information of grammar and meaning for machine translation. There are many mistakes in machine translation. Then, it is very difficult that a person correct the translation. Therefore, it is efficient for a person to give the information of grammar to translation machine.

## 3.1 ADAM Document

Additional information of ADAM document consists of a sentence, grammar and meaning. Error on machine translation is due to the analysis process of a sentence and its meaning. For the reason, the ADAM document provides the information in the part of analysis process. Detail of each information is mentioned in followings.

- Information of construction of a sentence
  It describes the information in the analysis process of structure. This information is based on English grammar. The construction of a sentence is composed of clause and phrase. The information is composed of subjective phrase (clause), verb phrase, adjective phrase (clause) and adverb phrase (clause). The construction of clause is composed of clause and phrase. The construction of phrase is composed of phrase only.
- Information of grammar
  It describe the grammar information of each word. For example, a part of speech, tense, singular or plural and so on.
- Information of meaning
  It describes the meaning of each word.

ADAM document is a type of XML document. Figure 2 is an example of ADAM document. The example sentence is 'My name is Tom .' The meaning of a tag is shown in APPENDIX Table 1. The ADAM Document starts from the <ADAM> tag. A sentence is surrounded by the <sentence> tag. For information of tag, construction of a sentence, information of grammar, information of meaning are described in order. In the last section, the original form of the word is written.

## 3.2 Editing Tool for ADAM Document

I develop a support tool for editing the ADAM document. I explain the functions of the tool. Figure 3 illustrates the picture of top window. Figure 4 illustrates the window to attach the information tag of grammar of words.

**Function of File Menu**

1. Input the original sentence

```
1: <?xml version="1.0"
                  encoding="UTF-8"?>
2: <!DOCTYPE ADAM SYSTEM "adam.dtd">

3: <ADAM>
4:   <sentence>
5:     <u>
6:       <snp>
7:         <det>
8:           <pos>
9:             <mean id="0">My</mean>
10:          </pos>
11:        </det>
12:        <n>
13:          <sg>
14:            <mean id="0">name</mean>
15:          </sg>
16:        </n>
17:      </snp>
18:      <vp>
19:        <v>
20:          <pres>
21:            <be>
22:              <mean id="0">be</mean>
23:            </be>
24:          </pres>
25:        </v>
26:      </vp>
27:      <onp>
28:        <n>
29:          <sg>
30:            <prop>
31:              <mean id="0">Tom</mean>
32:            </prop>
33:          </sg>
34:        </n>
35:      </onp>
36:      <sign>.</sign>
37:    </u>
38:  </sentence>
39:</ADAM>
```

Figure 2: Example of Adam Document

- Input by keyboard
- Read from text file

2. Read or save the ADAM document
3. Output the ADAM document

**Grammar of Word Window**

1. Select the word
   It allocates the buttons of words. If one of these button is pushed, the corresponding word is selected.
2. Select the part of speech
   It allocates the buttons of parts of speech. If a word is selected, it is attached the information of a part of speech by pushing the button.

**Construction of Sentence Window**

1. Select a phrase or clause
   It allocates the buttons of a subjective phrase (clause), a verb phrase, a adjective phrase (clause) and a adverb phrase (clause). If the button of a phrase or a clause is pushed, it switches to the state to select the word.
2. Select the word
   If a button of a word is pushed, it is attached the information.

**Amend the Word Window**

1. Select the word
   It allocates the buttons of words. If one of these buttons is pushed, the corresponding word is selected.
2. Amend
   It amends the selected word to the original form by keyboard.

**Information of Meaning Window**

1. Select the word
   It allocates the buttons of words. If one of these button is pushed, the corresponding word is selected.
2. Select the meaning
   It allocates the meaning from a multi-language dictionary. If a button of meaning is pushed, the information is attached.

I pay the attention to the ability of speed and operation. For being more simple and fast, it can be used only by a mouse.

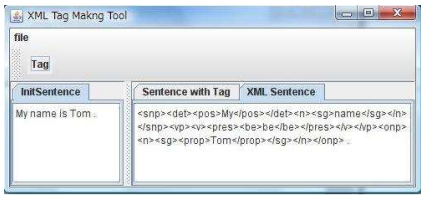


Figure 3: editing tool

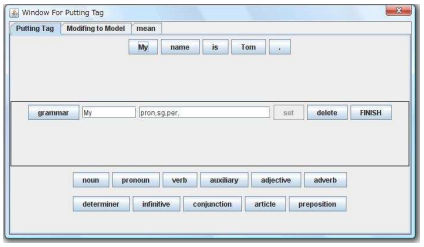


Figure 4: Window of attaching grammar information

### 3.3 Translation Machine System

The translation machine needs to analyze not natural language but an ADAM document. The following functions are necessary.

- Read the ADAM document
- Interpret the ADAM document
  Since the ADAM document is the XML document, only the XML parser is necessary.
- Translate to another language
  Translation rules to another language according to information of an ADAM document is necessary. It translates to another language by the rules.
- Dictionary
  One word has various meanings for many languages in this dictionary in order to translate to various languages.

## 4 CONCLUSIONS

In this paper, I proposed a semi machine translation system based on collective intelligence in order to obtain more precise translation for the case such as Wikipedia.
As a future work, I need to improve the method to attach tags for decreasing human error and add the function to check the ADAM document easily. Besides, I must develop a translation machine.

## REFERENCES

[1] Surowiecki, J.:*THE WISDOM OF CROWDS*, Anchor Books, England, 2005

[2] Eto, K.:*Origin and Evolution of Wiki*, IPSJ SIG technical reports, vol.2007, No.41 pp.11-18. (in Japanese)

## APPENDIX

Table 1: Tag list

| index | name | mean |
|---|---|---|
| A | ac | adjective clause |
| | adj | adjective |
| | adv | adverb |
| | advc | adverb clause |
| | advp | adverb phrase |
| | ap | adjective phrase |
| | art | article |
| | aux | auxiliary |
| B | be | Be verb |
| C | comd | comparative degree |
| | conj | conjunction |
| D | dem | demonstrative |
| | det | determiner |
| F | fut | future |
| | futpt | future perfect tense |
| G | ger | gerund |
| I | imp | imperative |
| | inf | infinitive |
| | int | interrogative |
| | intr | intransitive |
| | ints | interrogative sentence |
| N | n | noun |
| | neg | negative |
| O | onc | objective noun clause |
| | onp | objective noun phrase |
| P | p | past |
| | per | person |
| | pl | plural |
| | pos | possessive |
| | posd | positive degree |
| | pp | past participle |
| | ppt | past perfect tense |
| | prep | preposition |
| | pres | present |
| | presp | present participle |
| | prespt | present perfect tense |
| | pro | proverb |
| | pron | pronoun |
| | prop | proper |
| R | rel | relative |
| S | sg | singular |
| | sign | sign of end |
| | snc | subjective noun clause |
| | snp | subjective noun phrase |
| | sub | subjunctive |
| | supd | superlative degree |
| T | tran | transitive |
| U | u | usual |
| V | v | verb |
| | vp | verb phrase |

# Study of Antenna Radiation Efficiency by Computer Simulation

Student Number: 06M51326 Name: Shigeo YAMADA Supervisor: Jun-ichi TAKADA

# 計算機によるアンテナ効率測定法の検討

山田 重雄

日本語要約 アンテナ放射効率を簡易的に測定する Wheeler 法はよく使用されているものの, 理論的な裏づけが十分でなく, 適用範囲が不明確である. 本論文では, 共振周波数付近の Wheeler 法による放射効率の値が実際の放射効率よりも小さくなる現象に関して電磁界シミュレータを使用して検討を行った.

## 1 Introduction

There are a lot of parameters to represent the characteristics of the antenna. The radiation efficiency is one of them. The radiation efficiency is the ratio of radiated power from the antenna to the input power to the antenna. It is a most important parameter for the mobile terminal antenna as the size of the antenna is limited which leads the degradation of the efficiency. The radiation efficiency is defined as

$$\eta = \frac{P_{\text{radiation}}}{P_{\text{accepted}}} \tag{1}$$

However, it is known that the measurement of the radiation efficiency is rather difficult. The input power $P_{\text{accepted}}$ can be easily evaluated by measuring the reflection coefficient, but the radiated power $P_{\text{radiated}}$ should be evaluated by measuring the electromagnetic field radiated to all the directions. This straightforward approach is called the radiated power integration method. Although the method is most popular, an anechoic chamber and a spherical antenna positioner are needed for the measurement, and it is very time consuming in measuring the whole solid angles. Alternatively, a simpler method known as the Wheeler method is often used. In the Wheeler method, the radiation efficiency is estimated by comparing the reflection coefficients of the antenna when it is set up in a free space and when it is covered with a conductive cap. This method needs only a conductor cap and a network analyzer, but no anechoic chamber nor spherical antenna positioner. Therefore, this method is advantageous from the viewpoint of cost and measurement time. However, Wheeler method has the following limitations:

- The antenna should be within the radian sphere, i.e. the sphere of $1/2\pi$ wavelength in radius.
- The wall of the cap should be placed further than the radian length, i.e. $1/2\pi$ wavelength, from the antenna.

The mobile terminal antenna may be integrated into the handset. In the case, the measurement condition is relaxed as:

- The measured antenna size is in the order of half wavelength.

Unfortunately, Wheeler method does not always provide the good estimate of the radiation efficiency. This study investigate the mechanism of error in the Wheeler cap method to clarify the applicability.

## 2 Wheeler Cap Method and Problem Statement

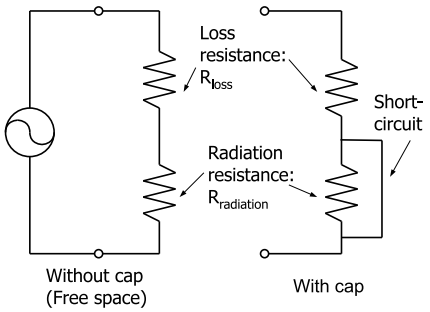


Figure 1: Equivalent circuit for Wheeler method

The equivalent circuit proposed by Wheeler [1] is shown in Fig. 1. The power is represented as the resistance in the equivalent circuit. When the antenna is placed in the free space, the loss and the radiation are represented as two series resistors $R_{\text{loss}}$ and $R_{\text{radiation}}$.

On the other hand, only the radiation resistance is short-circuited when the antenna is capped as the radiation power does not exist.

The radiation efficiency is calculated from these equivalent circuits as follows [2] [3]. Where $\Gamma_{\text{cap}}$ and $\Gamma_{\text{free}}$ are the reflection coefficients of the antenna with and without the cap. In this study $\eta_w$ is called the Wheeler efficiency, in comparison with the true radiation efficiency.

$$\eta_w = \frac{R_{\text{radiation}}}{R_{\text{radiation}} + R_{\text{loss}}} \tag{2}$$

$$= 1 - \frac{1 - |\Gamma_{\text{cap}}|^2}{1 - |\Gamma_{\text{free}}|^2} \tag{3}$$

It is known that the Wheeler efficiency does not always coincide with the radiation efficiency.

When the cap is resonant, strong electromagnetic field is generated inside the cap and the radiated power is not reflected by the cap to the feed.

When the antenna is near resonant, the dip of the efficiency is often observed, although the reason is not clear. As the antenna is usually used around the resonant frequency, this is a serious problem.

# 3 Simulation

## 3.1 Simulation Condition

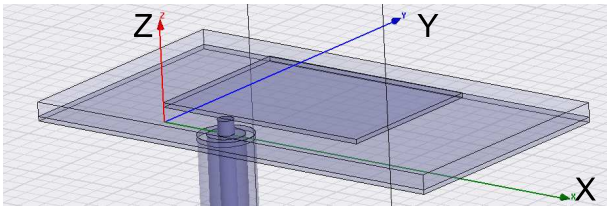


Figure 2: Patch antenna structure

A microstrip antenna is chosen for the study. The current distribution and the reflection coefficient are calculated by using the commercial electromagnetic simulator Ansoft HFSS [4], which utilizes the finite element method as the solver of the Maxwell's equation.

The structure of the microstrip antenna is shown in Fig. 2. The antenna consists of two parallel conductor plates with different sizes. The top plate is sized 25 mm × 18 mm × 0.5 mm in (X,Y,Z) directions. The bottom plate is sized 50 mm × 28 mm × 0.5 mm. The plates are made of copper with the conductivity of $5.8 \times 10^7$ S/m. The dielectric substrate of 1.6 mm thickness in Z direction is placed between to conductors. The substrate is made of Duroid, whose relative permittivity is 2.2 and the dielectric loss tangent is 0.0009. The target system is IMT-Advanced. The antenna is fed by the coaxial cable. The diameter of the inner conductor is 1.78 mm, and the inner diameter of the outer conductor is 2.055 mm. The thickness of the outer conductor is 1 mm. The characteristic impedance of the coaxial cable is designed to be 50 Ω. The feed point of the top conductor is offset at 8 mm along X direction from the corner of the top conductor. The size of the analytical space truncated by the absorbing boundary condition is sized 65 mm × 60 mm × 60 mm in (X,Y,Z) directions. The cap is made of perfect conductor to distinguish the loss of the antenna from the loss of the cap. The cap is sized 65 mm × 60 mm × 40 mm in (X,Y,Z) directions.

## 3.2 Radiation Efficiency

The simulation results are shown from Fig. 3 to Fig. 8.

The magnitude of the reflection coefficient calculation is shown in Fig. 3. The antenna is resonance at 3.85 GHz. Fig. 4 compares the radiation efficiency and Wheeler efficiency. The very deep dip A is due to the resonant of the cap. In the frequency range B, the radiation

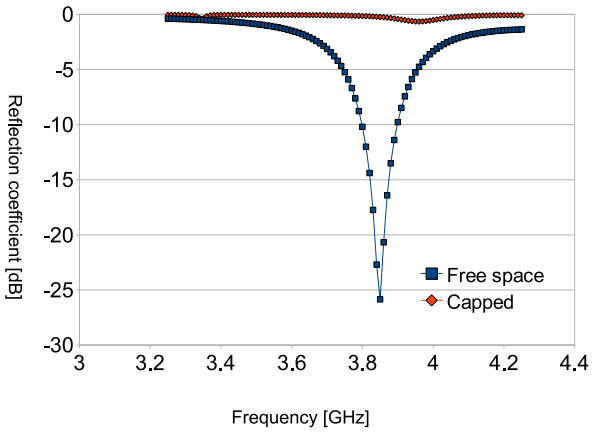


Figure 3: Reflection coefficient of the antenna

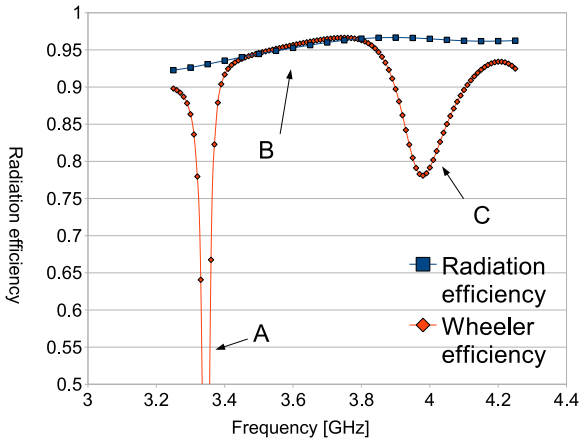


Figure 4: Radiation efficiency and Wheeler efficiency

efficiency and the Wheeler efficiency are in good agreement.

In the frequency range C, which is around the resonance frequency of the antenna, the Wheeler efficiency does not represent the radiation efficiency.

## 3.3 Current Distribution

Fig. 5 - 8 show the surface current distribution of the bottom conductor of the patch antenna. The real part of the current distribution consists of the element that contributes to the radiation. The imaginary part of the current distribution contributes to storage of the reactive energy. The Conductor loss dissipated on the antenna is represented by the magnitude of current distribution.

Fig. 5 shows the current distribution in free space at 3.60 GHz which is sampled within range B. The real part of the current has decreased more than the imaginary part because the radiation is suppressed. Fig. 6 shows the current distribution when covered with the cap. It is shown that the real part of the current has decreased obviously compared to the current distribution in free

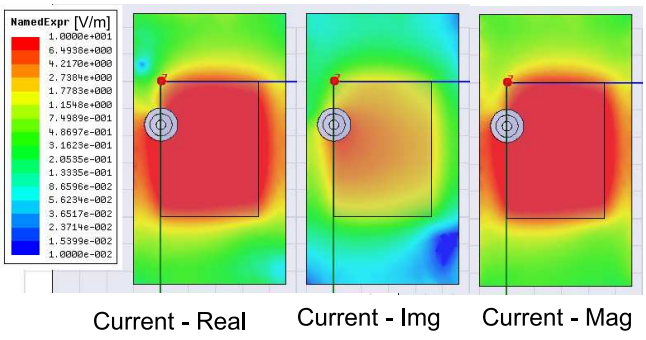


Figure 5: Current distribution without cap @ 3.60GHz

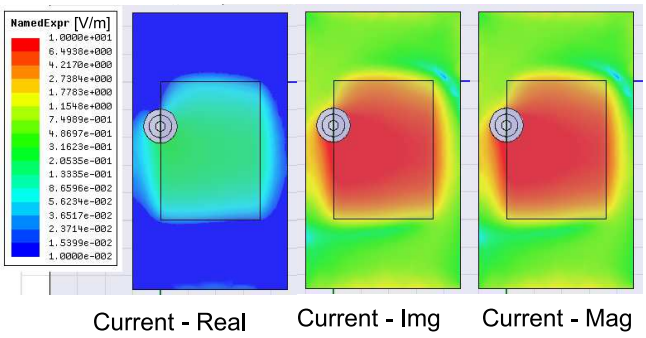


Figure 6: Current distribution with cap @ 3.60GHz

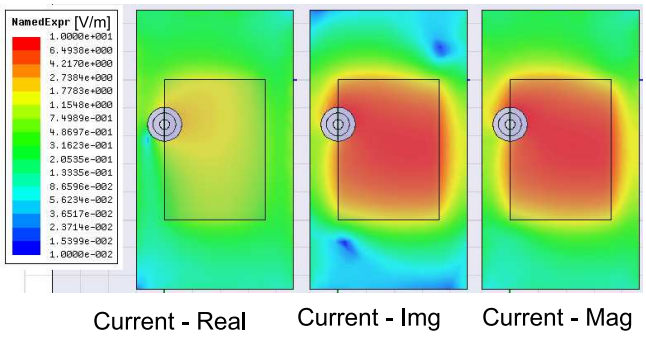


Figure 7: Current distribution without cap @ 3.96GHz

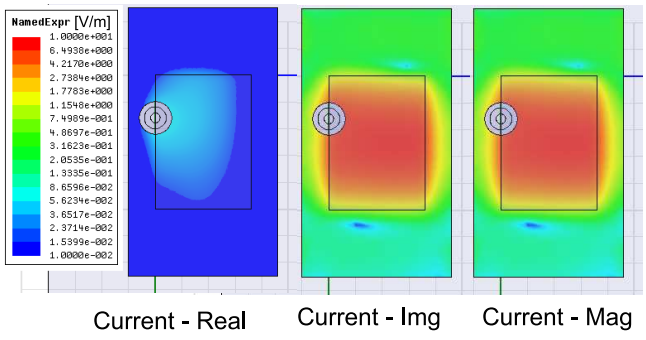


Figure 8: Current distribution with cap @ 3.96GHz

space. It can be interpreted that the radiative component was suppressed by the cap according to Wheeler's expectation. On the other hand, imaginary part is not changed. This shows that a reactive component is not seriously influenced.

Fig. 7 and 8 show the current distributions at 3.96 GHz, which is sampled within the range C where the Wheeler efficiency exhibits large error due to the unkown reason. Fig. 8 shows that the magnitude of the current has decreased when the antenna is capped. However, The similarity of the shape of current distribution is still preserved. Therefor, the error is not due to the change of the current distribution, which violates the Wheeler's assumption.

## 3.4 Impedance

Equation 3 based on Wheeler's assumption. It does not consider the change in the current without adjustment of impedance. New equation that introduces this element is derived as follow.

It assume that equivalent circuit exist like Fig. 9

In this case, $E$ is an input voltage. A new equivalent circuit for computing the radiation efficiency mention below.

$$\eta_w = \frac{\frac{1}{2}(\frac{E}{R_{\rm rad}})^2 R_{\rm rad}}{\frac{1}{2}(\frac{E}{R_{\rm loss}})^2 R_{\rm loss} + \frac{1}{2}(\frac{E}{R_{\rm rad}})^2 R_{\rm rad}} = \frac{R_{\rm loss}}{R_{\rm rad} + R_{\rm loss}} \quad (4)$$

Reflection coefficient $\Gamma_{\rm free}$ without cap becomes,

$$\Gamma_{\rm free} = \frac{\frac{R_{\rm loss}R_{\rm rad}}{R_{\rm loss}+R_{\rm rad}} - R_{\rm cir}}{\frac{R_{\rm loss}R_{\rm rad}}{R_{\rm loss}+R_{\rm rad}} + R_{\rm cir}} \quad (5)$$

In a similar way, reflection coefficient $\Gamma_{\rm cap}$ with cap becomes,

$$\Gamma_{\rm cap} = \frac{R_{\rm loss} - R_{\rm cir}}{R_{\rm loss} + R_{\rm cir}} \quad (6)$$

When these two expressions are transformed, the following relational expressions are obtained.

$$R_{\rm cir}\left(\frac{1}{R_{\rm loss}} + \frac{1}{R_{\rm rad}}\right) = \frac{1-\Gamma_{\rm free}}{1+\Gamma_{\rm free}} \quad (7)$$

$$\frac{R_{\rm cir}}{R_{\rm loss}} = \frac{1-\Gamma_{\rm cap}}{1+\Gamma_{\rm cap}} \quad (8)$$

Therefore, if this relational expression is substituted in equation 4, the radiation efficiency becomes,

$$\eta_w = \frac{R_{loss}}{R_{\rm loss} + R_{\rm rad}} = \frac{R_{\rm loss} + R_{\rm rad} - R_{\rm loss}}{R_{\rm loss} + R_{\rm rad}} \quad (9)$$

$$= 1 - \frac{R_{\rm rad}}{R_{\rm loss} + R_{\rm rad}} = 1 - \frac{\frac{R_{\rm cir}}{R_{\rm loss}}}{\frac{R_{\rm cir}}{R_{\rm loss}} + \frac{R_{\rm cir}}{R_{\rm rad}}} \quad (10)$$

$$= 1 - \frac{(1-\Gamma_{\rm cap})(1+\Gamma_{\rm free})}{(1+\Gamma_{\rm cap})(1-\Gamma_{\rm free})} \quad (11)$$

$$= 1 - \frac{1-|\Gamma_{\rm cap}|^2}{1-|\Gamma_{\rm free}|^2}\frac{(1+\Gamma_{\rm free})^2}{(1+\Gamma_{\rm cap})^2} \quad (12)$$

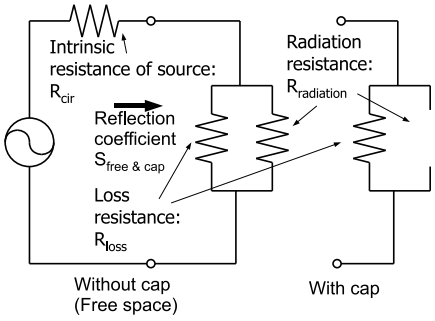


Figure 9: New equivalent circuit

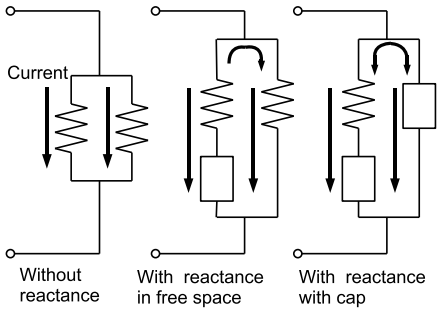


Figure 11: The model of problem of proposed expression

It is easy to compare the new formulation with the traditional wheeler efficiency using an existing reflection coefficient.

Fig. 10 shows the comparison between proposed expression. "Weff" shows traditional Wheeler efficiency as explained section 3.2. "Weff2" shows traditional Wheeler efficiency with resized cap. The cap size is 60 mm × 65 mm × 40 mm. Two result show that the radiation efficiency has depressed, the part where the error has occurred. However, The other part is nearly correct. "New_eff" and"New_eff2" show the results of proposed wheeler efficiency. "New_eff" is better than "Weff" at the part where the error has occurred. But in other part, "Weff" is better than "New_eff". "New_eff2" shows considerable result. This difference may be caused by the influence of the reflection that due to the disagreement of impedance. In other word, the change in the current is not considered in traditional expression.

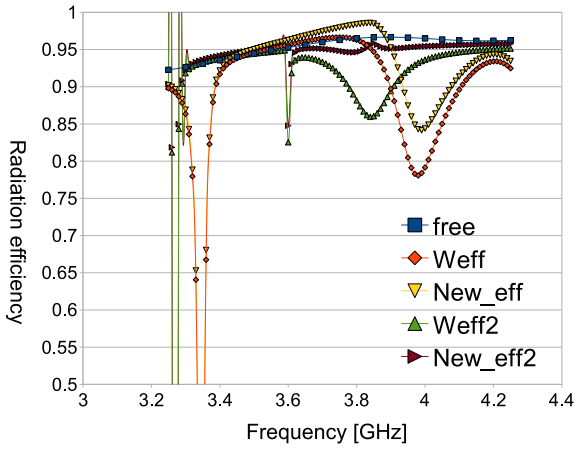


Figure 10: Comparison of proposed expression and existing expression

### 3.5 Problem of This Expression

The reactance element is not considered in this expression. Therefore, only a limited correction can be done. The model is shown in Fig. 11.

When there is no reactance element, The current in phase will flow in both losses and the radiation resistance. The electric power charged in the reactance element on the radiation loss side flows as shown in Fig. 11 when the reactance element exists. This doesn't become a problem. However, if the anteenna is capped, the resonant circuit was composed on the reactance element of the cap mutually and the reactance element of the antenna. Then, even if a new expression is used, a correct acoustic radiation efficiency can not be calculated because the current flows by behavior different from the expression thought above only due to the loss.

## 4 Conclusions

The Wheeler method was examined for the patch antenna based on the simulation. The current distribution in the frequency, where the error of the radiation efficiency has occurred without clear reason, was made visible with the simulator. In addition, We proposed the expression that was able to allow the change in impedance. Moreover, it can be applied in a part of the band where the error has occurred in the calculation.

## References

[1] H. A. Wheeler, "The Radiansphere Around a Small Antenna", Proceedings of IRE, vol. 47, no 8, pp.1325-1331, Aug. 1959.

[2] E. H. Newman, P. Bohley, and C. H. Walter, "Two Methods for the Measurement of Antenna Efficiency", IEEE Transactions on Antennas and Propagation, vol. 23, no. 4, pp.457-461, July. 1975.

[3] K. Sakurai, K. Kikuchi, H. Arai, M. Ando and N. Goto, "Measurements of Antenna Efficiency Using Scaled Models by Wheeler Method," 1987 Spring National Convention Record, IEICE, S8-3, Mar. 1987.

[4] Ansoft HFSS, http://www.ansoft.com/products/hf/hfss/

# Determination of Material Parameters for Compacted Soil and Its Application to Stability Analysis

Student Number : 06M51332 Name : Shinichi WATANABE Supervisor : Prof.Hideki Ohta

## 締固め粗粒材料の土質定数決定法と安定解析への適用性

06M51332 太田研究室 渡邉 真一

道路盛土やフィルダム等の土構造物は，さまざまな粒径の土粒子からなる粗粒材料を締固めて作られる。これらの土構造物に要求される性能（構造物や車両重量の支持，透水性等）を満たす様に設計・施工を行うには，締固め土の強度・変形特性に関する土質定数を求める必要がある。本研究では等価先行圧密応力の考え方に基づき締固め土の土質定数を求める。また求めた土質定数を用いて地震時の安定解析を行いその適用性を調べた。

## 1 Introduction

Most of geotechnical structures, such as road and airport embankment, dam, river bank, are made of compacted granular materials. In construction of the structures, quality management of compaction is made by indicators represented by D value in connection with dry density and water content of soil. This is based on Proctor's principle. However, the dry density of soil is not directory connected with deformation and strength parameters. In order to achieve required performances of compacted earth structures such as safety factor of slope failure, bearing capacity and permeability, it is very important to accurately estimate the material parameters for use in design and prediction of deformation behaviour of the compacted earth structures. The purpose of this research is 1) to suggest the procedure of material parameter determination of compacted granular materials using large-scale constant volume direct simple shear test, based on the theory of Ohta and Hata (1977), and 2) to verify applicability of the estimated parameters for using the stability problem of highway embankment in earthquake.

## 2 Description of analyzed site

Noto toll road is connected between Kanazawa and Noto region which was opened to traffic in 1982. Since passing along the 45m - 245 m altitude in north of Yanagida IC, most of this road are comparatively high embankment sections which are over 20m in height. The characteristics of fill materials are the remarkable swelling one and the strength reduction by slaking. Disasters due to heavy rain have been frequently occurred in the past. Noto-Hanto earthquake was occurred on March 25, 2007 which was the maximum acceleration of 945gal and considered as the maximum scale of earthquake which have occurred in this area since 1600's. There were 11 slope failures at parts of the Noto toll road. In this study, Section 9 is selected as analyzed site which occurred the large-scale slope failure. Fig.1 shows the collapse of the Section 9 after Noto-Hanto earthquake. The Section 9 was the high embankment section about 30m high, it got down over about 140m of length, and the traffic lane assumed three blocks on the west side was collapsed, and collapsed soil were pushed out by the lower slope surface.


Fig. 1 NOTO tall way section 9

## 3 Analysis method

In this research, stability analysis of embankment in case of the earthquake using the estimated material parameters by large-scale constant volume direct simple shear test is conducted. A method of seismic coefficient is used for evaluating the influence on the earth structure by earthquake motion. As for method of seismic coefficient, when the earthquake acceleration A acts on foundation ground, the inertia force of AW/g acts on the superstructure of a weight W. A/g at this time is defined as seismic coefficient $K_h$. In this study, stability analysis is conducted by applying this method of seismic coefficient to both the slice method and the two-dimensional finite element analysis. The slice method is one of the limit equilibrium methods using the strength parameters of soil. This method is the approach of estimating for the factor of safety using the shear force and the shearing resistance of acting on a fracture surface of embankment. In the slice method, each shear force and shearing resistance are calculated by

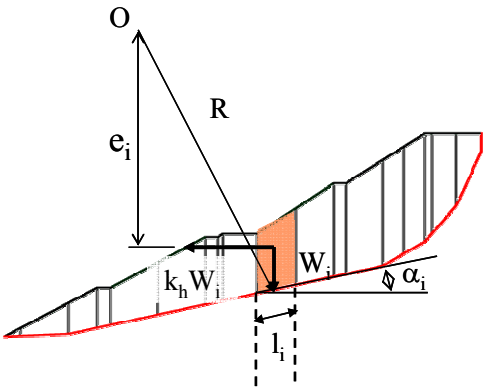


Fig. 2 Applied force of slice

dividing the block on the fracture surface shown in Figure 2. Moreover, the strength of soil is formulated by the failure criterion of Equation 1.

$$\tau_f = \sigma_v \tan\phi + c \qquad (1)$$

where $\tau_f$ : shear strength, $\sigma_v$ :normal stress, c,$\phi$ :strength parameter

The factor of safety is shown in Equation 2.

$$F_s = \frac{\sum_{i=1}^{n}\left\{c_i l_i + \left(W_i \cos\alpha_i - k_h W_i \sin\alpha_i - u_i l_i\right)\tan\phi_i\right\}}{\sum_{i=1}^{n} W_i\left(\sin\alpha_i + \frac{e_i k_h}{R}\right)} \qquad (2)$$

where variables in Eq.2 are shown Fig.2.

Finite element method is the numerical approach of dividing structure into many elements and calculating deformation behavior etc. Finite element code used in this study is DACSAR-M proposed by Takeyama (2007) employing the elasto plastic model of EC model proposed by Ohno (2006).

## 4 Determination of material parameters

### 4.1 Sample Data

By using undisturbed samples collected from the construction site for laboratory test, the experimental results can be obtained and classified as soil parameters in Table.1.

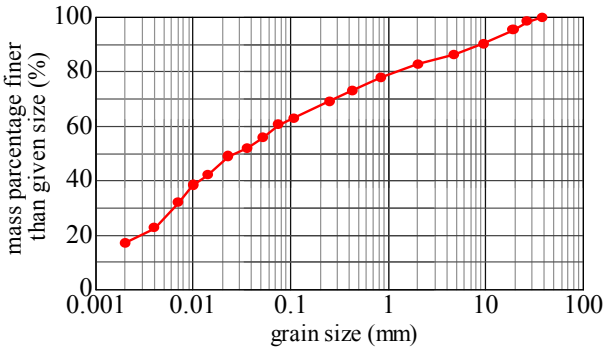


Fig. 3 Gading curves

Table. 1 Soil parameter

| soil property | | | |
|---|---|---|---|
| dry density | $\rho_d$ | (kN/m$^3$) | 13.6 |
| soil density | $\rho_d$ | (kN/m$^3$) | 26.5 |
| void ratio | e | | 0.95 |
| saturated water content | $w_{sat}$ | (%) | 35.7 |

### 4.2 Pre-consolidation stress

An attempt was used to simple dynamic compaction by static consolidation stress at laboratory level. The concept referred to previous research by Ohta and Hata. (1977) said that pre-consolidation stress can be defined through $e-\log\sigma_v'$ curve which is converted from the settlements plotted against the static consolidation pressures (believed to be equivalent with dynamic compaction).

From the prospected pre-consolidation stress applied as a normal pressure in constant volume direct simple shear test, the shear strength of compacted soil can be then obtained from the laboratory experiment.

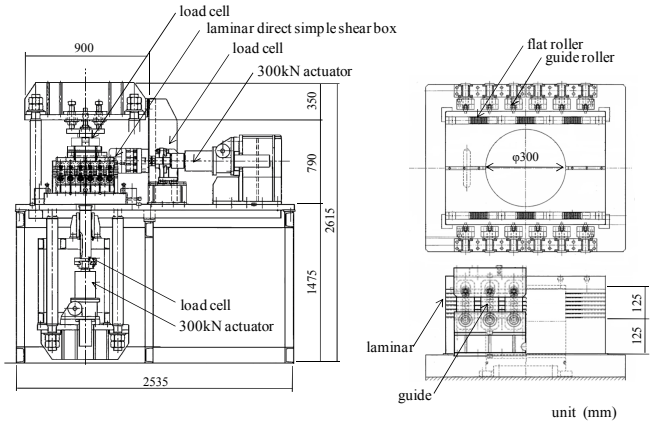


Fig. 4 Large-scale simple shear apparatus

In this study, large-scale constant volume direct simple shear apparatus developed by Ishigaki et.al.(2008) was employed in order to estimate the shear resistance of sample soil. Firstly, pre-consolidation stress was defined by referring to the $e-\log\sigma_v'$ curve and the void ratio at the construction site. Experimental result shows that the pre-consolidation stress is about 848.9 kPa.

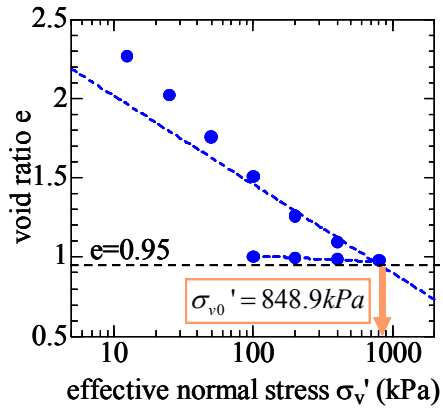


Fig. 5 e-logσ'$_v$ and pre-consolidation stress

### 4.3 Strength Parameter

Shear strength parameter can be obtained form direct simple shear test. In this study constant volume direct simple shear (DSS) test has been conducted with specimen consolidated under pre-consolidation pressure 800.0 kPa approximated to the real construction site. Test condition of DSS is shown Fig.6.

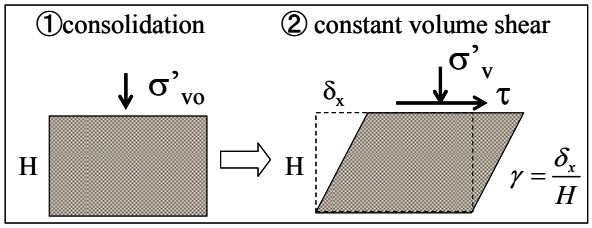


Fig. 6 Condition of specimen while DSS

Constant volume DSS test were conducted 4 stages with 4 different consolidation pressures. And each initial normal stress is 100kPa, 200kPa, 400kPa and 800kPa. The experimental result is shown in Fig.7.

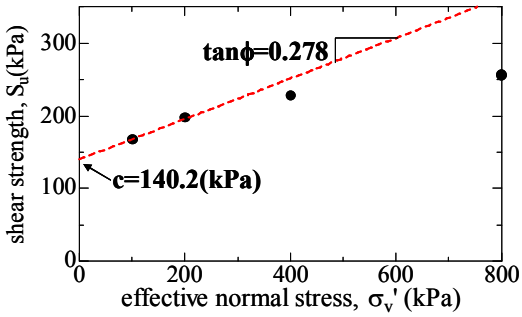


Fig. 7 failure criterion and strength parameter

From this result strength parameters are determined with c=140.2 kPa and ϕ =15.5 degrees.

### 4.4 Constitute parameters

Constitute parameters for modeling are determined by the result of consolidation test and DSS test. According to the flow chart shown in Fig.8 constitute parameters were determined as Table.2.

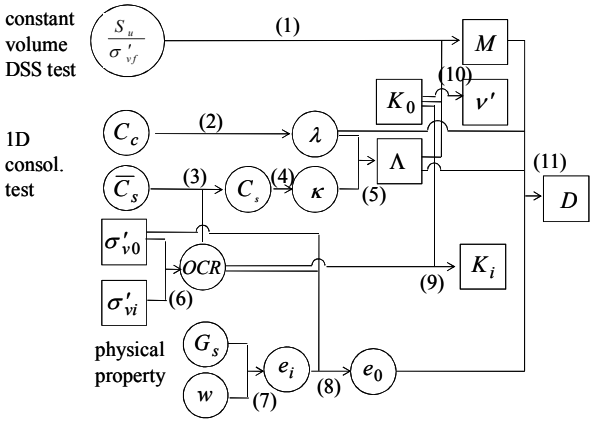


Fig. 8 Flow chart of parameter determination

Table. 2 constitute parameters

| D | Λ | λ | M | ν | $\sigma_{v0}$ | $K_0$ |
|---|---|---|---|---|---|---|
| 0.106 | 0.920 | 0.243 | 1.195 | 0.333 | 869 | 0.500 |

Fitting parameter $n_E$ is determined by trial value (herein 2.5) to fit the DSS simulation result to the experimental result. Result of simulation and experiment of DSS are shown in Fig.9.

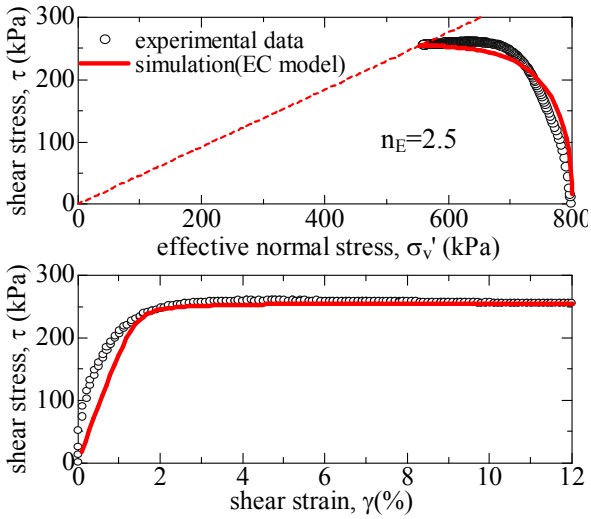


Fig. 9 constant simple shear test result and simulation result

It is confirmed that the constitutive parameters shown in Table 2 are adequately determined. Because the result of simulation agrees with experimental result.

## 5 Result of analysis

### 5.1 Slice method

2 kinds of failure surfaces 1 and 2 are set as shown in figure 10. Failure surface 1 is considered as a true failure surface, whereas failure surface 2 is considered as an optimum circular arc fitting the true failure surface.

Safety factors against the seismic coefficients are analyzed under condition of fully saturated and unsaturated. The analysis results under those different conditions can be plotted as shown in figure 11.

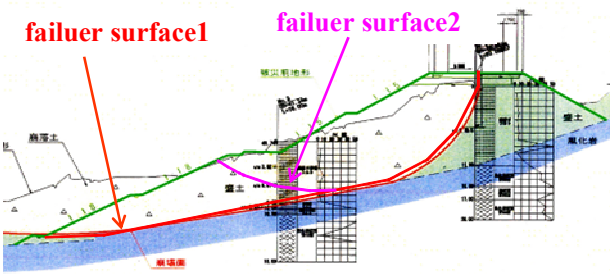


Fig. 10 failure surface

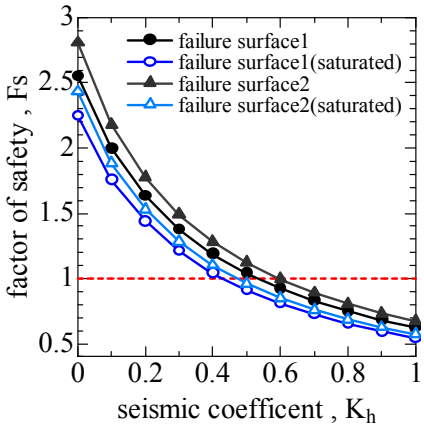


Fig. 11 Result of slice method

Observed maximum seismic acceleration was about 1G.Then estimated $K_h$ is 1.0 and coresponding Fs is smaller than 1.0. Therefore this analysis is considered reasonable.

### 5.2 Elasto-plastic FE analysis

Another attempt was carried on the same failure slope by using elasto-plastic FE analysis. Mobilized mass was meshed as small elements and boundary was assumed by the potential discontinuity plane which separated the mobilized mass from the rigid body. Seismic coefficient was simplified as horizontal force acting laterally and subjected to increase the driving moment (see Fig.12).

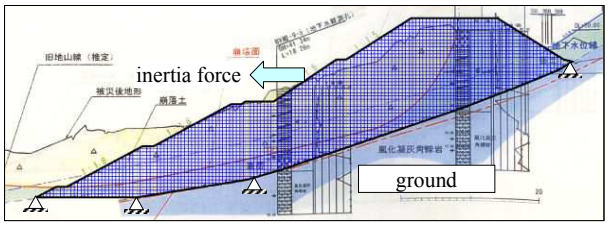


Fig. 12 Mesh formulation in FE analysis

Deformation displayed by the FE analysis result showed as in Fig.13 without tension crack and in Fig.14 with assumed crack element respectively. Each result shows the failure elements are developed at boundary. However, observational data of failure does not coincident with this result. Therefore, elasto-plastic FE analysis is not practice in this case.

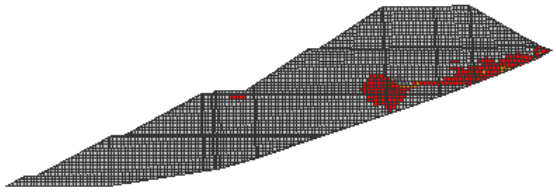

Fig. 13 Result of FE analysis (no clack elements)

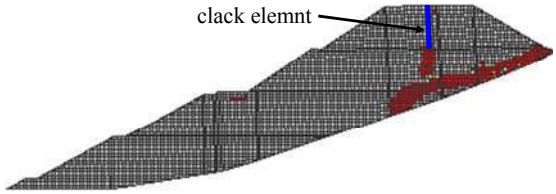


Fig. 14 Result of FE analysis (with clack elements)

To obtain reasonable result by FE analysis applied method of seismic coefficient, more reasonable conditions are needed to be considered.

## 6 Conclusions

- Adequate soil parameters have been obtained from experiment with specimen which is equivalently consolidated to site fill material
- Slice method considering 4case has been conducted and obtained reasonable result.
- Because of unreasonable Boundary condition, elasto-plastic FEM applied the method of seismic coefficient shows unreliable deformation compared to the site observation.

## References

Ohta,H. and Hata,S.: Strength of dynamically compacted soils, Proceedings of the 9th Conference of JCSMFE, Tokyo, pp.239-242, 1977

竹山智英 ： 土／水連成有限要素解析手法における解の信頼性に関わる諸問題とその理論的解決方法，東京工業大学学位論文, 2007

大野進太郎：非線形コントラクタンシー表現関数に基づく地盤材料の弾塑性構成モデル，東京工業大学学位論文,2006

石垣勉，渡邉真一，尾本志展，太田秀樹：静的締固め粗粒材料の等体積単純せん断挙動，土木学会舗装工学論文集，第 13 巻, 2008

# THE APPLICATION OF MACRO-ELEMENT METHOD TO ANALYSIS FOR BEHAVIOR OF SOFT GROUND IMPROVED BY VERTICAL DRAINS

Student Number: 07M18013 Name: Aki Arai Supervisor: Hideki OHTA and Thirapong PIPATPONGSA

# 鉛直ドレーンが打設された軟弱地盤の動態解析におけるマクロエレメント法の適用

荒井　亜希

鉛直ドレーンが打設された現場に対しては、三次元的な取り扱いが必要となる。しかし、このような現場を二次元平面ひずみ条件で解析する場合には再現が難しい。そこで、この問題を解決するため、関口ら(1986)は鉛直ドレーンの排水効果を要素レベルで忠実に考慮できるマクロエレメント法を提案した。本研究では、鉛直ドレーンが打設された現場を対象に、マクロエレメント法を適用した土／水連成有限要素解析を行い、当該手法の妥当性の検討を行った。また、実地盤の挙動をより正確に再現できる土の構成モデルを選択するため、せん断速度に着目した非排水三軸圧縮試験を行い、シミュレーションと比較することにより考察を行った。

## 1. Introduction

Original Cam-Clay model[1] and Modified Cam-Clay model[2] are widely used as a constitutive model of soils. The undrained effective stress path obtained by a normal shear tests are said to be good agreement with the simulation by Modified Cam-Clay model rather than Original Cam-Clay model. However, the shear rate required by the normal test is about two orders than the shear rate measured at the real construction site. Therefore I perform undrained triaxial compression tests at two different constant shear axis strain rates are performed in order to clarify which model is better used for analysis.

From the laboratory test results, the performance of each constitutive model represented the behavior of the true ground will be able to be justified.

In addition, analysis is also extended to the ground improvement by vertical drains (see Fig-1) under 2-dimentional plain strain condition. Even thought the treatment of 3 dimensions is needed, an application of the macro-element method suggested by Sekiguchi (1986)[3] to overcome the problem is believed. And I thus examined the validity of this method.

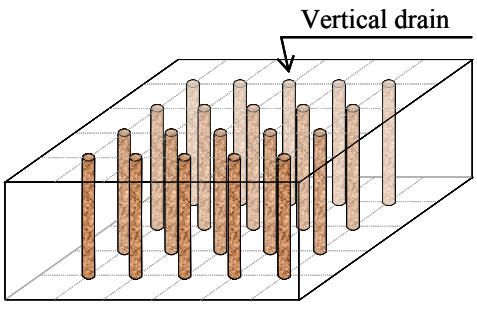


Fig-1 Ground improvement by vertical drains

## 2. The Outline of Triaxial Tests

The samples[4] used in this study are the undisturbed samples of clay obtained from various sites in Japan. By boring investigation, soil data were obtained for each sample and shown in Table-1.

The test procedure is as follows: At first I saturate a specimen and take back pressure ($u$=290kPa). Then, I perform an isotropic consolidation and a constant volume compression test. About 2 times pressure of the pre-consolidated stress is applied during 24 hours. In the shearing process, the axis strain rate was set to be 0.05%/min and 0.005%/min. The details of the test condition are shown in Table-2.

Table-1 Test samples

| Sampling Position | Saitama | Urayasu | Urayasu | Urayasu |
|---|---|---|---|---|
| Depth (m) | GL -11.50 ~ -12.33 | GL -29.0 ~ -29.9 | GL -22.0 ~ -22.7 | GL -29.00 ~ -29.88 |
| Specific gravity $G_s$ | 2.743 | 2.693 | 2.679 | 2.68 |
| Natural water content $w_n$ (%) | 43.8 | 61.9 | 64.3 | 80.4 |
| Void ratio $e$ | 1.224 | 1.749 | 1.775 | 2.164 |
| Liquid limit $w_L$ | 45.4 | 74.2 | 92.3 | 112.4 |
| Plastic limit $w_p$ | 25.4 | 29.9 | 33.3 | 37.4 |
| Plasticity index $I_p$ | 20 | 44.3 | 59 | 75 |
| Compression index $C_c$ | 0.45 | 0.68 | 0.93 | 1.14 |
| Pre-consolidated stress $P_c$ (kN/m²) | 139 | 260 | 290 | 300 |

Table-2 Test cases

| No. | Sampling Position | Depth (m) | Consolidation stress (kN/m²) | Axial strain rate (%/min) |
|---|---|---|---|---|
| ① | Saitama | GL -11.50 ~ -12.33 | 300 | 0.05 |
| ② | Urayasu | GL -29.0 ~ -29.9 | 550 | 0.05 |
| ③ | Urayasu | GL -22.0 ~ -22.7 | 600 | 0.05 |
| ④ | Urayasu | GL -29.00 ~ -29.88 | 600 | 0.05 |
| ⑤ | Saitama | GL -11.50 ~ -12.33 | 300 | 0.005 |
| ⑥ | Urayasu | GL -29.0 ~ -29.9 | 550 | 0.005 |
| ⑦ | Urayasu | GL -22.0 ~ -22.7 | 600 | 0.005 |

## 3. The Results of Triaxial Tests

In the simulation, A specimen is modeled as one element, and used the elasto-viscoplastic constitutive model proposed by Sekiguchi and Ohta[5].The input parameters needed for the Sekiguchi and Ohta's model are summarized in Table.3. These are the parameters for the elasto-plastic materials.

Table-3 Material parameters

| | |
|---|---|
| $\Lambda$ | Irreversibility ratio |
| $M$ | Critical state parameter |
| $D$ | Coefficient of dilatancy |
| $\nu'$ | Effective poisson ratio |
| $\alpha$ | Coefficient of secondary compression |
| $\dot{v}_0$ | Initial volumetric strain rate |
| $\sigma'_{v0}$ | Preconsolidation vertical pressure |
| $K_0$ | Coefficient of earth pressure at rest |
| $\sigma'_{vi}$ | Effective overburden pressure |
| $K_i$ | Coefficient of in-situ earth pressure at rest |

First, plasticity index $I_p$, void ratio at preconsolidated state $e_0$, compression index $\lambda$ and swelling index $\kappa$ that was already obtained by boring investigation are used in the simulation. $K_i$ and $K_0$ assumed as 1.0, $\nu'$ is also assumed as 0.3. $M$ is obtained from the experimental result. The input parameters used for the simulation are summarized in Table-4.

Table-4 Input parameters for simulation

| No. | $I_p$ | $e_0$ | $\lambda$ | $\kappa$ | $D$ | $\Lambda$ | $M$ | $\nu'$ | $\alpha$ | $\dot{v}_0$ | $K_0$ | $\sigma'_{v0}$ (kPa) | $K_i$ | $\sigma'_{vi}$ (kPa) |
|---|---|---|---|---|---|---|---|---|---|---|---|---|---|---|
| ① | 20 | 1.224 | 0.195 | 0.00638 | 0.0502 | 0.8617 | 1.508 | 0.3 | 0.0044 | 2E-05 | 1 | 300 | 1 | 300 |
| ② | 44.3 | 1.749 | 0.295 | 0.00885 | 0.0613 | 0.8914 | 1.56 | 0.3 | 0.0054 | 2E-05 | 1 | 550 | 1 | 550 |
| ③ | 59 | 1.775 | 0.404 | 0.01645 | 0.0831 | 0.8543 | 1.495 | 0.3 | 0.0073 | 2E-05 | 1 | 600 | 1 | 600 |
| ④ | 75 | 2.164 | 0.495 | 0.02083 | 0.0894 | 0.8657 | 1.515 | 0.3 | 0.0078 | 2E-05 | 1 | 600 | 1 | 600 |
| ⑤ | 20 | 1.224 | 0.195 | 0.00638 | 0.0502 | 0.8954 | 1.567 | 0.3 | 0.0044 | 2E-05 | 1 | 300 | 1 | 300 |
| ⑥ | 44.3 | 1.749 | 0.295 | 0.00885 | 0.0613 | 0.8331 | 1.458 | 0.3 | 0.0054 | 2E-05 | 1 | 550 | 1 | 550 |
| ⑦ | 59 | 1.775 | 0.404 | 0.01645 | 0.0831 | 0.8543 | 1.495 | 0.3 | 0.0073 | 2E-05 | 1 | 600 | 1 | 600 |

The results are shown in Fig-2. From Fig-2, the effective stress path at fast strain rate adopted in normal laboratory test becomes close to an undrained shear simulation of Modified Cam-Clay model (MCC). And the effective stress path of the shear rate that occurred in the real site is slow and closed to an undrained simulation of Original Cam-Clay model (CC). From this results, when we choose a constitutive model of FEM analysis, it is thought that a choice may reproduce real ground behavior model more precisely with Original Cam-Clay model (CC) than with Modified Cam-Clay (MCC).

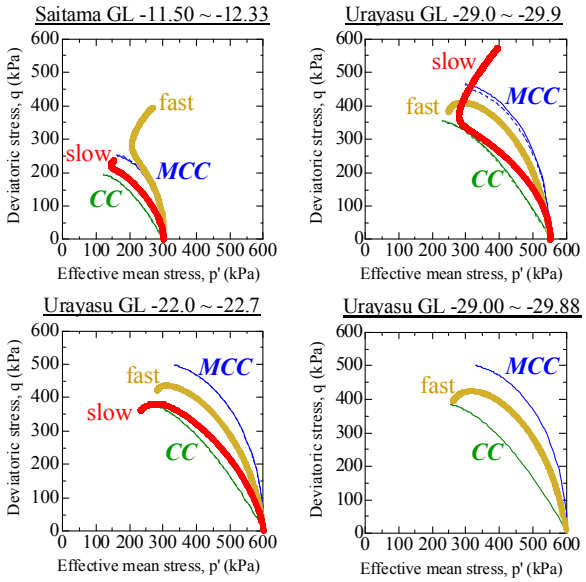


Fig-2 Comparison of effective stress path

## 4. Macro-Element Method

As shown in the Fig-3, it is supposed that there is one vertical drain in a macro-element. The water discharge from a macro-element is calculated as water discharge from the perimeters of element and vertical drain. By using this method, the effect of vertical drains can be considered appropriately even under 2-dimensional condition.

In this study 2 construction sites are simulated by employing this method.

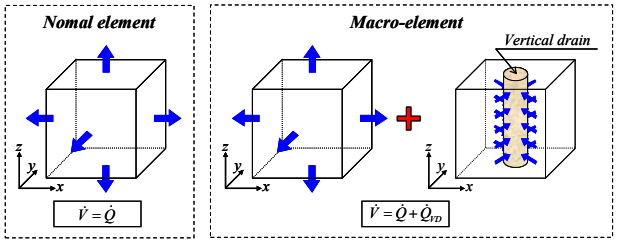


Fig-3 Basic concept of continuity condition equation

## 5. Site Ⅰ (Ohsawago, Akita)

The first site of the analysis is the highway embankment constructed on Ohsawago-site of Akita line of Tohoku transversal highway.[6] Fig-4 shows the analyzed cross section of the embankment.

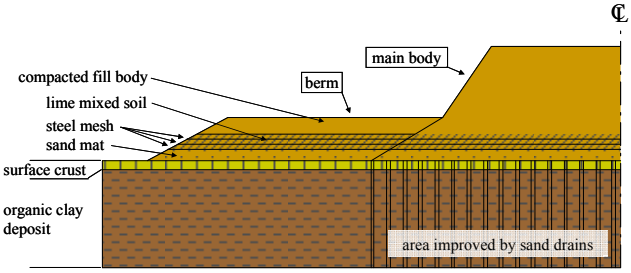


Fig-4 Analyzed cross section

## 6. The Input Conditions in Analyses

From a consideration of the experimental results, Sekiguchi and Ohta's model was employed in the analysis. Sekiguchi and Ohta's model is expanded from the Original Cam-Clay model so that can express the aisotropic state.

### 6-1 The material parameters

The list of the material parameters used for analysis is presented in Table-5.

Table-5 Material parameters

| Type of soil | Depth [m] | Thickness [m] | $\sigma_{vi}$ [kN/m$^2$] | $\sigma_{vi}$ [kN/m$^2$] | $K_0$ | $M$ | $K_i$ | $\nu'$ | $\lambda$ | $\lambda_0$ | $\Lambda$ | $e_0$ | $D$ | $k$ [m/day] |
|---|---|---|---|---|---|---|---|---|---|---|---|---|---|---|
| Embankment | | | 6.9 | 92.1 | 0.70 | 1.850 | 1.00 | 0.330 | 0.210 | 0.210 | 0.900 | 1.36 | 0.04300 | 8.60E-03 |
| Sand mat | | | 11.5 | E = 51.2E+03 [kN/m$^2$] | | | 1.00 | 0.330 | | | | 1.36 | | 6.00E-01 |
| Surface crust | 0.0 ~ 0.7 | 0.7 | 2.0 | E = 7.5E+03 [kN/m$^2$] | | | 1.00 | 0.330 | | | | 8.70 | | 3.32E-04 |
| Peat | 0.7 ~ 1.0 | 0.3 | 4.1 | 21.0 | 0.34 | 1.693 | 0.12 | 0.254 | 2.127 | 2.127 | 0.854 | 9.22 | 0.10494 | 3.32E-04 |
| | 1.0 ~ 2.0 | 1.0 | 4.6 | 10.4 | 0.34 | 1.693 | 0.19 | 0.254 | 2.127 | 2.127 | 0.867 | 9.52 | 0.10355 | 3.32E-04 |
| | 2.0 ~ 3.0 | 1.0 | 5.4 | 5.4 | 0.34 | 1.693 | 0.34 | 0.254 | 2.127 | 2.127 | 0.890 | 9.79 | 0.10362 | 3.32E-04 |
| | 3.0 ~ 4.0 | 1.0 | 6.2 | 6.2 | 0.34 | 1.693 | 0.34 | 0.254 | 2.127 | 2.127 | 0.941 | 9.80 | 0.10941 | 3.32E-04 |
| | 4.0 ~ 5.0 | 1.0 | 7.8 | 7.8 | 0.40 | 1.501 | 0.40 | 0.286 | 1.116 | 1.116 | 0.918 | 5.14 | 0.11109 | 1.20E-04 |
| | 5.0 ~ 6.0 | 1.0 | 10.4 | 10.4 | 0.42 | 1.429 | 0.42 | 0.297 | 0.743 | 0.743 | 0.914 | 3.55 | 0.10444 | 1.20E-04 |
| | 6.0 ~ 7.0 | 1.0 | 12.9 | 12.9 | 0.42 | 1.448 | 0.42 | 0.294 | 0.841 | 0.841 | 0.948 | 4.29 | 0.10401 | 1.20E-04 |
| | 7.0 ~ 8.0 | 1.0 | 15.3 | 15.3 | 0.41 | 1.467 | 0.41 | 0.291 | 0.939 | 0.939 | 0.969 | 5.11 | 0.10149 | 1.20E-04 |
| | 8.0 ~ 9.0 | 1.0 | 17.4 | 17.4 | 0.40 | 1.485 | 0.40 | 0.288 | 1.036 | 1.036 | 0.978 | 5.98 | 0.09772 | 1.20E-04 |
| | 9.0 ~ 9.5 | 0.5 | 19.0 | 19.0 | 0.44 | 1.382 | 0.44 | 0.305 | 0.496 | 0.496 | 0.955 | 3.00 | 0.08582 | 1.20E-04 |
| Clay | 9.5 ~ 10.0 | 0.5 | 21.0 | 33.8 | 0.55 | 1.155 | 0.70 | 0.355 | 0.287 | 0.287 | 1.136 | 1.80 | 0.08507 | 8.00E-05 |
| | 10.0 ~ 11.0 | 1.0 | 25.3 | 40.7 | 0.55 | 1.155 | 0.70 | 0.355 | 0.260 | 0.260 | 1.149 | 1.64 | 0.08156 | 8.00E-05 |
| | 11.0 ~ 12.0 | 1.0 | 31.2 | 50.2 | 0.55 | 1.155 | 0.70 | 0.355 | 0.260 | 0.260 | 1.149 | 1.64 | 0.08156 | 8.00E-05 |
| Silty sand | 10.0 ~ 11.0 | 1.0 | 25.3 | E = 5.9E+04 [kN/m$^2$] | | | 0.50 | 0.330 | | | | 1.59 | | 1.0E+00 |
| | 11.0 ~ 12.0 | 1.0 | 31.2 | E = 5.9E+04 [kN/m$^2$] | | | 0.50 | 0.330 | | | | 1.59 | | 1.0E+00 |
| | 12.0 ~ 13.0 | 1.0 | 37.1 | E = 5.9E+04 [kN/m$^2$] | | | 0.50 | 0.330 | | | | 1.59 | | 1.0E+00 |
| | 13.0 ~ 14.0 | 1.0 | 43.0 | E = 5.9E+04 [kN/m$^2$] | | | 0.50 | 0.330 | | | | 1.59 | | 1.0E+00 |
| Sand | 10.0 ~ 11.0 | 1.0 | 25.3 | E = 5.9E+04 [kN/m$^2$] | | | 0.50 | 0.330 | | | | 1.59 | | 1.0E+00 |
| | 11.0 ~ 12.0 | 1.0 | 31.2 | E = 5.9E+04 [kN/m$^2$] | | | 0.50 | 0.330 | | | | 1.59 | | 1.0E+00 |
| | 12.0 ~ 13.0 | 1.0 | 37.1 | E = 5.9E+04 [kN/m$^2$] | | | 0.50 | 0.330 | | | | 1.59 | | 1.0E+00 |
| | 13.0 ~ 14.0 | 1.0 | 43.0 | E = 5.9E+04 [kN/m$^2$] | | | 0.50 | 0.330 | | | | 1.59 | | 1.0E+00 |
| | 14.0 ~ 15.0 | 1.0 | 48.8 | E = 5.9E+04 [kN/m$^2$] | | | 0.50 | 0.330 | | | | 1.59 | | 1.0E+00 |

### 6-2 Modeling of sand drains

The modeling of the sand drain can be performed by two kinds of method. One is macro-element method and another is a method to reproduce the clay ground by increasing coefficient of permeability of the ground. In the case of this method, Coefficient of permeability is converted so that times for 50% consolidation of horizontal and vertical direction are the same. The factor for permeability is obtained as 75.3.

### 6-3 The mesh formation and the boundary conditions

The mesh formation used in analysis is shown in Fig-5 and boundary condition is also shown in Fig-5.

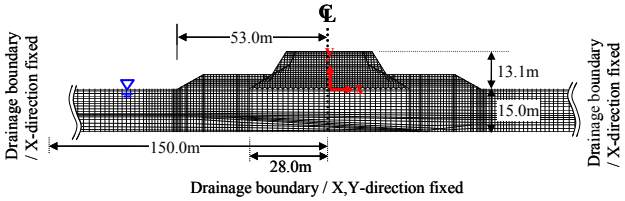


Fig-5 Mesh formation

## 7. The Results of Analyses

The locations obtained from the measurement instrument and the locations indicated by the result of the analysis are shown in Fig-6.

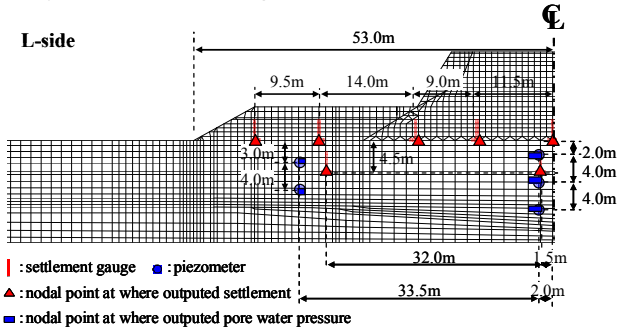


Fig-6 Setting positions of observation instruments

The results of the analysis are shown in Fig-7 and Fig-8. A solid line is the result of macro-element method applied and a dashed line is the result obtained by the method of changing a coefficient of permeability. It may be said that the analysis result used macro-element method can reproduce a behavior of the ground at the center of embankment.

Although the measured values near the center of embankment are smooth, there are the moments of which suddenly large settlement has occurred under the berm (is represented by the number at (c), (d), (e), (g) in Fig-7). According to this sudden large settlement suddenly occurred and the cracks observed at the slope of the main body and the center of the berm, it is thought that the slip was occurred as shown in Fig-7. The FEM program used in this research is not able to represent a discontinuous surface such as a slip surface.[7] This caused the difference between the computed settlement and the measured value under the beam after the extrapolated time when the slip occurred.

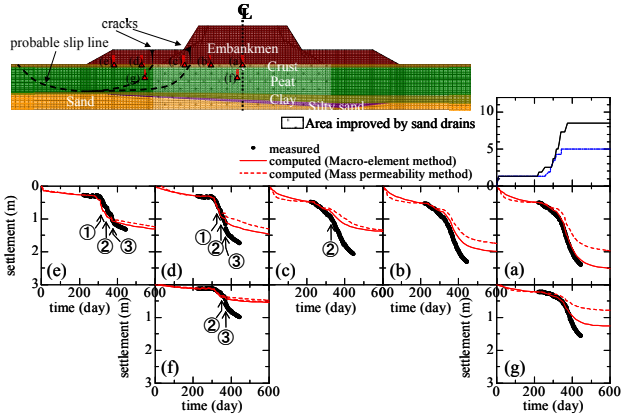


Fig-7 Settlement

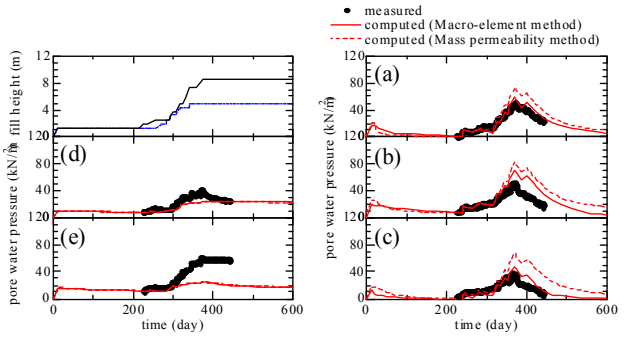


Fig-8 Excess pore water pressure

## 8 Site Ⅱ (Sri Lanka)

The second site of analysis is the highway embankment constructed on the site of the southern part of Sri Lanka.[8] Fig-9 shows the analyzed cross section.

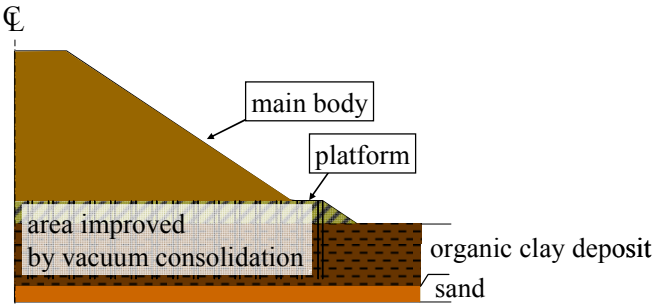


Fig-9 Analyzed cross section

## 9. The Input Conditions in Analysis

### 9-1 The material parameters

The material parameters used for analysis is listed in Table 6.

Table-6 Material parameters

| Type of soil | Depth [m] | Thickness [m] | $\sigma_{ci}$ [kN/m²] | $\sigma_{c0}$ [kN/m²] | $K_0$ | $M$ | $K_i$ | $\nu'$ | $\lambda$ | $\lambda_2$ | $\Lambda$ | $e_0$ | $D$ | $k$ [m/day] |
|---|---|---|---|---|---|---|---|---|---|---|---|---|---|---|
| Embankment | | | 6.900 | 92.1 | 0.700 | 1.850 | 1.00 | 0.330 | 0.210 | 0.210 | 0.900 | 1.360 | 0.043 | 8.60E-03 |
| Platform | | | 6.900 | 92.1 | 0.700 | 1.850 | 1.00 | 0.330 | 0.210 | 0.210 | 0.900 | 1.360 | 0.043 | 8.60E-03 |
| Peat | 0.0 ～ 0.5 | 0.5 | 0.549 | 14.0 | 0.595 | 1.619 | 4.88 | 0.373 | 1.736 | 1.736 | 0.803 | 4.018 | 0.172 | 4.00E-03 |
| | 0.5 ～ 1.0 | 0.5 | 1.648 | 14.0 | 0.595 | 1.619 | 2.39 | 0.373 | 1.736 | 1.736 | 0.817 | 4.209 | 0.168 | 4.00E-03 |
| | 1.0 ～ 1.5 | 0.5 | 2.757 | 14.0 | 0.595 | 1.619 | 1.72 | 0.373 | 1.736 | 1.736 | 0.824 | 4.297 | 0.167 | 4.00E-03 |
| | 1.5 ～ 2.0 | 0.5 | 3.855 | 14.0 | 0.595 | 1.619 | 1.38 | 0.373 | 1.736 | 1.736 | 0.828 | 4.356 | 0.166 | 4.00E-03 |
| Peaty clay | 2.0 ～ 2.5 | 0.5 | 5.082 | 14.0 | 0.595 | 1.412 | 1.01 | 0.373 | 0.651 | 0.651 | 0.853 | 2.514 | 0.112 | 4.00E-03 |
| | 2.5 ～ 3.0 | 0.5 | 6.435 | 14.0 | 0.595 | 1.412 | 0.90 | 0.373 | 0.651 | 0.651 | 0.855 | 2.529 | 0.112 | 4.00E-03 |
| | 3.0 ～ 3.5 | 0.5 | 7.779 | 14.0 | 0.595 | 1.412 | 0.81 | 0.373 | 0.651 | 0.651 | 0.856 | 2.542 | 0.111 | 4.00E-03 |
| | 3.5 ～ 4.0 | 0.5 | 9.133 | 14.0 | 0.595 | 1.412 | 0.75 | 0.373 | 0.651 | 0.651 | 0.857 | 2.552 | 0.111 | 4.00E-03 |
| Sand | 4.0 ～ 4.5 | 0.5 | 11.18 | E = 5.9E+04 [kN/m²] | | 0.50 | 0.330 | | | | | | | 1.00E-03 |
| | 4.5 ～ 5.0 | 0.5 | 15.29 | E = 5.9E+04 [kN/m²] | | 0.50 | 0.330 | | | | | | | 1.00E-03 |

### 9-2 Modeling of vacuum consolidation

The modeling of vacuum consolidation is represented by two kinds of method. One is macro-element method and another is a method to reproduce the clay ground by decreasing coefficient of permeability of the ground. Then I alternate the mesh formation to perform negative pressure at the element boundary. But it overestimates a drainage effect by applying negative pressure. Therefore it is necessary to decrease the coefficient of permeability[9]. In this case method, coefficient of permeability is converted so that times for 50% consolidation of horizontal and vertical direction are the same. The factor for permeability is obtained as 0.175.

### 9-3 The mesh formation and the boundary conditions

The mesh formation used in analysis is shown in Fig-10 and boundary condition is also shown in Fig-10.

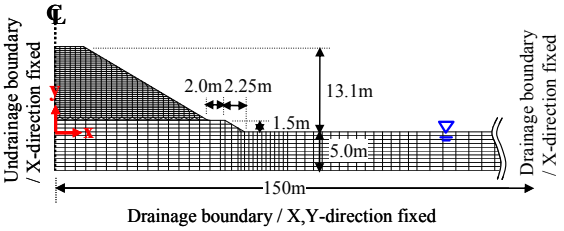


Fig-10 Mesh formation

## 10 The Result of Analysis

The locations obtained from the measurement instrument and the locations indicated by the result of the analysis are shown in Fig-11.

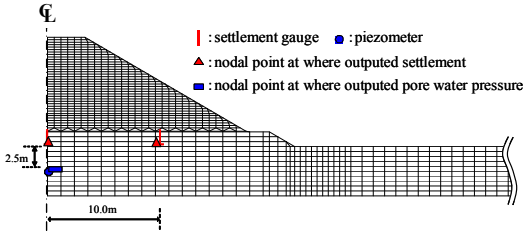


Fig-11 Setting positions of observation instruments

The results of the analysis are shown in Fig-12 and Fig-13. A solid line is the result obtained by using macro-element method and a dashed line is the result of the method of changing a coefficient of permeability. It may be said that the analysis result used macro-element method can reproduce a behavior of the ground at the center of embankment.

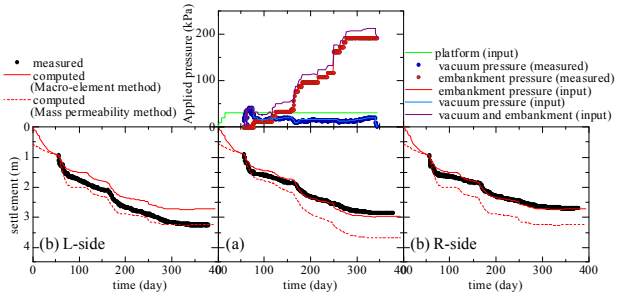


Fig-12 Settlement

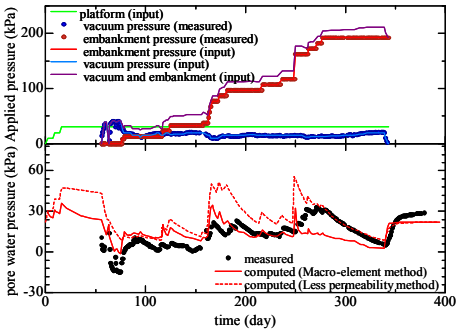


Fig-13 Pore water pressure

## 11. Conclusions

・The effective stress path by the triaxial compression tests in which shear rate is relatively fast agreed well with the simulation by employing the Modified Cam-Clay model. But the effective stress path by the triaxial compression tests with low shear rate derails from that of Modified Cam-Clay model, and get closer to the simulation by employing the Original Cam-Clay model. Therefore, we should choose the Original Cam-Clay model when simulating a real behavior of the ground with site artificial construction and the change of the external force by the natural phenomenon.

・ Simulation that reflected a process of the real construction could well reproduced settlement and pore water pressure observed on the site. So I was able to confirm validity of the macro-element method.

## References

1) Schofield,A.N. and Wroth,C.P. : Critical state soil mechanics, Chap.6, McGRAW-HILL, pp.135-166, 1968
2) Roscoe, K.H. and Burland, J.B. On the generalized stress-strain behavior of 'wet' clay. Engineering Plasticity, ed. J. Heyman and F.A. Leckie, Cambridge University Press: Cambridge, 1968; 535-609.
3) 関口秀雄, 柴田徹, 藤本朗, 山口博久 : 局部載荷を受けるバーチカル・ドレーン打設地盤の変形解析, 第31 回土質工学シンポジウム講演集, pp.111-116, 1986.
4) 応用地質資料
5) Ohta,H. and Sekiguchi,H. : Constitutive equations considering anisotropy and stress reorientation in clay, Proc. 3rd. Int. Conf. on Numerical Methods in Geomechanics, Vol.1, pp.475-484, 1979
6) 松永泰直 :「東北地方の地盤工学」, (社)地盤工学会, pp.252-258, 1997.
7) Ohta,H., Iizuka,A., Monda,S., Kuwahara,M. and Muta,T. : Progressive failure of soft clay under embankment, Proc. of 13th International Conference on Soil Mechanics and Foundation Engineering (ICSMFE), ISSMGE, Vol.2, pp.751-754, 1994.1
8) 大成建設資料
9) 竹山智英, 荒井亜希, 太田秀樹 : 真空圧密による改良域のモデル化, 地盤工学会関東支部発表会, 2008.

# Effect of Initial Water Curing Period on Chloride Permeability of Hardened Blast Furnace Cement

Student Number: 07M18020 Name: Shohei KIMURA Supervisor: Nobuaki OTSUKI

# 初期水中養生が高炉セメント硬化体の塩化物イオン拡散性におよぼす影響

木村祥平

現在，コンクリートの湿潤養生終了時期の決定等，コンクリートの品質を表す指標として広く用いられているのは圧縮強度であるが，コンクリートの物質透過性をはじめとした耐久性と圧縮強度は一義的な関係にないと考えられており，養生期間が耐久性に及ぼす影響は事実上考慮されていない状態にあるといえる．一方，従来から耐塩化物イオン浸透性が高いとされている高炉セメントは，短期の初期養生期間によりその性能が低下することが指摘されており，特に圧縮強度よりも耐塩化物イオン拡散性の低下が著しいといわれている．そこで，本研究では初期養生期間が高炉セメント硬化体の耐久性に及ぼす影響を水和反応および空隙構造の変化を関連付けて検討し，さらに高炉セメント硬化体の初期養生期間の短縮についても検討を行った．

## 1 introduction

Blast furnace slag is a material that is expected to be an action for environmental problems. According to Kyoto Protocol Aim, there is a policy that says amount of $CO_2$ emission in Japan must decrease by to increase proportion of blended cement to 24.8%. The percentage of blast furnace slag cement in blended cement is over 90%. Therefore it is a necessity to increase usage of blast furnace slag cement. However, recently the usage of blast furnace slag cement does not increase because blast furnace slag cement has several problems that are include low early strength.

Meanwhile, initial curing period of concrete is decided by JASS5J or Standard Specification for Concrete Structures and barometer of deciding initial curing period is compressive strength. However, Okazaki[1)] said that compressive strength and durability such as permeability do not have a principal concern. Nakarai[2)] said that short initial curing period occur the low compressive strength and low resistance of permeability compared with enough curing was given the concrete. Hara[3)] focus on relationship between initial curing period and pore distribution ,they said that short initial curing period affects the pore distribution of the range from 0.1μm to 1.0μm and concluded short curing period remain coarse pore.

There are some reports that examined an initial curing period and material permeability and a relationship of the pore distribution including an above-mentioned report. However it cannot be said that it was still argued enough. The research that considers even the continuousness of the pore in the pore distribution is few. It aimed to understand the effect that the initial curing period exerted on the chloride diffusive quantitatively in this research based on above, and to examine the change in the pore distribution according to the hydration mechanism. Moreover, examined the possibility of shorten the initial curing period of the early strength slag cement

## 2 Experimental Procedure

### 2.1 Materials Used

The materials used in this study are ordinary portland cement (OPC) and high early strength portland cement(HPC) to remedy low early strength and blast furnace slag powder(BFS , slag basicity:1.89 )

Table.1 shows chemical composition of these materials. BFS was added the gypsum 2mass% as $SO_3$ concentration. Fine aggregate used in this study is land sand from Chiba prefecture (Density 2.62 g/cm$^3$, water absorption 1.58%) .

Table.1 Chemical composition

| | Chemical composition (mass%) | | | | | | | | | Blaine(cm2/g) |
|---|---|---|---|---|---|---|---|---|---|---|
| | ig.loss | $SiO_2$ | $Al_2O_3$ | Fe2O3 | CaO | MgO | $SO_3$ | $Na_2O$ | $K_2O$ | |
| OPC | 1.05 | 20.38 | 5.18 | 3.37 | 63.96 | 1.88 | 2.24 | 0.4 | 0.4 | 3420 |
| HPC | 1.12 | 20.59 | 4.88 | 2.42 | 65.03 | 1.35 | 3.25 | 0.29 | 0.36 | 4620 |
| BFS | 0.49 | 33.58 | 14.26 | 0.41 | 43.13 | 6.05 | - | 0.24 | 0.35 | 4550 |

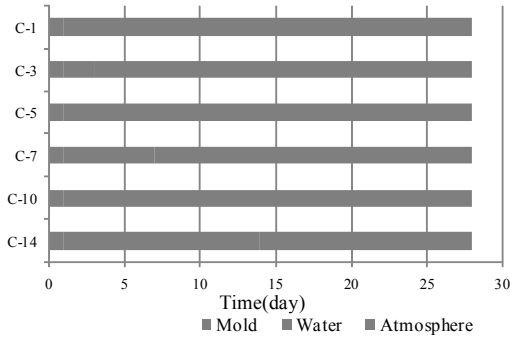


Fig.1 Details of curing

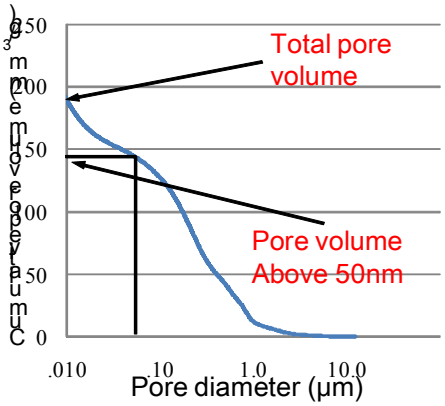


Fig.2
The example of mercury intrusion porosimetry test result

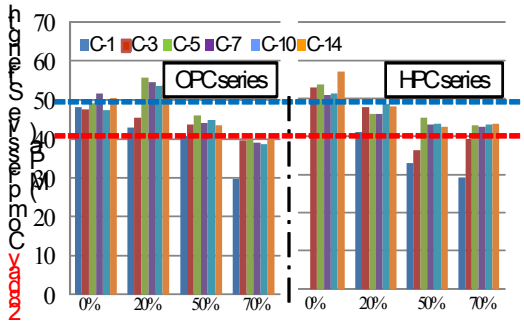


Fig.2 Results of compressive strength test

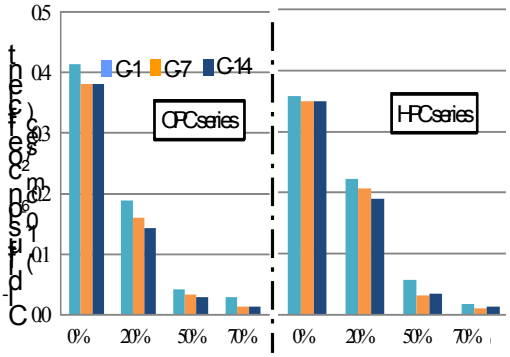


Fig.3 Results of chloride diffusion test

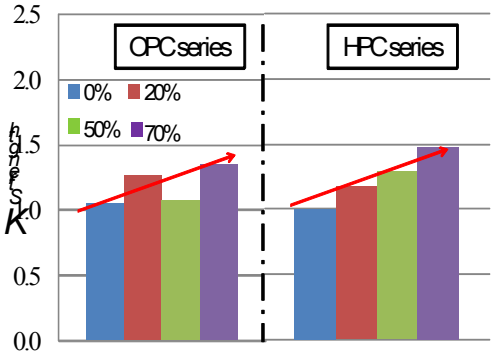


Fig.4 The sensitivity on compressive strength

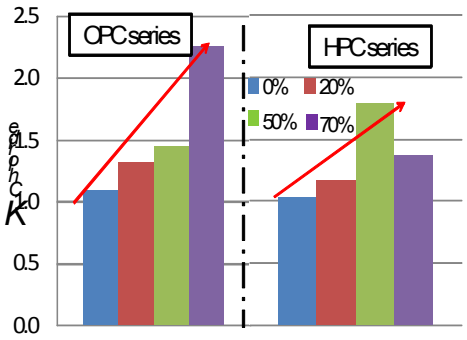


Fig.5
The sensitivity on chloride diffusion coefficient

## 2.2 Method of Manufacturing the Specimens

Water binder ratio was 0.5. Sand binder ratio was 3.0 of mortal for compressive strength test. The specimens for X-ray diffraction, exposure test and mercury intrusion porosimetry test were made by paste. Mixing of mortal for compressive strength test was cast into 4×4×16cm mold based on JIS R 5201. Mixing of paste which is for X-ray diffraction test and mercury intrusion test was by hand for three minute and cast into mold of φ2.5cm and hight1.5cm. The past for exposure test was cast into 4×4×16cm mold.

## 2.3 Setting of Curing

In this study, curing method is water curing. The detail of curing is presented in Fig.1. To put it briefly, at 1st day, specimens cured in mold. Afterward, specimens cured in water(20℃) while predefined period. After water curing, specimens cured in atmosphere(20℃ RH60%) until 28days. After atmosphere curing, specimens for exposure test were coated by epoxy except exposure surface. Later, specimens for exposure test were into salt water while 56days. Specimens for X-ray diffraction and mercury intrusion porosimetry were stop hydration by using acetone and then vacuums 24hours to dry on age of 28day.

### 2.4 Method of Experiment

Compressive strength were measured based on JIS R 5201. Chloride diffusion coefficient were measured based on JIS A 1154. Powder samples for chloride analysis were ground off by sliced specimens parallel to the exposed surface. Chloride diffusion was calculated by fick's second law.

The reaction ratio of chemical compound of cement was measured by internal reference method of X-ray diffraction test. X-ray source was used Cu-Kα. Speed of X-ray analysis was 0.2°/min. reference materials for internal reference method was used α-$Al_2O_3$ and add α-$Al_2O_3$ as 10mass% to samples.

Porosity was measured by mercury intrusion porosimetry. Fig.2 is shows an example of result of mercury intrusion porosimetry test. The amount of total volume and pore volume above 50nm diameter is shown at Fig.2.

## 3 Results and Discussion

### 3.1 Compressive Strength and Chloride Permeability

Fig.3 shows the experiment result of compressive strength test. The influence of initial curing period was not confirmed in the replacement level 0%. On the other hand, as for the blast furnace cement, the decrease in strength was confirmed at C-1 and C-3. However, the deterioration of strength was not confirmed in each composition if the initial curing period was five days or more.

All compositions is able to obtain the 40MPa. Moreover, OPC-B20 and HPC-B00 can obtain 50MPa if initial water curing period above 5days.

The result of the chloride diffusion test is shown in Fig4. It was confirmed that the chloride diffusion coefficient had decreased from C-1 to C-7 in each composition. Moreover, the diffusion coefficient had decreased from C-7 to C-14 was confirmed on several composition. In addition, a remarkable decrease was seen by the chloride diffusion coefficient as the high replacement levels. Moreover, it was confirmed that the blast furnace cement fell below the diffusion coefficient of the replacement level 0% even if initial curing condition was C-1.

That is, there is a possibility that initial curing period in which 28days strength and the chloride diffusion coefficient were considered can be shortened if it is a blast furnace cement of the HPC series and the initial water curing period above 5days.

The sensitivity on compressive strength of initial water curing period is shown on Fig.5. The sensitivity on compressive strength was calculated by following formula.

$$K_{Strength} = \sigma_{C-14} / \sigma_{C-1}$$

$K_{strength}$: the sensitivity on compressive strength

$\sigma_{C-1}$:Compressive strength on C-1

$\sigma_{C-14}$ : Compressive strength on C-14

The sensitivity of compressive strength is increase in increase with replacement levels at each cement series. The sensitivity of chloride diffusion coefficient is shown on Fig.6. The sensitivity on chloride diffusion coefficient was calculated by following formula.

$$K_{Chloride} = D_{C-1} / D_{C-14}$$

$K_{chloride}$ : The sensitivity on chloride diffusion coefficient

$D_{C-1}$: The chloride diffusion coefficient on C-1

$D_{C-14}$ : The chloride diffusion coefficient on C-14

The sensitivity of chloride diffusion coefficient is increase in increase with replacement levels. Moreover the sensitivity of chloride diffusion coefficient is higher than compressive strength cases especially on high replacement levels.

### 3.2 Pore Distribution

The total pore volume is shown in Fig7. The influence at the replacement level and the initial curing period was not able to be confirmed according to the total pore volume. The pore volume above 50nm is shown in Fig8. The pore volume above 50nm assumed to exert the influence on durability decreased with increasing at the initial curing period, and was especially remarkable in high replacement level. It was able to be confirmed to the blast furnace slag that there was an action that changed the pore above 50nm into a minuter pore.

## 4 Relationship between Chloride Permeability and Pore Distribution

The relation between a diffusion coefficient and an amount of pore above 50nm is shown in Fig9. Both were able to confirm both correlations by three layers "replacement level0%", "replacement level 20%", and "replacement level 50% and 70%".

Namely, increase in initial water curing period decrease amount of pore volume above 50nm diameter. Then, chloride diffusion coefficient is decreased.

## 5 Conclusions

- At the initial water curing period above 5days, decrease of compressive strength is not confirmed.
- Increase in initial water curing period decreased the chloride diffusion

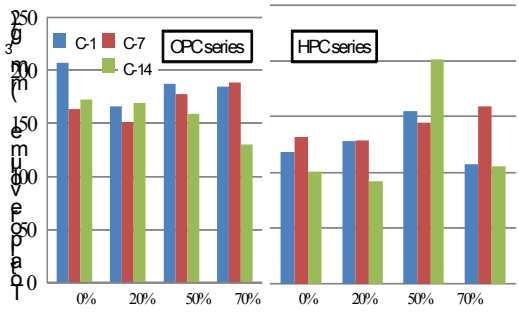


Fig.7 The amount of total pore volume

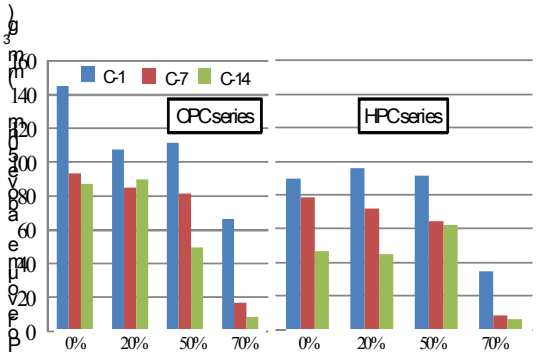


Fig.8
The amount of pore volume above 50nm diameter

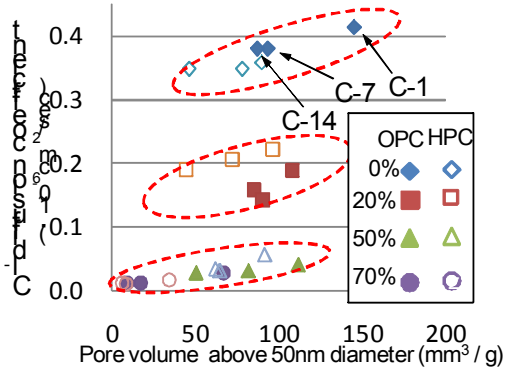


Fig.9
The relation between chloride diffusion coefficient and pore volume above 50nm diameter

coefficient. However increase of replacement level drastically decreased the chloride diffusion coefficient compared to the initial water curing period

- Any initial water curing period, blended cement is able to reach the lower chloride diffusion coefficient than ordinary portland cement
- The sensitivity of initial curing period on chloride diffusion coefficient is higher than that on compressive strength, especially, in cases of high replacement levels.
- Using HPC may shorten the initial water curing period. If the demould strength is enough.
- The effect of initial water curing period caused the decrease of pore volume above 50nm, thus, the chloride diffusion coefficient was decreased

【References】

1) Shinichiro.O et.al: The Study of The Influence of Curing Condition on Strength and Permeability,cement concrete, No.60, pp.227-234(2006)
2) Kenichiro.N et al : The analysis of permeability on several curing condition based on change of pore distribution of concrete, Concrete engineering annual thesis collection vol.29, No.1, pp.723-728(2007)
3) Kengo.H et.al : The effect of de-mold period on physicality of concrete, Concrete engineering annual thesis collection, vol.30, No.1, pp.681-686(2008)
4) Tsuyoshi.S et al: Evaluation of pore distribution of mortal specimen based on mercury intrusion porosimetry test, inorganic material

# Development of New Approach to Prepare $CoMo/Al_2O_3$ Catalyst for Deep Hydrodesulphurization

Student Number: 07M18036 Name: Tatsuya KUSAMA Supervisor: Hirofumi HINODE

深度水素化脱硫触媒開発を目指した $CoMo/Al_2O_3$ 触媒の新規合成法研究

草間　達也

本研究では、従来の前駆体とは異なり、酸化物を形成せずに直接、担体上に活性粒子である $MoS_2$ を形成することが出来る Ammonium Tetrathiomolybdate (ATTM)を前駆体として用い、担体($Al_2O_3$)の比表面積や水素化焼成時間が与える触媒活性への影響について研究を行った。活性試験の結果より、広い比表面積をもつ担体が最も高い活性を示した。XRD・BET の結果から、担体の比表面積が小さいために活性サイトの多層化が起こるのではなく、焼成・予備硫化の段階における比表面積の減少によって、多層化が起こると考えられる。また、水素化焼成時間の違いでは、明確な活性の差が得られなかったことから、焼成時間による影響については確かな結論は得られなかった

## 1. Introduction

The regulations on the sulfur content in liquid fuels have become stricter over the years in order to protect the environment (e.g. Japan: less than 10 ppm)[1].

The possible methods to produce “sulfur-free (less than 10 ppm)” fuel are (1) building additional reactor, (2) improving reactor or equipment and (3) improving catalyst performance. Due to relatively high cost of bulding or improving reactor, the studies of the hydrodesulphurization (HDS) catalyst are performed more widely these days.

Among the HDS catalysts that are widely studied, $CoMo/Al_2O_3$ attracts much attention because of its high hydrodesulphurization ability. The known active site for this catalyst is a kind of CoMoS phase proposed by Topsøe et al[2]. This CoMoS phase was formed because Co is located on the edge of $MoS_2$ on the supported material surface.

There are two types of CoMoS phase. Type I has strong interaction with support, forming single layer of $MoS_2$ slab and has low activity. On the other hand, Type II has weak interaction with support, forming multi layer of $MoS_2$ slabs and has high activity. Therefore, production of CoMoS phase Type II is more desirable.

In the previous study [3], the following three new preparation procedures using $(NH_4)_2MoS_4$ (ATTM) as the precursor were proposed:

- Route-1 (R1) includes impregnation of $Co(NO_3)_2 \cdot 6H_2O$, calcination under $H_2$ atmosphere, impregnation of ATTM, and vacuum calcination at 500ºC.
- Route-2 (R2) includes impregnation of $Co(NO_3)_2 \cdot 6H_2O$, calcination under air atmosphere, impregnation of ATTM, and vacuum calcination at 500ºC.
- Route-3 (R3) includes impregnation of ATTM, vacuum calcination at 500ºC, impregnation of $Co(NO_3)_2 \cdot 6H_2O$, and calcination under $H_2$ atmosphere.

It is reported that thiophene conversion of the catalyst prepared by Route-3 (R3) in the new procedure was higher than that of the commercial catalyst [3].

The aims of this study are (1) the investigation of the effect of the specific

surface area of $Al_2O_3$ supports and (2) the investigation of the effect of the $H_2$ calcination period.

## 2. Experimental

### 2.1 Catalyst preparation

#### 2.1.1 Materials used in preparation catalyst

The catalyst supports were JRC-ALO2, ALO5, ALO6 and ALO8 ($Al_2O_3$, Reference Catalyst, The Catalyst Society of Japan, BET specific surface area 148-285$m^2$/g).

The catalyst precursors were ammonium tetrathiomolybdate (ATTM), $(NH_4)_2MoS_4$, as Mo precursor and cobalt (Ⅱ) nitrate hexahydrate, $Co(NO_3)_2.6H_2O$, as Co precursor.

#### 2.1.2 Catalyst preparation

A series of $CoMo/Al_2O_3$ catalyst was prepared by double impregnation method. The Mo loading was 17.5wt% and the molar ratio of Co/Mo was fixed at 0.27. The catalyst was impregnated with ATTM, and calcined at 500ºC for 2h in vacuum. Then, the catalyst was impregnated with $Co(NO_3)_2.6H_2O$, and calcined at 400ºC for 2, 6, 12 and 24h under $H_2$ atmosphere. Presulfidation was carried out at 400ºC for 4h in $5\%H_2S/H_2$ gas stream.

### 2.2 Activity test

The reaction was carried out in a fixed-bed reactor under atmospheric pressure. The catalyst was pelletized, crushed and sieved to 0.71~1.00 mm. 0.2 g of the sample was packed in the reactor and the total flow rate of the feed mixture gas was fixed at 20 ml/min.

The concentration of thiophene in the feed stream was maintained at 2.1mol%. The reaction temperature was selected at 300ºC.

After the reaction had reached steady-state condition in two hours, the concetration of thiophene was quantitatively analyzed by GC-MS (Shimadzu Co. QP5050A).

### 2.3 Catalyst characterizations

The samples were characterized by powder X-ray diffraction (XRD, Rigaku Co., MultiFlex). Specific surface areas of the samples were measured with Brunauer-Emmett-Teller method (BET, Quantachrome Co., AUTOSORB-1 MP).

## 3 Result and discussion

Figure 1 shows thiophene conversions at 300ºC using catalysts with supports of different specific surface areas and Table 1 shows the specific surface area of support, before preparation and after impregnation.

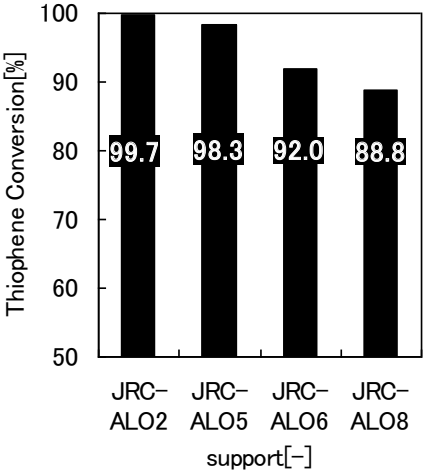


Figure 1 Thiophene conversion at 300ºC using catalysts with different supports

Table 1 Specific surface area of support before preparation and after impregnation

| Sample | Before preparation [$m^2$/g] | After impregnation [$m^2$/g] |
|---|---|---|
| JRC-ALO2 | 285 | 206 |
| JRC-ALO5 | 233 | 181 |
| JRC-ALO6 | 180 | 137 |
| JRC-ALO8 | 148 | 123 |

The catalyst with JRC-ALO2 showed the highest thiophene conversion of 99.7%. Thiophene conversion decreased with the decrease of specific surface area of support. At first, it was expected that the decrease of specific surface area of support using the same Mo loading would produce multi-layered $MoS_2$ and form CoMoS phase Type Ⅱ. However, from this result it was concluded that CoMoS phase Type II was not formed by only decreasing the specific surface area of support.

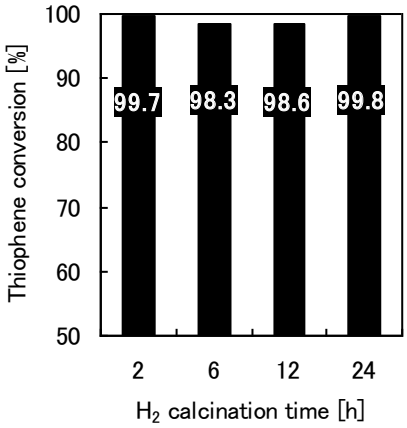


Figure 2 Thiophene conversion at 300ºC using catalysts with different $H_2$ calcination periods

Table 2 Specific surface areas of catalysts with different $H_2$ calcination period (support: JRC-ALO2)

| Sample | Before $H_2$ calcination [$m^2$/g] | After $H_2$ calcination [$m^2$/g] |
|---|---|---|
| 2h | 206 | 202 |
| 6h | 206 | 197 |
| 12h | 206 | 183 |
| 24h | 206 | 166 |

Figure 2 shows thiophene conversion at 300ºC using catalysts with different $H_2$ calcination periods and Table 2 shows specific surface area of catalysts with different $H_2$ calcination periods.

All catalysts showed almost the same thiophene conversions regardless of the decrease of specific surface area when the $H_2$ calcination period was increased. With this result, the influence of $H_2$ calcination period on the HDS activity could not be observed. With lower Mo loading or lower reaction temperature, a more comparable result between different calcination periods may be obtained.

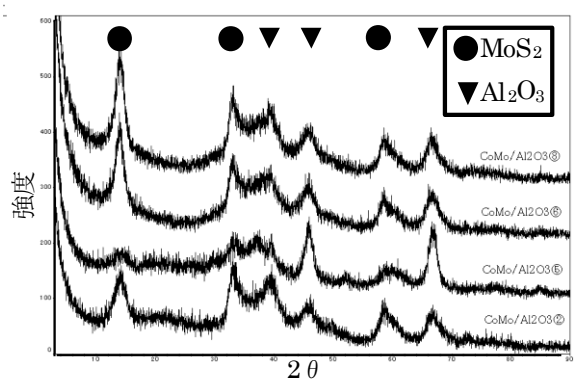


Figure 3 XRD patterns of catalysts with supports of different specific surface areas

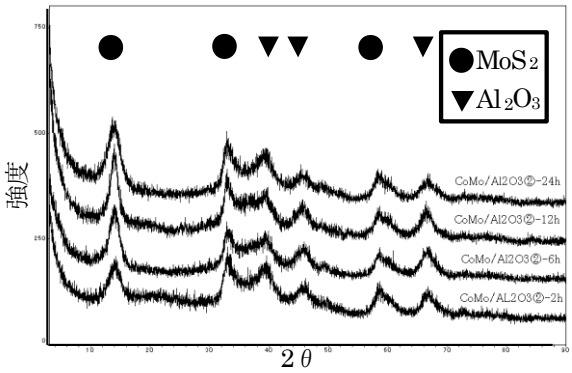


Figure 4 XRD patterns of catalysts with different $H_2$ calcination periods

Figure 3 shows the XRD patterns of catalysts prepared by different supports and Figure 4 shows the XRD patterns of catalysts prepared at different $H_2$ calcination periods. $MoS_2$ peaks at 14.5, 34.2 and 58.3 were observed in all XRD patterns in Figs.3 and 4. The relation

between the amount of $MoS_2$ and the HDS activity could not be observed.

## 4 Conclusion

The catalyst with JRC-ALO2 showed the highest conversion of 99.7%. Thiophene conversion decreased with the decrease of specific surface area of support using the same Mo loading. So, it was concluded that CoMoS phase Type II was not formed by only the decreasing the specific surface area of support.

The conclusion concerning the influence of $H_2$ calcination period was not obtained because almost the same thiophene conversion. With lower Mo loading or lower reaction temperature, a clearer result may be obtained.

## References

[1] Petroleum Association of Japan (http://www.paj.gr.jp/html/data/eco/lowsulphur.html)

[2] N. –Y., Topsøe, and H. Topsøe, J. Catal, 84, 386 (1983)

[3] ZHANG, Haibo, A Master Thesis, Tokyo Titech (2006)

# Modeling of Sand Transportation using Long-Term Observed Datasets in the Semi-Arid Shrub Desert

Student Number: 07M18042 Name: Yumi KONDO Supervisor: Manabu KANDA

砂漠における飛砂発生メカニズムのモデリング

近藤由美

本研究の目的は、アメリカ合衆国ニューメキシコ州の Chihuahuan Desert に所在するサイトにおいて、長期連続的に観測された飛砂データを用い、飛砂フラックスを定量的に風速で表現すること、ならびに各地表面パラメータの飛砂に与える影響をみることである。本研究から得られた結果として、Owen(1964)によって提案された飛砂式を援用し、飛砂を摩擦風速と臨界摩擦風速で表現する飛砂式が得られた。また、NDVI および降水量の飛砂に対する影響は見られなかった。

## 1. Introduction

Desertification is one of the most serious environmental problems in the world. Desertification is caused by various factors, including climatic variations and human activities. Sand transportation, the topic of this study, is one of the main mechanisms to cause desertification. In order to combat against desertification, revealing the mechanism of sand transportation is important.

Sand transportation is mainly driven by surface wind. Various slightly different equations for sand transportation are proposed by several researchers. In most sand-transport equations, total horizontal mass flux of sand $Q$ [kg m$^{-1}$ s$^{-1}$] is expressed as a function of friction velocity $u_*$ [m s$^{-1}$] and threshold friction velocity $u_{*t}$ [m s$^{-1}$]. In this study, the simple equation proposed by Owen (1964) is adopted;

$$Q = C\frac{\rho}{g}u_*^{\,3}\left(1-\frac{u_{*t}^{\,2}}{u_*^{\,2}}\right) \qquad (1)$$

where $C$ is the dimensionless empirical constant value, $\rho$ [kg m$^{-3}$] is air density and $g$ [m s$^{-2}$] is gravitational acceleration. Several researchers reported that Owen's equation best agrees with the acquired data (e.g. McKenna Neuman et al., 1997; Iversen and Rasmussen, 1999)

Sand transportation is also affected by many land-surface parameters, such as vegetation, roughness elements, soil particle size distribution, soil moisture, surface crust, snow cover etc. However, studies of the influence of these parameters on sand transportation are not fully developed yet.

The objective of this study is to describe sand transportation as a function of surface wind and assess the effect of land surface parameters on it. To achieve this objective, three goals are set in this study;

1) to check the bulk relation between sand transportation and parameters.
2) to determine the empirical constant $C$ and frictional threshold wind speed $u_{*t}$ for the equation of Owen (1964).
3) to investigate the effect of vegetation and precipitation on $C$ and $u_{*t}$ by using NDVI (Normalized Difference Vegetation Index) and precipitation datasets respectively.

Two advantages of this study are given below;

1) Sand trap datasets used in this study have been collected for more than 15 years since 1987. Simultaneously primary climatological datasets such as wind speed, precipitation and air temperature have been measured at the weather station. These datasets are the only datasets collected for such a long term continuously all over the world.
2) In this study sand trap is measured by BSNE sampler. The advantages of this instrument are low cost, electric free and the necessity of less maintenance thus suitable for the measurement in the desert. If we can establish the sand transportation model by using BSNE datasets, sand transport equations for various areas can be described.

## 2. Study Site

The Jornada Experimental Range (JER) is located in the northern Chihuahuan Desert, approximately 25km northeast of Las Cruces, New Mexico, USA (+32.5N, -106.8W, elevation 1188m). The climate of JER is characteristic of the northern region of the Chihuahuan desert with abundant sunshine, low relative humidity, wide ranges of daily temperature, and variable precipitation both temporally and spatially (Havstad et al., 2000). The surface of this study area is dominated by shrubs such as honey mesquite (*P. glandulosa*) or creosote (*Larrea spp.*).

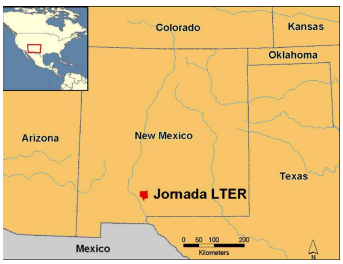


**Fig. 1.** Location of the Jornada Experimental Range (after McGlynn and Okin, 2006).

## 3. Materials and Methods

For the analysis in this study, the datasets of sand trap, wind speed, precipitation, air temperature and NDVI are used. The details of these datasets are summarized in Table 1. Sand trap datasets were directly passed from the research team who conducts the measurement at JER. Climatological parameters were provided by the Jornada Long-Term Ecological Research (LTER) project. NDVI was derived from MODIS (Moderate Resolution Imaging Spectroradiometer) images, allowing a 250m maximum spatial resolution with 16days temporal resolution.

Frictional wind velocity $u_*$ is calculated by using log-profile law assuming neutral condition;

$$u = \frac{u_*}{\kappa} \ln \frac{z}{z_o} \qquad (2)$$

where $\kappa$ is the Karman constant (0.4), $z_o$ [m] is the roughness length, $z$ [m] is the height of the anemometer (=2.5m) and $u$ [m $s^{-1}$] is the wind speed measured by anemometer. For this calculation the information of $z_o$ is necessary, however the products of LTER project do not include $z_o$. We assume $z_o$ =0.003m from the work of King et al. (2006) in which the measurements of roughness length was conducted at JER.

Since the amount of transported sand flux has vertical dependency due to gravity, the installation of vertically integrated horizontal sand flux $Q$ [kg $m^{-1}$ $s^{-1}$] is necessary;

$$Q = \int_0^\infty q(z)dz \qquad (3)$$

where $q(z)$ [kg $m^{-2}$ $s^{-1}$] is the horizontal sand flux density. From the sand flux density at three heights, 15cm, 50cm and 100cm, horizontal sand flux density was calculated using the empirical formula used by Shao and Raupach (1992);

$$q(z) = c \exp[az + bz^2] \qquad (4)$$

where $a$, $b$ and $c$ are dimensional functions.

## 4. Results

After the investigation of temporal changes of several parameters, i.e. sand trap, NDVI, climatological parameters such as wind speed, precipitation, air temperature and some climatological indexes, the relation between parameters were discussed. From the bulk point of view, sand transportation is provoked when the wind speed is high. This can be strengthen by the fact that the season of high quantity of sand flux is in correspondence to the season of high wind speed, i.e. February to April. The correlation between sand flux and wind speed exceeds those between sand flux and other parameters, which suggest that wind speed is the primary parameter for sand transportation.

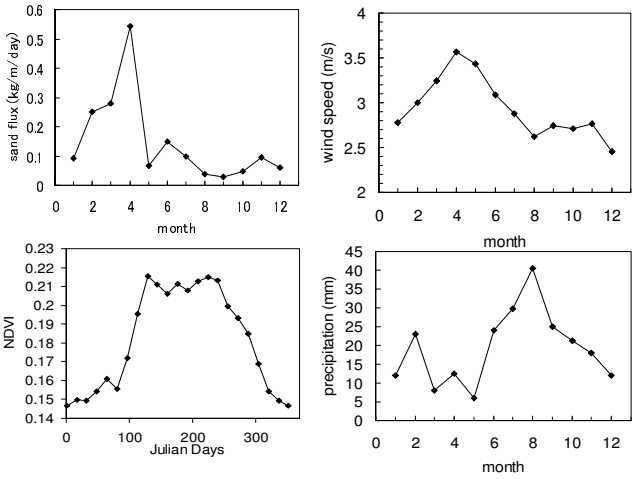


**Fig. 2.** Monthly change of sand flux, wind speed, NDVI and precipitation (mm) averaged from 2000 to 2005.

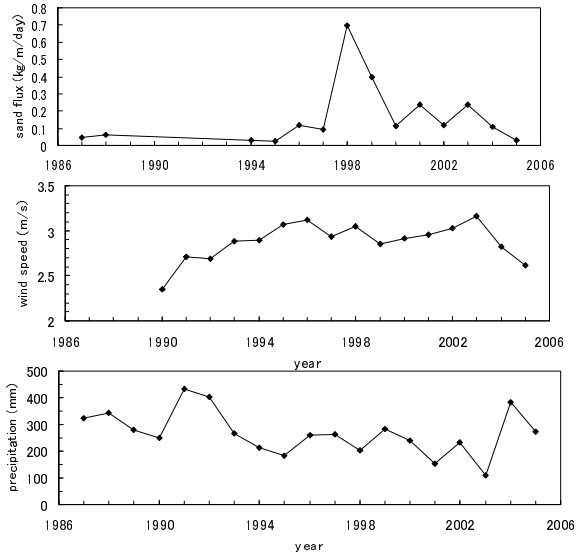


**Fig. 3.** Annual change of sand flux, wind speed and precipitation.

**Table 1.** Summary of datasets used in this study

| data | instrument | height of instrument | sampling interval | starting time |
|---|---|---|---|---|
| sand trap data | BSNE sampler | 15cm, 50cm, 100cm | not constant approximately one month | 1987 |
| wind speed | Met One Wind Speed Sensor | 2.5m | one hour | 1983 |
| precipitation | WeatherMeasure 6011 | at the surface | one hour | 1983 |
| air temperature | Temperature Probe 107 | 1.6m | one hour | 1983 |
| NDVI | earth observatory satellite Terra | ——— | 16 days | 2000 |

## 5. Discussion

### 5.1. Analysis Procedure

Since the sampling interval of sand trap is roughly one month whereas wind speed was recorded every one hour, an unique procedure was adopted in this study. Iterative calculation method was conducted for $C$ from 0 to 1 with the resolution of 0.0001 and for $u_{*t}$ from 0 to 1.2 with the resolution of 0.01 to decide $C$ and $u_{*t}$ simultaneously. First, sand flux was calculated for each $u_*$ above $u_{*t}$;

$$Q_{n,i} = 0 \qquad u_{i*}<u_{*t} \qquad (5),$$

$$Q_{n,i} = C\frac{\rho}{g}u_{i*}^{3}\left(1-\frac{u_{*t}^{2}}{u_{*}^{2}}\right) \qquad u_{i*}>u_{*t} \qquad (6).$$

After summing up all $Q_{n,i}$ for each sampling period of n set of data, we divided it by the number of $u_*$ in one sampling period of sand trap (N);

$$\overset{\vee}{Q} = \frac{\sum_{i=1}^{N} Q_i}{N} \qquad (7).$$

The best combination of $C$ and $u_{*t}$ was chosen to make the n set of residual error between $\overset{\vee}{Q}_n$ and observed $Q_n$ smallest.

### 5.2. All-In-One Analysis

From the non-linear least-squared method using the 68 datasets of sand flux and wind speed from 2000 to 2005 adopting the equation for sand transportation proposed by Owen (1964) and assuming roughness length $z_o$ to be 0.03m, $C$ was calculated as 0.0187 and $u_{*t}$ was calculated as 0.78 (m/s);

$$Q = 0.0187\frac{\rho}{g}u_{*}^{3}\left(1-\frac{(0.78)^{2}}{u_{*}^{2}}\right) \qquad (8).$$

Here we define deemed friction wind velocity $\hat{u}_*$ to represent $u_*$ through the sampling period. Since the sampling period of sand trap and wind speed do not match, we need the representative value of $u_*$. $\hat{u}_*$ is derived by calculating back (5) substituting calculated sand flux $q_c$ into $Q$.

Figure 4. shows the relationship between $\hat{u}_*$ and observed sand flux $Q$ [kg m$^{-1}$ s$^{-1}$]. Solid line is the theoretical curve of (5) which cross x-axis at $\hat{u}_*$=0.78 (m/s) which is the threshold wind velocity for this case. The open symbols on y-axis are the datasets in which all of the hourly $u_*$ were below $u_{*t}$ during the sampling period of sand trap. According to the procedure adopted in this study, these results are unavoidable regardless its unreality.

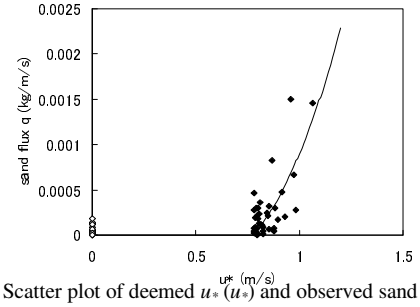


**Fig. 4.** Scatter plot of deemed $u_*$ ($\hat{u}_*$) and observed sand flux $Q$ (kg/m/s). Correlation coefficient $\rho$ was 0.756.

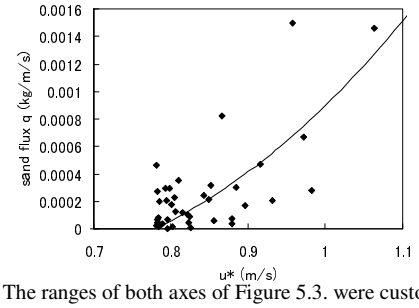


**Fig. 5.** The ranges of both axes of Figure 5.3. were customized into narrower region.

Comparing to the values of constant $C$ for Owen's equation from various other studies, the acquired value 0.0187 from this study is considerably small (Table 2.). Several possible reasons for this difference of $C$ can be considered;

(1)The land surface condition at JER is greatly different from those of existing studies. While the land surfaces of other studies are covered with fine sediment without vegetation, the land surface at JER is severely vegetated.

(2)Since the deviations of datasets from regression line are considerably large, there is an allowance for $C$.

(3)The difference of particle size distributions can generate a large difference of sand flux (Mikami et al., 2005)

(4)The procedures to derive C are different between this study and other studies. As for other studies, since the sampling intervals of sand flux and wind speed correspond each other and the intervals are enough short for the analysis, they can decide $u_{*t}$ from the relation between sand flux and wind speed. On the other hand, in this study $C$ and $u_{*t}$ was decided simultaneously by non-linear least-squared method because the sampling periods of sand flux and wind speed are not in accordance. This technical difference might cause some difference of $C$ between this study and other studies.

**Table 2.** Empirical constant $C$ and $u_{*t}$ from other studies. Most of $C$ are on the order of 1.

| Source | Detail | Surface Condition | C | $u_{*t}$ (m/s) |
|---|---|---|---|---|
| this study | field experiment | vegetated (shrubs) | 0.0187 | 0.78 |
| Gillette et al. (1996) | field experiment | loose, sandy, flat | 2.8 | 0.18-0.35 |
| Nickling and Neuman (1997) | indoor wind tunnel | very well sorted 0.2mm sand | 1.8 | 0.24 |
| McKenna Neuman et al. (1997) | field experiment | moderately sorted medium sands (0.3-0.5m | 0.54 - 1.8 | 0.21-0.28 |

### 5.3. *Four-Matrix Analysis*

In order to investigate into the effect of various land-surface conditions on sand transportation, we classified the land surface into four categories. NDVI=0.18 and precipitation of 0.4 (mm/day) were chose to divide the numbers of datasets into four categories, matrix *a*, *b*, *c*, and *d*, equally. *C* and $u_{*t}$ are acquired for each category by the non-linear least-squared analysis. The conclusion from four-matrix analysis is that any effect of NDVI or precipitation on *C* and $u_{*t}$ was not detected. Partial reason for this result is the poor accuracy of the non-linear least-squared method because of the shortage of datasets in each category. Another technical reason for this result is that derived *C* and $u_{*t}$ from this method are not independent each other; greater $u_{*t}$ leads *C* to larger value and smaller *C* follows smaller $u_{*t}$. Furthermore, the fact that the two land-surface parameters adopted in this study, NDVI and precipitation, are not independent each other, makes the interpretation of this result more difficult.

**Table 3.** Summary of the result of four-matrix analysis

| Category No. | NDVI | precipitation (mm/day) | C | u*t (m/s) |
|---|---|---|---|---|
| a | 0.14-0.18 | 0.4- | 0.0006 | 0.35 |
| b | 0.14-0.18 | 0-0.4 | 0.0234 | 0.80 |
| c | 0.18- | 0.4- | 0.0193 | 0.64 |
| d | 0.18- | 0-0.4 | 0.0030 | 0.66 |

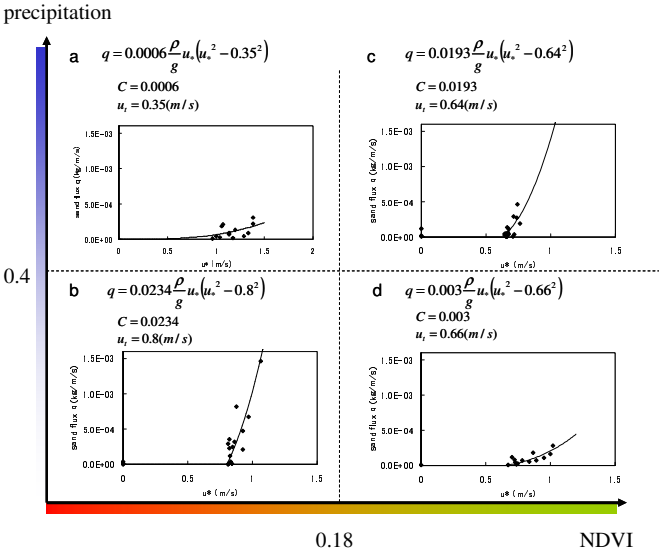


**Fig. 6.** Scatter plot of deemed $u_*$ ($u_*$) and observed sand flux *Q* (kg/m/s) for each category. The correlation coefficients in category *a, b, c, d,* were 0.529, 0.875, 0.703 and 0.798, respectively.

As for the effect of NDVI, in the previous studies it was pointed out that in the presence of vegetation, $u_{*t}$ severely increases and the amount of sand flux is limited. The primary reason for the insensitivity of sand flux to NDVI in this study can be considered that vegetation at this study site is dominated by shrubs which can block sand transportation even without leaves, which makes sand transportation at this study site insensitive to NDVI.

**Fig. 7.** Photograph near the sand trap station in JER taken in December 2001(left) and May 2002 (right). Note that even without leaves, shrubs can be enough obstacle for sand transportation.

As for the effect of precipitation, it was pointed out that precipitation increases $u_{*t}$ and limits sand flux via two effects; the growing of vegetation and increasing of soil moisture. The possible reason for the insensitivity of sand flux to precipitation in this study can be considered that precipitation is not a direct measure of soil moisture, which effect on sand transportation has been studied by numerous researchers.

## 6. Conclusion

This study is challenging on the point that *C* and $u_{*t}$ were decided by non-linear least-squared method simultaneously, which method is different from previous studies, using the sand flux datasets acquired by BSNE sampler. This study revealed that description of sand transport equation is possible with the datasets from BSNE sampler with approximately one month intervals, though the efficiency of this description still leaves space to be discussed.

## References

**[1]** Okin, G.S., Gillette, D.A., 2001; Distribution of vegetation in wind-dominated landscapes: Implications for wind erosion modeling and landscape processes, *J. Geophys. Res.*, 106, D9, 9673-9683

**[2]** McGlynn, I.O., Okin, G.S., 2006; Characterization of shrub distribution using high spatial resolution remote sensing: Ecosystem implications for a former Chihuahuan Desert grassland, *Remote Sens. Environ.*, 101, 554-566

**[3]** Shao, Y., Raupach, M.R., 1992; The overshoot and equilibration of saltation, *J. Geophys. Res.*, 97, D18, 20559-20564

**[4]** Owen, P.R., 1964; Saltation of uniform grains in air, *J. Fluid Mech.* 20, 2, 225-242

**[5]** MeKenna-Neuman, C., Lancaster, N., Nickling, W.G., 1997; Relations between dune morphology, air flow, and sediment flux on reversing dunes, Silver Peak, Nevada, *Sedimentology*, 44, 1103-1113

**[6]** Iversen J.D., Rasmussen, K.R., 1999; The effect of wind speed and bed slope on sand transport, *Sedimentology*, 46, 723-731

**[7]** Havstad, K.M., Kustas, W.P., Rango, A., Ritchie, J.C., Schumugge, T.J., 2000; Jornada Experimental Range: a unique arid land location for experiments to validate satellite systems, *Remote Sens. of Environ.*, 74, 13-25

**[8]** Mikami, M., Yamada, Y., Ishizuka, M., Ishimaru, T., Gao, W., Zeng, F., 2005; Measurement of saltation process over gobi and sand dunes in the Taklimakan desert, China, with newly developed sand particle counter, *J. Geophys. Res.*, 110, D18S02, doi:10.1029/2004JD004688

# Permeation of coal tar absorption oil through ionic liquid supported liquid membrane

Student Number: 07M18059 Name: Yoshiyuki SHIMADA Supervisor: Ryuichi EGASHIRA

# イオン液体支持液膜におけるコールタール吸収油の透過

島田　義之

コールタール吸収油ーヘプタン系などのモデル混合物を原料、イオン液体( 1-ブチル-3-メチルイミダゾリウムテトラフルオロほう酸塩）水溶液を膜液、及びトルエンを溶媒として回分透過を行った。いずれの条件においても、吸収油中の他の成分に比較して含窒素複素環式化合物が選択的に膜液を透過し、これらの成分間の分離が可能であることを確認した。膜液にイオン液体を添加することによりいずれの成分の透過速度も劇的に増加した。さらにこれらの結果に基づいて透過の速度過程について検討した。

## 1. Introduction

Coal tar absorption oil (AO) is one of distillation fractions of a coal tar (b.p. = 470~550K) which is obtained coal carbonization. There are many kinds of chemical compounds contained in it, the nitrogen heterocyclic compounds such as quinoline (Q), isoquinoline (IQ), indole (I); the homocyclic compounds such as 1-methylnaphthalene (1MN), 2-methylnaphthalene (2MN), etc. The mass fraction of some main compounds in AO is shown in **Table 1**. These compounds are useful as raw materials for agricultural chemicals, medicines, perfumes, and many other useful chemicals. Generally, the current method mainly used to separate these compounds in AO is carried out in two steps: first step is a rough separation of AO into several fractions by acidic and basic extraction; and second step are further separation and purification of these fractions into respective products by other methods. The separation for this first step in the industrial fields has some drawbacks, e.g., corrosion of the equipments and difficulties in solvent recovery. To solve these problems, several alternative methods, such as liquid-liquid extraction method and O/W/O supported liquid membrane method (SLM) have been studied[1,2,3].

Ionic liquids (ILs) are emerging as alternative green solvents to the volatile organic compounds typically used in separation processes because they are air and water stable, have a non-measurable vapor pressure. ILs are organic salts that are liquid close to room temperature, constituted by an organic cation and either an organic or an inorganic anion.

It has been already reported that the organic nitrogen compounds by supported liquid membranes based on ionic liquids, etc. However there is no report of the separation from an actual multi-component like AO.

In this work, the separation of AO by the ionic liquid supported liquid membrane was conducted. The permeation rate process through the ionic liquid supported liquid membrane was investigated.

Table 1 Mass fractions of some main compounds in AO

| $x_{Q,0}$ | $x_{IQ,0}$ | $x_{I,0}$ | $x_{N,0}$ | $x_{1MN,0}$ | $x_{2MN,0}$ | $x_{BP,0}$ | $x_{DBF,0}$ |
|---|---|---|---|---|---|---|---|
| 0.077 | 0.019 | 0.036 | 0.012 | 0.107 | 0.263 | 0.064 | 0.098 |

## 2. Experimental

### 2.1. Preparation of ionic liquid supported liquid membrane

The structure of the ionic liquid used in this work is described in **Fig. 1** and the properties of it are shown **Table 2**. 1-butyl-3-methylimidazolium tetrafluoroborate [$bmim^+$][$BF_4^-$] was selected as the membrane liquid due to the property of solubility[4]. This ionic liquid was purchased from Wako Chemical Co., Ltd. 3 kinds of the membrane liquid were prepared ($C_{IL}$=0,0.5,1).

The specifications of the hydrophilic filter paper (cellulose, advantec filter paper no.5B) used as a supporter in the previous work[2] are shown in **Table 3**. The filter paper was purchased from Toyo Roshi Kaisha, Ltd.

The filter paper was impregnated with the ionic liquid by dropping carefully. Then, the excess of the ionic liquid from the membrane surface was removed and the mass of the liquid membrane was adjusted.

### 2.2. Batch permeation

**Figure 2** illustrates a permeator for the supported liquid membrane (SLM). The liquid membrane was placed between two Pyrex glass vessels. The operation temperature was kept constant by the constant-temperature water passing through the tube coiled around the permeator. The principal conditions of permeation runs are shown in **Table 4**. The 12 permeation runs on 12 conditions were conducted by varying the following factors; the mass fraction of the

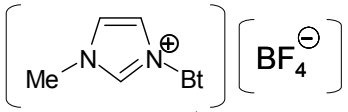


Fig. 1 Structure of [$bmim^+$][$BF_4^-$]

Table 2 Physicality and miscibility of [$bmim^+$][$BF_4^-$]

| m.p. | density | viscosity (298K) | $T_d$ | electrical conductivity |
|---|---|---|---|---|
| [K] | [kg/m$^3$] | [cP] | [K] | [mS/m] |
| 202 | 1370 | 118.3 | 573 | 343 |

| solubility with traditional solvents | | | | | | |
|---|---|---|---|---|---|---|
| $H_2O$ | MeOH | EtOH | Acetone | THF | Heptane | Toluene |
| ○ | ○ | ○ | ○ | △ | × | × |

Table 3 Specifications of the filter paper

| material | mass | diameter | thickness | mean pore size | real density |
|---|---|---|---|---|---|
| | [kg/m$^2$] | [m] | [m] | [μm] | [kg/m$^3$] |
| cellulose | 0.104 | 0.07 | 2.2×104 | 4 | 1550 |

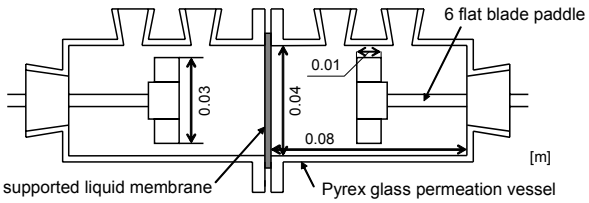


Fig. 2 Schematic diagram of experimental apparatus

Table 4 Material systems and experimental conditions

| | | | |
|---|---|---|---|
| Feed | AO ($V_F$=1.2×10$^{-4}$ m$^3$) | | |
| | model solution ( $x_{Q,0}$=0.08, $x_{2MN,0}$=0.25, $x_{Hp,0}$=0.67) | | |
| | AO-heptane solution ($v_{AO,0}$=0.5, $v_{Hp,0}$=0.5) ($V_F$=1.2×10$^{-4}$ m$^3$) | | |
| Solvent | toluene ($V_E$=1.2×10$^{-4}$ m$^3$) | | |
| Number of supporters | $n$ = 1, 2, 3 | | |
| Membrane Liquid | water, ionic liquid([bmim$^+$][BF$_4^-$]) aqueous ($C_{IL}$=0, 0.5, 1) | | |
| Stirring Velocity | $N_{SLM}$ | [h$^{-1}$] | 6000 or 12000 |
| Temperature | $T$ | [K] | 298 |
| Time | $t$ | [h] | 12 |

membrane liquid ($C_{IL}$=0, 0.5, 1), the stirring velocity in both phases ($N_{SLM}$=6000, 12000), the number of supporters ($n$=2, 3). The feed and solvent were poured into the respective vessels simultaneously and quickly, and then the agitation of the feed and solvent phases were started ($t$=0) to begin the batch permeation run. The raffinate and extract phases were sampled at specified operating times, for analysis by a gas chromatograph (GC-2010, Shimadzu Corp.).

## 3. Results and Discussion

### 3.1. Composition of extract phase

For all permeation runs, the membrane remained stable during the operation run because of low solubility in the raffinate and extract phases and the affinity for the supporter sheet[5]. **Figure 3** shows examples of time courses of mass fractions in the extract phases. The mass fraction of each component increased linearly with time. The permeation rates, especially for I, drastically increased with the addition of the ionic liquid, because the addition of the ionic liquid widely increased solubilities of all components. The permeation rates of Q were largest in the case without the ionic liquid and those of I were largest in the case with the ionic liquid. The overall mass transfer from raffinate to extract phase was governed by the permeation through the membrane, because the permeation rate was not affected by the stirring velocity and was inversely proportional to the number of membrane supporter sheets.

### 3.2. Yield

The yield of component $i$, $Y_i$, was defined as,

$$Y_i = \frac{E \cdot y_i}{R_0 \cdot x_{i,0}} \qquad (1)$$

**Figure 4** shows the examples of time courses of $Y_Q$. Under all conditions, $Y_i$ of nitrogen heterocyclic compounds were larger than those of other compounds, namely, it was confirmed that these compounds were separated into each other by the ionic liquid membrane. The yields of Q were the largest in the case without the ionic liquid and those of I were the largest in the case with the ionic liquid. The yields, especially for I, drastically increased with the addition of the ionic liquid.

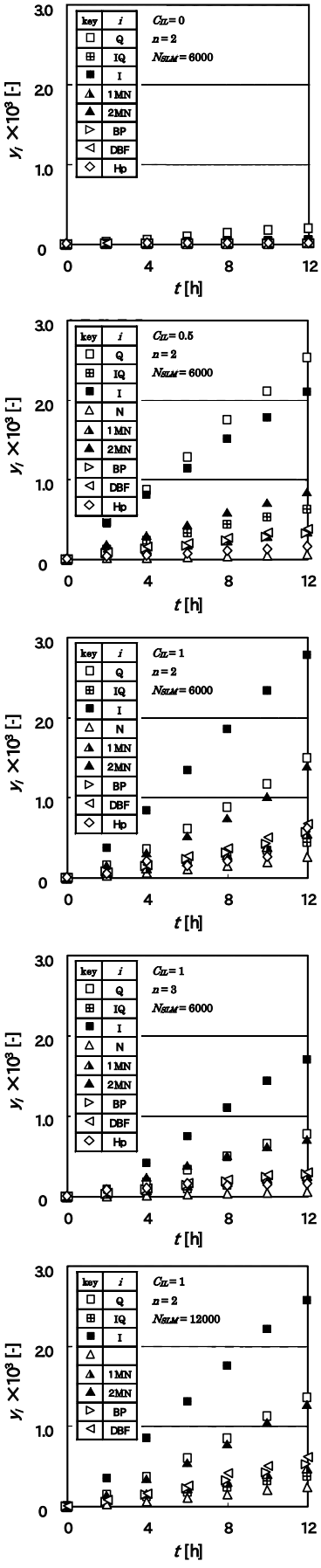


Fig.3 Time courses of mass fraction in extract phase

### 3.3. Overall permeation coefficient

Since the mass fraction of each component increased linearly with time, namely, it could be assumed that the permeation rates were proportional to the mass fraction of the feed and the overall permeation coefficients were constant in each component, the permeation rate was expressed by[2],

$$E_0 \cdot \frac{dy_i}{dt} = P_{x,i} \cdot A \cdot x_{i,0} \quad (2)$$

**Figure 5** shows the examples of the effects of $C_{\mathrm{IL}}$ on $P_{x,i}$ calculated by Eq. (1). Regardless of the concentration of the ionic liquid, $P_x$ of the nitrogen heterocyclic compounds was higher than those of other compounds, which means that the nitrogen heterocyclic compounds were selectively permeated through the liquid membrane to extract phase and could be separated from other compounds. The overall permeation coefficient was expressed by[2],

$$P_{x,i} \propto \frac{\rho_{ML} \cdot D_i \cdot m_i}{n} \quad (3)$$

where $\rho_{ML}$, $D_i$ and $m_i$ denote the density of the membrane liquid, diffusivity of component *i* in the liquid membrane and distribution coefficient, respectively. The results that $P_{x,i}$ widely increased with the addition of the ionic liquid and $P_x$ of I decreased with the increase of $C_{IL}$ are most affected by $m_x$.

### 3.4. Separation selectivity

The separation selectivity of the nitrogen heterocyclic compounds relative to 2MN, $\beta_{i,2\mathrm{MN}}$, was defined as,

$$\beta_{i,2MN} = \frac{P_{x,i}}{P_{x,2MN}} \quad (4)$$

**Figure 6** shows examples of the effects of $C_{IL}$ on $\beta_{i,2\mathrm{MN}}$. Whereas $\beta_{i,2\mathrm{MN}}$ of Q and IQ decreased with the addition of the ionic liquid into the membrane, $\beta_{\mathrm{I},2\mathrm{MN}}$ increased. The effect of the addition of the ionic liquid on the other components was not observed and $\beta_{i,2\mathrm{MN}}$s of them are about 1. The number of the supporter sheets had no effect on $\beta_{i,2\mathrm{MN}}$. The highest $\beta_{\mathrm{I},2\mathrm{MN}}$ was about 18 in the case of $C_{IL}$=0.5.

## 4. Conclusions

The nitrogen heterocyclic compounds were separated from AO by the ionic liquid supported liquid membrane. The overall mass transfer from raffinate to extract phase was governed by the permeation through the membrane. The permeation rates and the yields of all components dramatically increased with an addition of the ionic liquid. The yields of nitrogen heterocyclic compounds were larger than those of other compounds. The separation selectivities of each nitrogen heterocyclic compound were affected by the mass fraction of the ionic liquid.


## Acknowledgment

The author wish to thank JFE Chemical Co., Ltd. for providing coal tar absorption oil.


## Nomenclatures

| | | |
|---|---|---|
| $A$ | = contact area | [$m^2$] |
| $C_{IL}$ | = mass fraction of an ionic liquid in membrane liquid | [-] |

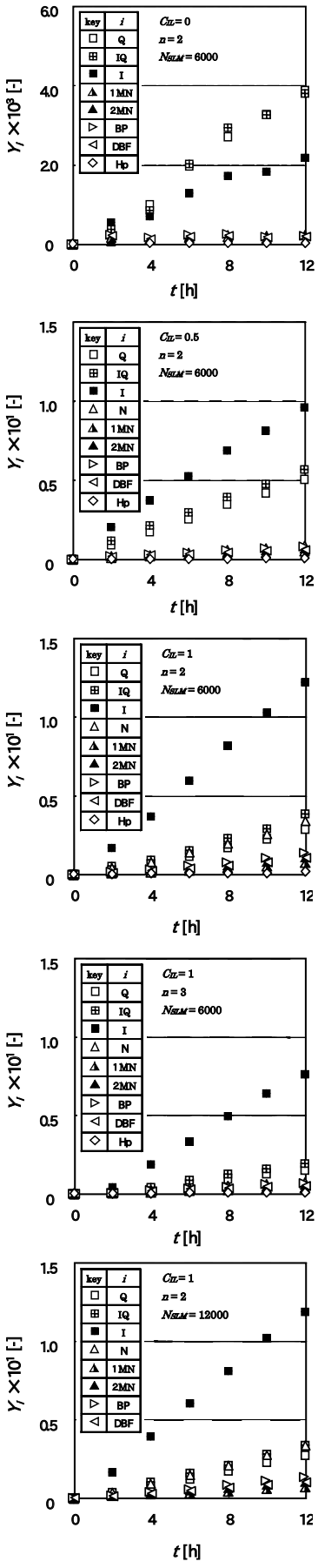


Fig.4 Time courses of yields in extract phase

$D_i$ = diffusivity of component $i$ in the liquid membrane [$m^2h^{-1}$]
$E$ = mass of extract phase [kg]
$m_i$ = distribution coefficient of component $i$ [-]
$N_{SLM}$ = stirring velocity in permeation vessel [$h^{-1}$]
$n$ = number of supporters [-]
$P_x$ = overall permeation coefficient based on mass fraction in raffinate phase [$kgh^{-1}m^{-2}$]
$R$ = mass of raffinate phase [kg]
$V$ = volume [$m^3$]
$v$ = volume fraction in feed solution [-]
$x$ = mass fraction in raffinate phase [-]
$y$ = mass fraction in extract phase [-]

<Greek>

$\beta_{i,2MN}$ = separation selectivity of component $i$ relative to 2-methylnaphthalene [-]
$\rho_{ML}$ = density of the membrane liquid [$kgm^{-3}$]

<Subscript>

0 = at initial state
1MN = 1-methylnaphthalene
2MN = 2-methylnaphthalene
AO = absorption oil
BP = biphenyl
DBF = dibenzofuran
E = extraction solvent
F = feed solution
Hp = heptane
I = indole
IQ = isoquinoline
N = naphthalene
Q = quinoline

**Literature Cited**

[1] C. Salim; "Process to Separate Coal Tar Fraction using Solvent Extraction," Doctor Thesis, Tokyo Tech (2005)
[2] R. Egashira *et al.*; "Separation of coal tar fraction by O/W/O liquid membrane," 7th World Congress of Chemical Engineering, pp, C23-004, (2005)
[3] H. Habaki, *et al.*; "Separation of Coal Tar Absorption Oil by Emulsion Liquid Membrane -Effects of Additives in Membrane Phase on Permeation Behavior-," 8th International Conference on Separation Science and Technology (ICSST08), FP-07 (2008)
[4] M. Matsumoto *et al.*; "Selective separation of aromatic hydrocarbons through supported liquid membranes based on ionic liquids," Journal of Membrane Science, vol.246, 77-81, (2005)
[5] Raquel Fortunato *et al.*; "Supported liquid membranes using ionic liquids: study of stability and transport mechanisms," Journal of Membrane Science, vol.242, 197-209, (2004)

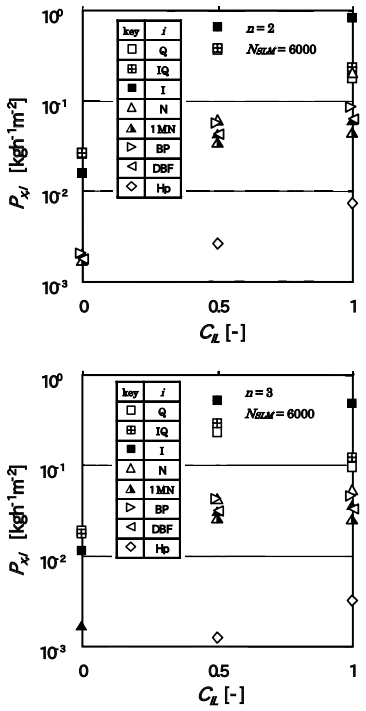


Fig.5 Effects of IL concentration on the overall permeation coefficient based upon raffinate concentration

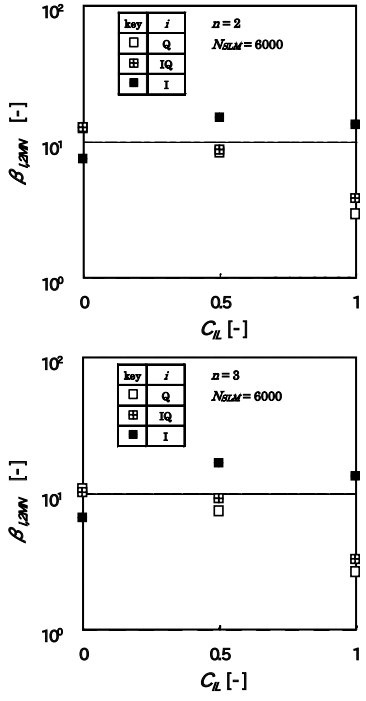


Fig.6 Effects of IL concentration on separation selectivity of nitrogen heterocyclic compounds relative to 2MN

# PIV MEASUREMENTS OF ATMOSPHERIC TURBULENCE WITHIN AND ABOVE AN OUTDOOR URBAN SCALE MODEL

Student Number: 07M18065 Name: Hiroshi TAKIMOTO Supervisor: Manabu KANDA

屋外模型都市における PIV を用いた大気乱流計測

瀧本 浩史

大気中の熱や物質の輸送は主に乱流が担っており，都市の大気環境問題を考える上で，乱流の時空間構造の把握は重要である．本研究では，空間的に高解像度で流速を計測することのできる粒子画像測定法(PIV)を用いて，屋外大気乱流下での模型都市における乱流計測を行った．その結果，屋外特有の風向変動が運動量交換の大きさに与える影響や，非定常的な上昇流の存在が明らかとなった．

## 1 Introduction

Exchange processes of heat, pollutants, and water between the earth's surface and the atmosphere are mainly induced by turbulent motions. Therefore, understanding of temporal and spatial characteristics of turbulent motion is a fundamental approach for the improvements of atmospheric environment in cities. However, measurements in urban cities are usually tough. It is very difficult to take spatial measurements in cities as compared to laboratory or numerical experiments. Most of the measurements of urban atmospheric turbulence were performed with single point sensors such as ultrasonic anemometer [1], [2], [3]. For the measurements of spatial flow characteristics, a large number of instruments are required.

The main aim of this study is to investigate the flow inside street canyons in more detail, by applying Particle Image Velocimetry (PIV) to an outdoor urban canopy flow. PIV is one of the highly-advanced measurement techniques that can capture flow velocity vectors at high spatial resolution without any disturbances from measurement instruments. Velocities are obtained from image analysis of visualized images of flow fields. This technique has been utilized for turbulence measurements, mainly in laboratory experiments [4], [5]. Despite the high efficiency of PIV, applications of this method for atmospheric turbulence are still rare [6]. Flow visualizations in outdoor environments are difficult, due to highly-fluctuated wind direction and intensive turbulent diffusivity. This is the first application of PIV to the flow characteristics over an outdoor urban-like roughness.

As a counterpart of field experiments, results from wind tunnel experiments are also presented. The settings of the experiments were similar to that of the outdoor case. By comparing these results, the influences of large scale disturbance and wind direction fluctuation are inspected, which are distinctions between field and laboratory experiments.

Unfortunately, field PIV is possible only in night time. Results from this study do not include the most part of the effects of solar radiation.

## 2 Experimental setup

### 2.1 Field experiment

A PIV measurement was carried out on September 4th, 2008, from 2100 JST to 2200 JST at an outdoor urban scale model (COSMO, Figure 1). COSMO is a simplified model city with no human activity and no

Figure 1. Comprehensive Outdoor Scale MOdel.

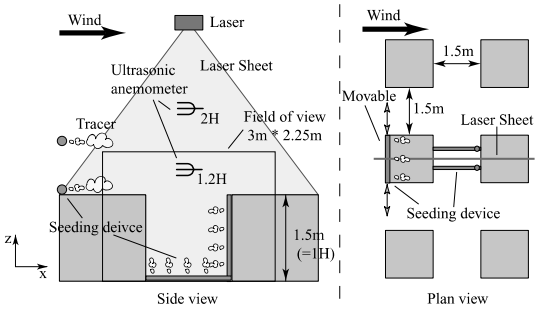


Figure 2. Setup of field PIV measurement.

heterogeneity of the surface geometry. It can provide supplementary information to indoor and real-urban experiments, under realistic synoptic conditions of sunshine and wind fluctuations. This scale model consists of 512 pieces of 1.5m (=H; average building height) concrete cubes. That is a fifth of the scale of the typical residential building in Japan [2]. They are aligned in square array on a flat concrete plate with a plan area density of 0.25. The dimensions of the concrete plate are 100m x 50m, and the longitudinal axis corresponds with the dominant wind direction of Asian monsoon. Hereinafter, longitudinal axis and vertical axis of the site are described as x-axis and z-axis. The velocity components of each axis are $u$ and $w$, respectively. The target area of the PIV measurement was a vertical cross section 3m (H) x 2.25m (V) at the center of a street canyon (Figure 2). The position of this street canyon was 60m (40H) downstream from the edge of the COSMO.

For flow visualization, continuous-wave Nd:YAG laser (1000mW) was mounted on a tower at a height of 5m. Tracer particles were oil-based fog and they were supplied from multiple fog generators. The tracer was released through perforated PVC pipes (φ20mm) that were set at the upstream of the measurement section and the inside of the street canyon. To make sure that tracer was sufficiently seeded in highly fluctuating wind direction, PVC pipes were placed such that they can move perpendicularly to the x-axis of the site. The outlet velocity of the tracer was controlled so that it would not disturb the flow field. For removing the fog heats, aluminum pipes wrapped in wet towels were joined between PVC pipes and fog generators. As an imaging device, a 30frame/sec CCD camera (1392 x 1040 pixel$^2$) was used.

For complementary measurement of PIV, two sonic anemometer-thermometers, which can measure three-dimensional wind velocity and temperature fluctuation, were set at a height of 1.2H and 2H at the center of the street canyon. The sampling frequency of sonic anemometer was 50Hz.

The measurement time was set to an hour, to ensure the reliable turbulence statistics under the atmospheric environments. The mean wind speed $U_{2H}$ during the experiment was 0.73m/s at 2H, and the mean wind direction was inclined at 26.2° to the x-axis of the site. Atmospheric stability was slightly unstable; the value of $z'/L$ was -0.15. Roughness Reynolds number $\mathrm{Re}_* \ (=u_* z_0/\nu)$ of this measurement was about $8.1\times10^2$.

### 2.2 Wind tunnel experiments

A series of wind tunnel experiments were conducted in a wind tunnel (WT) facility of Central Research Institute of Electric Power Industry. The test section was 10m-long with a cross-sectional area of 1m x 1m. As building models, 75mm (=H) Styrofoam cubes were used. Cubes are regularly aligned with a plan area density of 0.25 in the same way as COSMO. Buildings were set in 47 rows in streamwise direction and 5 lines in spanwise direction. PIV measurement section was a street canyon between 43rd and 44th rows, located at 6.4m (85H) downstream of the entrance of the WT.

The WT PIV system contains a pulsed Nd:YAG laser (120mJ/pulse), a fog generator, and a CCD camera (1344 x 1024 pixel$^2$). Double-pulsed images were taken for 3minutes at a rate of 4Hz, and the interval of each pair of particle images was set to 2.5msec. Oil-based tracer was released from the entrance of the WT through a perforated PVC pipe. The size of the target area of PIV measurements was 288mm x 219mm. Roughness Reynolds number $\mathrm{Re}_*$ was 68. This value is much larger than the critical Reynolds number [7]. If roughness Reynolds number is larger than a certain critical value ( $\mathrm{Re}_* = 5.4$ ), the flow would be independent of Reynolds number, except the vicinity of the wall.

# 3 Results and discussion

### 3.1 Accuracy of PIV

The accuracy of field PIV dataset was examined in comparison with sonic anemometer dataset. PIV data was of a grid point nearby the sonic anemometer at 1.2H. The PIV data was not fully continuous but temporarily lacking mainly due to the highly-fluctuated wind direction along the x-axis of the site. Thus the comparison was done only for the period of valid PIV data. Table 1 shows turbulence statistics obtained from PIV and sonic anemometer measurements. Here $\sigma_u$, $\sigma_w$ are standard deviation of $u$, $w$, and $u_*$ is friction velocity defined as $u_* = (-\overline{u'w'})^{1/2}$. Every statistics were closely matching within the error of 10%. Not only mean statistics, instantaneous values also agree well, indicating a good reliability of PIV measurement.

Table 1. Comparison of turbulence statistics.

| | PIV (m/s) | SONIC (m/s) | PIV/SONIC |
|---|---|---|---|
| $\bar{u}$ | 0.65 | 0.67 | 0.96 |
| $\sigma_u$ | 0.37 | 0.38 | 0.97 |
| $\sigma_w$ | 0.18 | 0.17 | 1.06 |
| $u_*$ | 0.12 | 0.11 | 1.03 |

### 3.2 Mean flow characteristics

Mean velocity vector maps of COSMO and WT are shown in Figure 3. The results are normalized with $U_{2H}$. Averaging time was 60 minutes for field measurement, and 3 minutes for WT measurement. Both airflows have one big circulation in the street canyons, but their characteristics are not the same. They have distinct influx at the canopy top and streamline near the floor.

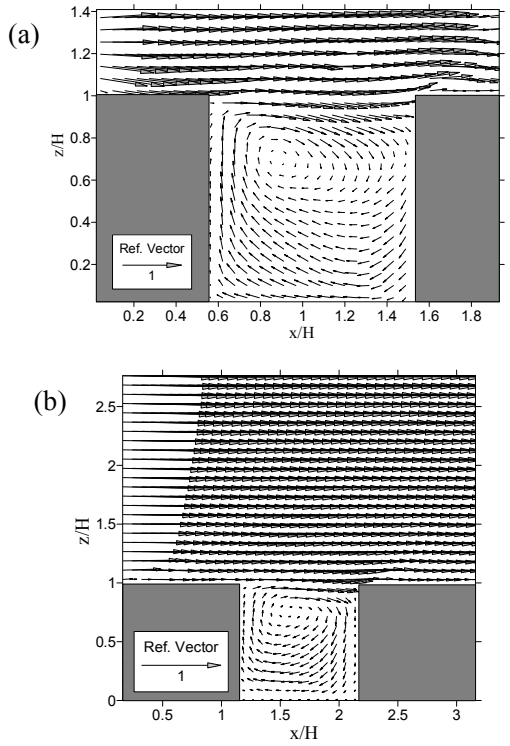


Figure 3. Mean velocity vector maps.
(a) COSMO, (b) WT.

One good reason of these differences is the existence of fluctuation in wind direction. Figure 4 are the conditionally averaged wind vector maps when instantaneous wind direction $\theta$ at 2H is (a) $|\theta| < 5°$, (b) $15° < |\theta| < 45°$. $\theta$ is the angle between wind direction and x-axis of the site. Both data used threshold of $u_{2H} > 0.5 m/s$. When wind is flowing perpendicularly to the street canyon, lower part of the canyon flow became near-parallel to the floor. In contrast, inclined wind direction makes stronger circulation and stronger influx at the canopy top. That is why mean flow is different between COSMO and WT. Field measurement had inclination and larger fluctuation in wind direction, compared to WT. For further understanding of these differences, 3-dimensionality is needed to be taken into account.

Figure 5 are the contours of Reynolds stress normalized with inner-layer scale $u_*^2$. Good agreements between two graphs suggest that Reynolds stress is determined by inner-layer variables and the effect of outer-layer disturbance is small. However, it is found that oblique wind direction leads to larger Reynolds stress. This is due to the transition of surface property with wind direction change. Square array becomes like a staggered array when wind direction is inclined. Staggered array induces higher drag to the flow [8].

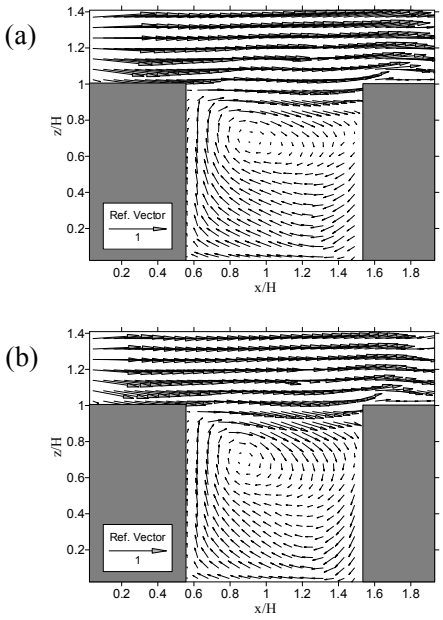


Figure 4. Wind vector maps filtered by wind direction.
(a) $|\theta| < 5°$, (b) $15° < |\theta| < 45°$.

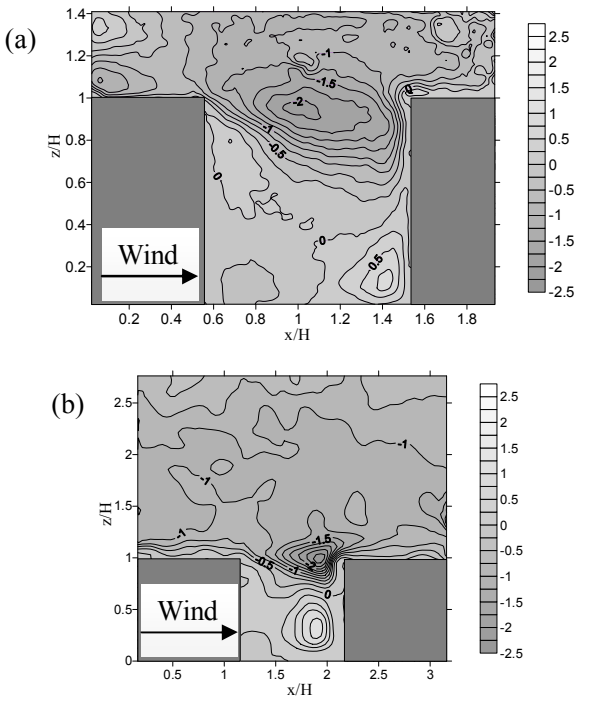


Figure 5. Contour maps of Reynolds stress $\overline{u'w'}/u_*^2$.
(a) COSMO, (b) WT.

### 3.3 Instantaneous flow structures

While one big circulation appeared in the mean flow, snapshots of each moment exhibit various flow structures. Especially, strong upward motions from the bottom of street canyon were most interesting phenomena (Figure 6). Intensities of these events varied widely, but visual inspection indicates that generally they have duration time of 2 to 5 seconds, and interval of 1 to 5 minutes. Similar flushing events were also observed in WT experiments. Although it is difficult to identify the flushing events due to its diversified intensity, one possible definition is "more than 60 % of vectors satisfy the condition of $w > |u|$ inside the street canyon". This condition still contains arbitrariness, but it detected the flushing events well from WT result. It revealed that the duration time of upward motions in WT were less than quarter of a second, and the frequency was once in 10 to 20 seconds. Considering the structures and the normalized cycles of the phenomena in COSMO and WT, these events seem to be generated by same mechanism.

Most likely cause of flushing events was considered to be Turbulent Organized Structure (TOS) developed in urban boundary-layer [3]. TOS in urban boundary-layer is characterized by its streaky pattern of low-momentum region. Such coherent structures account for most part of momentum transport. From visual inspection of WT results, we found strong correlation between flushing events and large scale low-momentum region. More than 80% of flushing events were occurred under the existence of such large scale turbulent structures.

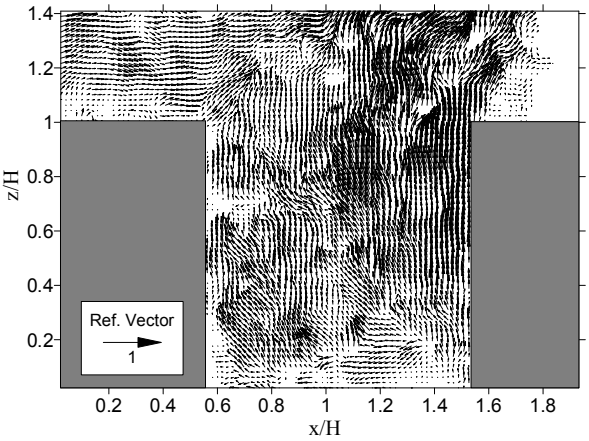


Figure 6. Instantaneous flow structure observed in COSMO.

# 4 Conclusions

In this study, a system of particle image velocimetry for the flow in field urban canopy was constructed. Using this system, atmospheric turbulence flow over urban-like roughness was observed. We exhibited the flow structure minutely, and the results from field experiment were compared with that of wind tunnel experiments. The investigation revealed following results.

1) Flow structure inside the urban canopy was successfully obtained with high spatial resolution. The quality of PIV dataset was good in comparison with the dataset from sonic anemometer.
2) Mean flow structures and Reynolds stresses were found to be similar between field and wind tunnel, although they have a little bit different characteristics. Inclination and fluctuation of wind direction are significant factors for these differences.
3) Strong intermittent upward motions from the bottom of street canyons were observed, which are expected to make a contribution to the ventilation in urban canopies. Our investigation suggested that the turbulent organized structure developed in urban boundary-layer is strongly related to the occurrence of the upward motion.

# References

[1] Roth, M.: 2000, 'Review of atmospheric turbulence over cities', *Quart. J. Roy. Meteorol. Soc*., **126**, 941-990.

[2] Moriwaki, R., Kanda, M.: 2006, 'Flux-gradient profiles for momentum and heat over an urban surface', *Theor. Appl. Climatol.*, **84**, 127-135.

[3] Inagaki, A.: 2008, 'Atmospheric turbulence over an array of massive cubes', Ph.D. Dissertation, Tokyo Institute of Technology.

[4] Adrian, R.J., Meinhart, C.D., Tomkins, C.D.: 2000, 'Vortex organization in the outer region of the turbulent boundary layer', *J. Fluid Mech.*, **422**, 1-54.

[5] Liu, H., Liang, B., Zhu, F., Zhang, B., Sang, J.: 2003, 'A laboratory model for the flow in urban street canyons induced by bottom heating', *Advances in Atmos. Sci.*, **20**, 554-564.

[6] Zhu, W., van Hout, R., Luznik, L., Kang, H.S.: 2006, 'A comparison of PIV measurements of canopy turbulence perfomed in the field and in a wind tunnel model', *Exp. in Fluids*, **41**, 309-318.

[7] Uehara, K., Wakamatsu, S., Ooka, R.: 2003, 'Studies on critical Reynolds number indices for wind-tunnel experiments on flow within urban areas', *Boundary-layer meteorol.*, **107**, 353-370.

[8] Kanda, M.: 2006, 'Large-eddy simulations on the effects of surface geometry of building arrays on turbulent organized structures', *Boundary-layer Meteorol.*, **118**, 151-168.

# Mechanism of ammonia nitrogen uptake by sterile *Ulva* sp. and its application to water quality control for intensive shrimp culture pond in developing country

Student Number: 07M18071 Name: Shin TAJIRI Supervisor: Ryuichi EGASHIRA

## 不稔性アオサによるアンモニア窒素摂取の機構と

## 開発途上国型エビ養殖池の水質制御に対する適用

田尻　新

まず、アオサのキャラクタリゼーション（炭素、水素、窒素、クロロフィル組成、等の測定）、様々な条件における培養液－藻体内部間のアンモニア窒素の分配平衡、アオサ表面の膜におけるアンモニア窒素の透過速度、およびアオサ内部におけるアンモニア窒素同化速度の実測、等を行った。昼間を想定した条件において透過速度は内部濃度基準の総括濃度差に比例し、昼間の条件の場合に比較して夜間の条件における透過速度は著しく低かった。アンモニア窒素同化速度と摂取速度はほぼ同等であった。これらの実験結果および既往のエビ養殖池における窒素循環モデルを用いてアオサによる水質制御計算を行った。養殖水中のアンモニア窒素濃度を低く抑えることができ、本法を簡便な水質制御法として提案した。

### 1 Introduction

Since the 1990s the shrimp industry, which has given high profit and foreign exchange to developing countries, has suffered many disease outbreaks[1]. Some shrimp farmers introduced none or quite small water exchange culture system to avoiding the infection of disease. However, employing the system began to cause the serious water deterioration and the water quality control became more important. Ammonia-nitrogen (ammonia-N,AN) excreted by shrimp respiration and from decomposition of bottom sediment is main cause of water deterioration. Ammonia-N is toxic to fishes and crustaceans[2] and even if the concentration is low, the growth of shrimp is inhibited[3]. Most of nitrogen component in the shrimp feed supplied into pond is finally discharged into the pond as the form of ammonia-N through excretion by shrimp and decomposition of accumulated sediment.

In this study, we investigated mechanism of ammonia nitrogen uptake by sterile *Ulva* sp. and simulated water quality control in basis of nitrogen balance and ammonia-N uptake mechanism of alga.

### 2 Mechanism of ammonia nitrogen uptake by sterile *Ulva* sp.

#### 2.1 Materials

Sterile *Ulva* sp. collected from April to November 2008 at Kanazawa Bay (Yokohama, Japan 35°20’32N, 139°38’32E). Commercial sea salt was used to prepare artificial seawater (salinity: 30‰).

#### 2.2 Experimental

##### 2.2.1 Characterization of alga

A vessel made of glass of which capacity $5\times10^{-2}m^3$ and used to store algae. Light source was 400W metal halide lamp.

Elemental analysis was carried out by CHN corder MT-6. Chlorophyll concentration was determined by Scor/Unesco method.

##### 2.2.2 Distribution of ammonia-nitrogen between culture medium and nitrogen pool in alga and permeation through surface film of algae

Algae were cultivated for 2h in artificial seawater containing 1mM methionine sulfoximine, which inhibits the assimilation of ammonia-N, before uptake runs. Concentrated ammonia-N solution added to culture medium at the beginning of uptake run and measured ammonia-N concentration of culture medium.

**Table 2.2.2-1** shows the principal conditions of uptake runs. Some conditions were assumed daytime, others were nighttime. In all runs, the algae without ammonia-N assimilation ability were used to know the distribution equilibrium of ammonia-N between the culture medium and the ammonia-N pool in alga. After equilibration, ammonia-N excretions were also conducted by exchanging the medium with ammonia-N free seawater.

##### 2.2.3 Assimilation of ammonia-nitrogen in alga

Concentrated ammonia-N solution added to culture medium at the beginning of uptake run and measured ammonia-N concentration of culture medium. The ammonia-N concentration in alga was measured by adding carbonyl cyanide m-chlorophenilhydrazone into the medium.

#### 2.3 Results and discussion

##### 2.3.1 Characterization of alga

**Table 2.3.1-1** shows of mass of Carbon, Hydrogen, and Nitrogen per unit dry biomass. Wt% of CHN decreased with increase of stock cultivation time. This is considered those nutrients, which were pooled in the sea, were exhausted for growth.

**Table2.3.1-2** shows amount of chlorophyll-a,b,c per unit dry biomass. There is not great differences of chlorophyll concentrations in each sample of alga.

**Table 2.3 1-1 Results of elemental analysis**

| Stock cultivation time | Biomass $\times10^3$ | H | C | N |
|---|---|---|---|---|
| [day] | [kgDM] | [wt-%] | [wt-%] | [wt-%] |
| 0 | 0.0581 | 5.30 | 28.29 | 3.26 |
| 0 | 0.0281 | 5.34 | 29.39 | 3.50 |
| 0 | 0.0646 | 5.25 | 27.80 | 3.13 |
| 5 | 0.0589 | 4.31 | 22.09 | 2.35 |
| 5 | 0.0206 | 4.78 | 24.97 | 2.55 |
| 5 | 0.0229 | 4.66 | 24.42 | 2.39 |

Sampling date 2008, Oct, 17th

**Table2.3.1-2 Chlorophyll concentration of alga**

| Biomass $\times 10^3$ [kgDM] | $C_{\text{Chl-a}} \times 10^3$ [kg-Chl kgDM$^{-1}$] | $C_{\text{Chl-b}} \times 10^3$ [kg-Chl kgDM$^{-1}$] | $C_{\text{Chl-c}} \times 10^3$ [kg-Chl kgDM$^{-1}$] |
|---|---|---|---|
| 0.064 | 1.5 | 0.6 | 0.6 |
| 0.053 | 2.1 | 1.0 | 1.0 |
| 0.044 | 2.7 | 1.2 | 1.1 |
| 0.048 | 2.2 | 0.9 | 0.7 |
| 0.033 | 2.3 | 1.0 | 0.8 |
| 0.043 | 2.0 | 0.9 | 0.8 |

### 2.3.2 Distribution of ammonia-nitrogen between culture medium and nitrogen pool in alga and permeation through surface film of algae

**Figure 2.3.2-1** shows the equilibrium relation between ammonia-N concentrations in culture medium and in the ammonia-N pool of alga. In condition assumed daytime, equilibrium ammonia-N concentrations in alga after uptake were higher than those after excretion. Equilibrium ammonia-N concentrations of internal algae in condition assumed daytime were higher than that concentration in condition assumed nighttime. These differences of equilibrium relation were considered to be chemical potential deference between external and internal algae.

**Figure 2.3.2-2** shows the relation between ammonia-N uptake rate and concentration difference $C'^*_{\text{N}}-C'_{\text{N}}$. $C'^*_{\text{N}}$ was estimated by the equilibrium relationship after uptake given in Fig.2.3.2-1. Mean gradient of collinear approximations not through origin was 0.73 h$^{-1}$

**Table 2.2.2-1 Experimental condition**

| | | |
|---|---|---|
| Initial concentration of culture medium $C_{\text{TAN},0}$ [kg-N m$^{-3}$] | 0.25~2.00 | |
| Culture density of alga $\rho_{\text{U}}$ [kgDM m$^{-3}$] | 0.07~0.66 | |
| Cultivation time [h] | 7~12 | |
| | Daytime | Nighttime |
| Light intensity, PPF [μmol s$^{-1}$ m$^{-2}$] | 1800 | 5> |
| Temperature [K] | 303 | 298 |

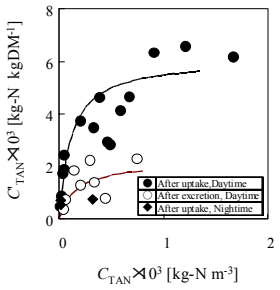


**Fig.2.3.2-1** Equilibrium between AN concentrations in culture medium and in alga

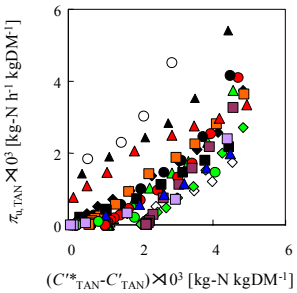


**Fig.2.3.2-2** Relation between A uptake rate and overall concentratic difference, $C'^*_{\text{TAN}}-C'_{\text{TAN}}$

### 2.3.3 Assimilation of ammonia-nitrogen in alga

The material balance in a unit volume of the culture medium is given by,

$$\rho_{\text{U}}\pi_{\text{u,TAN}} = -\frac{\mathrm{d}C_{\text{TAN}}}{\mathrm{d}t} = \rho\frac{\mathrm{d}C'_{\text{TAN}}}{\mathrm{d}t} + \rho_{\text{U}}\pi_{\text{a,TAN}} \qquad \textbf{(1,2)}$$

where $\pi_{\text{u,TAN}}$ is ammonia-N uptake rate by alga, $C'_{\text{TAN}}$ is the ammonia-N concentration in alga, and $\pi_{\text{a,TAN}}$ is the assimilation rate. Integration of this equation from time $t_1$ to $t_2$ leads to,

$$C_{\text{TAN},1} + \rho C'_{\text{TAN},1} = C_{\text{TAN},2} + \rho C'_{\text{TAN},2} + \rho\overline{\pi_{\text{a,TAN}}}(t_2 - t_1) \qquad \textbf{(3)}$$

where $\pi_{\text{a,TAN}}$ is mean assimilation rate between $t_1$ and $t_2$. **Figures 2.3.3-1** and **2.3.3-2** show the time courses of ammonia-N concentration in medium and those in alga with assimilation, respectively. **Figure 2.3.3-3** shows relation between mean ammonia-N concentration in alga and ammonia-N assimilation rate. Assimilation rate increased with increase of ammonia-N concentration in alga at first 1 hour. However, assimilation rates rapidly decreased with time. This decrease is provably due to exhaustion of other nutrients such as carbon.

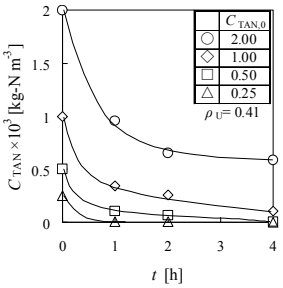


**Fig.2.3.3-1** Time courses of AN concentration in culture medium

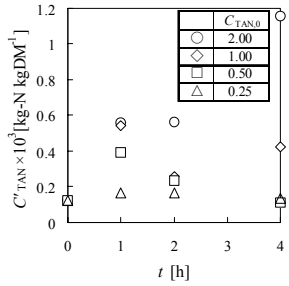


**Fig.2.3.3-2** Time courses of AN concentration in alga

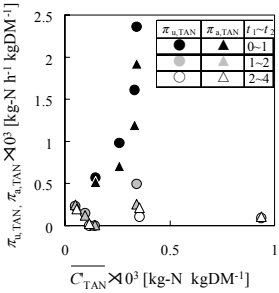


**Fig.2.3.3-3** Relation between mean AN concentration in alga and AN assimilation rate

**Table 2.3.3-1 Experimental conditi**

| | |
|---|---|
| $C_{\text{TAN},0}$ [kg-N m$^{-3}$] | 0.25~2.00 |
| $\rho_{\text{U}}$ [kgDM m$^{-3}$] | 0.41 |
| PPF [μmol s$^{-1}$ m$^{-2}$] | 1800 |
| Temperature [K] | 303 |

## 3 Water quality control for shrimp pond

### 3.1 Nitrogen balance in shrimp pond

**Figure3.1-1** shows a concept of nitrogen dynamics model.

Nitrogen as the form of the shrimp feed are supplied into pond. Much of feed is eaten by shrimp(1), and a portion of feed is uneaten(2). Shrimp excretes ammonia-N through respiration (4) and other nitrogen metabolite(feces, shed shell etc.)(3). Ammonia-N also generate from sediment decomposition(7). Ammonia-N in water column was removed by algal uptake(5), water exchange(8), and other removal process(9). Algae are removed from pond(6) as one of final form of nitrogen.

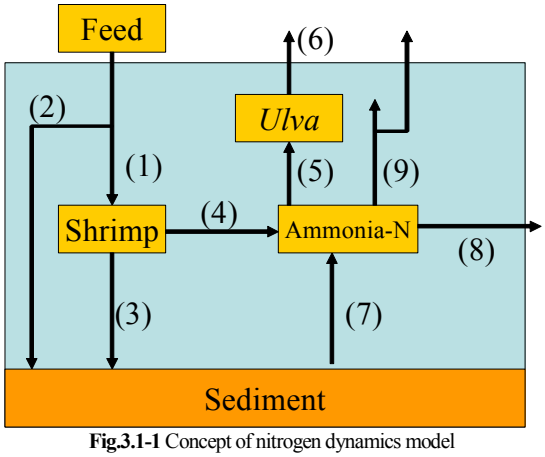


**Fig.3.1-1** Concept of nitrogen dynamics model

### 3.2 Basic equation and calculation

**Material balance;**

The material balance in a unit volume of pond water is given by,

$$\frac{dC_{TAN}}{dt} = r_{total,TAN} - r_{total,remove} \quad (4)$$

where $r_{total,TAN}$ is generation rate of ammonia-N, $r_{total,remove}$ is removal rate of ammonia-N.

**Ammonia-N generation**

Generation rate of ammonia-N is given by,

$$r_{total,TAN} = r_{e,TAN} + r_{sed,TAN} \quad (5)$$

where $r_{e,TAN}$ is rate of ammonia-N excreted by shrimp respiration, $r_{sed,TAN}$ is rate of ammonia-N generated by sediment decomposition.

$r_{e,TAN}$ is given by,

$$r_{e,TAN} = q_{TAN} r_{mtb,N} \quad (6)$$

where $q_{TAN}$ is ratio of ammonia-N from shrimp respiration to total nitrogen metabolite. $r_{mtb,N}$ is excretion rate of nitrogen metabolite from shrimp per unit volume of pond water and given by,

$$r_{mtb,N} = a_{mtb,N} \rho_s M_s^{\gamma} \quad (7)$$

where $a_{mtb,N}$ is nitrogen metabolite from shrimp per unit shrimp mass. $\rho_s$ is culture density of shrimp. $M_s$ is average shrimp mass and estimated from growth model. $\gamma$ is allometric scaling of shrimp metabolism.

On the other hand, $r_{sed,TAN}$ is given by,

$$r_{sed,TAN} = r_r M_{sed,N} \quad (8)$$

where $r_r$ is rate constant of decomposition. $M_{sed,N}$ is amount of nitrogen contained in sediment per unit volume of pond water. $M_{sed,N}$ include the sediment derived from uneaten feed and nitrogen metabolite from shrimp.

**Ammonia-N removal**

Removal rate of ammonia-N is given by,

$$r_{total,remove} = \rho_U \overline{\pi_{u,TAN}} + fC_{TAN} + oC_{TAN} \quad (9)$$

Where $\overline{\pi_{u,TAN}}$ is average uptake rate, $f$ and $o$ is rate constants of water exchange and other removal process, respectively. In the case that saturation ratio of photosynthesis affect uptake performance, $\overline{\pi_{u,TAN}}$ is given by,

$$\overline{\pi_{u,TAN}} = \overline{q_{light}} \pi_{u,TAN} \quad (10)$$

where $\overline{q_{light}}$ is average saturation ratio of photosynthesis ($\overline{q_{light}}$ equaled 1 in case of not taking the effect of saturation ratio of photosynthesis on uptake into account.) Relation between saturation ratio of photosynthesis $q_{light}$ and light intensity is approximated following equation,

$$q_{light}\left(=\frac{p}{p_{MAX}}\right) = \frac{I}{I + K_{light}} \quad (11)$$

where $I$ is light intensity at specific depth from pond surface. $K_{light}$ is constant depending on temperature. $I$ can be described by Beer-Lambert law as,

$$I = I_0 \, exp(-kz) \quad (12)$$

where $I_0$ is light intensity of pond surface, $k$ is overall light extinction coefficient, $z$ is distance from pond surface. $k$ is given by,

$$k = k_U + k_{other} \quad (13)$$

where $k_U$ and $k_{other}$ is light extinction coefficient of alga and pond water, respectively. $k_U$ is determined by chlorophyll concentration in alga and $\rho_U$ and given by,

$$k_U = k_{Chl} \rho_U C_{Chl} \quad (14)$$

where $k_{Chl}$ is light extinction coefficient per unit mass of chlorophyll-a, $C_{Chl}$ is chlorophyll-a amount per unit dry biomass of alga. $\pi_{u,TAN}$ is, from relation between $\pi_{u,TAN}$ and overall concentration difference, given by

$$\pi_{u,TAN} = P_u \left( C'^{*}_{TAN} - C'_{TAN} \right) \quad (15)$$

where $P_u$ is overall mass transfer coefficient. Change rate of ammonia-N concentration in alga can be obtain from material balance and given by below equation including growth dilution of ammonia-N in alga pool,

$$\frac{dC'_{TAN}}{dt} = -C'_{TAN} \overline{\pi_{a,TAN}} R_{Biomass/N} + \left( \overline{\pi_{u,TAN}} - \overline{\pi_{a,TAN}} \right) \quad (16)$$

where $R_{Biomass/N}$ is ratio of dry biomass to nitrogen in dry biomass. As with $\overline{\pi_{u,TAN}}$, $\overline{\pi_{a,TAN}}$ is given by

$$\overline{\pi_{a,TAN}} = \overline{q_{light}} \pi_{a,TAN} \quad (17)$$

From Fig. 4-3, assimilation rate is almost the same as uptake rate and that can be written by,

$$\pi_{a,TAN} = \pi_{u,TAN} \quad (\text{when } \pi_{a,TAN,MAX} \geq \pi_{u,TAN}) \quad (18)$$

$$\pi_{a,TAN} = \pi_{a,TAN,MAX} \quad (\text{when } \pi_{a,TAN,MAX} \leq \pi_{u,TAN}) \quad (19)$$

where $\pi_{a,TAN,MAX}$ is maximum assimilation rate of ammonia-N.

**Calculation**

Parameters of equations in chapter3.2 were estimated from chapter2 and cited previous study[4][5].

**Table3.2-1** shows the parameters of fixed value in all calculation. *Penaeus* monodon was selected as culture target. Cultivation time was 120days. It was assumed nitrogen input was only feed and was assumed 20% of total nitrogen input was assimilated by shrimp and 10% of that was uneaten by shrimp.

**Table3.2-2** shows the parameters that were varied in each calculation run. (1) was calculated as standard condition, (2) as prediction of effect of culture density of shrimp, (3) effect of saturation ratio of photosynthesis, (4) effect of water exchange and other removal process, (5) effect of ratio of nitrogen metabolite through respiration to total nitrogen metabolite, (6) effect of water turbidity, and (7)effect of algal harvest.

**Table3.2-1 Parameters of fixed value**

| | |
|---|---|
| $a_{mtb,N}$ [kg-N $h^{-1}$ kg-shrimp] | 0.0000274 |
| $C_{Chl}$ [kg-chl $kgDM^{-1}$] | 0.002131 |
| $P_U$ [$h^{-1}$] | 0.7307 |
| $\pi_{a,TAN,MAX}$ [kg-N $h^{-1}$ $kgDM^{-1}$] | 0.002042 |
| $R_{Biomass/N}$ [kgDM kg-$N^{-1}$] | 30.40 |
| $h$ [m] | 1.0 |
| $k_{Chl}$ [kg-$Chl^{-1}$ $m^{-1}$] | 11800 |
| $I_{0,day}$ [μmol $s^{-1}$ $m^{-2}$] | 1800 |
| $I_{0,night}$ [μmol $s^{-1}$ $m^{-2}$] | 0 |
| $T_{day}$ [K] | 303.15 |
| $T_{night}$ [K] | 298.15 |
| $\gamma$ [-] | 0.75 |
| $r_r$ [$h^{-1}$] | 0.0025 |

**Table3.2-2 Calculatiuon conditions**

| | $\rho_{u,0}$ [kgDM m$^{-3}$] | $\rho_{s,0}$ [m$^{-3}$] | $\overline{q_{light}}$ [-] | $f$ [h$^{-1}$] | $o\times10^3$ [h-1] | $q_{TAN}$ [-] | $k_{other}$ [m$^{-1}$] | $H_u$ [kgDM h$^{-1}$m$^{-3}$] |
|---|---|---|---|---|---|---|---|---|
| (1) | 0~2.0 | 40 | 1 | 0 | 0 | 1 | 2.5 | ※3 |
| (2) | 0~2.0 | 40~120 | 1 | 0 | 0 | 1 | 2.5 | ※3 |
| (3) | 0~2.0 | 40~120 | ※1 | 0 | 0 | 1 | 2.5 | ※3 |
| (4) | 0~2.0 | 40~120 | 1 | ※2 | 8.33 | 1 | 2.5 | ※3 |
| (5) | 0~2.0 | 40~120 | 1 | 0 | 0 | 0~1 | 2.5 | ※3 |
| (6) | 0~2.0 | 40 | ※1 | 0 | 0 | 1 | 1.0~4.0 | ※3 |
| (7) | 0~2.0 | 40 | 1 | 0 | 0 | 1 | 2.5 | 0 |

※1, $q_{light}$ was calculated by equation(10)~(14)

※2,Water exchange was carried out at night; Change rate is 0.8%, 8%, 12%, and 16% day$^{-1}$ in 0~30, 31~60, 61~90 and 91~120 day, respectively

※3, Algae were harvested to keep culture density of alga

### 3.3 Results and Discussion

**Figure3.3-1** shows effect of culture density of shrimp(calculation run(1)(2))**.** Ammonia-N concentration increase with time, also increase with increase of culture density of shrimp.

**Figure3.3-2** shows relation between initial culture density of algae and limit culture density of shrimp (calculation run(2)(3)). Limit culture density of shrimp, which was defined that maximum value of average ammonia-N concentration in nighttime does not exceed 0.001kg-N m$^{-3}$, slightly decreased with degree of light limitation $\overline{q_{light}}$.

increased by water exchange and decreased by light limitation.

**Figure3.3-3** shows relation between ratio of nitrogen metabolite through respiration to total nitrogen metabolite $q_{TAN}$ and limit of culture density of shrimp. Limit culture density of shrimp was increase with increase of $q_{TAN}$.

**Figure3.3-4** shows relation between light extinction coefficient of pond water and limit of culture density of shrimp.

In the case that harvest of algae was not conducted, final culture density of algae exceeded 2.0 kgDM m$^{-3}$. This

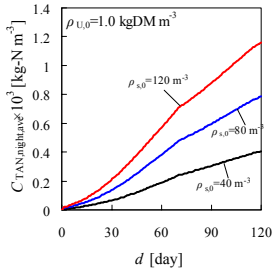


**Fig.3.3-1** Time courses of average ammonia-N concentration at nighttime on each day

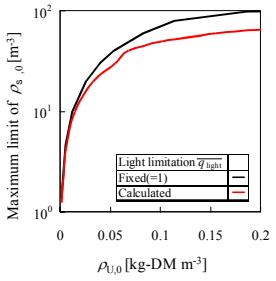


**Fig.3.3-2** Relation between initial culture density of alga and limit of culture density of shrimp

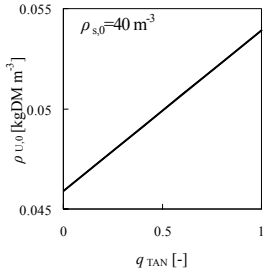


**Fig.3.3-3** Relation between ratio of nitrogen metabolite through respiration to total nitrogen metabolite and minimum limit of

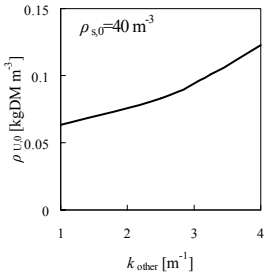


**Fig.3.3-4** Relation water turbidity and minimum limit of culture density of alga

range of culture density may inhibit the shrimp culture management.

## 4 Conclusion

We measured the ammonia-N distribution equilibrium relation between culture medium and in alga, ammonia-N permeation rate, and assimilation rate. Secondly, we carried out calculation of water quality based on these data.

The water quality control method by using sterile ulva can remove ammonia-N in shrimp pond more effectively

## Nomenclature

$a_{mtb,N}$ Nitrogen metabolite excretion rate [kg-N h$^{-1}$ kg-shrimp$^{-1}$]
$\gamma$ Allometric scaling of metabolism [-]
$C_{TAN}$ Ammonia-N concentration [kg-N·m$^{-3}$]
$C_{TAN,night,ave}$ Average ammonia-N concentration in nighttime [kg-N·m$^{-3}$]
$C_{TAN,night,MAX}$ Maximum value of average ammonia-N concentration in nighttime [kg-N·m$^{-3}$]
$C'_{TAN}$ Ammonia-N concentration in alga[kg-N·kgDM$^{-1}$]
$C'^{*}_{TAN}$ Equilibrium ammonia-N concentration in alga [kg-N·kgDM$^{-1}$]
$C_{Chl\text{-}a}$ Chlorophyll concentration in alga [kg-Chl-a kgDM$^{-1}$]
$d$ Cultivation time[day]
$f$ water exchange rate [h$^{-1}$]
$H_U$ Harvest rate of algae[kgDM h$^{-1}$ m$^{-3}$]
$h$ Pond depth[m]
$I$ Light intensity [μmol s$^{-1}$ m$^{-2}$]
$k$ Overall light extinction coefficient [m$^{-1}$]
$k_{Chl}$ Light extinction coefficient of chlorophyll [m$^2$ kg-Chl-a]
$k_{other}$ Light extinction coefficient of pond water [m$^{-1}$]
$k_U$ Light extinction coefficient of alga [m$^{-1}$]
$K_{light}$ Constant of apporoximation [μmol s$^{-1}$ m$^{-2}$]
$M_s$ Shrimp mass [kg-shrimp]
$M_{sed,N}$ Nitrogen in sediment per unit volume of pond water[kg-N m$^{-3}$]
$o$ Overall Rate constant of other ammonia-N removal process [h$^{-1}$]
$p$ Photosynthesis rate [μl-$O_2$ cm$^{-2}$ h$^{-1}$]
$p_{MAX}$ Saturated photosynthesis rate [μl-$O_2$ cm$^{-2}$ h$^{-1}$]
$P_U$ Overall mass transfer coefficient [h$^{-1}$]
$q_{light}$ Saturation ratio of photosynthesis [-]
$q_{TAN}$ Ratio of nitrogen metabolite through respiration to total nitrogen metabolite [-]
$R_{Biomass/N}$ Ratio of dry biomass to nitrogen in alga
$r_{e,TAN}$ Excretion rate of ammonia-N by shrimp respiration[kg-N h$^{-1}$ m$^{-3}$]
$r_{mtb,N}$ Nitrogen metabolite excretion rate by shrimp [kg-N h$^{-1}$ m$^{-3}$]
$r_r$ Rate constant of sediment decomposition [h$^{-1}$]
$r_{sed,TAN}$ Ammonia-N generation rate from sediment [kg-N h$^{-1}$ m$^{-3}$]
$r_{total,TAN}$ Total rate of ammonia-N generation [kg-N h$^{-1}$ m$^{-3}$]
$r_{total,remove}$ Removal rate of ammonia-N [kg-N h$^{-1}$ m$^{-3}$]
$t$ Cultivation time [h]
$T_{day}$ Temperature at daytime [K]
$T_{night}$ Temperature at nighttime [K]
$\pi_{a,TAN}$ Assimilation rate of ammonia-N [kg-N·kgDM$^{-1}$·h$^{-1}$]
$\pi_{a,TAN,MAX}$ Maximum assimilation rate of ammonia-N [kg-N·kgDM$^{-1}$·h$^{-1}$]
$\pi_{u,TAN}$ Uptake/permeation rate of ammonia-N [kg-N·kgDM$^{-1}$·h$^{-1}$]
$\rho_s$ Culture density of shrimp [m$^{-3}$]
$\rho_U$ Culture density of algae[kgDM·m$^{-3}$]

**<Subscript>**

a = assimilation ,Chl = chlorophyll, f = feed, mtb = metabolism, N = nitrogen, s = shrimp, TAN = Total Ammonia-Nitrogen, u = uptake, U = *Ulva*, 0 = initial or pond surface, ¯ = average

**Literature Cited**

[1]Primavera, J.H.; "Tropical Shrimp Farming and Its Sustainability," *Tropical Mariculture*, S. S. De Silva ed., pp. 257-289, Academic Press, San Diego, U.S.A. (1998)

[2]Haywood, G.P.; "Ammonia Toxicity in Teleost Fishes: A Review," Can. Tech. Rep. *Fish Aquat. Sci*., 1177, 1-35 (1983)

[3]Chen, J. C. and C. C. Tu; "Influence of Ammonia on Growth of Penaeus monodon Fabricius Post–Larvae," *Aquaculture and Fisheries Management*, 22, 457-462 (1991)

[4]Burford, M. A., Lorenzen, K., "Modeling nitrogen dynamics in intensive shrimp ponds: the role of sediment remineralization," *Aquaculture*, 229, 129-145(2004)

[5]Lorenzen, K., Struve, J., Cowan, V.J., "Impact of farming intensity and water management on nitrogen dynamics in intensive pond culture; a math mathematical model applied to Thai commercial shrimp farms," *Aquaculture Research*, 28, 493-507(1997)

# METHOD OF PROBABILITY DENSITY ESTIMATION FOR MAHALANOBIS METRIC IN VECTOR SPACE

Student Number:07M18088 Name:Toshinori Nakamoto Supervisor:Yukihiko Yamashita

パターン認識や統計的解析において，扱うデータに相関が存在することが多いが, 扱うデータの分布が非正規性を持つ場合，Mahalanobis 距離では正確な評価は困難である。そのため，ベクトル空間上の Mahalanobis 計量の研究が行われているが，標本点から Mahalanobis 計量を求める手法は存在していない。本研究では，Mahalanobis 計量を求めるために適した確率密度関数を与える，ノンパラメトリックな密度関数推定法を提案する。さらに，数値計算により，標本点から密度関数を推定し，それをもとに Mahalanobis 計量方程式を解く実験を行い，提案手法の有効性を確認する。

## 1 Introduction

The Mahalanobis distance [2], which is a distance normalized by a variance-covariance matrix of a distribution, is widely used for pattern recognition and data analysis. It enables to improve the accuracy of recognition comparing to the Euclidean distance.

For example, if two vectors differ in the direction in which the variance is small, the difference is small in terms of Euclidean distance but may be large from the viewpoint of probability (Fig.1 (a))

When the distribution of patterns is normal, the normalization by the variance-covariance matrix is reasonable. However, suppose that the contour lines of a probability distribution function (p.d.f.), which is not normal, is given as in Fig.1 (b). It is natural to evaluate the distance not along a straight line but along a curve. In order to realize such a distance, the Mahalanobis metric was proposed.


Figure 1: Mahalanobis metric

In the $n$-dimensional Euclidean space, the normal distribution with an average $\mu$ and a variance-covariance matrix $\Sigma$ is expressed by the p.d.f.:

$$p(x) = \frac{1}{\sqrt{(2\pi)^n \det(\Sigma)}} \exp(-\langle \Sigma^{-1}(x-\mu), (x-\mu)\rangle/2) \quad (1)$$

where $\langle \cdot, \cdot \rangle$ denotes the inner product and $\Sigma$ is assumed to be regular. Let $I$ be the identify matrix. When $x$ is mapped to $y$ by a linear transformation $y = \Sigma^{(-1/2)}x$, $p$ is transformed to the p.d.f. of a normal distribution of which variance-covariance matrix is $I$. The inner product that expresses the Mahalanobis distance is given as the pull back of the inner product as $\langle y, y' \rangle = \langle \Sigma^{-1}x, x' \rangle$.

The equation of geometrically local isotropic independence(GLII) was proposed to define a normal distribution in a manifold [5]. It provides an normal distribution of which variance-covariance matrix is $aI$ ($a > 0$) in the Euclidean space, the von Mises-Fisher distribution on a hyper-spherical surface, and an distribution proportional to $e^{-\kappa \cosh \theta}$ in the Lobachevsky space. The Mahalanobis metric equation was defined by extending the linear transformation to a diffeomorphism and using the equation of GLII [5]. It is remarkable that its differential equation does not depend on the coordinate system or the original metric. Furthermore, the diffeomorphism will disappear in it.

In this paper, a p.d.f. is estimated from sample points by maximum likelihood approach, and we conduct an experiment to solve the mahalanobis metric equation.

## 2 Mahaklanobis metric equation

A normal distribution is characterized by the equality between the sample mean and the maximum likelihood estimator (C.F.Guass), by isotropic independence (Maxwell), by the entropy, or by the central limit theorem [1], [3]. Let $X_1$ and $X_2$ be random variables and $(Y_1, Y_2)$ be the rotation of $(X_1, X_2)$ by an angle $\theta$ ($\neq 0, \pm\pi/2, \pm 2\pi/2, \pm 3\pi/2, \cdots$). If $X_1$ and $X_2$ are independent and $Y_1$ and $Y_2$ are also, then the distribution of $X_1$ and $X_2$ should be normal and its variance-covariance matrix is $aI$ ($a > 0$). By using this characterization, Maxwell provided the velocity distribution of the ideal gas.

Here, we consider an $n$-dimensional Riemannian manifold [4]. We use the summation rule in the notation of equations. For a small displacement $dx^\mu$ in a coordinate system $\{x^\mu\}$, its distance is given by $(ds)^2 = g_{\mu\nu}dx^\mu dx^\nu$. $g_{\mu\nu}$ is called the metric tensor. Its inverse tensor is denoted by $g^{\mu\nu}$. Let $g$ be the determinant of $g_{\mu\nu}$.

The covariant differential for an antivariant vector field $X^\mu$ is given by $\nabla_\nu X^\mu = \partial_\nu X^\mu + \Gamma^\mu_{\nu\beta} X^\beta$, where $\partial_\mu = \frac{\partial}{\partial x_\mu}$ and $\Gamma^\mu_{\nu\beta}$ is the connection [4]. The Levi-Chivita connection can be derived from $g_{\mu\nu}$ as

$$\Gamma^\alpha_{\mu\nu} = \frac{1}{2} g^{\alpha\beta}(\partial_\mu g_{\beta\nu} + \partial_\nu g_{\mu\beta} - \partial_\beta g_{\mu\nu}). \quad (2)$$

In an Euclidean space, if a p.d.f. $p(x^1, x^2)$ satisfies

$$\partial_1 \partial_2 \log p(x^1, x^2) = 0 \quad (3)$$

it is clear that $x^1$ and $x^2$ are independent ($p(x^1, x^2) = p_1(x^1)p_2(x^2)$). Based on the characterization by Maxwell and eq(3), the equation of GLII for a normal distribution in a manifold is defined.

For a p.d.f. $p$ in a manifold $M$, suppose that a diffeomorphism from $M$ to a manifold $M'$ transforms $p$ to a solution of the equation of GLII in $M'$. Then, the Mahalanobis metric $\tilde{g}_{\mu\nu}$ in $M$ is defined by the pull back of the metric in $M'$ and is given by the Mahalanobis metric equation:

$$\tilde{\nabla}_\mu \tilde{\nabla}_\nu \left( \log p - \frac{1}{2} \log \tilde{g} \right) - f \tilde{g}_{\mu\nu} = 0 \tag{4}$$

where $\tilde{g} = \det \tilde{g}_{\mu\nu}$ and $\tilde{\nabla}_\mu$ is the covariant differential derived from $\tilde{g}_{\mu\nu}$. A scalar $f$ is determined according to the topology of $M$. When $M$ is an $n$-dimensional real space (but not an Euclidean space), we can let $f = -1$. Furthermore, since we assume that $M$ is a vector space, we add the condition $R = g^{\alpha\beta} R^\gamma_{\alpha\gamma\beta} = 0$, where $R^\kappa_{\lambda\mu\nu} = \partial_\mu \Gamma^\kappa_{\nu\lambda} - \partial_\nu \Gamma^\kappa_{\mu\lambda} + \Gamma^\eta_{\nu\lambda} \Gamma^\kappa_{\mu\eta} + \Gamma^\eta_{\mu\lambda} \Gamma^\kappa_{\nu\eta}$.

# 3 Mahalanobis metric by Newton Raphson method

We explain an algorithm to solve the Mahalanobis metric equation by the Newton-Raphson method. Here, we discuss the case when the dimension of the space is two. For brief, $\tilde{g}_{\mu\nu}$, $\tilde{\nabla}$, etc. are denoted without $\tilde{\ }$. We expand the Mahalanobis metric equation (4) and let its left hand side be $F_{\mu\nu}$. Then, we have

$$\begin{aligned} F_{11} &= \partial_1\partial_1 \log p - \Gamma^1_{11}\partial_1 \log p - \Gamma^2_{11}\partial_2 \log p \\ &\quad + \Gamma^1_{11}(\Gamma^1_{11} + \Gamma^2_{21}) + \Gamma^2_{11}(\Gamma^1_{12} + \Gamma^2_{22}) \\ &\quad - \frac{\partial}{\partial x^1}(\Gamma^1_{11} + \Gamma^2_{21}) + g_{11} \end{aligned} \tag{5}$$

$$\begin{aligned} F_{12} &= \partial_1\partial_2 \log p - \Gamma^1_{12}\partial_1 \log p - \Gamma^2_{12}\partial_2 \log p \\ &\quad + \Gamma^1_{12}(\Gamma^1_{11} + \Gamma^2_{21}) + \Gamma^2_{12}(\Gamma^1_{12} + \Gamma^2_{22}) \\ &\quad - \frac{\partial}{\partial x^2}(\Gamma^1_{11} + \Gamma^2_{22}) + g_{12} \end{aligned} \tag{6}$$

$$\begin{aligned} F_{22} &= \partial_2\partial_2 \log p - \Gamma^1_{22}\partial_1 \log p - \Gamma^2_{22}\partial_2 \log p \\ &\quad + \Gamma^1_{22}(\Gamma^1_{11} + \Gamma^2_{21}) + \Gamma^2_{22}(\Gamma^1_{12} + \Gamma^2_{22}) \\ &\quad - \frac{\partial}{\partial x^2}(\Gamma^1_{12} + \Gamma^2_{22}) + g_{22}. \end{aligned} \tag{7}$$

$\Gamma^\mu_{\nu\beta}$ and $R$ can be calculated from $g_{\mu\nu}$ and its first and second order derivatives.

For numerical analysis, $g_{\mu\nu}$ is defined on the $N_1 \times N_2$-lattice. Since the differentials are approximated by differences, we cannot have $F_{\mu\nu}$ and $R$ on the boundaries. Then, we have their values on $(N_1-2)\times(N_2-2)$ -lattice. When we consider small changes of $g_{\mu\nu}$, $F_{\mu\nu}$ and $R$ change at the point and its neighbors. Then, we renew $g_{\mu\nu}$ on $(N_1-4)\times(N_2-4)$-lattice. The $g_{\mu\nu}$ not on the $(N_1-4)\times(N_2-4)$-lattice is set to the value at the nearest point in the lattice. We denote points in $(N_1-2)\times(N_2-2)$-lattice by $r_1, r_2, \cdots, r_{(N_1-2)(N_2-2)}$ and points in $(N_1-4)\times(N_2-4)$-lattice by $s_1, s_2, \cdots, s_{(N_1-4)(N_2-4)}$.

Let $\frac{\partial F_{\mu\nu}}{\partial g_{\alpha\beta}}$ and $\frac{\partial R}{\partial g_{\alpha\beta}}$ be the $(N_1-2)(N_2-2)\times(N_1-4)(N_2-4)$-matrices of which $(i, j)$ -elements are given by

$$\left( \frac{\partial F_{\mu\nu}}{\partial g_{\alpha\beta}} \right)_{i,j} = \frac{\partial F_{\mu\nu}(r_i)}{\partial g_{\alpha\beta}(s_j)}, \left( \frac{\partial R}{\partial g_{\alpha\beta}} \right)_{i,j} = \frac{\partial R(r_i)}{\partial g_{\alpha\beta}(s_j)} \tag{8}$$

respectively. We define the $4(N_1-2)(N_2-2)\times 3(N_1-4)(N_2-4)$ -matrix by

$$D = \begin{pmatrix} \frac{\partial F_{11}}{\partial g_{11}} & \frac{\partial F_{11}}{\partial g_{12}} & \frac{\partial F_{11}}{\partial g_{22}} \\ \frac{\partial F_{12}}{\partial g_{11}} & \frac{\partial F_{12}}{\partial g_{12}} & \frac{\partial F_{12}}{\partial g_{22}} \\ \frac{\partial F_{22}}{\partial g_{11}} & \frac{\partial F_{22}}{\partial g_{12}} & \frac{\partial F_{22}}{\partial g_{22}} \\ \frac{\partial R}{\partial g_{11}} & \frac{\partial R}{\partial g_{12}} & \frac{\partial R}{\partial g_{22}} \end{pmatrix} \tag{9}$$

and the $4(N_1-2)(N_2-2)$-dimensional vector by

$$\begin{aligned} F &= (F_{11}(r_1), F_{11}(r_2), \cdots, F_{11}(r_{(N_1-2)(N2-2)}), \\ &\quad F_{12}(r_1), F_{12}(r_2), \cdots, F_{12}(r_{(N_1-2)(N2-2)}), \\ &\quad F_{22}(r_1), F_{22}(r_2), \cdots, F_{22}(r_{(N_1-2)(N2-2)}), \\ &\quad R(r_1), R(r_2), \cdots, R(r_{(N_1-2)(N2-2)}))^T. \end{aligned}$$

Furthermore, we define the $3(N_1-4)(N_2-4)$-dimensional vector by

$$\begin{aligned} G &= (g_{11}(s_1), g_{11}(s_2), \cdots, g_{11}(r_{(N_1-4)(N2-4)}), \\ &\quad g_{12}(s_1), g_{12}(s_2), \cdots, g_{12}(r_{(N_1-4)(N2-4)}), \\ &\quad g_{22}(s_1), g_{22}(s_2), \cdots, g_{22}(r_{(N_1-4)(N2-4)})). \end{aligned}$$

Let $D^{(l)}, F^{(l)}$, and $G^{(l)}$ be the values of $D$, F and $G$ after the $l$-th iteration, respectively. The algorithm with a relaxation parameter $\epsilon$ is expressed as

$$G^{(l+1)} = G^{(l)} - \epsilon \left( (D^{(l)})^T D^{(l)} \right)^{-1} (D^{(l)})^T F^{(l)}. \tag{10}$$

# 4 Probability density estimation

We propose an estimation method of p.d.f. for Mahalanobis metric equation from sample points in 2-dimensional-lattice by maximum likelihood approach. $\boldsymbol{p}_S$ and $\boldsymbol{p}_G$ stand for values of p.d.f. on sample points and grid points, respectively. We let $\boldsymbol{l}_S = \log \boldsymbol{p}_S, \boldsymbol{l}_G = \log \boldsymbol{p}_G$. Let $n$ denote the number of sample points, and a log likelihood $L(\boldsymbol{l}_S)$ is defined as

$$L(\boldsymbol{l}_S) = \log(p_{S_1} p_{S_2} \cdots p_{S_n}) = \sum_{k=1}^{n} l_{S_k}. \tag{11}$$

$\boldsymbol{l}_G$ has to be calculated from $\boldsymbol{l}_S$ because we maximize $L(\boldsymbol{l}_S)$ under the condition of

$$\sum_{\mu=1}^{N_1} \sum_{\nu=1}^{N_2} p_{G_{\mu\nu}} = 1. \tag{12}$$

Here, we provide a matrix to calculate $\boldsymbol{l}_S$ from $\boldsymbol{l}_G$ by the least square approach and solve this inverse problem. Now, we assume that $\boldsymbol{l}_G$ is given in 2-dimensional lattice, and calculate the matrix $A$ which expresses the interpolation from $\boldsymbol{l}_G$ into $\boldsymbol{l}_S$ by least square approach with the nearest $3 \times 3$-grid points of the sample point as

$$\boldsymbol{l}_S = \boldsymbol{A} \boldsymbol{l}_G. \tag{13}$$

Next, we let that $\boldsymbol{l}_G$ is smooth, so assume that its third derivatives are small. Matrices $\boldsymbol{D}_{x^1x^1x^1}, \boldsymbol{D}_{x^1x^1x^2}, \boldsymbol{D}_{x^1x^2x^2}$, and $\boldsymbol{D}_{x^2x^2x^2}$, which expresses the differentials of rank 3 as

$$\frac{\partial^3}{\partial(x^1)^3}\boldsymbol{l}_G = \boldsymbol{D}_{x^1x^1x^1}\boldsymbol{l}_G,\ \frac{\partial^3}{\partial(x^1)^2(x^2)}\boldsymbol{l}_G = \boldsymbol{D}_{x^1x^1x^2}\boldsymbol{l}_G$$

$$\frac{\partial^3}{\partial(x^1)(x^2)^2}\boldsymbol{l}_G = \boldsymbol{D}_{x^1x^2x^2}\boldsymbol{l}_G,\ \frac{\partial^3}{\partial(x^2)^3}\boldsymbol{l}_G = \boldsymbol{D}_{x^2x^2x^2}\boldsymbol{l}_G.$$

When we let $\boldsymbol{D}_{all} = \boldsymbol{D}_{x^1x^1x^1}{}^\top\boldsymbol{D}_{x^1x^1x^1} + \boldsymbol{D}_{x^1x^1x^2}{}^\top\boldsymbol{D}_{x^1x^1x^2} + \boldsymbol{D}_{x^1x^2x^2}{}^\top\boldsymbol{D}_{x^1x^2x^2} + \boldsymbol{D}_{x^2x^2x^2}{}^\top\boldsymbol{D}_{x^2x^2x^2}$, we have

$$\begin{aligned}
&\left\|\frac{\partial^3\boldsymbol{l}_G}{\partial(x^1)^3} + \frac{\partial^3\boldsymbol{l}_G}{\partial(x^1)^2(x^2)} + \frac{\partial^3\boldsymbol{l}_G}{\partial(x^1)(x^2)^2} + \frac{\partial^3\boldsymbol{l}_G}{\partial(x^2)^3}\right\|^2 \\
= &\ \langle\boldsymbol{D}_{x^1x^1x^1}\boldsymbol{l}_g, \boldsymbol{D}_{x^1x^1x^1}\boldsymbol{l}_g\rangle + \langle\boldsymbol{D}_{x^1x^1x^2}\boldsymbol{l}_g, \boldsymbol{D}_{x^1x^1x^2}\boldsymbol{l}_g\rangle \\
&+\langle\boldsymbol{D}_{x^1x^2x^2}\boldsymbol{l}_g, \boldsymbol{D}_{x^1x^2x^2}\boldsymbol{l}_g\rangle + \langle\boldsymbol{D}_{x^2x^2x^2}\boldsymbol{l}_g, \boldsymbol{D}_{x^2x^2x^2}\boldsymbol{l}_g\rangle \\
= &\ \langle\boldsymbol{D}_{all}\boldsymbol{l}_g, \boldsymbol{l}_g\rangle. \qquad (14)
\end{aligned}$$

Considering with eqs.(13) and (14), we obtain the minimization problem of $J_C$

$$\begin{aligned}
J_C(\boldsymbol{l}_G) &= \|\boldsymbol{A}\boldsymbol{l}_G - \boldsymbol{l}_S\|^2 + \mu\|\boldsymbol{D}_{all}\boldsymbol{l}_G\|^2 \\
&= \langle\boldsymbol{A}^\top\boldsymbol{A}\boldsymbol{l}_G, \boldsymbol{l}_G\rangle - 2\langle\boldsymbol{A}^\top\boldsymbol{l}_S, \boldsymbol{l}_G\rangle \\
&\quad +\langle\boldsymbol{l}_S, \boldsymbol{l}_S\rangle + \mu\langle\boldsymbol{D}_{all}\boldsymbol{l}_G, \boldsymbol{l}_G\rangle. \qquad (15)
\end{aligned}$$

By the variation of $\boldsymbol{J}_C$, we have the matrix $B$ for estimating $\boldsymbol{l}_G$ from $\boldsymbol{l}_S$ as $\boldsymbol{l}_G = \boldsymbol{B}\boldsymbol{l}_S$. $\mu$ stands for a smoothing parameter.

We define the $n$-dimensional vector by

$$\boldsymbol{J}_L = \left(\frac{\partial L(\boldsymbol{l}_S)}{\partial l_{S_1}} \quad \cdots \quad \frac{\partial L(\boldsymbol{l}_S)}{\partial l_{S_n}}\right)^\top. \qquad (16)$$

Let $\boldsymbol{l}_S^{(\kappa)}$, $\boldsymbol{l}_G^{(\kappa)}$ and $\boldsymbol{J}_L^{(\kappa)}$ be the values of $\boldsymbol{l}_S$, $\boldsymbol{l}_G$ and $\boldsymbol{J}_L$ after the $\kappa$-th iteration, respectively. After we adjust $\boldsymbol{l}_S^{(\kappa)}$ in condition of normalizing $\boldsymbol{l}_G^{(\kappa)}(= \boldsymbol{B}\boldsymbol{l}_S^{(\kappa)})$, update $\boldsymbol{l}_S^{(\kappa+1)}$ by the steepest descent method with a parameter $\lambda$ as

$$\boldsymbol{l}_S^{(\kappa+1)} = \boldsymbol{l}_S^{(\kappa)} + \lambda\boldsymbol{J}_L^{(\kappa)}. \qquad (17)$$

# 5 Experimental results

In experiment, we generate sample points along a normal isotropic distribution of which variance is 1 in the coordinate system $\{x^\mu\}$. Next, we let variances in the direction of $x^1$ and $x^2$ be $\sigma^1$ and $\sigma^2$. We define an coordinate system $\{y^\mu\}$ with rotation of $\{x^\mu\}$ by $\theta$. In addition, $\{z^\mu\}$ is given by a nonlinear transformation of $\{y^\mu\}$. We assume that sample points in $\{z^\mu\}$ are obtained. We define a coordinate transform from $\{y^\mu\}$ into $\{z^\mu\}$ as

$$\begin{aligned}
z^1 &= y^1 \qquad (18)\\
z^2 &= y^2 + \beta h(y^1)h(y^2) \qquad (19)
\end{aligned}$$

with constants $\alpha$, where

$$h(y) = \begin{cases} e^{4\left(1-\frac{1}{1-(y/\alpha)^2}\right)} & (-\alpha < y < \alpha) \\ 0 & (\text{else}) \end{cases}. \qquad (20)$$

To estimate p.d.f. we consider the coordinate system $\{w^\mu\}$ given by a liner whitening of sample points of which variance is $\gamma^2$. And the proposed algorithm is applied to the sample points.

We calculate the Mahalanobis metric with the estimated p.d.f. In this experiment, we set $\alpha = 27, \beta = 2.7$, $N_1 = N_2 = 55$, $\sigma^1 = 2.5$, $\sigma^2 = 1$, $\theta = \pi/6$, $\gamma = 3$, $\lambda = 0.1$ and $\epsilon = 0.05$. The number of sample points generated in coordinate system $\{x^\mu\}$ is 500. The $53 \times 53$-lattice is assumed to be the region of $[-26, 26] \times [-26, 26]$ in the coordinate system $\{x_\mu\}$.

Figs.2 (a), (b), and(c) illustrate the results of estimated p.d.f. with $\mu$=200. Figs.2 (d) and (g) illustrate the calculated $g_{\mu\nu}$ with $\mu$=200. Figs.2 (e) and (g) illustrate the calculated and the original $g_{\mu\nu}$. Figs.2 (h) and (i) illustrate the squared errors of $g_{\mu\nu}$, and $F_{\mu\nu}$ with the number of iterations.

# 6 Conclusion

From those results, we can obtain the Mahalanobis metric by estimating the p.d.f. from sample points and solving the Mahalanobis metric equation. However, the method does not have enough accuracy. Then, it is necessary to survey parameter and to introduce the Newton method to maximum likelihood approach.

# References


[1] W.Feller. *An introduction to probability theory and its application*, third edition, **vol.1**, John Wiley & Sons, New York, 1968.

[2] P.Mahalanobis. Normalization of statistical variates and the use of rectangular co-ordinates in the theory of sampling distributions. Sankhay, 3:1-40, 1937.

[3] L.Maistrov. *Probability theory, a historical sketch* Academic Press, New York and London, 1974. (Translated and Edited by Kotz, S.)

[4] M.Spivak. *A comprehensive introduction to differential geometry*, second edition, **vol.1–5**, Publish or Perish, Inc., Houston, Texas, 1979.

[5] Y.Yamashita, M.Numakami, and N.Inoue. Maxwell normal distribution in a manifold and mahalanobis metric. In D.-Y. Yeung, J. T.Kwok, A. Fred, F. Roli, and D. de Ridder, editor, *tructural, Syntactic and Statistical Pattern Recognition*, pp.604-612. Springer Berlin Heidelberg, August 2006.

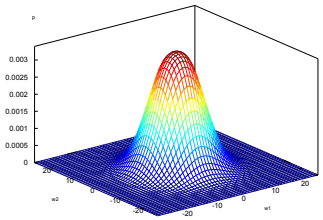

(a) Estemated $p$(3D) with $\mu = 200$

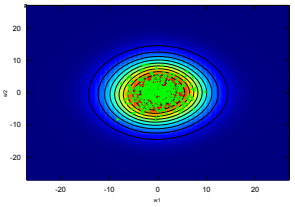

(b) Estimated $p$(2D) with $\mu = 200$

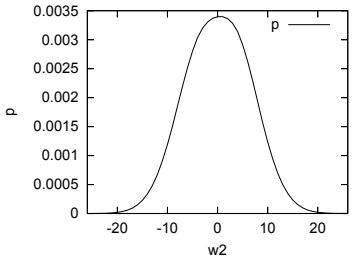


(c) Estimated $p(w^1 = 0)$ with $\mu = 200$

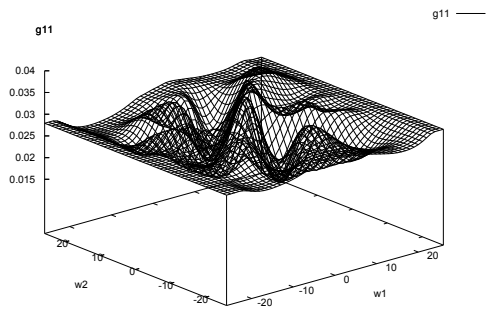


(d) $g_{11}$(3D) with $\mu = 200$

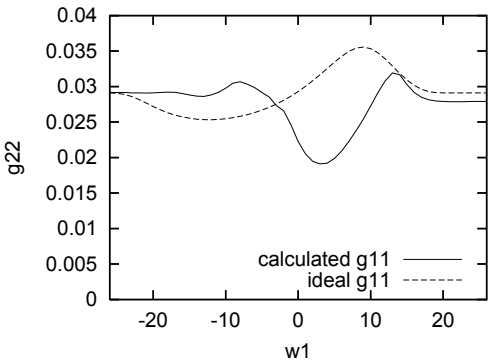


(e) $g_{11}(w^2 = 0)$ with $\mu = 200$

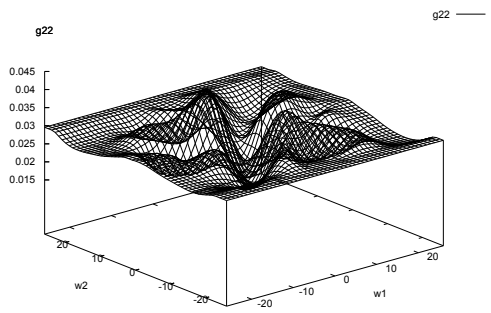


(f) $g_{22}$(3D) with $\mu = 200$

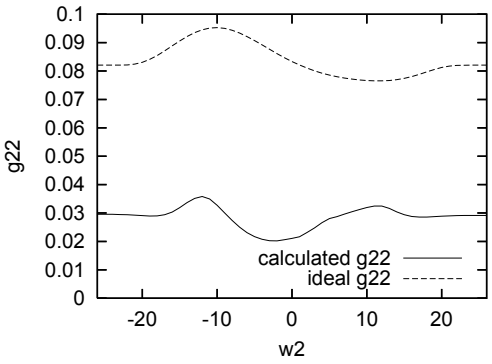


(g) $g_{22}(w^1 = 0)$ with $\mu = 200$

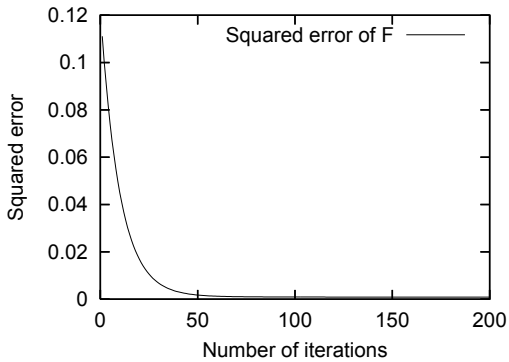


(h) Mean square errors of $F_{\mu\nu}$ vs. the num. of iterations

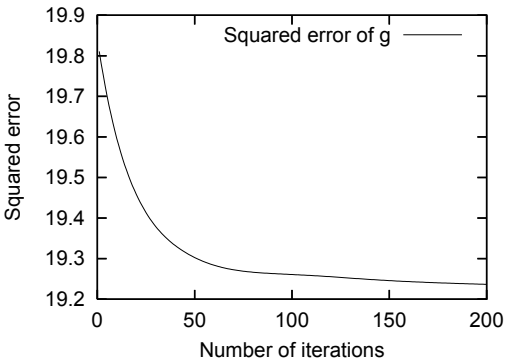


(i) Mean square errors of $g_{\mu\nu}$ vs. the num. of iterations

Figure 2: Experimental results

# LAGRANGIAN HUMAN METEOROLOGY

Student Number: 07M18094 Name: Makoto Nakayoshi Supervisor: Manabu Kanda

# ラグランジュアン人間気象学の試論

仲吉信人

本論文では“ラグランジュアン人間気象学（LHM）”を提案しその有用性を議論する．LHMは，個々人が計測器を装着し，動線に沿って変化する熱環境，それに伴う人体生理の変化を監視評価するものである．2008年夏季晴天日に行った都心を周回する現地観測から以下のことが示された．①通勤ラッシュ時の混雑駅ホームは熱中症の危険を伴う暑熱環境が形成されていた．②満員電車内の環境は被験者の心拍・血圧値を上昇させていた．③都市街路空間は大手町アメダス気温を最高で3℃上回る熱環境であった．

## 1 Introduction

Due to the global warming and the heat island phenomenon, problems such as warmer environments and the increasing incidence of heat stroke patients are usual in several Asian mega-cities. Monitoring the meteorological information in cities is important for urban environmental amenity and human health. However, official meteorological information can be largely different from actual micro-climate in urban canyons where we are living, because the data are measured over managed grasslands. In addition, our physiological response to micro-climate can be different by individuals depending on their lagrangian movements and physical and mental conditions. Thus, lagrangian observational data along human pathways are better suitable for urban meteorological information on health rather than that from fixed-point observations in Euler sense. Here I propose a new lagrangian concept for urban bio-meteorology named "Lagrangian Human Meteorology (LHM)".

## 2 Concept of LHM

The concept of LHM is to investigate continuous changes of micro-climate and the dynamical physiological response along human pathways carrying small bio-meteorological sensors. The sensors monitor ambient temperature (Ta), relative humidity (RH), wind velocity (U), mean radiative temperature (MRT), body temperature (Tb), heart rate (HR), and blood pressure (BP). The perspective merits of LHM include contributions to 1.) self-monitoring and precaution of health disorder such as heat stroke and 2.) evaluation of actual micro-climate absent of eulerian fixed-observation points.

Table 1 Measurement items

| Item | Sensor | Manufacturer | Sampling frequency |
|---|---|---|---|
| Ta | Thermocouple (0.2 mm) | NEWC*2 | 1 Hz |
| MRT | Globe temperature sensor (40 mm) | Self-produce | 1 Hz |
| RH | Humidity transmitter | Vaisala | 1 Hz |
| U | Hot-wire anemometer | Kanomax | 1 Hz |
| HR BP | Sphygmomanometer (wrist type) | Omron | — |
| Tb*1 | Thermocouple (0.2 mm) | NEWC*2 | 1 Hz |

*1: Axillary body temperature

*2: Ninomiya Electrical Wire CO., Ltd.

## 3 Lagrangian observation

To confirm the effectiveness of LHM, The author conducted a lagrangian observation in central Tokyo on a typical fair day in summer, 20th August in 2008. Measuring items are represented in Table 1. All of the meteorological sensors were packed in a carry bag (Figure 1). The summary of the event records and the observational route map are shown in Table 2 and Figure 2, respectively.

### 3.1 Results and Discussion

Standard effective temperature (SET*) and Ta are focused here for micro-climate variables (Figure 3 (a) and 4). SET*

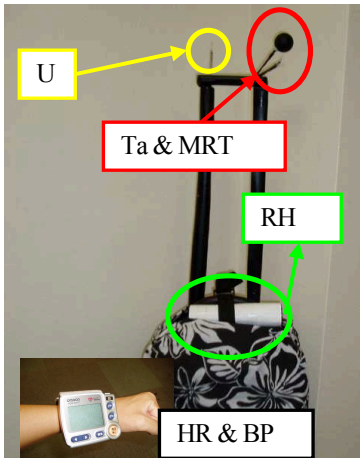


Figure 1 Measurement system

Table 2 Summary of event records of the lagrangian observation. Alphabet in ID column corresponds to that in Figure 2 and Figure 4.

| Time | ID | Event | Time | ID | Event |
|---|---|---|---|---|---|
| 6:55 | | Leaving home (by foot) | 16:01 | | Boarding Toei-Oedo line |
| 7:06 | a | Arriving at Okayama station | 16:03 | g | Arriving Roppongi station |
| 7:08 | a' | Boarding Oimachi line | 16:20 | h | On the street at Roppongi area |
| 7:21 | | Arriving at Futakutamagawa station | 16:30 | i | Walking around at Roppongi hills |
| 7:22 | b' | Boarding Denentoshi line | 18:32 | | Arriving at Mid town |
| 7:41 | b | Arriving at Nagatuda station | 18:39 | j | Moviegoing at garden theater of Mid town |
| 7:50 | c' | Boarding Denentoshi line | 21:51 | k | Chatting with a friend (open-air cafe) |
| 8:31 | c | Arriving at Shibuya station | 23:01 | | Leaving Mid town |
| 8:39 | | On the street at Shibuya area | 23:11 | | Arriving at Roppongi-itchome station |
| 12:08 | d | Taking in the sun at Miyashita park | 23:19 | | Boarding Toei-Oedo line |
| 14:40 | | Shopping around Shibuya and Harajuku area | 23:31 | m | Arriving at Shibuya station |
| 14:16 | e | Lunch | 23:34 | | On the street at Shibuya area |
| 15:05 | f | Shopping at Tokyu hands | 23:54 | | Boarding Denentoshi line |
| 15:41 | | Arriving at Shibuya station | 0:08 | | Arriving at Futakotamagawa station |
| 15:48 | | Boarding Hanzomon line | 0:28 | | Arriving at Okayama station |
| 15:50 | | Arriving at Aoyama-itchome station | 0:41 | | Going home |

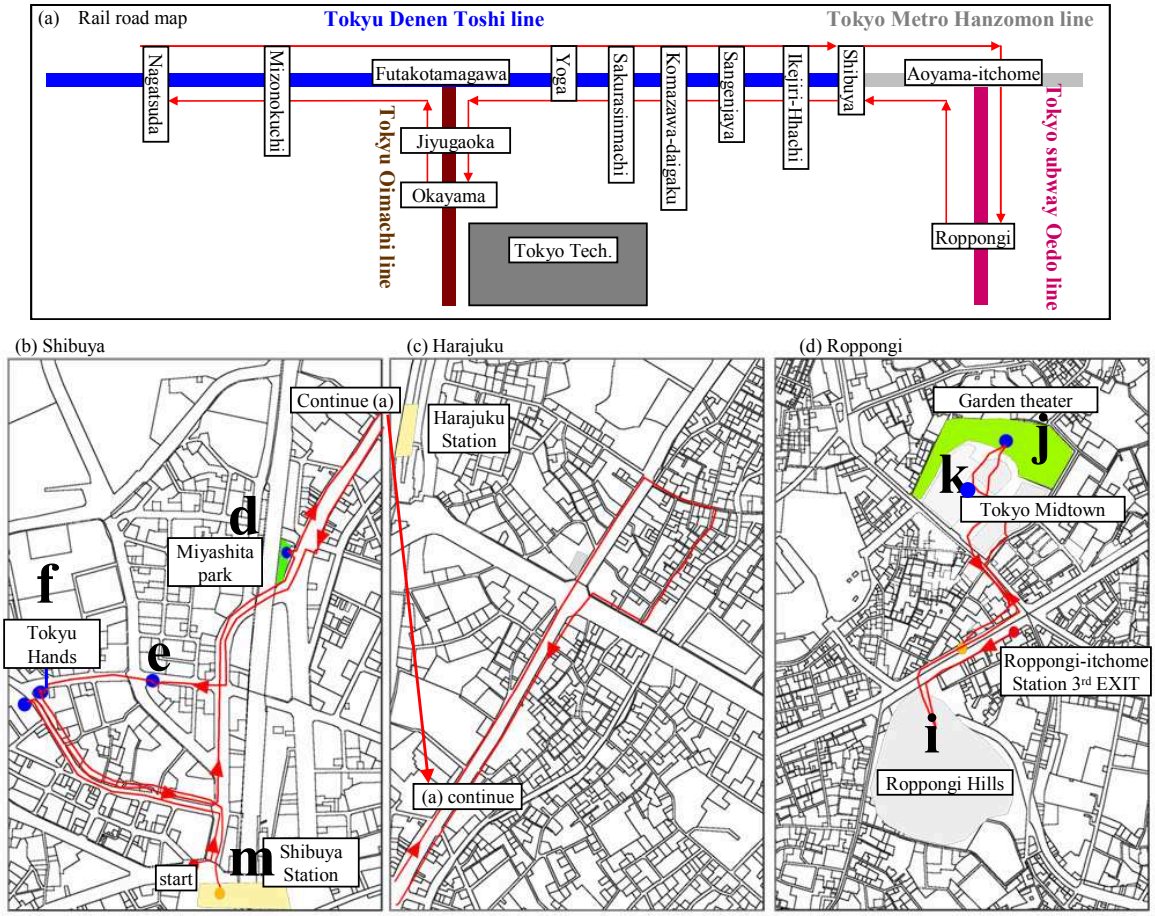


Figure 2 Lagrangian observational route map

is a physical index for thermal sensitivity based on mathematical models of both human thermoregulatory mechanism and energy budget on human body[1]. SET* is computed from Ta, RH, U, and MRT. Figure 3 (a) shows the time series of SET* and Ta from the lagrangian observation. Ta at Tokyo meteorological observational site is also plotted in Figure 3 (a) for comparison of the lagrangian data and the eulerian data. Time series of the physiological responses are plotted in Figure 3 (b).

**(1) Micro-climate in train and station platform in rush hour**

The data on 7:06-8:31 include trains and station platforms in

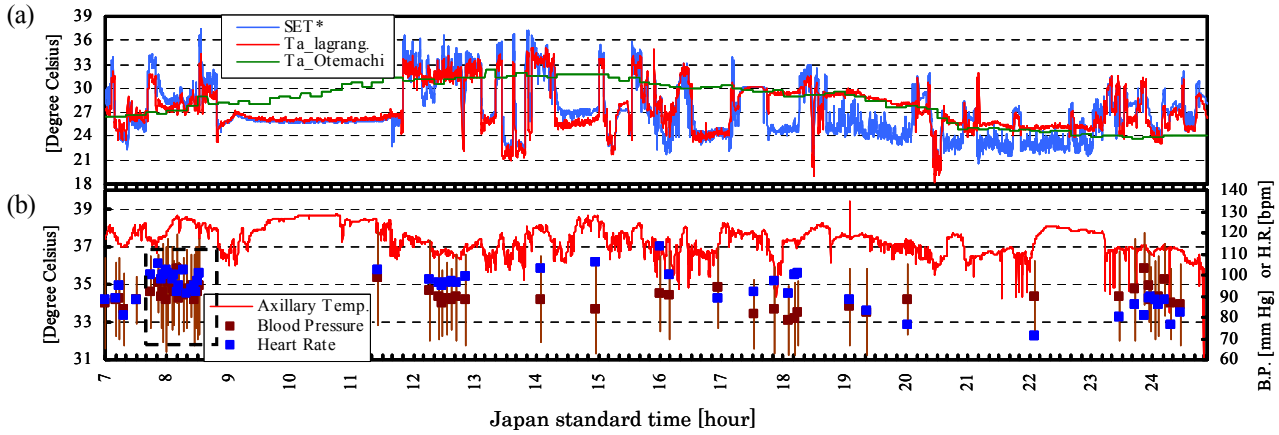


Figure 3 Time series of the lagrangian observation.

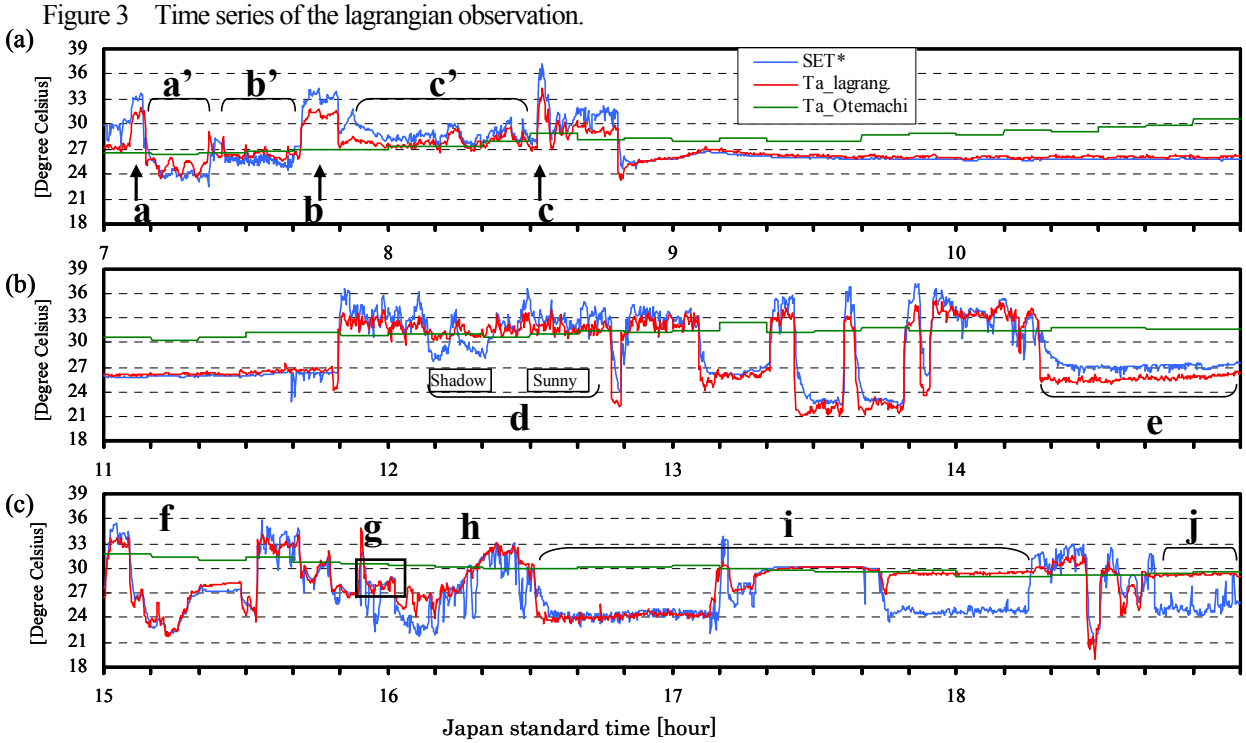


Figure 4 Time series of the lagrangian observation. Time axis of Figure 3 is enlarged. (a):7-11, (b):11-15, (c):15-19

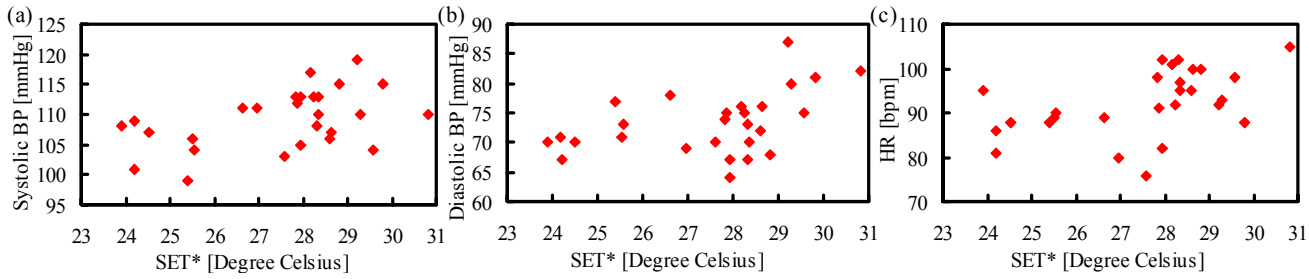


Figure 5 Relation between (a) systolic BP and SET*, (b) diastolic BP and SET*, and (c) HR and SET*.

rush hour. 3-times leap of SET* and Ta occurred in the platform of Ookayama station (32.0 C, Figure 4 (a), a), Nagatsuda station (31.8 C, Figure 4 (a), b), and Shibuya station (34.4 C, Figure 4 (a), c), respectively. Even in the early morning, Ta in Shibuya-station platform was higher than the daily maximal temperature in Otemachi-meteorological site by 2 C, and SET* was over 37 C. It involved heat stroke risk. Average Ta in a train for Shibuya of Tokyu Denentoshi line (STD) was 27.8 C (Figure 4 (a), c') and higher than the preset temperature of the air conditioner (25~26 C, Tokyu railway company HP). Meanwhile, average Ta in trains for Futakotamagawa of Tokyu Oimachi line (FTO) and for Nagatsuda of Tokyu Denentoshi line (NTD) was 25.2 C (Figure 4 (a), a') and 26.4 C (Figure 4 (a), b'), respectively, and ranged in the preset temperature. The congestion degree in the train may

affect the thermal environment in the trains, which means that, the anthropogenic heat emission from passengers may be a non-negligible factor for the micro-climate in trains.

**(2) HR and BP in train and station platform**

The values of HR and BP in STD were high compared to those in NTD and FTD (Figure 3 (b), region enclosed by broken line); average HR in STD is 97 bpm and 88 bpm in NTD and FTO; average systolic BP in STD is 111 mmHg and 104 mmHg in NTD and FTO. Figure 5 shows the relation between HR and SET* and between BP and SET*. HR and systolic/diastolic BP appeared to be correlated with SET*. Some studies reported that the enhancement of heat stress resulted in an increase of HR but a small decrease of BP[2, 3]. However, our findings are not consistent with them. These previous surveys also assessed the relation between physical-mental stresses and HR/BP, and inferred that exercises increase both HR and BP[4] and acute mental stresses increase BP[5]. Therefore, the current results may suggest that the influence of physical/mental stress in the packed train might lead to the increase of both HR and BP rather than influences of micro-climate in the trains; SET* in the train and the station platform air-conditioned is likely to be influenced by the congestion degree, namely anthropogenic heat emission from passengers. Human physiology is affected by micro-climate, physical/mental conditions, and activities of subjects. Further studies on human physiology in commute trains are required.

**(3) Micro-climate in street canyons**

The data on 11:50~15:50 include the street canyons in Shibuya and Harajuku (Figure 4 (b) and (c)). Except for the indoor environment, Ta from the lagrangian observation was higher than Ta at Otemachi by 3 C at a maximum. Figure 4 (b) and (c) indicate the subject underwent the abrupt changes of thermal environment (over 10 C for Ta and SET*). Unfortunately, this measurement system could not detect the exact response of BP and HR accompanied by abrupt transition of heat environment. Sudden heat exposure enhances the heat stoke risk (guideline for heat stroke prevention by Japanese Society of Biometeorology), and vital signs may be affected by abrupt shift of micro-climate. Continuous measuring system of vital signs is necessary for lagrangian observations. Possibilities of developing such measuring system are discussed in Chapter 4.

## 4 Re-development of the measurement system

The sensors used in the observation were not specialized for largangian measurements and the observational system was heavy and bulky. In addition, the current BP and HR sensor operates intermittently and it is difficult to detect the continuous change of BP and HR accompanied by abrupt shift of micro-climate. In order to solve such problems, a prototype of the bio-meter was developed. Figure 6 shows the appearance of the instrument. Specific features of the prototype are as follows; (1) it can measure Ta, RH, MRT, and HR, (2) the data are stored up to 2 GB, (3) it is much smaller and lighter than the current measurement system (72 x 75 x 25 mm, 110 g). A wind velocity and BP sensors are to be mounted on the compact measurement system.

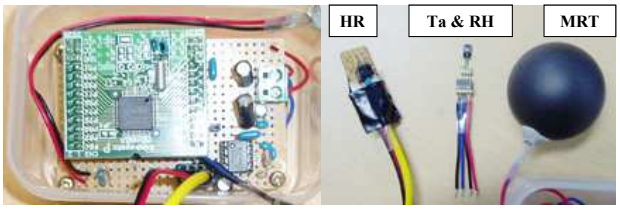


Figure 6 Photo of bio-meter prototype.
Left half: CPU and logger. Right half: sensors.

## 5 Conclusions

I proposed the new lagrangian concept for urban bio-meteorology. The concept is to investigate continuous changes of micro-climate and the physiological response along human pathways carrying a compact measurement system. The first results of the observation suggested that LHM has a potential to evaluate the micro-climate and physiological response along human pathways and contribute to urban biometeorology.

## References

[1] Gagge, A.P., Stolwijk, J.A.J., Nishi, Y.: An effective temperature scale based on a simple model of human physiological regulatory response, *ASHRAE*, pp. 247-262, 1971.

[2] Niimi, Y., Matsukawa, T., Sugiyama, Y., Shamsuzzaman, A.S.M., Ito, H., Sobue, G., Mano, T.: Effect of heat stress on muscle sympathetic nerve activity in humans, *Journal of the Autonomic Nervous System,* pp. 61-67, 1997.

[3] Gaebelein C.J., Senay L.C. Jr., Ladd C.M.: Changes in blood pressure, heart rate and blood constituents during heat exposure in men with elevated blood pressure, *Eur J Appl Physiol, 54*, pp.506-510, 1985

[4] Matsuda M., Haga S., Kitao H., Nosaka T., Iida K., Sugishita Y., Ito I.: Influence of arterial blood pressure level during strength exercise on left ventricular hypertrophy, *Adv. Exerc. Sports Physiol., 2*, pp. 13-18, 1996

[5] Douglas C., George D.S., Martin J.S., Andrew S., Eric J.B., Michael G.M.: Blood pressure reactions to acute phychological stress and future blood pressure status: A 10-year follow-up of men in the Whitehall II study, *Psychosomatic Medicine, 63*, pp.737–743, 2001.

# Influence of mixing γ-$C_2S$ on $Cl^-$ penetration in concrete cured using autoclave

Student Number: 07M18102 Name: Masayo Horioka Supervisor: Nobuaki OTSUKI

γ-$C_2S$ の混和が高温高圧養生を用いたセメント系材料の $Cl^-$ 浸透性に及ぼす影響

堀岡昌代

セメントとケイ石微粉末にγ－$C_2S$ を混和し，オートクレーブ養生と炭酸化養生を施した場合，γ－$C_2S$ は部材の化学的安定性と外部からのイオン浸透に対する抵抗性の向上の双方に寄与する．本研究では，(1) γ－$C_2S$ を混和し，オートクレーブ養生および炭酸化養生を併用したセメント供試体を用いて，反応生成物とそれに伴う空隙構造の変化および塩化物イオン拡散係数を総合的に検討し，(2)実際の鉄筋コンクリートパイルに応用して，コンクリートパイルにおける塩化物イオンの拡散係数と比較検討を行った．

## 1. Introduction

Generally, in order to improve the durability of concrete structures, it is important to consider the resistivity against external degrading materials. In has been shown in previous research, that the use of the material called γ-$C_2S$ (γ-2CaO・$SiO_2$) as admixture for concrete, improves the durability of the member because of the 2 abilities of γ-$C_2S$ for durability : (1) it reacts with $CO_2$ and become $CaCO_3$ (vaterite); (2) γ-$C_2S$ assist in making tobermorite under autoclave curing. Crystalline tobermorite has a stable structure so it can affect the dimensional stability and chemical stability of the specimen,

The group of Morioka, Yokozeki and Watanabe[1)2)] made an attempt at improving the strength and permeability of the concrete by exposure of specimen to carbonation with γ-$C_2S$. Further research was done on the utilization of γ-$C_2S$ in concrete by adding the utilization of autoclave curing. In the study by Saito et. al.[3)4)], it was shown that γ-$C_2S$ can possibly make a more durable member. But the possibility only considered the neutralization test in durability. So far, consideration to relation of production, pore distribution, and permeability of $Cl^-$, as important deterioration factors in reinforced concrete are not yet done. Moreover, the examination of the use of γ-$C_2S$ for concrete is not yet performed.

Therefore in this study, the technique of using γ-$C_2S$ was applied for concrete pile. The concrete pile was also cured by autoclave. The main objective of this study is to design a high-durability concrete pile by investigating the optimum replacement ratio of γ-$C_2S$. Specific objectives are:

(1)To design a paste specimen with a surface densified with vaterite and with core structure made of tobermorite using 180℃ autoclave curing and $CO_2$ acceleration.

(2) To investigate the relationship between pore distribution and the permeability of chloride ion of paste specimen with γ-$C_2S$.

(3) To compare the chloride ion permeability between γ-$C_2S$ containing paste specimen and RC piles, and using this conclusion, design a high-durability RC pile

## 2.The change of product in carbonated cement paste with γ-$C_2S$

### 2.1 Methods of manufacturing the test specimen

#### 2.1.1 XRD

Paste test specimens containing OPC and γ-$C_2S$ at substitution levels of 0, 20, 40, 60 and 80% were prepared as the source of lime. The lime source (OPC+γ-$C_2S$) and α-quartz were mixed in a ratio of 5:5 and deionized water was added to the powder at water-to powder ratio of (w/p)of 0.3 (mass ratio). The prepared paste was cast in a mould with dimensions of 1 x 1 x 8 cm and allowed to harden at 100%RH for 4 hours at 65℃. The hardened paste specimen was removed from the mould and autoclaved for 8 hours at 180℃. Accelerated carbonation of the samples was carried out in a carbonation chamber with settings of 5% $CO_2$ by volume, 20℃ temperature and 60%RH for 28days. After carbonation, each sample was completely submerged in acetone at 20℃for 1 hour inside a vacuum containment, in order to terminate hydration .Afterwards, reduced pressure drying was carried out for 24 hours.

The test sample was cut in layers as follows: 0-2 mm as Surface layer; 4-6 mm as Middle layer and 8-10mm as Core layer. The mix proportions for the paste are shown in **Table.2.1.**

**Table.2.1 Mix proportions for the paste specimens**

| W(g) | C (g) | γ -C2S (g) | AD (g) | CA (g) |
|---|---|---|---|---|
| 5.555 | 10～0 | 0～10 | 10 | 0.045 |

**W…water**
**C…cement**
**AD…ground silica sand**
**CA…water-reducing admixture**

### 2.1.2 Compression test

The specimen for compression test was made using the same mix proportion as shown in **Table. 2.1**. The mixed paste was cast in cylindrical moulds, φ5cm×10cm, autoclave cured and exposed to carbonation using the same settings explained in 2.1.1. Autoclaved compression tests specimens without carbonation were also prepared.

### 2.1.3 Dimensional stability test

Paste test specimens were prepared as explained in section 2.1.1. Gauge plugs were bonded on the samples using quick curing adhesive. An initial value of dimension was measured immediately after autoclave curing. The specimens were then stored in moist chamber for 22 hours at 20℃ and were later tested of its dimension using a strain gauge at 70%RH for 24 hour at 20℃ following the measuring standard set by **JIS A1129-1.**

## 2.2 Results & Discussions

### 2.2.1 Result of x-ray diffraction

**Fig.2.2** shows the XRD peak intensity of crystalline tobermorite while **Fig.2.3** shows the $CaCO_3$ peaks made from $CO_2$ acceleration. of the 0% and 80% substituted specimens.

**(ⅰ) peak of tobermorite**

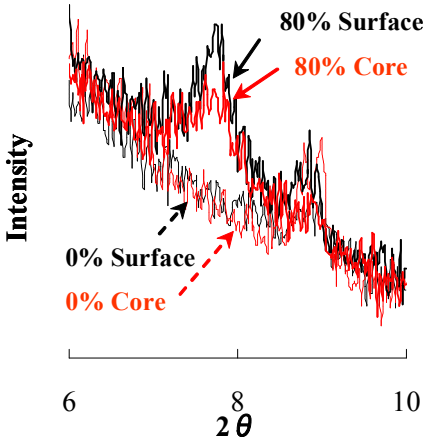


**Fig.2.2 XRD peak intensity of crystalline tobermorite**

**(ⅱ) peak of $CaCO_3$**

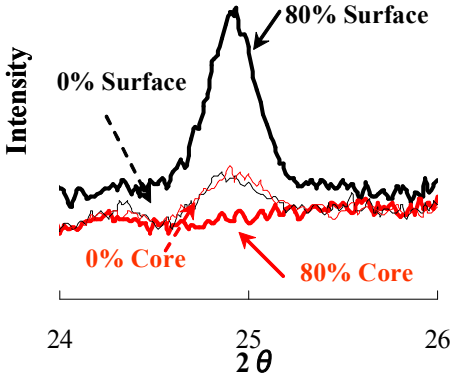


**Fig.2.4 vaterite peak of 0% & 80%**

In the case of 0% and 20% γ -$C_2S$ substitution, the XRD peaks of crystalline tobermorite have completely disappeared at all layers from the exposed surface. This result may have been due to the complete carbonation of the specimen that lead to the destruction of the structure of the crystalline tobermorite that were formed during autoclave curing. On the other hand, In the case of 40% and 60% γ -$C_2S$ substitution, the peak of crystalline Tobermorite remained in all layers. This means that the voids were filled up thus retarding the progress of carbonation. These voids were actually filled with Vaterite as evidenced by **Figs.2.3** which shows high Vaterite peaks after carbonation. This was seen especially in the case of 80% γ -$C_2S$ substitution where the crystalline tobermorite peak found in the core layer has the same intensity as that found in the non-carbonated case. Also, there are no carbonation products found in the core layer. From both these results, it is deduced that carbonation only reached the middle layer.

### 2.2.2 Result of compression test

In the non-carbonated case, the compression strength of the cylinder specimen decreased as the γ -$C_2S$ replacement ratio was increased. When carbonation was induced for 28days, improvement was observed as the compressive strength increased in all levels of replacement ratios.

The 60% substitution turned out to have the highest improvement rate of compressive strength (45%) after carbonation. This was followed by 80%, then 40% substitution ratios. This maybe due to the of γ -$C_2S$ generated vaterite[3] from carbonation.

### 2.2.3 Result of dimension stability test

In all replacement ratios, the rate of length change for specimens that underwent autoclave curing was smaller by at least 50% than those specimens that underwent moist curing. It turns out that using autoclave curing can lead to the formation of tobermorite crystals that helped improved shrinkage deformation.

## 3.The change of pore distribution in carbonated cement paste with γ -$C_2S$

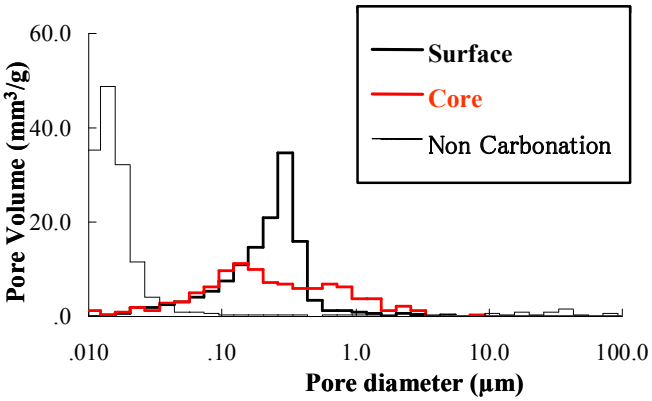


**Fig.3.1 0% Pore Volume**

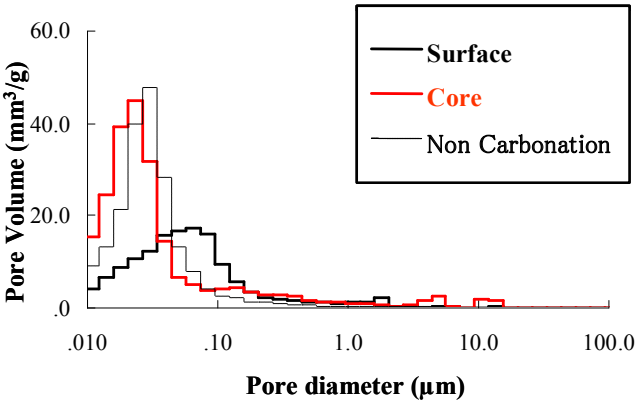


**Fig.3.2 80% Pore Volume**

In the case of 0% and 20% substitution ratio, carbonation deterioration occurred in all layers. After carbonation, the behavior of the threshold pore diameters shifted to the larger diameter. This result is in agreement with the results of the XRD test. On the other hand, in the case of 40% and 60% substitution, the behavior of the threshold pore diameters shifted to the small values of diameter. After autoclave curing, the remaining unreacted γ-$C_2S$ was exposed to carbonation thus forming Vaterite that eventually filled the voids and prevented further penetration of $CO_2$. This was seen especially in the case of 80% substitution where there was no significant change in the threshold pore diameter behavior in the surface and middle layers although the amount of voids with size 0.03μm or less decreased. In the core layer, the voids and pore size distribution did not change at all before and after the exposure to carbonation. Thus, it can be deduced that the surface layer was extremely densified, leaving carbonation to reach only the middle layer, and preventing further progress of carbonation from reaching the core layer.

According to Dr .Saito[3], there is a report that replacement of 80% ratio or more of γ-$C_2S$ in 150℃ cured specimens lead to lower deterioration factor. In this study, it was shown that using 40% or more replacement ratio of γ-$C_2S$ in 180℃ autoclaved cured and carbonated specimens can lead to the possibility of lowering the factor of deterioration.

## 4. The influence the change of pore distribution on $Cl^-$ diffusivity

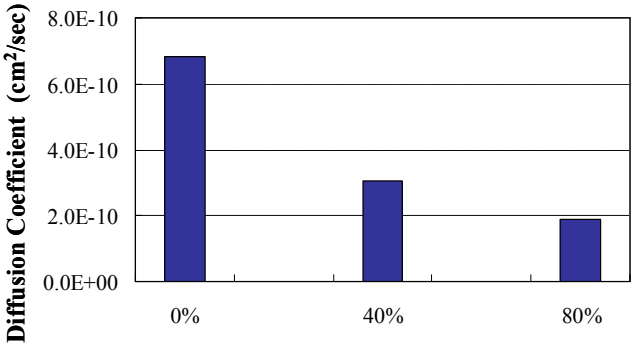


**Fig.4.1 Cl- diffusion Coefficient**

In the case of 0% substitution, the $Cl^-$diffusivity is decreased in order of Surface, Middle, and Core layer. In contrast, the $Cl^-$ diffusivity on 40% and 80% substitution ratios is increased in order of Surface, Middle, and Core layer. Looking at the results for the surface layer the specimen, the value with the smallest $Cl^-$diffusivity is 80% replacement ratio. Thus 80% replacement ratio has the lowest permeability to $Cl^-$ . Moreover, this result agrees to the result of the product change before and after undergoing carbonation, and also with the results of the voids structure.

In the surface layer of the specimen with replacement ratio of 0%, because of carbonation deterioration, the pore diameter becomes higher thus increasing the $Cl^-$ diffusivity. On the other hand, in the case of 40% and 80% replacement ratio, the threshold pore diameter of the Surface layer becomes small due to the filling of voids thus the $Cl^-$ diffusivity becomes lower.

In the Core layer of the specimens with replacement ratio of 80%, it is deduced that the $Cl^-$ diffusion coefficient is increasing due to the presence of Tobermorite crystals, the formation of which is card shaped thus containing larger voids.

## 5. Comparing Cl- diffusion coefficient of RC Pile and paste

### 5.1 Method of manufacturing the test specimen

Concrete piles embedded with steel bars were prepared following the mix proportions shown in **Table.5.1.**

**Table.5.1 mix proportion of concrete pile**

| slump (cm) | Air (%) | W/ (C+AD) (%) | S/a (%) | AD/ (C+AD) (%) | CA/ (C+AD) (%) |
|---|---|---|---|---|---|
| 12±3 | 2.0 | 32.9 | 50 | 14.4 | 1.25 |
| Amount of Unit (kg/m3) | | | | | |
| W | C | S | G | AD | CA |
| 148 | 385 | 905 | 905 | 65 | 5.63 |

Centrifugal conditions were used in the casting of the specimens. The specimens were then pre-cured in hot water (65°C). After pre-curing, the specimens were autoclaved followed by exposure to accelerated carbonation as that explained for cement paste. The specimens were then soaked in water bath for four months.

### 5.2 Results of test of chloride content in RC pile

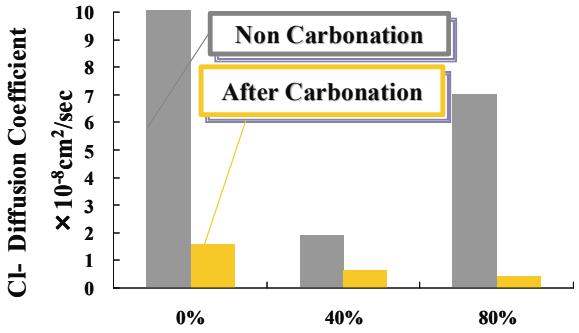


**Fig.5.2 Diffusion coefficient of RC pile**

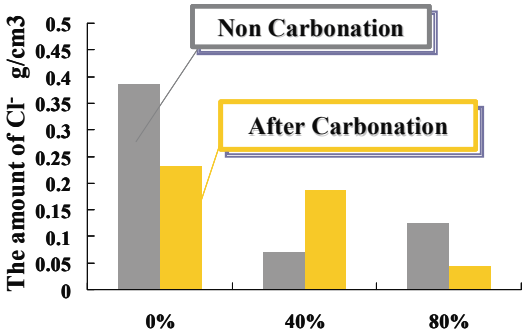


**Fig.5.3 Cl- around of steel bar**

**Fig.5.2** shows the diffusion coefficient of Cl⁻. In any replacement ratio, the Cl⁻ content in the pile exposed to carbonation has decreased. Moreover, the results show that after carbonation, the specimen with 40% or more γ-$C_2S$ show lower Cl⁻ diffusion. It was thought that the material γ-$C_2S$ had demonstrated the effects of reducing the permeability to Cl⁻ at the replacement ratio 40% with carbonation and corresponds to the results observed previously for cement paste.

**Fig.5.3** shows the total amount of Cl⁻ around the steel bar. After carbonation, as replacement ratio of γ-$C_2S$ was increased, the amount of Cl⁻ content decreased. The amount of Cl⁻ content of the specimens with replacement of 80% is about half that found for the specimens with 0% replacement.


**Fig.5.4 High durability concrete pile**

In this study, the replacement of 80% γ-$C_2S$ showed the lowest permeability of Cl⁻. The surface zone of the member has high densification and the inner portions contain crystalline tobermorite which has good dimensional and chemical stability.

## 6. Conclusions

(1)In cement paste with 0 to 20% γ-$C_2S$ substitution, carbonation proceeded throughout all layers and the tobermorite structure was destroyed. In cement paste with 40 to 60% γ-$C_2S$ substitution, the tobermorite structure was kept intact and the pore distribution was improved due to filling with Vaterite. In cement paste with 80% γ-$C_2S$ substitution, the surface layer was highly densified keeping the tobermorite and pore distributions of the core layer intact.

(2)Substitution of 0 to 20% γ-$C_2S$ to cement paste lead to the decrease in resistance against penetration of of Cl⁻ ion. Substitution of 40 to 60% γ-$C_2S$ dramatically increased the density of the outer layers of the cement paste and improved its resistance against penetration of Cl⁻. In the case of 80% substitution with γ-$C_2S$, the penetrations of both $CO_2$ and Cl⁻ were prevented by the formation of very dense surface layer.

(3)Tests on the amount of chloride ions concentration in RC piles γ-$C_2S$ after 4 months exposure show the same trend of chloride penetration resistance as in cement pastes with γ-$C_2S$

## References

[1] Minoru Morioka, Takayuki Higuchi, Cement Science and Concrete Technology, No.57, 2003

[2] Minoru Morioka, Kouji Okuyama, Kenzou Watanabe, Yasuhiro Yokozeki, Cement Science and Concrete Technology, No.58, 2004

[3] Tsuyoshi Saito, Thesis of Doctoral Degree, Tokyo Tech, 2006

[4] Tsuyoshi Saito, Etsuo Sakai, Nobuaki Otsuki , kenzou Watanabe, Minoru Morioka, Meeting & Research in Cement Concrete ,P1-6,2008

# LIQUID-LIQUID EXTRACTION RATE OF COAL TAR ABSORPTION OIL IN A CONTINUOUS COUNTERCURRENT SPRAY COLUMN

Student Number: 07M18119 Name: Toshiya MASUDA Supervisor: Ryuichi EGASHIRA

## 連続式向流接触スプレー塔におけるコールタール吸収油の液液抽出速度

増田　敏也

含窒素複素環式化合物、同素環式化合物、などの有用成分を含むコールタール吸収油を原料分散相、メタノール水溶液を溶媒連続相として、これらを向流接触させた。他の成分に比較して含窒素成分は選択的に溶媒相に抽出され、これらの成分間の分離が可能であることを確認した。含窒素複素環式化合物の収率、その他の成分に対する分離の選択度は、それぞれ最大で 0.5、20 程度であった。総括物質移動容量係数を求め、物質移動係数の相関関係を導き既往の研究と比較し抽出速度過程を検討した。

### 1. Introduction

Coal tar, one of the byproducts from coal carbonization, contains many useful compounds to chemical industry. Absorption oil (AO) which is one of the fractions of coal tar (b.p.=470~550K) contains nitrogen heterocyclic compounds (nitrogen compounds) such as quinoline (Q), isoquinoline (IQ), indole (IL), etc., homocyclic compounds such as naphthalene (N), 1-methylnaphthalene (1MN), 2-methylnaphthalene (2MN), biphenyl (BP), etc., and oxygen heterocyclic compounds such as dibenzofuran (DBF), etc. Generally, the separation and purification of these compounds in AO are carried out in two steps; 1: AO is separated into several fractions by reactive extraction with acid and/or base, 2: these fractions are separated and purified into respective products by distillation, crystallization, adsorption, etc. However, this process is relatively costly because the acid and base used as solvent are very difficult to be recovered and cause corrosion of the equipments. For this problem, the ordinary solvent extraction method with aqueous methanolic solution (MeOH aq.) and the liquid membrane method have been studied[1-6]. In the continuous countercurrent liquid-liquid extraction[6], a spray column was chosen for the equipment, because it was the simplest differential-contact device in laboratory studies, and mass transfer rate was measured and examined.

Mass transfer occurs in three steps which are drop formation, drop coalescence and drop falling. The mass transfer from the single drop during its falling to the continuous phase has been studied [7,8]. Some researchers [7,8] correlated the continuous mass transfer coefficient by using $N_{Re}$, $N_{Sc}$ and $N_{Sh}$.

In this study, a countercurrent spray column was applied to the extraction of AO and the separation performance was examined. The mass transfer coefficients were experimentally measured and compared with the previous correlations[7,8].

### 2. Experimental

#### 2.1. Apparatus

The schematic diagram of the apparatus is shown in **Fig.1**. Iwaki Magnet Gear Pumps are equipped with each tank to supply the column with each phase. The column is made of pyrex glass of which the inner diameter is 0.0037m and effective height is 0.495m. **Figure 2** shows the details of the distributors. The distributor of the dispersed phase has 8 needle nozzles of which the inner diameter is $6\times10^{-4}$m. The distributor of the continuous phase has outlets on side of the cylinder to prevent from falling drops entering in it.

#### 2.2. Procedure

AO and MeOH aq. were stocked in the tanks. AO, dispersed phase, was fed to the top of the column, MeOH aq., continuous phase, to the bottom and these two phases contacted countercurrently. The inlet flow rates were kept constant by controlling the flow valves and the level of the interface between the continuous phase and accumulated raffinate phase at the bottom was maintained by adjusting the drain valve of raffinate phase. The inlet and outlet flow rates were determined by weighing the mass collected in 10 minutes. The holdup of the dispersed phase in the column was determined by measuring the rise of the interface after about 1hour

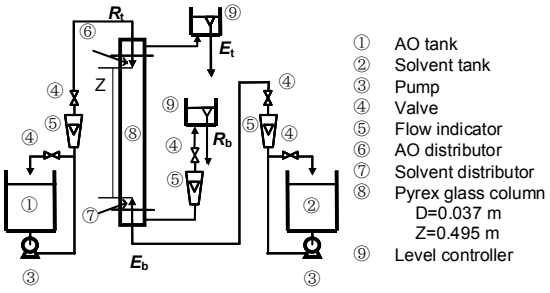


**Fig.1** Schematic diagram of the experimental apparatus

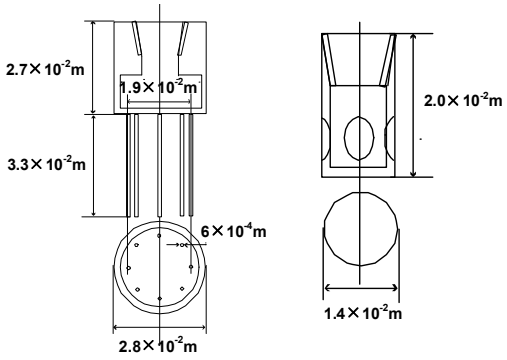


**Fig. 2** Details of distributors;

from closing AO inlet and drain at the same time. Each operation was carried out in 3 hours to reach steady state. Each phase was analyzed by GC-2010 (Shimadzu Corp.) The dispersed drop diameters were determined by taking photos of column and measuring the sizes of the drops. **Table 1** shows the principle experimental conditions. The density and viscosity of each phase were measured with pycnometers and Ostwald viscometers.

**Table 1** Experimental condition

| No. | feed: AO | solvent: MeOH aq. | |
|---|---|---|---|
| | $R_t$ [kg・m$^{-2}$・h$^{-1}$] | $y_{MeOH,b}$ [-] | $E_b$ [kg・m$^{-2}$・h$^{-1}$] |
| EC1 | 500～2500 | 0.73±0.03 | 1600±100 |
| EC2 | 500～2500 | 0.73±0.03 | 3200±100 |

## 3. Result and discussion

### 3.1. Composition of absorption oil

**Table 2** shows the compositions of feed AO. The compositions of the feed AO changed every runs, because the raffinate phase in the previous run was recovered and used as feed in the next run. If necessary, fresh AO was added to the recovered raffinate phase. The ranges of compositions of nitrogen compounds were large, because the transferred amounts to continuous phase were high.

**Table 2** Compositions of feed AO

| component $i$ | mass fraction, $x_{i,t}$ [-] |
|---|---|
| Quinoline, Q | 0.025~0.071 |
| Isoquinoline, IQ | 0.007~0.020 |
| Indole, IL | 0.017~0.036 |
| Naphthalene, N | 0.025~0.030 |
| 1-Methylnaphthalene, 1MN | 0.093~0.103 |
| 2-Methylnaphthalene, 2MN | 0.230~0.254 |
| Biphenyl, BP | 0.064~0.072 |
| Dibenzofran, DBF | 0.105~0.125 |
| Methanol, MeOH | 0~0.012 |

### 3.2. Operability

#### 3.2.1. Density and viscosity

**Table 3** shows the densities and viscosities of the materials. The density of the dispersed phase was larger than that of the continuous phase. The viscosities of MeOH aq. and the extract phase were same.

**Table 3** Densities and viscosities of materials

| materials | density [kg・m$^{-3}$] | viscosity [cP] at 290K |
|---|---|---|
| Absorption oil | 1040~1100 | - |
| Aqueous methanolic solution | 870 | 1.533 |
| Raffinate phase | 1100 | - |
| Extract phase | 885~890 | 1.533 |

#### 3.2.2. Behavior in the column

In all runs, entrainment of the dispersed phase drops into the continuous phase and flooding were not observed. The substantial mass transfers of these compounds could be detected with this bench scale column of which effective contact height was 0.495m. In the range of higher $R_t$, the drops were falling down with zig-zag movement and the coalescence of the dispersed phase and axial mixing were observed.

**Figure 3** shows the results of the holdup of dispersed phase in the column, $H$. $H$ increased with $R_t$. **Figure 4** shows the results of the drop diameter, $d_p$. $d_p$ decreased with an increase in $R_t$. Specific interfacial area, $a$, was

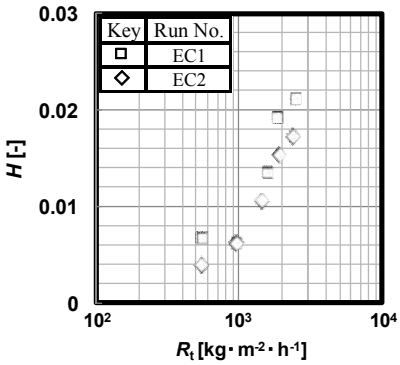


**Fig.3** Holdup of dispersed phase

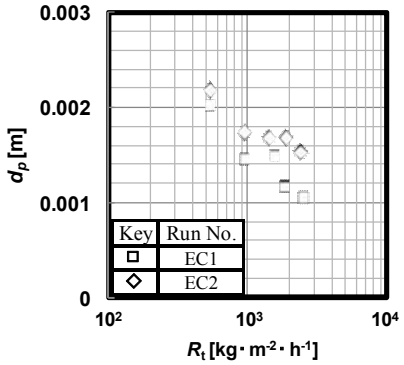


**Fig.4** Drop diameter of dispersed phase

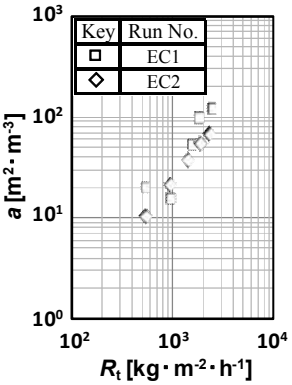


**Fig.5** Specific interfacial area

calculated by,

$$a=6H/d_p \quad (3.1)$$

**Figure 5** shows the results of $a$. $a$ increased with $R_t$ and decreased slightly with an increase $E_b$.

### 3.3. Separability

#### 3.3.1. Composition of extract phase

**Figure 6** shows the result of compositions in the extract phase, $y_{i,t}$. $y_{i,t}$ of nitrogen compounds were higher than those of other compounds. In the range of $R_t$<1500, $y_{i,t}$ of nitrogen compounds increased with $R_t$, and in the range of $R_t$>1500, the changes of $y_{i,t}$ were small. This was because $y_{i,t}$ of nitrogen compounds reached equilibrium compositions in the range of $R_t$>1500. $y_{i,t}$s of other compounds were almost constant against $R_t$ because those reached equilibrium compositions.

#### 3.3.2. Yield

Yield of component $i$, $Y_i$, was defined as

$$Y_i=E_t \cdot y_{i,t}/(R_t \cdot x_{i,t}) \quad (3.2)$$

**Figure 7** shows the results of $Y_i$. $Y_i$ decreased with an increase in $R_t$. $y_{i,t}$ increased with $R_t$ and $y_{i,t}$ almost approached $y_{i,t}^*$. However, $R_t$ became bigger than the

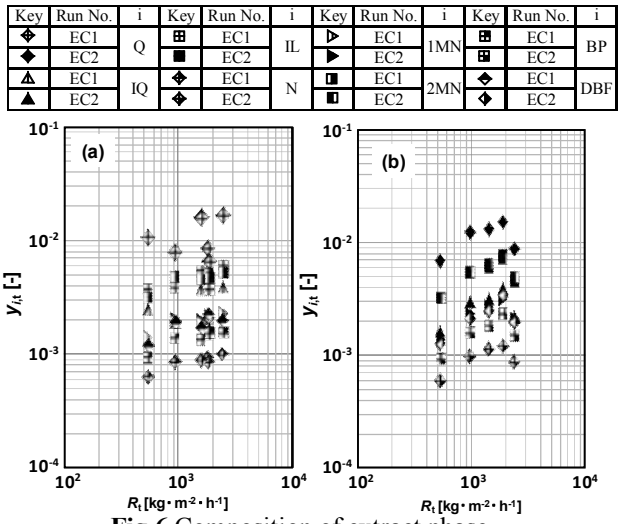


**Fig.6** Composition of extract phase
(a) in EC1, (b) in EC2

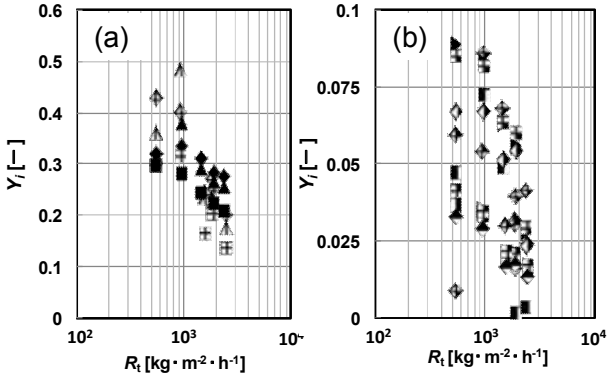


**Fig.7** Yield
(a) nitrogen compounds, (b) other compounds
(keys are the same as **Fig.6**)

increase of the transferred amount of these components. $Y_i$ slightly increased with $E_b$. The maximum $Y_i$ values of nitrogen compounds and other compounds were 0.5 and 0.1.

### 3.3.3. Separation selectivity

The separation selectivity of component $i$ relative to 2MN, $\beta_{i/2MN}$, was defined as

$$\beta_{i/2MN}=(y_{i,t}/y_{2MN,t})/(x_{i,b}/x_{2MN,b}) \quad (3.3)$$

**Figure 8** shows the results of $\beta_{i/2MN}$. $\beta_{i/2MN}$ did not change so much as $R_t$ changed. $\beta_{i/2MN}$ of nitrogen compounds and other compounds were around 15 and 1. This was because the difference between the distribution coefficients of nitrogen compounds and other compounds was about 10 times. Therefore, the distribution coefficients affected $\beta_{i/2MN}$.

### 3.4. Mass transfer rate

### 3.4.1. Overall mass transfer coefficient

The overall mass transfer coefficient based on the continuous phase concentration, $K_{c,i}$, was calculated by,

$$d(E\cdot y_i)/dz=-K_{c,i}\cdot a\cdot(y_i^*-y_i) \quad (3.4)$$

The equilibrium composition, $y_i^*$, was calculated by,

$$y_i^*=m_i\cdot x_i \quad (3.5)$$

where $m_i$ ($=y_{i,1}/x_{i,1}$) was distribution coefficient and the value estimated in previous[6] study was used. **Figure 9** shows the results of $K_{c,i}$. In the range of $R_t$<1500, $K_{c,i}$

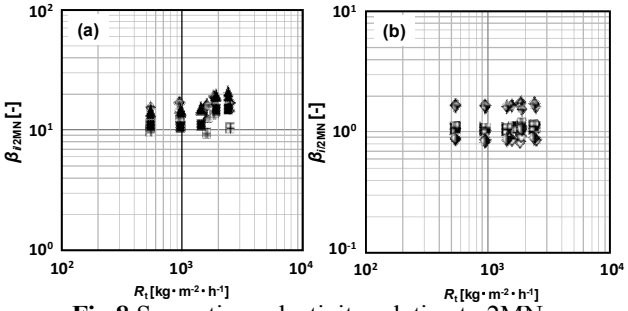


**Fig.8** Separation selectivity relative to 2MN
(a) nitrogen compounds, (b) other compounds
(keys are the same as **Fig.6**)

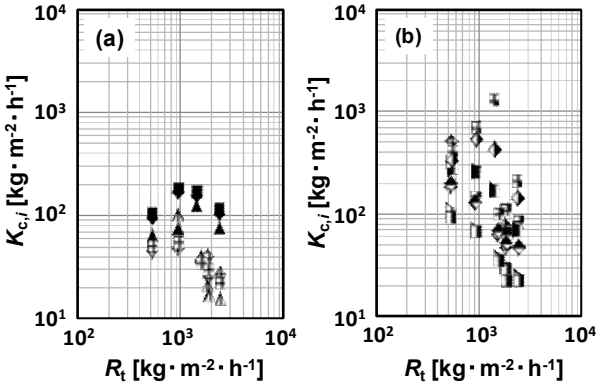


**Fig.9** Overall mass transfer coefficient based on continuous phase concentration
(a) nitrogen compounds, (b) other compounds
(keys are the same as **Fig.6**)

did not change so much, and in the range of $R_t$>1500, $K_{c,i}$ decreased with an increase $R_t$. This was because the axial mixing of the dispersed phase in the column was occurred. $K_{c,i}$ also increased with $E_b$. $K_{c,i}$ of nitrogen compounds was smaller than that of other compounds.

### 3.4.2. Correlation of mass transfer coefficient

In previous work[6], the mass transfer within continuous phase was more dominant than within the dispersed phase in the overall mass transfer. The mass transfer coefficient in the continuous phase, $k_{c,i}$, was, thus, assumed to be equal to $K_{c,i}$ and compared with the previous correlations[7,8]. Thorsen and Terjesen have correlated the continuous phase mass transfer coefficients from the single drop to the continuous phase by using $N_{Re}$, $N_{Sc}$ and $N_{Sh}$ as:

$$N_{Sh}=-178+3.62\cdot N_{Re}^{1/2}\cdot N_{Sc}^{1/3}$$

This equation was applied to the mass transfer by the internal circulation of the drop. They confirmed the rigid drop by the addition of surfactants. Garner and Suckling[8] used solid spheres as dispersed phase drops and obtained the correlation below:

$$N_{Sh}=2+0.95\cdot N_{Re}^{1/2}\cdot N_{Sc}^{1/3}$$

This was applied to the mass transfer of rigid sphere drop.

Here, $N_{Re}$, $N_{Sc}$ and $N_{Sh}$ are expressed as follows;

$$N_{Re}=\rho_c u d_p/\mu_c \quad (3.6)$$

$$N_{Sc}=\mu_c/\rho_c D_i \quad (3.7)$$

$$N_{Sh}=k_{c,i}d_p/D_i \quad (3.8)$$

$u$ is slip velocity in the column and obtained from below equations.

$$u_d=R_t/(\rho_d H) \quad (3.9)$$

$$u_c=E_b/\{\rho_c(1-H)\} \quad (3.10)$$

$$u=u_d+u_c \quad (3.11)$$

The diffusivities of component $i$ were determined by using Wilke-Chang equation.

$$D_i=7.4\times10^{-8}(BM_c)^{1/2}T/(\mu_c v_i^{0.6}) \quad (3.12)$$

$N_{Sh}$ is plotted versus $N_{Re}^{1/2}\times N_{Sc}^{1/3}$ in **Fig.10**. In this study, $N_{Sh}$ increased with increasing $N_{Re}^{1/2}\times N_{Sc}^{1/3}$. The results in this study were closer to the correlation by Thorsen and Terjesen than to that by Garner and Suckling. So, it was confirmed that in this separation system of AO the mass transfer occurred by the internal circulation of the dispersed drops. $N_{Sh}$s of nitrogen compounds were below the two lines. Meanwhile, $N_{Sh}$s of other compounds were above the line of Thorsen and Terjesen. In this work, this system was of multi-components and this should make the mass transfer process more complicated. In this case, it was assumed for the mass transfer to be controlled by the continuous phase and this assumption might not be able to fully explain this situation, causing the $N_{Sh}$ trend.

## 5. Conclusion

The separation of AO with continuous countercurrent spray column was favorably carried out. The yields, $Y_i$, and selectivity, $\beta_{i/2MN}$, were about 0.5 and 20 at maximum, respectively. It was confirmed that nitrogen compounds could be selectively separated.

The overall volumetric mass transfer coefficient based on the continuous phase concentration, $K_{c,i}\cdot a$ increased with $R_t$. The correlation of the continuous phase mass transfer coefficients approximately corresponded to the equation obtained by Thorsen and Terjesen. The disagreement of the mass transfer coefficient correlation of nitrogen compounds was due to the difference of the range of $N_{Sc}$.

## Acknowledgment

AO was provided by JFE Chemical Corporation.

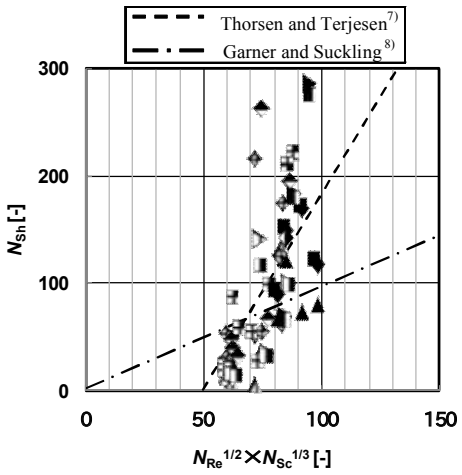


**Fig.10** Correlation of continuous phase mass transfer coefficients
(keys are the same as **Fig.6**)

## Nomenclatures

| | | |
|---|---|---|
| $a$ | : specific interfacial area | [$m^2\cdot m^{-3}$] |
| B | : associated factor of solvent | [-] |
| $D$ | : diffusivity | [$m^2\cdot h^{-1}$] |
| $E$ | : superficial mass flow rate of continuous phase | [$kg\cdot m^{-2}\cdot h^{-1}$] |
| $H$ | : holdup of dispersed phase | [-] |
| $K_c$ | : overall mass transfer coefficient based of continuous phase concentration | [$kg\cdot m^{-2}\cdot h^{-1}$] |
| $m_i$ | : distribution coefficient of component i | [-] |
| M | : molecular weight | [$kg\cdot mol^{-1}$] |
| $N_{Re}$ | : Reynolds number | [-] |
| $N_{Sc}$ | : Schmidt number | [-] |
| $N_{Sh}$ | : Sherwood number | [-] |
| $R$ | : superficial mass flow rate of dispersed phase | [$kg\cdot m^{-2}\cdot h^{-1}$] |
| T | : temperature | [K] |
| $u$ | : velocity of fluids | [$m\cdot h^{-1}$] |
| $v$ | : molecular volume at standard boiling point | [$m^3\cdot mol^{-1}$] |
| $x$ | : mass fraction in oil phase | [-] |
| $y$ | : mass fraction in aqueous phase | [-] |
| $y^*$ | : equilibrium mass fraction in aqueous phase | [-] |
| $Y$ | : yield | [-] |
| $z$ | : distance from top of the column | [m] |
| $\beta_{i/2MN}$ | : separation selectivity of component $i$ relative to 2MN | [-] |
| $\rho$ | : density | [$kg\cdot m^{-3}$] |
| $\mu$ | : viscosity | [cP] |

<Subscripts>

| | |
|---|---|
| 1 | : at equilibrium |
| 1MN | : 1-methylnaphthalene |
| 2MN | : 2-methylnaphthalene |
| b | : at bottom of the column |
| BP | : biphenyl |
| DBF | : dibenzofuran |
| IL | : indole |
| IQ | : isoquinoline |
| $i$ | : component $i$ |
| MeOH | : methanol |
| N | : naphthalene |
| Q | : quinoline |
| t | : at top of the column |

## Reference

1) Egashira, R., Nagai, M., *Sekiyu Gakkaishi (J. Jpn. Petrol. Inst.)*, **43**, (5), 339 (2000)
2) Egashira, R., Salim, C., *Sekiyu Gakkaishi (J. Jpn. Petrol. Inst.)*, **44**, (3), 178 (2001)
3) Salim, C., Saito, J., Egashira, R., *Journal of the Japan Petroleum Insititute*, **48**, (1), 60 (2005)
4) Salim, C., *Journal of the Japan Petroleum Insititute*, **49**, (6), 326 (2006)
5) Egashira, R., Solv. Ext. Res. Dev. Jpn., **14**, 63 (2007)
6) Egashira, R., *Journal of the Japan Petroleum Insititute*, **50**, (4), 218 (2007)
7) Thorsen and Terjesen, *Chem. Eng. Sci.*, **17**, 137 (1962)
8) Garner and Suckling, *Aemr. Inst. Chem. Eng. J.* **4**, 114 (1958)

# EXTRACTION OF TEXT AREA USING SCALE INVARIANT FEATURE TRANSFORM

Student Number:07M18125 Name:Jo Matsuda Supervisor: Yukihiko Yamasita

SIFT アルゴリズムを用いた文字領域特定

松田 穣

携帯電話のカメラやデジタルカメラの普及，その高解像度化に伴い，それらを入力手段とする文書画像解析，文字認識への期待が高まりつつある。そこで本研究では Scale-Invariant Feature Transform(SIFT) を利用した文字領域抽出・認識法を提案する。

SIFT は，特徴点の検出とその点の特徴量を抽出する手法である。SIFT により検出される特徴点やその特徴量は，画像の回転・スケール変化・照明変化等に頑健であるため，環境の変化に対して頑健性を持つ文字領域抽出・認識の実現が期待できる。本研究では，SIFT を利用した文字領域抽出プログラムを作成し，その性能確認実験を行った。

## 1 INTRODUCTION

Recently, the digital camera and the digital video recorder are miniaturized and have very high resolution. Such features are progressing rapidly and many functions are added to them. The digital camera can be used to acquire character information from the environment.

The digital camera and the cellular phone are very attractive as instruments for the character recognition and the document analysis. Different from the two-dimensional environment for a scanner, the three-dimensional environment for such instruments has many difficulties such as background, deformation, lighting and so forth.

To solve such problems, we propose a new character area extraction method using Scale-Invariant Feature Transform algorithm[1] [2]in this research.

## 2 OVERVIEW OF TEXT ANALYSIS

Recently, the accuracy of optical character recognition has reached to high level. Usually in optical character recognition, the image of document is taken by the scanner, and it is converted into the form that we can edit in the computer. The recognition of the Latin typed document is practical. However, the technology that extracts the character from the scene image with a digital camera and a portable camera is still incomplete.

## 3 OVERVIEW OF SIFT

Scale-Invariant Feature Transform (SIFT) is a method for detecting and extracting local feature descriptors that are reasonably invariant to changes in illumination, image noise, rotation, scaling, and small changes in viewpoint. We will explain the algorithm of SIFT.

### 3.1 Algorithm of SIFT

The processing of SIFT consists of two stages. That is, the detection of the key point and the description of the feature. SIFT is done by the following flows.

1) Detection of scale and key point.
2) Localization of key point.
3) Calculation of orientation.
4) Description of features.

In 1), the scale and the key point candidates are detected by the DoG (Different of Gaussian) processing. In 2), from the candidates, the key point are chosen by it's main curvature. Next, the sub-pixel-position is specified. In 3), for the calculation of the orientation, the histogram is generated from gradient information on the key point. The orientation is calculated from the histogram. The invariance of rotation is obtained by this operation. In 4), the area for describing features is rotated in the direction of the orientation previously determined. Afterwards, the the features are calculated by using gradients within the rotated area. The feature vector is normalized at the end. Because of normalization, the influence of light and shade are eliminated.

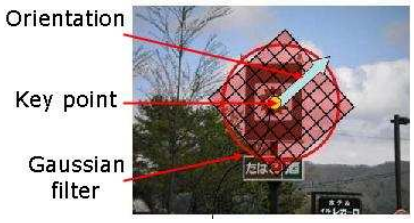


Figure 1: orientation

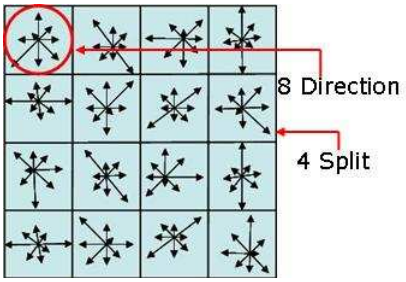


Figure 2: feature vector

# 4 Proposed technique

## 4.1 Over view

The proposed technique aims at the text extraction that is robust to rotation, scale, and lighting changes. A flow of the process is described as follows.

1) the feature vector is described with the detection of the key point by SIFT. 2) The key points in the learning data and input data are matched. 3) Matched point is selected from them by using the each other position. 4) the area where the density of match points is thigh is extracted. 5) The extracted area is Binarized. Afterwards, a final text area is extracted.

## 4.2 Feature vector

The feature vector for input and learning images are extracted by SIFT.

## 4.3 Matching

The matching is done by comparing the feature vectors. The pair of feature vectors of which distance is the smallest is extracted as matched points. The distance is evaluated by the following expressions.

$$d(v^{k_{I_1}}, v^{k_{I_2}}) = \sqrt{\sum_{i=1}^{128} (v_i^{k_{I_1}} - v_i^{k_{I_2}})^2} \qquad (1)$$

$$d_1 < w d_2 \qquad (2)$$

$d_1$ : *The distance of the nearest point*
$d_2$ : *The distance of the second nearest point*
$w$ : *threshold*

## 4.4 Selection match point

According to the difference of fonts, the matching condition is loosely set. Therefore, the matched points exist except in the text area. Then, we select matched points by the parallel relation and their density. In order reduce the number of matched points, we select a matched point that has other matched points in its neighbor such that the segment between the two key points of the matched point is parallel to those of matched points. Then, isolated matched points are discarded. By using Gaussian filter a high density region of matching points are extracted.

## 4.5 Binarzation

The area is separated by overlapping blocks. The blocks in which the integral of the filtered density of matching points calculated on section 4.4 excess the threshold is labeled as a character region.

# 5 Experimental Results

## 5.1 Experiment using various type of image

The experiment is conducted by using the various images. The types of images used in this experiments are scene images, web image and poster image. We used five images for each experiments. And the representative results are shown as following figures.


*The area around red line is extracted area
Figure 3: scene image

In Figure 3, it includes natural background information. In Figure 4, it includes the information of web object. In Figure 5, it is conducted to check

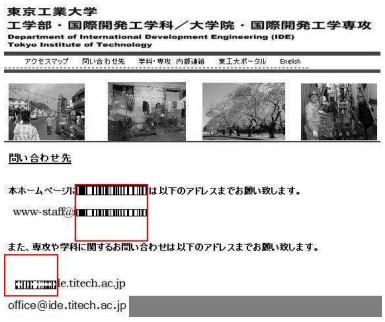


*The area around red line is extracted area
Figure 4: web image


*The area around red line is extracted area.
Figure 5: poster image

the resistance for the poster image. From the experiments result, we can say the proposed system extracts target text area in many case(scene image=4/5 web image=3/5 poster image=4/5). And, the proposed system extract target area completely in their experiments.

However, the proposed system was not able to defect precisely when the font size is too small, proximity background is complex, the target image has lots, and the target text uses special font. For example, the font size is too small in the Figure 4. Then, the non-target text area is included.

## 5.2 Experiment using added change image

In the following experiment, changes are added to the original images. The changes used in this experiment are symmetric transformation, rotation, reduction and expansion, lighting, and projective transformation.

In Figure 6 and 7, the robustness for symmetric transformation is examined. In Figure 8, the robustness for rotation is examined. In Figure 9, the robustness for projective transformation is examined. In Figures 10 and 11,the robustness for scaling is examined. In Figures 12 and 13, the robustness for lighting change is checked.


*The area around red line is extracted area.
Figure 6: symmetric 1


*The area around red line is extracted area.
Figure 7: symmetric 2


*The area around red line is extracted area.
Figure 8: rotation=90degree

From the results, the proposed system shows robustness in many case (Figure 6, Figure 7, Figure 8, Figure 10, Figure 12, Figure 13). For the reduction


*The area around red line is extracted area.
Figure 9: Projective transformation=20degree

(Figure 11), it does not extract completely. Because the target font size in reduced image is too small. But target areas are extracted more than 70 percent.

However, for the projective transform(Figure 9), it does not extract precisely, when the text includes characters that are symmetric to each other.


*The area around red line is extracted area.
Figure 10: expansion


*The area around red line is extracted area.
Figure 11: Reduction


*The area around red line is extracted area.
Figure 12: Lighting change1


*The area around red line is extracted area.
Figure 13: Lighting change2

## 6 Conclusions

We proposed a new character area extraction method that uses SIFT. We show its robustness for image transformation, and lighting change.

For future tasks, we have to develop a method that has a robustness against projective transformation.

## REFERENCES

[1] D. G. Lowe:*Object recognition from local scale-invariant features*, IEEE International Conference on Computer Vision (ICCV), pp.1150-1157(1999)

[2] Hironibu Fujiyoshi: *Extract feature vector by gradient base -SIFT and HOG-* , PRMU, pp.511-517(2007)

# CORRELATION ANALYSIS OF COHERENT TURBULENCE OVER REDUCED URBAN MODEL

Student Number:07M18131 Name: Ayako MARUYAMA Supervisor:Manabu KANDA

# 屋外模型都市における乱流構造の時空間解析

丸山 綾子

本論文では，屋外模型都市において発達する乱流構造の時空間解析を行うことによって，渦の移流速度を算出し，乱流構造の時間と空間の対応関係を明らかにした．さらに相関係数の水平形状から乱流構造の定量化を試み，地表面形状との比較を行うことで地表面形状によらない乱流構造の相似性が明らかとなった．

## 1 Introduction

Recently, various environmental problems in urban cities, such as heat island and concentrated heavy rain, were observed. Urbanization significantly impact the transport processes of momentum, water vapor and heat. Various studies reveal that these processes are dominated by turbulent coherent structures (Inagaki and Kanda [1]). For a flat surface, Adrian et al. [2] indicated the schematic diagram of the coherent strucures using PIV (particle image velocimetry) measurements. In addition, these structures were also observed over vegetation canopies (Finngan [3]). Nevertheless, there is a dearth of research quantifying coherent structures due to the difficulty of establishing relationships between spatial and temporal aspects of such structures. In the present study, I investigated these relationships by evaluating the spatial and temporal scales of these structures, and comparing with other studies. Furthermore, we evaluated the convective velocity over the reduced urban model. The convection velocity $Uc$ is instrumental in Taylor's hypothesis, which converts temporal data to spatial data. This hypothesis is the time-history of the flow signal measured from a stationary probe, and regards the convection flow as a 'frozen' spatial pattern of turbulence past the probe. The mean wind velocity $\overline{U}$ is approximated by the value of $Uc$ in Taylor's hypothesis. Yet, various studies suggested the Taylor's hypothesis does not work on various surface conditions. Shaw et al. [4] found that $Uc/\overline{U}$=1.2 at a height of 2 times the vegetation canopy by using correlation analysis, while Castro et al. [5] yielded $Uc/\overline{U}$=1.3 at the canopy height using wind tunnel experiment with a staggered pattern of cubes.

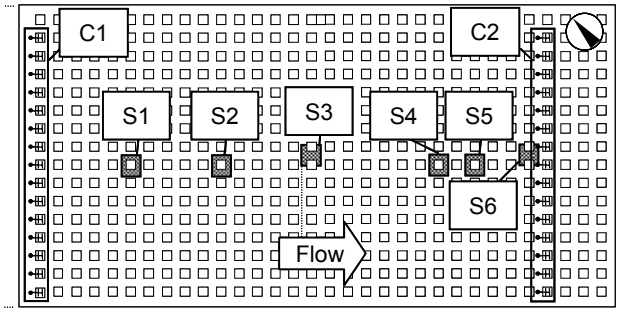


**Figure 1** COSMO

## 2 Experimental methods

### 2.1 COSMO

The experiments were conducted at the COSMO (Comprehensive Outdoor Scale Model), Nippon Institute of Technology, which was constructed for urban climate studies. The floor area is 50m by 100m, covered with concrete cubes of 1.5-m dimension (H) to represent urban type roughness, arranged in a symmetrical and aligned pattern with an area coverage density of 25% (**Fig.1**).

### 2.2 Installation of the instruments

**Figure 1** shows the installation positions of instruments for the 3 cases. For case 1, 15 anemometers were located at each spanwise-line through C1 and C2. For case 2, 4 sonic anemometers were located at S3, S4, S5, and S6, along with 7 other probes arranged in a spanwise-line

aligned to S6. Case 3 is similar to case 2, except that probes at S1 and S2 replace those at S4 and S5, respectively. The spatial intervals of each probe $dx$ are shown in **Table 1**. For simplification, I substituted symbols for each $dx$. All anemometers were located at 2H (H: canopy height). Sampling frequency is 10Hz for case 1, and 50Hz for cases 2 and 3.

**Table 1** Spatial intervals of each probe

| symbol | $dx$ (m) | instrument number | |
|---|---|---|---|
| | | leeward | windward |
| D6 | 5.6 | S5 | S4 |
| D9 | 8.85 | S6 | S5 |
| D14 | 14.45 | S6 | S4 |
| D22 | 21.55 | S4 | S3 |
| D27 | 27.15 | S5 | S3 |
| D36 | 36 | S6 | S3 |
| D50 | 50.35 | S6 | S2 |
| D66 | 65.85 | S6 | S1 |
| D84 | 84 | C1 | C2 |

# 3 Analytical Procedures

## 3.1 Definition of space-time correlations

Two-point correlation coefficients were calculated as follows,

$$R_{uu} = \frac{\overline{u(r,t)u(r+dr,t+dt)}}{\sqrt{\overline{u^2(r,t)}}\sqrt{\overline{u^2(r+dr,t+dt)}}} \qquad (1)$$

where $r$ represents the position with spatial coordinates $(x, y, z)$, $t$ is time, $dr$ is the distance between 2 points, $dt$ is the time lag. $R_{uu}$, $R_{vv}$, and $R_{ww}$ are calculated from velocity fluctuation components for the streamwise, spanwise and vertical directions ($u'$, $v'$, $w'$).

## 3.2 Computation approach

The convection velocity is calculated using the equation:

$$Uc = dx / \tau \qquad (2)$$

where $\tau$ is the time delay required to maximize the space-time correlation. Specifically for D84 (case 1), decomposition of inner- and outer-scales described by Inagaki and Kanda [1] was used, with the following equation:

$$u = [u] + \overline{u_s'} + u_s'' \qquad (3)$$

where the square brackets represent spatial averaging, the over-bar symbolizes temporal averaging, the prime represents spatial fluctuation, and the double prime indicates the temporal and spatial fluctuation component. That is to say, the outer-scale motion is evaluated from $[u]$, and the inner-scale motion is evaluated from $u_s''$.

## 3.3 Filtering condition

I set thresholds for turbulent intensity (<0.5), wind direction ($\pm$ 10 degree) and stability (neutral) exclusively for the S6 probe. Furthermore, mean velocity increment of 0.5 $(m \cdot s^{-1})$ from 0.5 $(m \cdot s^{-1})$ was selected. Additional threshold values for all probes were set as follows: mean temperature (0< $\overline{T}$ <50), momentum ($u'w'$ <0), and angle of elevation ($\pm$15 degree). Number of samples per threshold velocity range are shown in **Table 2**.

**Table 2** Number of samples per threshold velocity range

| threshold velocity $(m/s)$ | Number of sample | | |
|---|---|---|---|
| | case1 | case2 | case3 |
| | neutral | neutral | neutral |
| 0.5～1.0 | 3 | - | 5 |
| 1.0～1.5 | 4 | 14 | 23 |
| 1.5～2.0 | 9 | 12 | 37 |
| 2.0～2.5 | 3 | 7 | 43 |
| 2.5～3.0 | 3 | 6 | 45 |
| 3.0～3.5 | 4 | 9 | - |
| 3.5～4.0 | 9 | - | - |
| 4.0～4.5 | 7 | - | - |
| 4.5～5.0 | 7 | - | - |
| 5.0～5.5 | 5 | - | - |
| 5.5～6.0 | 2 | - | - |
| 6.0～6.5 | 2 | - | - |

# 4 Results

## 4.1 Convection velocity for 30-min averaging time

**Figure 2** shows a comparison of $Uc$ computed from two-point correlations (Equation (2)) and the local mean streamwise wind velocity calculated from $u'$.

The scattered plots indicate that the $Uc$ exceed the mean wind velocity. When the distances between instruments are relatively close (D6 to D14), the corresponding plots are closer to the 1:1 gradient-line with respect to the other plots. The plots for D84 are linear and exceed the 1:1 gradient-line, indicating that the outer-scale eddies significantly exceed the mean wind speed. Furthermore, the plots corresponding to large $dx$ (>22 m) gather near the 1:1.6 approximation line. This suggests that the $Uc$ of inner- and outer-scale eddies can be distinguished by the spatial interval size. It can be deduced that small interval-sized plots (D6 to D14) represent inner-scale $Uc$ because it seems that the

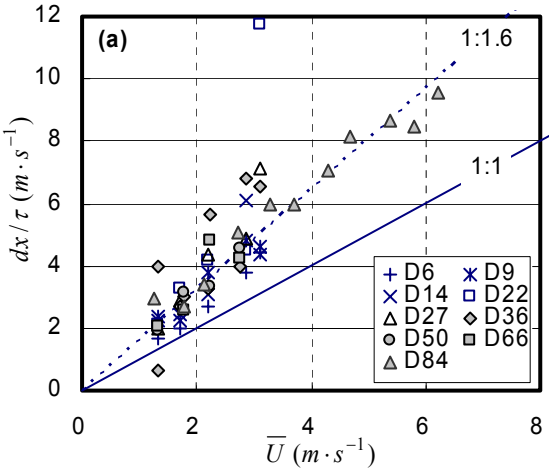


**Figure 2** Convection velocities computed from time lag
Each scattered plots for the distance between probes; solid line is 1:1 line; dashed line is the approximation line of D84

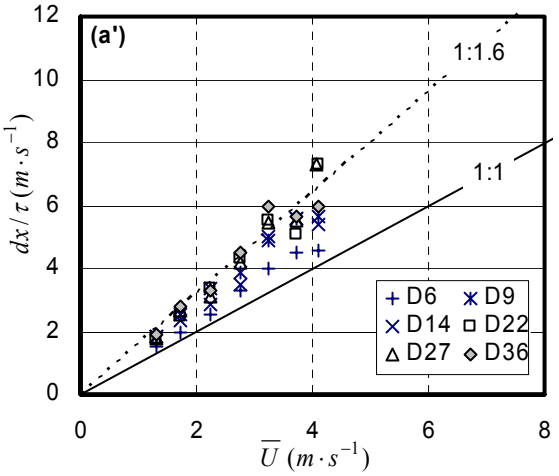


**Figure 3** Convection velocities computed from time lag
Each scattered plots for the distance between probes; solid line is 1:1 line; dashed line is the same line of **Fig.2**

eddies involved retain their shape in the streamwise direction. On the other hand, larger interval-sized plots (D27 to D84) appear to capture outer-scale $Uc$, wherein the corresponding inner-scale eddies do not retain their shape due to their shorter life-time. Therefore, the correlation of outer-scale motion becomes stronger than of inner-scale motion.

### 4.2 Convection velocity for 3-min averaging time

To clearly distinguish the inner- and outer-scale eddies associated with $Uc$, I reduced the averaging time from 30 minutes to 3 minutes. The reduced averaging time allows us to focus on the inner-scale motion, which has smaller time scale than the outer scale motion, by eliminating large-scale motions which are included in the mean component of this shorter time average.

**Figure 3** shows the result of this 3-minute averaging calculated from $u'$. The difference in $Uc$ previously observed in **Figure 2** is more obvious since there is now less scatter around the corresponding approximation lines. The 3-minute plots of D6 to D14 are closer to 1:1 line, while the 3-minute plots of D27 and D36 vary less than the 30-minute plots. This verifies that the smaller averaging time eliminates the influence of eddies with frequencies greater than 3 minutes. Nevertheless, the influence of outer-scale motion is still apparent for large interval plots.

### 4.3 Comparison with other studies

The $Uc$ from the previous plots are shown in **Table 3**. These are approximated from the gradient of

**Table 3** Convection velocity

| | $Uc/\overline{U}$ | |
|---|---|---|
| | ~D14 | D84 |
| $u'$ | 1.3 | 1.6 |

approximation lines using the 3-minute plots of D6 to D14 for the inner-scale, and the 30-minute plot of D84 for the outer-scale, respectively. These $Uc$'s are faster than the mean wind velocity, especially for the outer-scale motion. Considering inner-scale fluctuation and outer-scale fluctuation are independent and have no interaction with each other [6], and the structure attributed to the inner-scale eddies [7], it was considered the structure above COSMO is transported by the inner-scale convection velocity.

This inner-scale $Uc$ agrees with other studies, such that over vegetation ( $Uc/\overline{U}$ =1.2: Shaw et al. [4], $Uc/\overline{U}$ =1.3: Su et al. [8])) and rough surfaces ($Uc/\overline{U}$ =1.3, Castro et al. [5]). These indicate that the convective velocities of the inner-scale motions are similar over vegetation and COSMO.

### 4.2 Horizontal distribution of correlations at 2H

**Figure 4** shows a comparison of horizontal distribution computed from two-point correlations of ($u'$, $v'$). The horizontal axis is the converted time scale to length scale using mean wind velocity and normalized by H. 'TD' represents the outer-scale motion, and 'SD' represents the temporal and spatial fluctuation in Equation (3). It can be observed from **Fig.4(a)-(b)** that the influence of

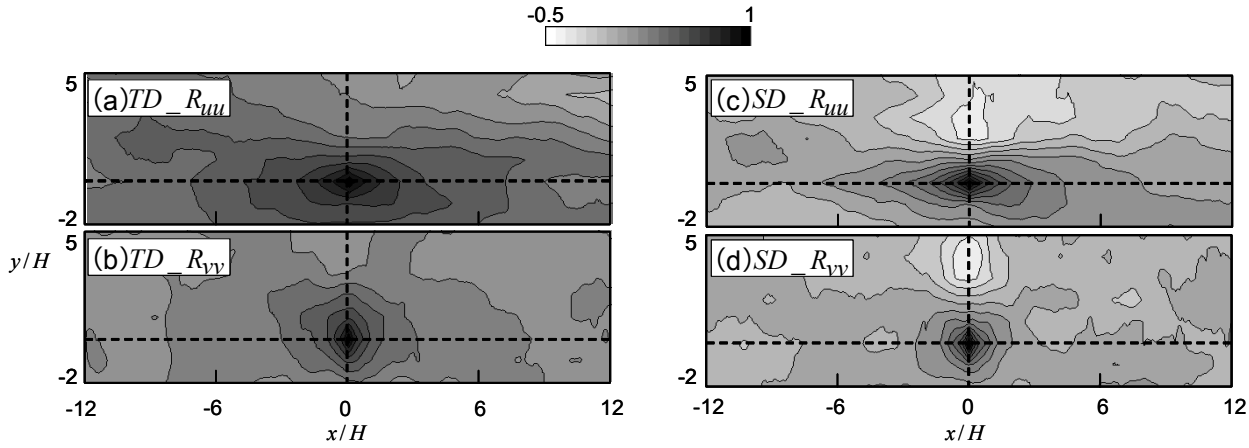


**Figure 4** Correlations in the horizontal plane
TD: including outer-scale fluctuation SD: remove outer-scale fluctuation

the outer-scale motion is elongated in the streamwise direction. The shape of $R_{vv}$ distribution is more rounded since the coherent structure is meandering. Outer-scale motion does not affect $w'$ fluctuation (not shown).

### 4.3 Quantification and Comparison

From **Fig.4(c)**, the length in streamwise direction is 11.0H using $Uc/\overline{U}$ =1.3. Calculating the spatial and temporal scales of the coherent turbulence from SD, the horizontal to vertical ratio is 9:2. Using $Uc/\overline{U}$ =1.3, the ratio becomes 11:2. This is shown that the conveciton velocity is important parameter for quantification. Furthermore, this result is in agreement with the findings of LES over rough surface of Zhang [9] (2H), wind tunnel over vegetation of Shaw et al. [4] (H) and wind tunnel over flat surface of Ganapathisubramani et al. [10].These results suggest that the structure of inner-scale motion is geometrically similar regardless of surface condition.

## 5 Conclusions

The conclusions of this study were summarized as follows:

1. The inner-scale convection velocity is 1.3 times faster than the mean wind velocity at 2H, and that of outer-scale is 1.6 times faster at COSMO.
2. At COSMO, the horizontal to vertical ratio of the streamwise structure is 11:2. The ratio is in good agreement with studies for vegetation canopy and LES of rough and flat surface.

These results indicate the coherent structures of inner-scale motions are similarity irrespective of the surface conditions.

### References

[1] Inagaki, A. and Kanda, M.: 2008, 'Turbulent flow similarity over an array of cubes in near-neutrally stratified atmospheric flow', *J. Fluid Mech.*, **615**, 101-120.

[2] Adrian, R. J., Meinhart, C. D. and Tomkins, C. D.: 2000, 'Vortex organization in the outer region of the turbulent boundary layer', *J. Fluid Mech.,* **422**, 1-54.

[3] Finnigan, J. J.: 2000, 'Turbulence in Plant Canopy', *Annu. Rev. Fluid Mech.*, **32**, 819-571.

[4] Shaw, R.H., Brunt, Y. and Finnigan, J.J and Raupach, M.R.: 1995, 'A wind tunnel of flow in waving wheat: two-point velocity statistics', *Boundary layer meteorology*, **76**, 349-376.

[5] Castro, I. P., Cheng, H. and Reynolds, R.: 2006, 'Turbulence Over Urban-Type Roughness: Deductions From Wind-Tunnel Measurement', *Boundary layer meteorology*, **118**, 109-131.

[6] McNaughton, K. G. and Raubach, J.: 1998, 'Unsteadiness as a cause of non-equality of eddy diffusivities for heat and vapour at the base of an advective inversion', *Boundary-Layer Meteorol.*, **88**, 479-504.

[7] Inagaki, A.: 2008, 'Atmospheric turbulence over an array of massive cubes', Phd thesis, Tokyo Institute of Technology.

[8] Su, H. B., Shaw, R.H. and Kyaw tha paw u: 2000, 'Two-point correlation analysis of neutrally stratified flow within and above a forest from large-eddy simulation', *Boundary layer meteorology*, **49**,423-460.

[9] Zhang, J.: 2009, 'LES study on hierarchical turbulence organized structure above urban canopy', Master thesis, Tokyo Institute of Technology.

[10] Ganapathisubramani, B. et al.: 2005, 'Investigation of large-scale coherence in a turbulent boundary layer using two-point correlations', *J. Fluid Mech.*, **524**, 57-80.

# System to Make Teaching Materials Based on Collective Intelligence

Student Number: 07M18148 Name: Mandana AMIR KHOSRAVI Supervisor: Yukihiko YAMASHITA

# 集合知に基づく 教材作成システム

アミル ホスラビ マンダナ

テキスト ベースの e-Learning を実現する tobe システムと，Wiki の概念を取り 入れた，集合知に基づく 教材作成システムを構築する。Wiki を使うことによって e-Learning の教材の作成を行い，維持管理問題を解決し ている。Wiki システムは，世界中の多数の人々が参加することによって，広範囲で詳し い情報を持続的に提供する。本研究では，Wiki の考え方に基づき，特別な IT スキルを必要せず，ネット ワーク 上で多数の人々が容易に 1 つの教材の作成に参加すること，及び，利用することを可能にするシステムを構築する。

## 1 Introduction

After 1990, due to the innovations of Information Technology, utilization of equipments like PC has become widespread among general households. Then nowadays, according to development of the Internet and WWW, we can exchange information regardless of time and place. And utilization of e-Learning system gives a chance to learners to use PC for learning anytime and anywhere. But the problem is that to make teaching materials for e-Learning, not only teaching methodology skill but also IT skill are necessary, and correction and changing of materials are difficult. Therefor making materials costs much. Furthermore, using Wiki systems gives an opportunity to people around the world to exchange their information. And according to Wiki philosophy, applying Wiki does not need any especial skill, and making materials in a group is possible. However, Wikis are static pages, thus Wikis cannot be an effictive learning/studing system.

Then in this research, we proposed a new system, combined the tobe (Text Oriented Bi-Stream Explanation) system and Wiki system. The tobe system is an text-base learning system that makes animation from tobe text. The tobe text has to be written in tobeML (XML based markup language). Then, its combination with Wiki enables to create a tobe text easily in a group via a network.

## 2 e-Learning

Electronic Learning (or e-Learning)[1] is a type of technology supported education/learning, where the medium of instruction is computer technology, particularly involving digital technologies. e-Learning has been defined as "pedagogy empowered by digital technology". e-Learning is used interchangeably in a wide variety of contexts. In companies, it refers to the strategies that use the company network to deliver training courses to employees. Lately in some universities, e-Learning is used to define a specific mode to attend a course or programs of study where the students rarely attend face-to-face for on-campus access to educational facilities. Table 1 shows the e-Learning history.

## 3 tobe system

The tobe system[2] is a system to change the text-base data to animation. In the tobe system, the player that does this conversion is called“ Expositor ”. In this system all the data are written in text-base, therefor the correction and changing data are easy. And Expositor makes a situation similar to real classroom on the PC screen. Expositor just can read the text which is written in the tobeML language. The tobeML is a markup language based on XML which is defined originally for this system.

When a learner plays the Expositor, Fig.1 ap-

Table 1: e-Learning history

| | |
|---|---|
| **first generation** | CBT(Computer Based Training): Have to install materials directly to the PC or use CDs, learners can study in any where and at any time, but the problem is information exchanging is just one-way. |
| **second generation** | WBT(Web Based Training): Using web browser, and using network makes a possibility to have two-way learning. |
| **third generation** | LMS (Learning Management System): In addition to WBT functions, we can manage the records and and check the learners' progress. |

pears on the screen. As you can see in Fig.1 the tobe system includes three main parts, board, professor with pointer and talk part (the part that professor explains by voice).

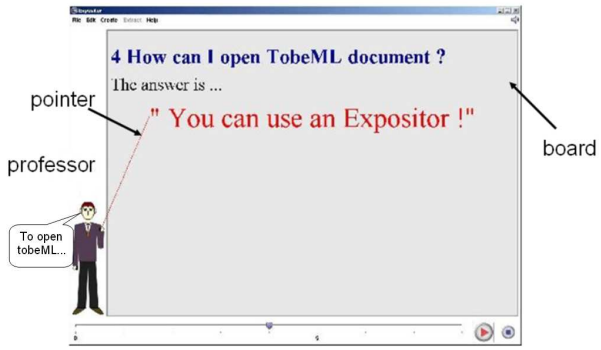


Fig. 1: tobe system

However making materials in tobeML language is not easy and the data creator has to memorize tobeML tags. To solve this problem, in this research we proposed the tobeWiki system.

# 4 Collective Intelligence

Collective intelligence (CI)[3] is a shared or group intelligence that emerges from the collaboration and competition of many individuals. CI can also be defined as a form of networking enabled by the rise of communications technology, namely the Internet. Web 2.0 has enabled interactivity and thus, users are able to generate their own content. Collective Intelligence draws on this to enhance the social pool of existing knowledge. Communications tools enable humans to interact and to share and collaborate with both ease and speed. With the development of the Internet and its widespread use, the opportunity to contribute to community-based knowledge forums, such as Wiki systems become possible.

## 4.1 Wiki

Wiki[4] is a Hawaiian word for "fast". "Wiki Wiki" is a reduplication. A wiki is a page or collection of Web pages designed to enable anyone who accesses it to contribute or modify content, using a simplified markup language. Wikis are often used to create collaborative websites and to power community websites. The collaborative encyclopedia Wikipedia is one of the best-known wikis. Wikis are used in business to provide networks and knowledge management systems. Ward Cunningham, the developer of the first wiki software, WikiWikiWeb, originally described it as "the simplest online database that could possibly work".

Wiki is a piece of server software that allows users to freely create and edit Web page content using any Web browser. And Wikis have a simple text syntax for creating new pages.

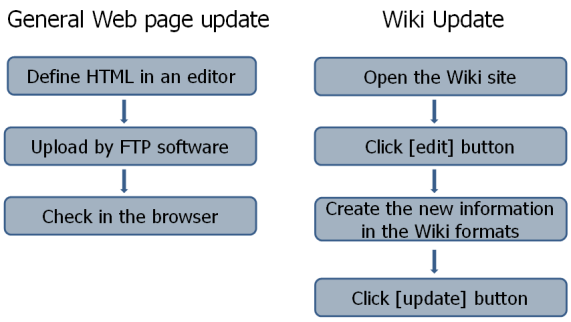


Fig. 2: Wiki and general web page

And the main characteristics of Wiki are:

- Wiki invites all users to edit any page or to create new pages within the wiki Web site.

- Wiki promotes meaningful topic associations between different pages by making page link creation almost intuitively easy and showing whether an intended target page exists or not.
- Ordinarily, the structure and formatting of wiki pages are specified with a simplified markup language, sometimes known as "wiki-text". For example, starting a line of text with an asterisk ("*") is often used to enter it in a bulleted list.

## 5 Proposed system

The proposed system, the tobeWiki system, is the combination of the tobe system and the Wiki system. In this system we define the formatting rules for tobeWiki to make teaching materials easily in a group. And after making materials as a text on Wiki, the text-base data will be changed to the tobe text and tobeML tags will be added to the Wiki text automatically to be readable in Expositor. Fig.3 illustrates the tobeWiki system. To define wiki formatting rules, we used simple symbols. The defined formatting rules on tobeWiki are as below.

- To make the header part: we put the title, author, panel size and professor character information in the bracket and divide up them by "/".

[title/author name/panel size/professor character]

- To make the board part (the part which is going to appear on the board): in this part, on the Wiki pages we use simple symbols to make text-base data which are going to appear on the board. The symbols are listed in Table 2.
- To make the talk part (the part that professor is going to explain by voice): in this part, on the Wiki pages we use simple symbols to make text-base data which are going to change to audio. The symbols are listed in Table 3.

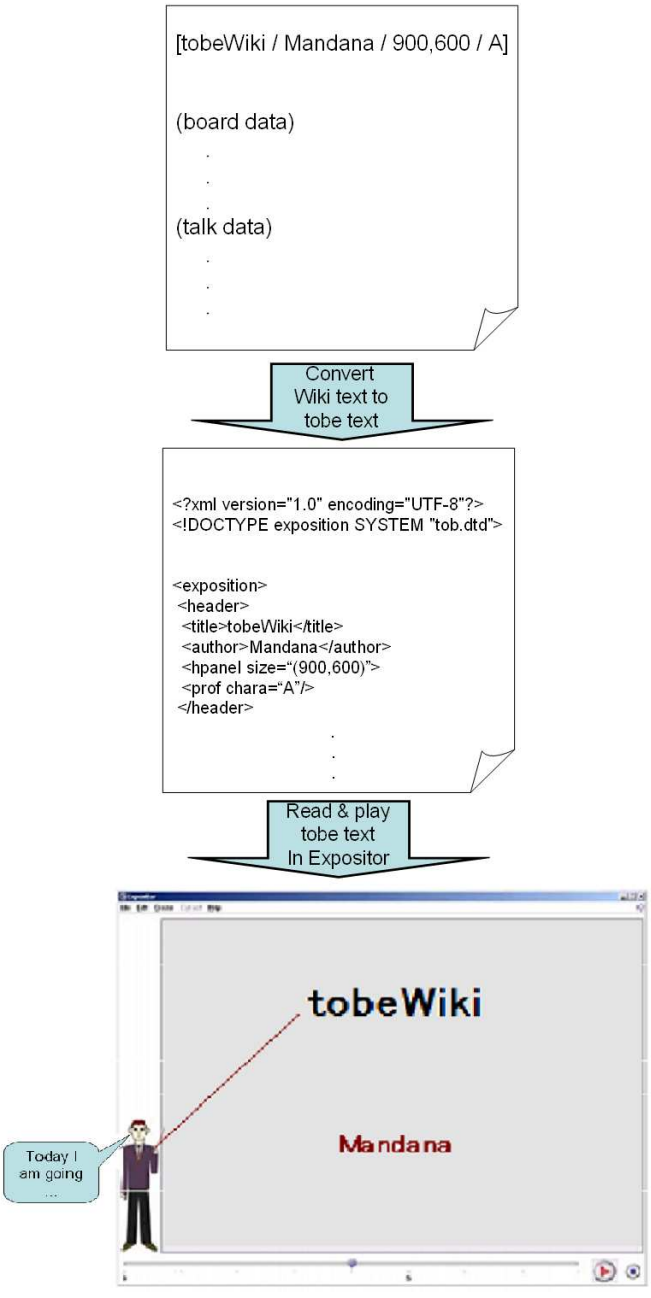


Fig. 3: tobeWiki system

Table 2: Board symbols

| symbol | meaning |
|---|---|
| **=}** | pointer target |
| * | section |
| ** | subsection |
| *** | subsubsection |
| **-** | itemize |
| **#** | figure |
| **\|** | table |
| **Q( )** | question |
| **A( )** | answer |
| **Ex( )** | example |
| **P( )** | proof |
| **D( )** | definition |
| **center** | center |
| **right** | right |
| **left** | left |
| **=（ more than 4）** | new panel |

Table 3: Talk symbols

| symbol | meaning |
|---|---|
| **T====** | new panel |
| **T=}** | pointer target |
| {{ | back |
| }} | next |
| ^^ | jump |
| **:]..** | nod |
| **..** | pause |
| **;;** | walk |
| **:)..** | smile |

The advantages of this system for a creator are:

- Creator does not need to use videos for making materials, just have to download Wiki on the PC.
- Creator does not need to memorize tobeML tags, just have to memorize Wiki symbols.
- Creator does not need to have any special IT skills.
- Because the created data are text-base, correction and changing are easy.
- Makng Materials in a group is possible.

The advantages of this system for a learner are:

- Because of the created data are text-base, learner does not need to care about amount of data and environment.
- Learner can choose the necessary data by checking tobeML tags. tags.

And finally, (header)+(boerd part)+(talk part) form a tobe text, and Expositor converts the tobe text to animation.

# 6 Conclusion

In this research we developed a system to improve the learning through the Internet and making teaching material easier in a group. According to this system, first we make data on Wiki pages, and as a next step these data will be changed to tobe texts. And finally convert these data to animation.

However, still the system need to be improved, and as a future work we have to improve it graphically. And now the tobeWiki system works only in English, but it should correspond to other languages, too. And we also need to define more formatting rules for Wiki to have easier way for making tobe texts.

# References

[1] SATT: e ラーニングとは, http://satt.jp/tech/e-learning.htm.

[2] 戸部章子: XML ベースの説明記述言語およびその講義形式プレ イヤに関する研究 (2005).

[3] Wikipeida: CI, http://en.wikipedia.org/wiki/Collective-intelligence/.

[4] Wikipedia: ウィキ, http://ja.wikipedia.org/wiki/.

# The property of dislocation motion tracks which formed in deformation of aluminum and influence on the dislocation

Student Number: 07M18154 Name: Chao Hu Supervisor:Kunio Takahashi

# 変形する Al 内部に形成される転移移動痕の性質とそれが転移におよぼす影響

胡　超

透過型電子顕微鏡の中でアルミニウムを引張り破断し、その場観察実験を行った。常温と５０℃における結果を比較した。いずれの場合も材料内部に転位のすべり痕が形成された。そのすべり痕は面欠陥であり，時間が経てばやがて消失するが、５０℃における消失速度は常温のそれよりも小さい。また，すべり痕は後続の転位の移動の障害となることが観察された。したがってすべり痕はアルミニウムの力学的性質に多大な影響を及ぼしていると推察された。

## 1 Introduction

In the recent studies by Kiritani et al[1–6], many experimental results which imply the existence of deformation mechanism without dislocation were reported. In this deformation, they observed few dislocations at the fractured tip of thin metal foil at which heavy deformation occurred. Instead, they observed an anomalous number of point defect clusters. They proposed the existence of a plastic deformation mechanism that proceeds without dislocation. Kiritani et al[1,7,8] proposed the new deformation mechanism but the detail of the deformation is still unknown. To interpret the phenomenon discovered by Kiritani et al, motion of the dislocations has been observed by electron microscopy.

Plastic deformation in metals occurs by the gliding of line-type crystal lattice defects called dislocations. The theory of the strength of metals is based on interactions between these dislocations and various kinds of crystal lattice defects, including the dislocations themselves, all of which act as barriers to the gliding motion of the dislocations. In this study, we show the slip traces of dislocations formed inside of the aluminum foil which has been discovered in aluminum by electron microscopy. It exists only under elastic strain and disappears completely when the stress is unloaded.

## 2 Experimental Method

### 2-1 Specimen

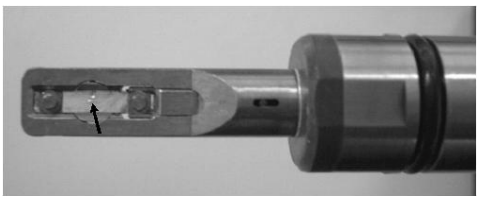

**Fig. 1 Specimen in tensile specimen holder**

The tensile deformation process of pure aluminum was observed by an electron microscope. The specimen used was pure aluminum with 99.999% purity. It is considered that few impurities in aluminum influence on the experiment, but the influence is still unknown. Specimen was cold rolled to a thickness of 50μm, annealed at 873 K, and then cut into pieces of size 2mm×10mm in order to accommodate it in a tensile specimen holder(Fig. 1). A notch cut where is the arrow was introduced in the center of the piece in order to render the rupture of the specimen to begin at the center. In order to remove the dislocations, we annealed the specimen at 773 K an

hour.

**Table. 1 Number of samples for the experiment and their experimental conditions**

| Temperature | 298K | 323K |
|---|---|---|
| Number of Samples | 8 | 11 |

### 2-2 In-situ tensile experiment

The in situ observation of tensile fractures was performed using a JEOL 2010 electron microscope, specimen observed with electron microscope at the acceleration voltage of 120keV.Crosshead speed of the straining holder was controlled to 0.1 μm/s. Specimen temperature was 298K and 323K. The direction of the observation is from <100> direction, and g=200 reflection beam was selected. Dark field observation for TEM image was recorded by a video recorder.

By pulling the specimen, cleavage proceeds from the notch cut. Dislocation motion tracks in aluminum has been observed by stop pulling the specimen just before the foil ruptures. And the tracks disappear when the tensile stress is unloaded.

## 3 Experimental Results

### 3-1 Appearance of dislocations and their motion tracks in aluminum

Figure 2 shows dislocation motion tracks images observed by transmission electron microscope (TEM) in aluminum foil. (a) Initial state before the appearance of new dislocations.(b)Dislocations have appeared from the directions of the arrows and stopped. The contrasts of the tracks are yet very faint at this stage. (c) The contrasts of the tracks have gradually become stronger. (d) The contrasts of the tracks have become clear. These dislocation motion tracks Fig. 3 were known type of planar defects (stacking fault) in a difference direction observation. Fig. 4 shows a schematic description of the dislocation motion track, the track consists of "surface track" and "internal track".

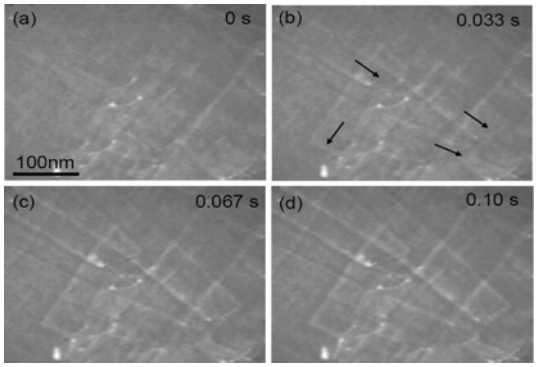


**Fig. 2 Appearance of dislocations motion tracks in aluminum**

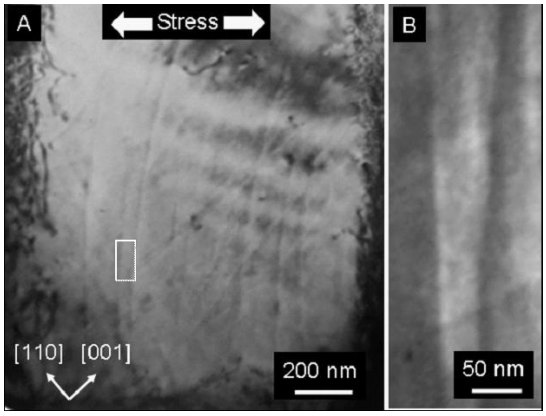


**Fig. 3 Dislocation motion tracks in a difference direction observation**

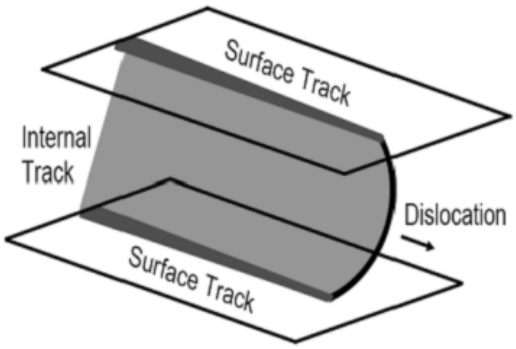


**Fig. 4 Schematic description of dislocation motion track**

### 3-2 Disappearance of dislocation motion tracks

Figure 5 shows variation of the image contrasts of the dislocation motion tracks with time at room temperature when the stress is unloaded. The images have gradually become faint after 12 seconds, they

have almost disappeared. Fig. 6 shows A,B and C field brightness change with time is dislocation motion track field, A is no specimen field and B is no dislocation motion track field in specimen. It is considered the dislocation motion tracks is not steady, they disappears completely when the stress is unloaded.

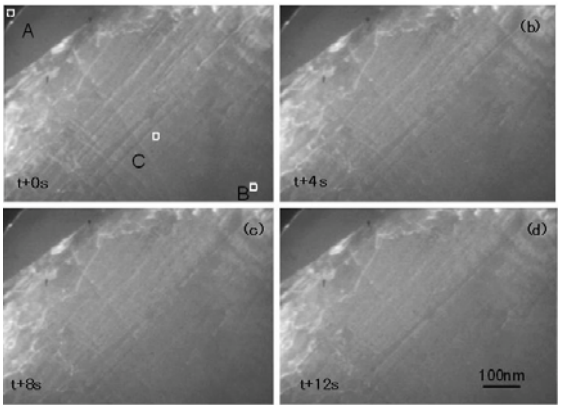


**Fig. 5 Contrasts of the dislocation motion tracks with time at room temperature**

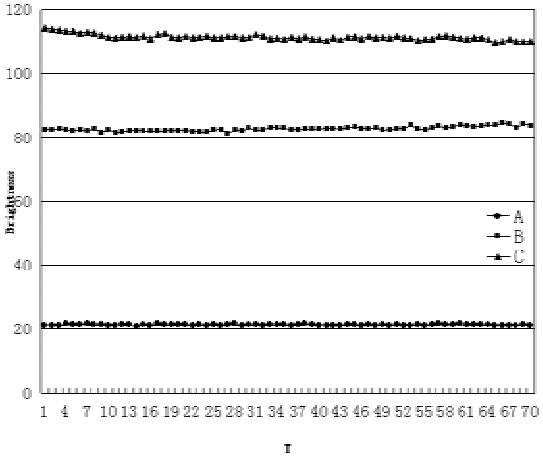


**Fig. 6 Brightness variation of dislocation motion tracks**

## 3-3 Difference of dislocation motion tracks disappears between room temperature and 323 K

Figure 7 shows variation of the image contrasts of the dislocation motion tracks with time at 323K when the stress is unloaded., In Fig. 5 after 12 seconds, the dislocation motion tracks images have gradually become faint, dislocation motion tracks variation of 323K is much slower than the variation at room temperature.

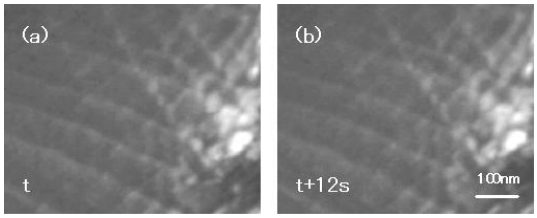


**Fig. 7 Contrasts of the dislocation motion tracks with time at 323K**

## 3-4 Interaction between dislocation and motion track

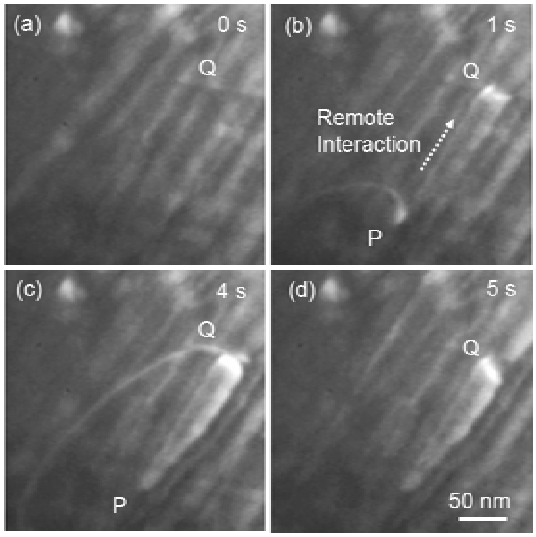


**Fig. 8 Interaction between dislocation and motion track**

Figure8 shows a very interesting sequence of the interaction between dislocations and dislocation motion tracks. Fig. 8(a) is the initial state. Then in Fig. 8(b), a dislocation appeared and stopped at P. Simultaneously, Q became bright. The bright part is considered to be an intersection line between two different dislocation motion tracks. In Fig8(c),P advanced again and stopped at barrier Q. In Fig. 8(d),P advanced upward and disappeared. When P broke through the barrier Q, the bright line image at Q rotated clockwise. It is obvious that the remote interaction between P and Q in Fig. 8(b), at Q, push out of atomic arrays toward the direction of the arrow is observed. It is surprising that the shift of atoms is taking place by the touch of far dislocations that exists at the distance of several hundreds nm. This role of dislocation motion tracks as a conductor of the stress

is extremely important when considering the mechanical properties of polycrystalline metals.

# 4 Discussions

## 4-1 Causation of dislocation motion tracks formed in aluminum

From the observed results of dislocation motion tracks images, The contrasts of the tracks was formed by motion dislocation, these dislocation motion tracks Fig.4 were known type of planar defects(stacking fault). Amplification of the amplitude of the horizontal wave of the lattice vibration is thought when the stress was loaded.

## 4-2 Influence to the mechanical properties

The interaction between dislocations and the tracks has been observed (Fig. 8). Since the tracks work as the barrier for dislocation motion, it is considered that they give a large influence to the mechanical properties of the aluminum including process hardening and serration, especially in the case of high strain rate. It is necessary to revise the theory of the strength of metals at least in the case of aluminum. And this discovers has possibility that elucidate the mechanism of anomalous vacancy cluster formation in tensile ruptured metal foils which was detected by Kiritani et al.

## 4-3 Possibility of dislocation motion tracks formed in other face-centred cubic (FCC) metals

The accumulated dislocation motion tracks serve as planes of slip for the synchronized rotation of nanolayers[4], and the anomalous formation of point defect clusters occurs at the intersection of dislocation motion tracks formed in different orientations. It might seem logical that dislocation motion tracks would also be formed in other face-centred cubic (FCC) metals since the morphology of the ruptured tip of the thin foil is the same for all[2,3], it would be expected that the elastic strain necessary to form an dislocation motion tracks in these FCC metals would be higher, considering their higher elastic strain observed. Aluminum has a rather large lattice constant of 0.405 nm for its low atomic number of 13. It is thought that this coarse structure enables the atoms to shift to the position with a low elastic strain compared to other FCC metals.

# Conclusion

Formation of dislocation motion tracks in aluminum has been discovered by the in-situ tensile experiment of transmission electron microscopy. The tracks are formed just behind the dislocations motion at the room temperature and 323K. These dislocation motion tracks were known type of planar defects (stacking fault) in a difference direction observation. The tracks disappear when the tensile stress is unloaded. In 323K the speed of the disappearance is slower than that of the room temperature. The interaction between dislocations and the tracks has been also observed. Since the tracks work as the barrier for dislocation motion, it is considered that they give a large influence on the mechanical properties of the aluminum.

# References

1) M. Kiritani, K. Yasunaga, Y. Matsukawa and M. Komatsu: Radiat. Eff. Def. Solids 157 (2002) 3-24.

2) Y. Matsukawa, K. Yasunaga, M. Komatsu and M. Kiritani: Mater. Sci. Eng. A350 (2003) 8-16.

3) Y. Matsukawa, K. Yasunaga, M. Komatsu and M. Kiritani:Mater. Sci. Eng. A350 (2003) 17-24.

4) S. Kojima and C. Hu: Mater. Sci. Eng. A489 (2008) 150-157.

5) Y. Satoh, T. Yoshiie, H. Mori and M. Kiritani: Mater. Sci. Eng. A350 (2003) 44-52.9

6) K. Arakawa, K. Ono, M. Iseki and M. Kiritani: Radiat. Eff. Def. Solids 157 (2002) 25-30.

7) M. Kiritani, Y. Satoh, Y. Kizuka, K. Arakawa, Y. Ogasawara, S. Arai and Y. Shimomura: Philos. Mag.Lett. 79 (1999) 797-804.

8) M. Kiritani: Radiat. Eff. Def. Solids 148 (1999) 233-267.

# LES Study on Hierarchical Turbulence Organized Structure Above Urban Canopy

Student Number: 07M18160 Name: Jin ZHANG Supervisor: Manabu KANDA

都市大気境界層の
大規模乱流組織構造の階層性に関する数値解析的研究

章 晋

大気境界層は混合層と接地境界層に分けられる。これらの層にある乱流運動は互いに影響し合っているにもかかわらず、従来の研究ではそれらの層を分けて研究してきた。本研究では、数値解析ツール(PALM)と東工大の超並列グリッドコンピュータ(TSUBAME)を用いて、それらの層を含む領域で計算することが可能とした。そこから得られた3次元データをもとに、スケール分離と条件抽出の手法を用いてその組織構造の階層性を明らかにした。

## 1 Introduction

The atmospheric boundary can be divided into two parts, mixed layer and surface layer. It is known that both of these layers influence the other to a certain degree. Most of the studies related to those layers, however, only focused on one of them. This is caused by the restriction of resources. In this study, a LES (Large-Eddy Simulation) model PALM (**PA**rallelized **L**arge-Eddy Simulation **M**odel) which is capable of calculation for large domain size was employed. By using this model with TSUBAME grid cluster system in TITech, this numerical study managed to simulate both layers together which made the investigation of the coherent organized structure of turbulence within a logarithmic region of urban boundary layer possible.

The coherent structure of turbulence plays an important role in the exchange process of momentum and scalars in the near-surface region, so the study of the coherent structure would be useful in understanding the physical background of the statistical structure of wall turbulence, modeling and controlling turbulence for industrial and geophysical applications.

To investigate coherent structures of turbulence in urban boundary layer, the results are analyzed by visualization of instantaneous flow fields and by conditional averaging. A filtering technique is also employed to exclude the large scale influence from the mixed layer and to educe small scale turbulence structures. In addition, quadrant analysis and two-point correlations are performed to determine the statistical characteristics of coherent structures.

## 2 Overview of the numerical setting

In this study we perform LES to elucidate the phenomenology of coherent structures in the log layer above three-dimensional roughness comprised of a regular array of cubes. Figure 1 shows a plan view of the computational domain, which has a size of $2560\mathrm{m} \times 2560\mathrm{m} \times 2600\mathrm{m}$ along x, y, z directions respectively, with 5m grid length. To close approximate the real atmospheric boundary, the initial temperature profile is set as showed in Figure 2. The geostrophic wind velocity and the ground heat flux are set to be 20m/s and $0.07\mathrm{K} \cdot \mathrm{m/s}$, respectively.

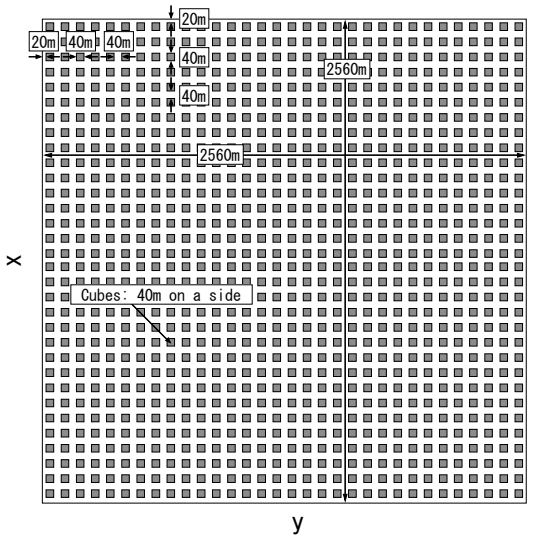


Figure 1: Plan view of computational domain

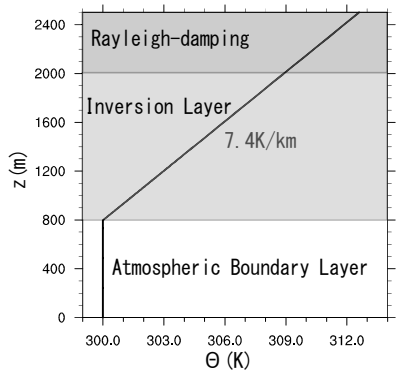


Figure 2: Initial temperature profile

# 3 Flow statistics

## 3.1 Performance evaluation

In this section, turbulence statistics from the simulation are presented, and detailed comparisons are made with measurements performed in outdoor scale model experiments for urban climate (COSMO).

Figure 3 shows the vertical profiles of potential temperature, sensible heat flux, variance of vertical velocity up to 40h (h:building height 40m) and mean streamwise velocity up to 10h. From Figure 3(a), Figure 3(b), the boundary layer height is determined as about 1200m and the influence of heat flux from entrainment layer is limited to 800m. It is critical that the boundary height is high enough so that surface layer and mixed layer are separable. From Figure 3 (c), two maximum values for $\sigma_w$ exist. The upper one is at about 10h and the lower one is at about 2h. This phenomenon is considered to be caused by the convection in mixed layer and the turbulence produced by the shear in surface layer.

Figure 3 (d) shows that a surface layer could be defined up to 5h approximately where the mean velocity profile is logarithmic. We follow the meteorological convention and write the log law over rough surface as (Raupach et al. 1991)

$$\frac{u(z)}{u_*} = \frac{1}{\kappa}\ln\frac{z-d}{z_0} \tag{3.1}$$

Where κ is von Kármán's constant, and the parameters $z_0$ and d are the roughness length and zero-plane displacement, respectively. In this study, $z_0$ and d are 1.4m and 33m respectively. Almost identical results for d/h were obtained by Cheng & Castro (2002), where its value is 0.825.

A stability parameter showed in equation (3.2) is also derived.

$$\frac{z'}{L} = -\frac{(g/T)(\overline{w'\ T'})}{u_*^3/kz'} \tag{3.2}$$

Here, $z' = z - d$. At 2h, $z'/L$ is -0.038, which can be considered to be neutral, consistent with the results referred by Inagaki & Kanda (2008) in COSMO.

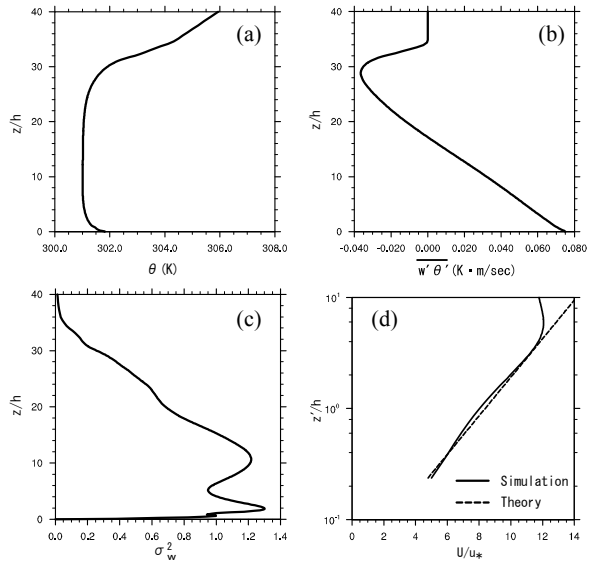


Figure 3: Vertical profiles of various flow statistics

## 3.2 Spectra and Cospectra

In the study of coherent structures in COSMO, Inagaki & Kanda(2008) observed that the low frequency part of the streamwise velocity spectra was larger than the field observation results in the Kansas experiments (Kaimal et al, 1972). In contrast, the counterpart of vertical velocity spectra and Reynolds stress cospectra had good agreements with Kaimal's results. By removing the instantaneous spatial mean component, the low frequency part of the streamwise velocity spectra decreased significantly. This means the low-frequency fluctuations of streamwise velocity didn't follow the inner-layer scaling similarity due to the outer-layer disturbance.

Figure 4 shows the spectral densities and wavenumbers which were normalized by the surface layer variables $u_*$ and $z'$, respectively. The reference curves are from the Kansas experiments and COSMO observations.

Two curves from this simulation are plotted in this figure. PALM_TS was derived from time series data at 8 points along the y direction at 2h. PALM_SP was derived from the averaging of the spatial data along the x direction. The results of PALM_SP were the largest. This reflects the energy imbalance problem in a point observation. It is known that the flux obtained by using time series data from point observations tends to be underestimated. Since PALM_SP evaluated all the velocity information at xy cross section, the spectral densities turn out to be larger.

The spectra and cospectra in the high frequency region of PALM_TS exhibit good agreement with other experiments results, but the low frequency spectra for this study was not produced. This could be caused by two possibilities: the small domain size along x direction, or the larger damping for outer layer vortices due to the large building size.

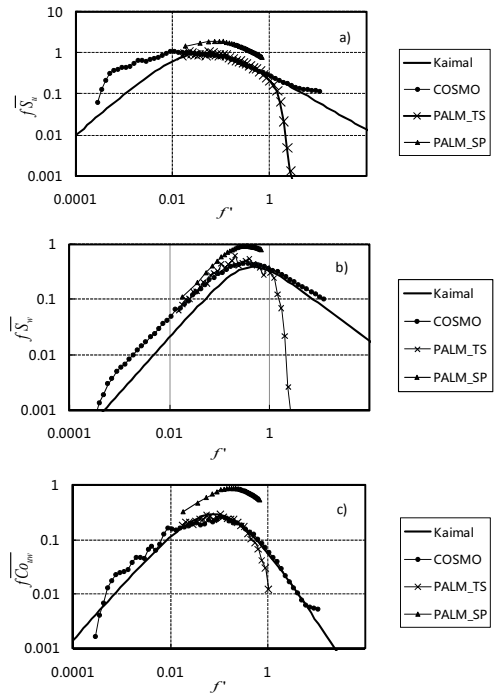


Figure 4: Comparison of spectra and cospectra

# 4 Coherent structures

In this section the coherent structures in the surface layer will be investigated through the methods of two-point correlations, quadrant analysis, spatial averaging and conditional averaging.

## 4.1 Two-point correlations

Two-point velocity correlation defined by

$$R_{uu}(\gamma, \delta\gamma) = \frac{\overline{u'(\gamma)u'(\gamma+\delta\gamma)}}{\sqrt{\overline{u'^2(\gamma)}}\sqrt{\overline{u'^2(\gamma+\delta\gamma)}}} \quad (4.1)$$

are computed for separation $\delta\gamma$ in the spanwise and streamwise directions at 2h, 3h, 4h heights, respectively. Figure 5 shows that the spanwise width and streamwise length increase with height. By comparing Figure 5 (a) and (b), it is obvious that the streamwise length is larger than spanwise width, but the aspect ratio of length to width of the $R_{uu} = 0.7$ is approximately constant as 2.4 with increasing height. This means that the streamwise and spanwise length scales increase roughly in the same proportion with distance from the wall. So the overall shape of the structures is preserved on average.

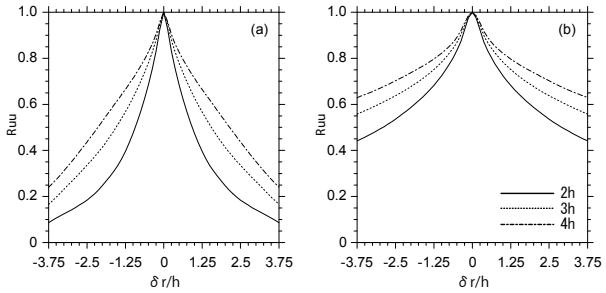


Figure 5: Two-point correlations $R_{uu}$
(a): spanwise, (b): streamwise

## 4.2 Quadrant analysis

In the quadrant analysis technique, one considers the frequency of occurrence and contribution to Reynolds stress of velocity fluctuations lying in the four quadrants defined by

$$\left.\begin{array}{l} S1: u' > 0, w' > 0 \\ S2: u' < 0, w' > 0 \\ S3: u' < 0, w' < 0 \\ S4: u' > 0, w' < 0 \end{array}\right\} \quad (4.2)$$

Figure 6 shows the relative number of ejections (S2), sweeps (S4), and their relative contribution to the Reynolds stress. Away from the roughness, there are more sweeps, but the ejections are more significant based on their contribution to the Reynolds stress. The results are different to what is observed in COSMO, where the S4 are dominant in surface layer due to large influence from the mixed layer. Since there is large correlation between ejection (S2) and coherent structures, by comparing with Figure 5, it seems that the larger coherent structures at higher level in the surface layer relatively contribute more ejections to the Reynolds stress.

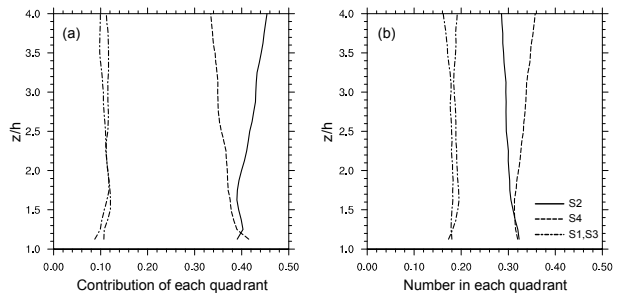


Figure 6: Quadrant analysis within surface layer

## 4.3 Spatial averaging

In COSMO's study, an instantaneous spatial average in a horizontal small section to separate the inactive turbulence

$$\phi' = [\phi'] + \phi'' \quad (4.3)$$

where the square brackets and the double prime indicate the mean and fluctuation of the spatial average in a finite area, respectively. In this study, two different averaging areas are used: a square area with 8h, and another with 2h on a side. The 8h averaging area is used to remove the inactive influence from the mixed layer, since this scale is in the middle of large scale turbulence in mixed layer, and small scale turbulence induced from the surface.

Figure 7 shows a contour plot of fluctuating streamwise velocity u″ at 2h. The low speed regions (black) are elongated in the streamwise, which corresponds to the results in section 4.1.

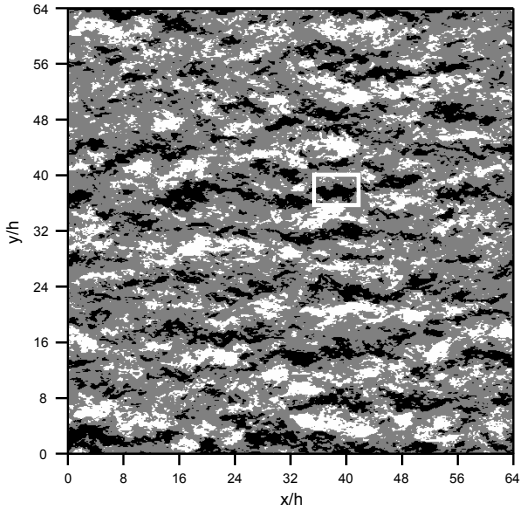


Figure 7: Instantaneous snapshot of streamwise velocity u″. Black regions: $u<0.8u_m$. White regions: $u>1.2u_m$.

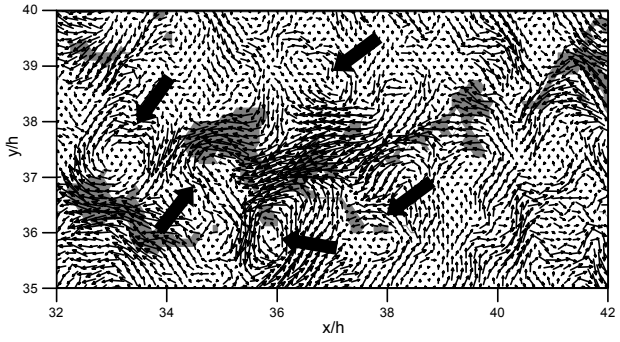


Figure 8: vector distribution in a part of the xy cross secion at 2h. Grey regions: strong ejections

In Figure 8, the area enclosed by the white box in Figure 7 is enlarged. The grey regions represent strong ejections that were two times larger in magnitude than the temporal mean of u′w′. It is observed that there are strong vortices on both sides of the ejection areas. To clarify the relationship between the ejections and their surrounding vector fields, a conditional averaging method is used.

## 4.3 Conditional averaging

To educe the dominant structures, a local minimun velocity below a threshold was set at 75% of the spatial mean velocity. Flow information around these threshold points were averaged three-dimensionally.

Figure 9 shows fluctuating velocity vector fields and contours of fluctuating streamwise velocity u″ from spatial averaging (8h) at $z = -0.5h$, 0, and 0.5h, where $z = 0$ is the reference height at 2h (Figure 10). At each height, there is a pair of counter-rotating vortices with an elongated low-speed region between. As height increases, the center of the vortices shifts from upwind to downwind. The counter-rotating vortices are considered to be the legs of the hairpin vortices and the shift of the vortex center means the legs of hairpin vortices have an inclination angle with respect to the ground.

Two-point correlations based on the spatial averaging results are also computed in the horizontal and vertical planes through conditional averaging. Figure 11 (A), (B) are the contours of $R_{uu}$ in xy cross section through z=0 and $R_{vv}$ in zx cross section through y=0, respectively. Figure 11 (a), (b) are the counterparts derived with small spatial averaging length 2h. Both of u and v show good similarity in structure with different spatial averaging lengths. The aspect ratio of spanwise width to streamwise length, as defined by the $R_{uu}$=0.4 contours, is approximately equal to 2 in both cases. The contours of $R_{vv}$ in Figure 11 (B), (b), show that both of the structures have an inclination angle with respect to the surface, which could be inferred as the vortex leg observed in Figure 9.

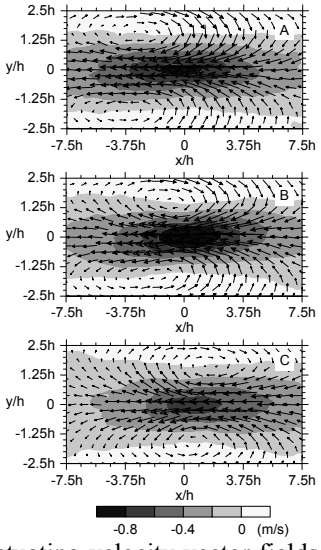


Figure 9: Fluctuating velocity vector fields and contours of fluctuating streamwise velocity u″. A, B, C are the cross sections showed in Figure 10.

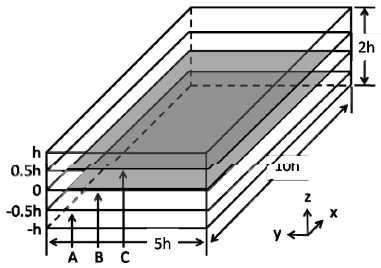


Figure 10: The domain size of conditional averaging for the data derived from large spatial averaging (8h). A, B, C correspond to the xy cross sections in Figure 9.

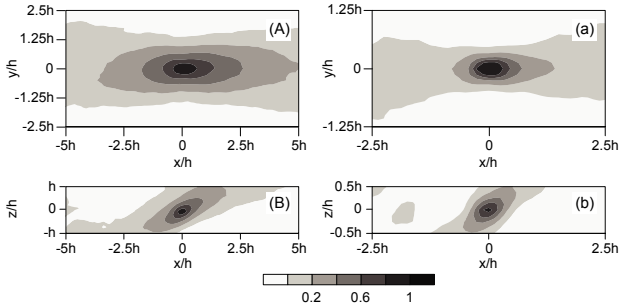


Figure 11: Contours of two-point correlations
(A), (B):$R_{uu}$ and $R_{vv}$ at xy cross section and zy cross section respectively.(a), (b): the counterparts of (A), (B) with small spatial averaging data (2h).

# 5 Conclusions

In this study, LES has been conducted to investigate the coherent structures of turbulence within the surface layer in urban atmospheric boundary layer. Following results have been obtained.

1. The similarity of the inner-layer statistics is applicable for urban boundary layer.
2. The averaged aspect ratios of the coherent structures are preserved in the surface layer.
3. The number of coherent structures decreases with height, but the contribution of ejections from coherent structures increase in the surface layer.
4. Counter-rotating vortices that are considered to be vortex legs of the hairpin vortices are observed along the sides of the low speed regions.
5. Large scale turbulence and small scale turbulence derived with different spatial averaging length exhibit good similarity in their structures.

## References

[1] Raupach, M.R., Antonia, R.A. and Rajagopalan, S.: Rough-wall turbulent boundary layer, *Appl. Mech. Rev.* 44, 1-25, 1991.

[2] Cheng, H. and Castro, I.P.: Near wall flow over urban-like roughness, *Boundary-Layer Met*, 104, 229-259, 2002.

[3] Inagaki, A. and Kanda, M.: Structure of active turbulence over an array of cubes within the logarithmic layer of atmospheric flow, *J. Fluid Mech*, (submitted).

[4] Kaimal, J. C., Wyngaard, J. C., Izumi, Y. & Cote, O. R. 1972 Spectral characteristics of surface layer turbulence. *Q. J. R. Met. Soc.* 98, 563–589.

# Impact of Angular Power Spectrum (APS) on the Achievable Diversity Gain and MIMO Capacity in a Mobile Terminal

Student Number: 07M18177 Name: Elnaz FOROUGHI SHAFIEI Supervisor: Jun-ichi TAKADA

## Abstract

The array antenna systems in the mobile terminals, such as antenna diversity has been evaluated under the uniform (omnidirectional) angular power spectrum. The influence of angular power spectrum (APS) together with the user rotation on the performance of antennas are examined. Omnidirectional and unidirectional angular power spectrum models are investigated for direction diversity and space diversity in a multipath environment. The goal of this research is to provide a guideline for how much in detail APS should be modeled for the evaluation of an array antenna system in a mobile terminal.

## 1 Introduction

An antenna in a wireless communication system is the device through which, in the transmission mode, radio frequency energy is coupled from the transmitter to the free space, and from free space to the receiver in the receiving mode. In many applications, it is necessary to design antenna with very directive characteristics (very high gain) or very high efficiency, to meet demands for different types of communication scenarios.

There are many classical parameters to evaluate antenna systems, of which directivity and efficiency are the most common. However, for the array antennas in the multipath environment, classical parameters of the antenna such as directivity and efficiency are not sufficient for the evaluation of the performance of the antenna system as a whole [2]. Propagation channel should be taken into account for the appropriate evaluation [1]. There exists some channel models proposed for antenna evaluation. However, they are too complicated for the comparative evaluation of the array antennas of the user terminal as those models are originally developed for the purpose of the system level performance evaluation [1]. Development of channel model for antenna evaluation is still a major issue.

In order to examine the performance of antennas in various environments, this research examines the influence of concentrated angular power spectrum (APS) on the performance of user terminal array antennas, using *diversity* technique. Diversity scheme refers to a method for improving the reliability of a message signal by utilizing two or more communication channels with different characteristics. The main purpose is to coherently combine the independent paths so that the effects of the multipath is mitigated. There are many diversity techniques, of which we focus on *space diversity* and *direction diversity* in this research.

One method is to use multiple transmit or receive antennas, where the elements of the array are separated in distance. This type of diversity is referred to as space diversity [4]. In this case, independent paths are realized without an increase in transmit signal power. In direction diversity, angle is provided by restricting the receive antenna beamwidth to a given angle [4]. The use of narrow beamwidth provides angle discrimination that can reduce interference.

In order to concentrate on only the impact of APS, very simple modeling and evaluation scheme are deployed. i.e. the APS and the directivity of the antenna are simplified and the diversity performance is evaluated.

## 2 Antenna Evaluation Approach

In this section the approach of the antenna evaluation is presented. To simplify the formulation, APS is concentrated into horizontal plane and only the azimuth APS is considered. In order to focus on the influence of concentrated APS together with the user rotation to the performance of the array antennas, a 2-Dimensional analysis is done for simple analytical treatment [2].

The correlation matrix of UT array can be derived in the same manner as the correlation matrix of the diversity antenna. APS for vertical polarizations are defined as $p_{\mathrm{UT}}(\varphi)$ to satisfy the following normalization condition.

$$2\int_0^{2\pi}\{p_{\mathrm{UT}_i}(\varphi)\}\,\mathrm{d}\varphi = 1 \tag{1}$$

To represent the UT antenna characteristics, polarimetric complex directivity of $i$-th user terminal antenna is defined as $e_{\mathrm{UT}_i}(\varphi)$ for $\varphi$ also to satisfy the normalized condition in the same manner as the antenna gain as

$$\frac{1}{2\pi}\int_0^{2\pi}\left\{|e_{\mathrm{UT}_i}(\varphi)|^2\right\}\mathrm{d}\varphi = \eta_i \tag{2}$$

where $\eta_i \leq 1$ is the efficiency of the $i$-th UT antenna considering the loss and mismatch.

The complex correlation matrix of $i$-th and $j$-th branches of UT array is then calculated by using APS and the complex antenna directivity of UT antenna array as

$$[\mathbf{R}_{\mathrm{UT}}]_{ij} = 2\int_0^{2\pi} \left\{ e_{\mathrm{UT}_i}(\varphi)\, e^*_{\mathrm{UT}_j}(\varphi)\, p_{\mathrm{UT}}(\varphi) \right\} \mathrm{d}\varphi \tag{3}$$

# 3 Impact of Angular Power Spectrum

In order to examine different environmental characteristics, two APS models are considered, omnidirectional APS $p_{\mathrm{O}}(\varphi)$ and Gaussian unidirectional APS $p_{\mathrm{G}}(\varphi)$. They are defined as

$$p_{\mathrm{O}}(\varphi) = \frac{1}{2\pi} \tag{4}$$

$$p_{\mathrm{G}}(\varphi, \varphi_0, \Delta\varphi_p) = A_{\Delta\varphi_p} \exp\left( \frac{(\varphi \quad \varphi_0)^2}{2\Delta\varphi_p^2} \right) \tag{5}$$

$$(\quad \pi < \varphi \quad \varphi_0 \le \pi)$$

It should be noted that $p_{\mathrm{G}}(\varphi)$ is a symmetrically truncated Gaussian function, and $A_{\Delta\varphi_p}$ is a constant, satisfying Eq. (1) as,

$$\frac{1}{A_{\Delta\varphi_p}} = 2\sqrt{2}\Delta\varphi_p \int_{-\pi}^{\pi} \exp\left( \frac{\varphi^2}{2\Delta\varphi_p^2} \right) \mathrm{d}\varphi \tag{6}$$

where $\varphi_0$ is the angle of arrival (AoA) varying within $[0, 2\pi)$ according to the rotation of the user terminal, and $\Delta\varphi_P$ is the standard deviation of the Gaussian functions for angular power spectrum (APS).

The two-element complex directivities of space diversity array with half-wavelength separated omnidirectional elements are defined as,

$$e_{\mathrm{S1}}(\varphi) = \frac{1}{\sqrt{2}} \exp\left( j\frac{\pi}{2}\cos\varphi \right), \quad \pi < \varphi < \pi \tag{7}$$

$$e_{\mathrm{S2}}(\varphi) = \frac{1}{\sqrt{2}} \exp\left( +j\frac{\pi}{2}\cos\varphi \right), \quad \pi < \varphi < \pi \tag{8}$$

The two-element complex directivities of direction diversity array $\pi$ separated Gaussian unidirectional elements are defined as follows:

$$e_{\mathrm{G1}}(\varphi) = B_{\Delta\varphi_e} \exp\left( \frac{\varphi^2}{2\Delta\varphi_e^2} \right), \quad \pi < \varphi < \pi \tag{9}$$

$$e_{\mathrm{G2}}(\varphi) = B_{\Delta\varphi_e} \exp\left( \frac{(\varphi+\pi)^2}{2\Delta\varphi_e^2} \right), \quad 2\pi < \varphi < 0 \tag{10}$$

where satisfying Eq. (2),

$$\frac{1}{B^2_{\Delta\varphi_e}} = \frac{\Delta\varphi_e}{\pi} \int_{-\pi}^{\pi} \exp\left( \frac{\varphi^2}{\Delta\varphi_e^2} \right) \mathrm{d}\varphi \tag{11}$$

The matrix elements of $[R_{UT}]_{ij}$ can be obtained by substituting $p_{\mathrm{G}}$, $e_{\mathrm{S1}}$ and $e_{\mathrm{S2}}$ in Eq.(3), and $p_{\mathrm{G}}$, $e_{\mathrm{G1}}$ and $e_{\mathrm{G2}}$ in Eq.(3) for space diversity and direction diversity respectively.

The eigenvalues are calculated by general *Eigenvalue decomposition* (EVG) as,

$$\mathbf{R}_{\mathrm{UT}} = \mathbf{E}\mathbf{\Lambda}\mathbf{E}^H \tag{12}$$

$$\mathbf{\Lambda} = \begin{pmatrix} \lambda_1 & 0 \\ 0 & \lambda_2 \end{pmatrix} \tag{13}$$

Where $\mathbf{E}$ is unitary and $\mathbf{\Lambda}$ is diagonal matrix of Eigenvalues $\lambda_1$ and $\lambda_2$.

In this research, the two-branch diversity is considered. The characteristic equation can be analytically solved and the eigenvalues are given as,

$$\lambda = \frac{1}{2}\Big\{ (R_{11} + R_{22}) \pm \sqrt{(R_{11} + R_{22})^2 \quad 4(R_{11}R_{22} \quad R_{12}R_{21})} \Big\} \tag{14}$$

Once the eigenvalues of the correlation matrix is known, cumulative distribution function (CDF) $F(\gamma \le x)$ of output SNR $\gamma$of the maximum ratio combining (MRC) is can be presented by the following equation [1],

$$F(\gamma \le x) = \frac{1}{\lambda_1 \quad \lambda_2} \left[ \lambda_1 \left\{ 1 \quad \exp(\quad \frac{x}{\lambda_1}) \right\} \quad \lambda_2 \left\{ 1 \quad \exp(\quad \frac{x}{\lambda_2}) \right\} \right] \quad \lambda_1 \ne \lambda_2 \tag{15}$$

Various parameters are used to represent the characteristics of the antenna and the environment.

*Beamwidth* is defined as the range of angle where the antenna power gain is within the half of the peak. Also, *Angular Spread* is the standard deviation of the angular power spectrum.

The *Reference Antenna* used in the study is a single omnidirectional antenna [5], under the same APS. The reference measurement is taken in the same setup as for the real measurement and then compared.

Diversity antenna gain-outage probability (DAG-OP), is the improvement of SNR from the reference antenna as the CDF of a certain probability, which is set to 1[%] in this study. The CDF graph for the reference antenna ($F_{\mathrm{REF}}(\gamma < x)$) and the measurement antenna ($F_{\mathrm{MES}}(\gamma < x)$),is obtained as shown in Fig.1, where $\gamma$ is the SNR at the reciever. Then the difference of respective SNRs when $F_{\mathrm{REF}}(\gamma_{\mathrm{RES}} < x) = 0.01$ and $F_{\mathrm{MES}}(\gamma_{\mathrm{MES}} < x) = 0.01$ is calculated as

$$\mathrm{DAG\_OP} = \gamma_{\mathrm{MES}} \quad \gamma_{\mathrm{REF}} \tag{16}$$

where, $\gamma_{\mathrm{RES}}$ is defined so that $F(x \le \gamma_{\mathrm{RES}}) = 0.01$ .

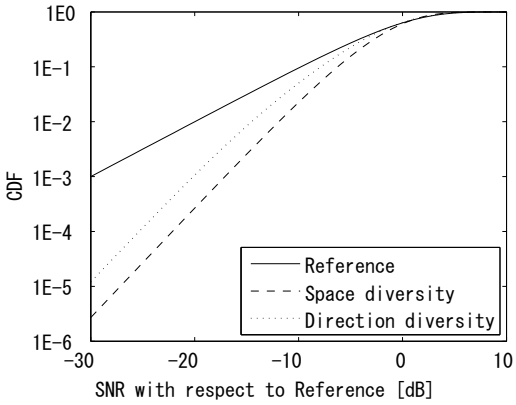


Figure 1: CDF of relative SNR for reference antenna, space diversity and direction diversity

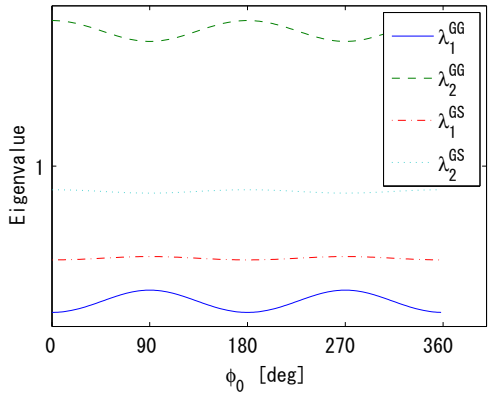


Figure 2: Angle of Arrival (AoA) dependence of the eigenvalues of correlation matrices

# 4 Numerical Results

The variation of eigenvalues for the four scenarios explained in section 3 is shown in Fig.2. The eigenvalues represent the equivalent uncorrelated branch powers. The eigenvalues are fluctuating along $\varphi_0$(AoA)for Gaussian unidirectional APS. The gap of the eigenvalues is the biggest when $\varphi_0$is 0 and $\pi$. The fluctuation of the graph is to a great extent reduced for the Gaussian omnidirectional APS.

To analyze the impact of APS on array antennas, simulations were conducted for space diversity and direction diversity antenna arrays under different angular spreads (AS), and the impact of beamwidth was also analyzed.

The simulation condition is presented in Table.1.

Table 1: Parameters Used in Simulation

| Parameters | AoA | | AS | | BW |
|---|---|---|---|---|---|
| Values | 0[deg] | 0 | 360[deg] | 0 | 360[deg] |
| Values | 90[deg] | 0 | 360[deg] | 0 | 360[deg] |

The DAG-OP characteristics of space diversity antenna for the two extreme cases of AoA=0[deg] and AoA=90[deg] is shown in Fig.3. As shown in the figure, when AoA=0[deg], when AS is very small,

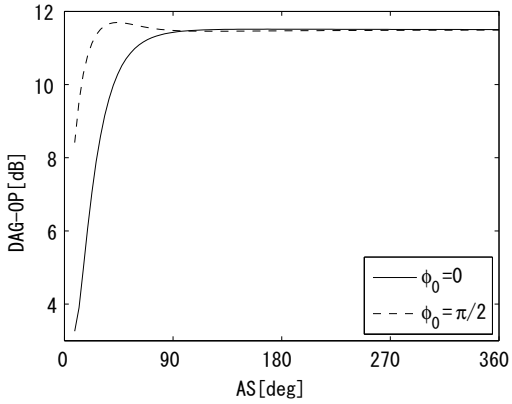


Figure 3: DAG-OP Characteristics of Space Diversity Antenna

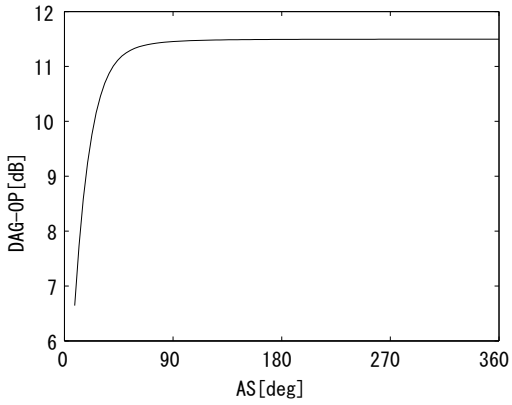


Figure 4: DAG-OP Characteristics of Space Diversity Antenna where AoA is averaged over $\varphi_0 = 0$ to $\varphi_0 = 2\pi$

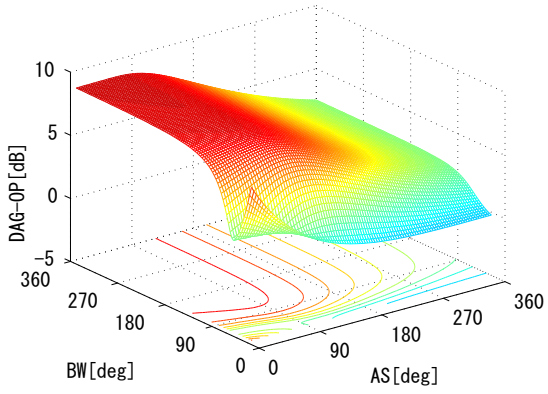


Figure 5: DAG-OP Characteristics where AoA $\varphi_0 =$ 0 -3D Plot

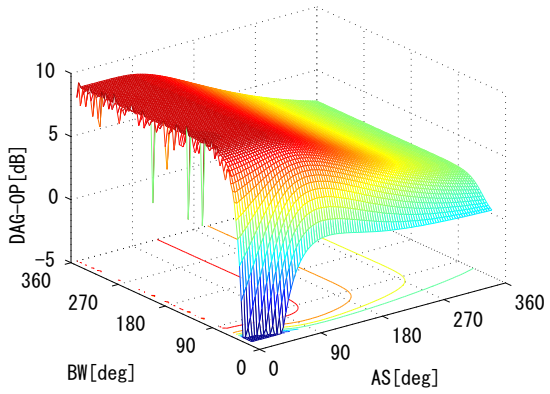


Figure 6: DAG-OP Characteristics where AoA $\varphi_0 = \frac{\pi}{2}$ -3D Plot

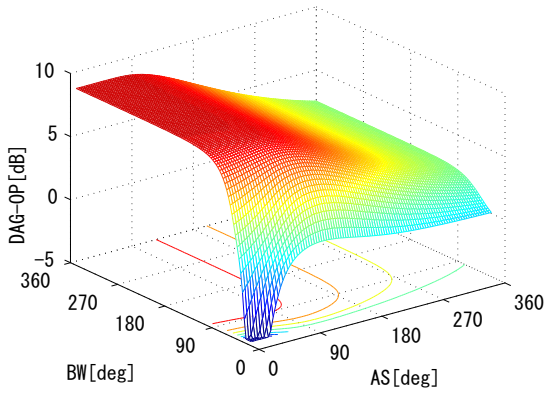


Figure 7: DAG-OP Characteristics where AoA is averaged over $\varphi_0 = 0$ to $\varphi_0 = 2\pi$ -3D Plot

the gain is low. The reason is, only one antenna has recognition in this case. When AS is small, for the AoA of 0[deg] and 90[deg], the DAG-OP starts from different values. However, after the AS increases more than 90[deg], the DAG-OP of both angle of arrivals of 0[deg] and 90[deg] reach the same value. This means when the AS is big, both cases they show omnidirectional behavior. Fig.4 shows the DAG-OP characteristics of space diversity antenna when the AoA is averaged over 0[deg] to 360[deg]. As shown in the figure, this case also shows a similar behavior to the previous ones.

The DAG-OP characteristics of direction diversity *(Gaussian)* antenna for angle of arrival of 0[deg] and 90[deg] the 3-D graphs are shown in Fig.5 and Fig.6 respectively.

For the case of A0A=0[deg], when the AS and BW are small, the gain is very high, and it reduces when the they increase. Also it could be observed that when BW increases, the antenna shows omnidirectional behavior. Meanwhile, as the AS increases, the gain also increases.

In contrast, for the case of angle of arrival of 90[deg], when the AS and BW are small, the DAG-OP starts from a very small value. This is because for this case, the unidirectional antenna almost can not recognize the APS. The gain then increases when the AS and BW increase. This also proves that similar to A0A=0[deg], for the A0A=90[deg], when the BW and AS are big, they show omnidirectional behavior.

Fig.7 shows the DAG-OP characteristics of direction diversity antenna when the AoA is averaged over 0[deg] to 360[deg]. As shown in the figure, this case also shows a similar behavior to the previous ones.

# 5 Conclusion

This research examined the influence of concentrated angular power spectrum (APS) on the performance of user terminal array antennas, for the cases of space diversity and direction diversity. In order to concentrate on only the impact of APS, very simple modeling and evaluation scheme was proposed, and the diversity performance was evaluated. It can be observed that for both cases space and direction diversity, when the angular spread is very high, the gain is independent of beamwidth and angle of arrival. Also in the direction diversity case, for very high beamwidth, the gain becomes independent of angle of arrival and angular spread. This study shows that the justification of use of omnidirectional APS instead of unidirectional APS is rejected. As shown in this research, in reality, when the angular spread is very small, the diversity antenna gain is also very small and so they show different behaviors.

# References

[1] J.Takada, "Impact of Concentrated Azimuth Power Spectrum for Performance Evaluation of User Terminal Array Antenna (invited)," International Union of Radio Science XXIX General Assembly (URSI-GA 08), Aug. 2008 (Chicago, IL, USA).

[2] J.Takada, "Propagation Modeling for Performance Evaluation of MIMO Antennas," 2007 Microwave Workshop and Exhibitions (MWE 2007), WS8-1, Nov. 2007.

[3] J.Takada and K.Ogawa, "Concept of Diversity Antenna Gain," COST273 7th Meeting of the Management Committee, TD(03)142, May 2003 (Paris, France).

[4] Andrea Goldsmith, *Wireless Communications*, Cambridge University Press, 2005

[5] A. Balanis, Panayiotis I. Ioannides, *Introduction to Smart Antennas*, Morgan and Clayborne 2007

# The applicability of one-dimensional & two-dimensional soil/water coupled analysis in settlement prediction of embankment

Student Number: 07M18183 Name: Longtao YOU Supervisor: Hideki OHTA & Thirapong PIPATPONGSA

# 盛土の沈下予測における 1 次元･2 次元土/水連成解析の適用性

尤 龍涛

本研究では，既往の研究において実務への適用性の検討が行われた土/水連成有限要素解析手法[1]を用い，過去に建設された盛土を実例にし，1 次元と 2 次元の解析を行なう。更に，1 次元解析と 2 次元解析による沈下量の違いを調べるために，*B/D* (盛土幅 B と軟弱地盤層厚 D の比)および近似度(1 次元･2 次元解析による沈下量の差と2 次元解析による沈下量との比)という指標を提案し，盛土の沈下予測における 1 次元解析の適用性について検討する。

## 1. Introduction

Constructing geotechnical structures such as an embankment on soft ground cause often more or less settlement deformation. Prediction of the settlement of the embankment is useful for taking appropriate measure in the planning/construction stage, and taking countermeasure such as rational reparation in the maintenance/management stage.

Recently, because of the technological advance of the computer and FEM (finite element method) technique, the case prediction of the settlement by two-dimensional analysis is gradually increasing. Although it is simple to understand the deformation of a geometric by two-dimensional analysis, there is the same time much disadvantage since high cost (demanded for time and talented people) and special technique such as some obvious analyzed conditions (boundary condition, geometrical condition) are required. And it is difficult to avoid completely the error. However, the one-dimensional consolidation analysis based on Terzaghi's[2] consolidation theory is still used up to now in engineering practice because of its low cost and simple technique.

In certain different geometrical condition of the embankment, analysis result showed that the settlement computed by two-dimensional analysis is close to the one computed by one-dimensional consolidation analysis.

In this study, some constructed embankments will be computed in one-dimensional and two-dimensional analysis by soil/water coupled analysis technique which was developed by Iizuka and Ohta (1987) [1] and revised by Takeyama (2007) [3], and the practicability was confirmed in past researches. The analysis technique employs an elasto-viscoplastic constitutive model proposed by Sekiguchi and Ohta (1977) [4]. In addition the applicability of one-dimensional and two-dimensional soil/water coupled analysis in settlement prediction of embankment will be discussed.

## 2. Difference between one-dimensional and two-dimensional settlement

Figure 1 shows the difference between one-dimensional and two-dimensional settlement.

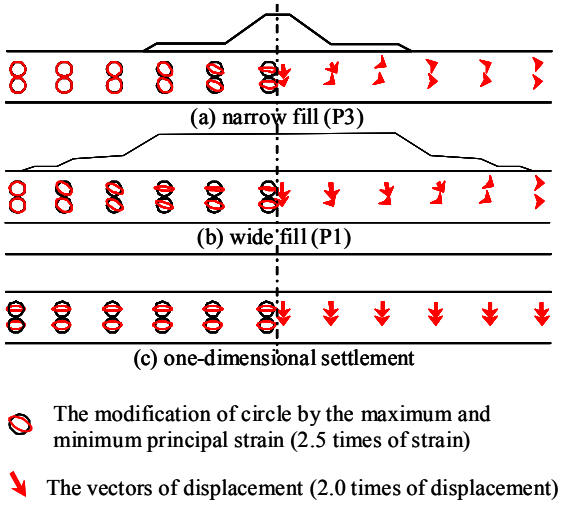


Figure 1: Difference between one-dimensional and two-dimensional settlement.

These two analysis results Figure 1(a) and Figure 1(b) are drawn based on the two-dimensional analysis results of Nagasaki Highway site which will be introduced in Chapter 4. Figure 1(c) shows

the deformation of the subsoil layers when the width of the embankment is infinite. The circles and the ellipses show the maximum and minimum principal strain on the left of the figure, and the arrows show the displacement of clay layer on the right of the figure.

When fill materials are laid on soft ground, the centre of an embankment settles right under, and the top of slope and the toe of the embankment settle and displace to the outside. In some cases, the toe of the embankment swells from the surface of the ground contrarily. Paying attention to the behavior of the subsoil elements beneath the embankment, we can find that the two-dimensional deformation strongly appear so as to leave the centre of the embankment. Overall, the settlement by two-dimensional analysis at the centre of the embankments is close to the one-dimensional analysis, but it does not mean that there is a one-dimensional consolidation.

For this reason, investigation on the difference between one-dimensional and two-dimensional analysis by referring to two evaluation indicators are proposed. First indicator is *B/D* which is the ratio of the filling width (B) to thickness (D) of soft ground, and second is A (approximation) which is the ratio of the difference between settlements computed by one-dimensional analysis and two-dimensional analysis to the settlement computed by two-dimensional analysis. It is considered that A will approximate to 0 when *B/D* is infinite, whereas this value reduced below unity when *B/D* is small.

## 3. Analysis Site (Akita Highway)

Akita Highway was constructed in 1993, and opened for traffic from 1997. This analysis site is called Soto-asahikawa in the part of Akita Highway project which was constructed on an overlain by very soft organic clay which deposited on sloping base. The three embankment cross-sections analyzed in this paper are also shown in Figure 2 as their name BC11, BC21, and BC31. The geologic figures of these sections are illustrated in Figure 3.

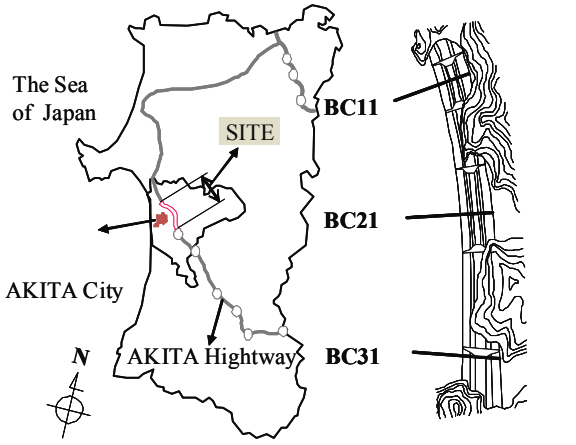


Figure 2: Location of Akita Highway site

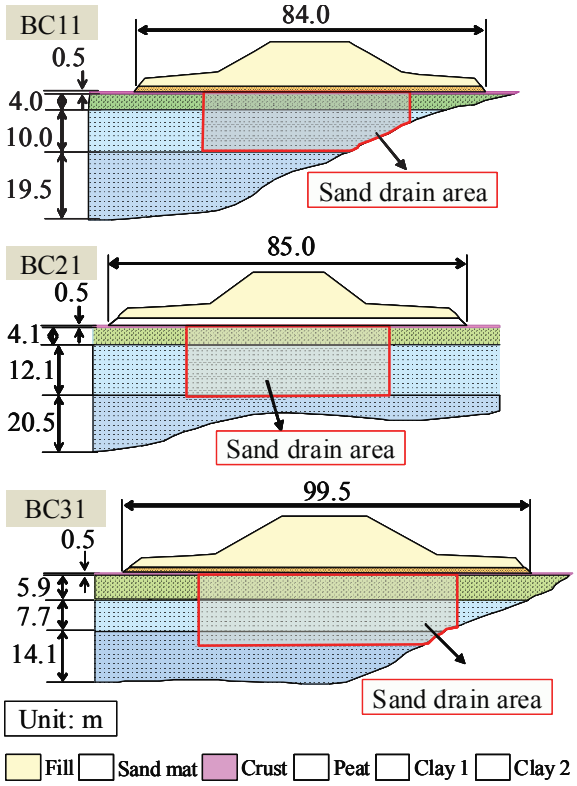


Figure 3: Shape of embankment, bedrock and subsoil layers

These three cross-sections are covered by a peat layer of about 5m thickness which has very high water content and plasticity index. Underneath the peat layer lays a soft clay layer (Clay 1) and a stiff clay layer (Clay 2). The bedrock is not symmetric, therefore analysis area should be considered to appropriate wide range.

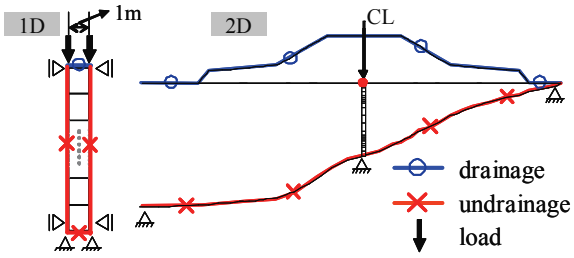


Figure 4: Boundary condition of one-dimensional and two-dimensional analysis

In one-dimensional analysis, just the boundary

drainage condition of upper surface of which the hydraulic head is set with 0 for modeling as drainage boundary shown in Figure 4. In two-dimensional analysis, the surface of the ground and embankment is set as drainage boundary. And input parameters used in one-dimensional analysis are completely the same as two-dimensional analysis.

Analysis of BC21 could not finish until completion of construction because critical failure occurred under the fill. The settlements at the centre of BC11 and BC31 of embankments computed in two-dimensional analysis agree well with the monitored settlement. But the one-dimensional analysis predicts settlement smaller than two-dimensional analysis. The simulation results are BC11 cross-section shown in Figure 5.

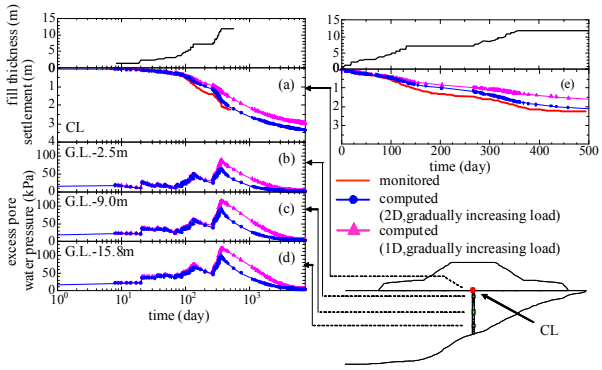


Figure 5: Simulation results (BC11)

## 4. Analysis Site (Nagasaki Highway)

This is another analysis site, Nagasaki Highway site. Six embankments were constructed as the preload at Nagasaki Highway in the Takeo-Kitakata Interchange project in Kyushu.

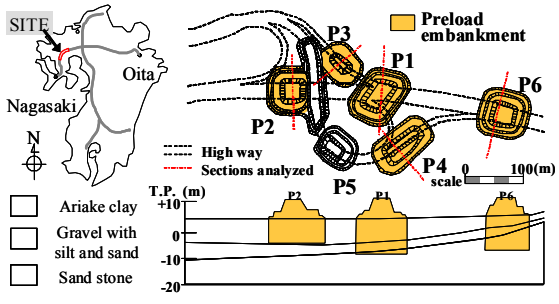


Figure 6: Location of Nagasaki Highway site

Site plan and soil profile are shown in Figure 6. Five case studies are carried out for embankments for P1 through P4 and P6. Embankment P5 is excluded from the analysis because of special improved with lime-treated columns. The subsoil foundation consists of an alluvial clay layer and gravel bed containing silt and sand. The soft clay is uniform and highly sensitive. The shape of each embankment and subsoil layers are summarized in Figure 7.

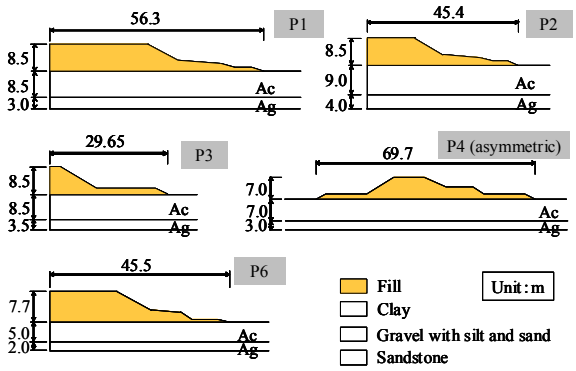


Figure 7: Shapes of embankments and subsoil layers

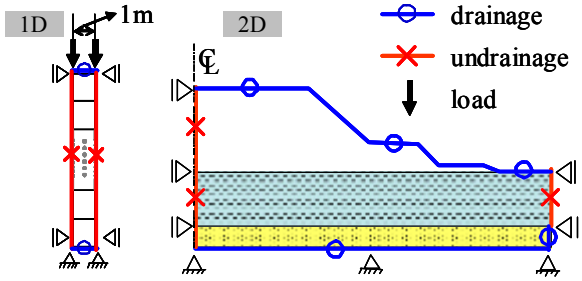


Figure 8: Boundary condition of one-dimensional and two-dimensional analysis

In one-dimensional analysis, the boundary drainage conditions of upper and lower surface of intermediate sand layer are set with the hydraulic head is 0 for modeling as drainage layer. And input parameters used in one-dimensional analysis are completely the same as in two-dimensional analysis.

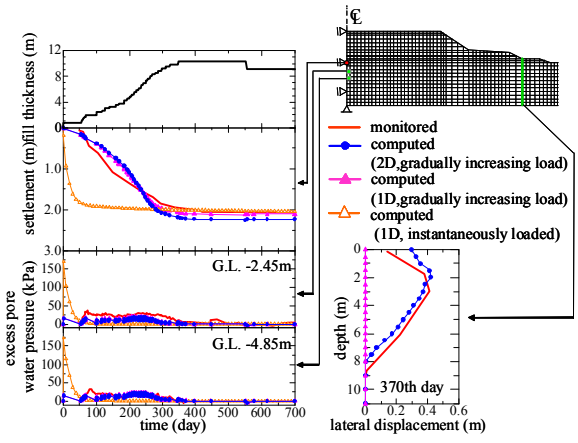


Figure 9: Simulation results (P1)

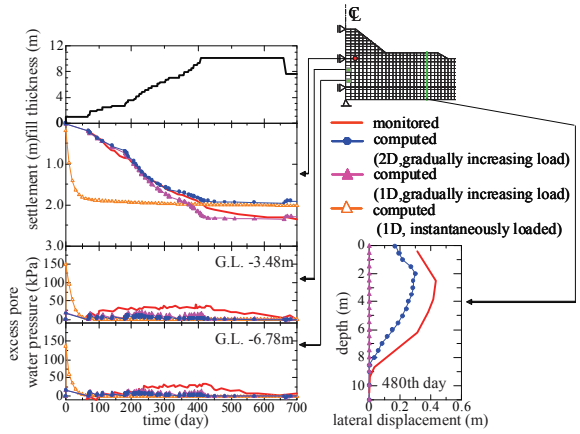


Figure 10: Simulation results (P3)

The simulation results of section P1 and P3 are shown in Figure 9 and Figure 10. Both the one-dimensional and two-dimensional analysis can simulate the settlement behavior well.

## 5. *B/D* and Approximation

Two indicators were proposed in Chapter 2. *B/D*s of all analyzed sections are summarized in Table 1 except BC21 of Akita Highway site of which the analysis actually stopped at about 370day because of critical failure of many elements. In Table 1, $S_{1D}$ is the settlement computed by one-dimensional analysis, and $S_{2D}$ is the settlement computed by two- dimensional analysis.

Table 1: *B/D*s and settlements in analysis sites

| section | Akita Highway | | Nagasaki Highway | | | | |
|---|---|---|---|---|---|---|---|
| | BC11 | BC31 | P1 | P2 | P3 | P4 | P6 |
| ***H*** (m) | 11.7 | 13.7 | 8.5 | 8.5 | 8.5 | 7.0 | 7.7 |
| ***B*** (m) | 84.0 | 99.5 | 112.6 | 90.8 | 59.0 | 69.7 | 91.0 |
| ***D*** (m) | 17.5 | 26.0 | 8.5 | 9.0 | 8.5 | 7.0 | 5.0 |
| ***B/D*** | 4.7 | 3.7 | 13.2 | 10.1 | 6.9 | 10.0 | 18.2 |
| $S_{2D}$ (m) | 3.38 | 4.70 | 2.22 | 2.62 | 1.95 | 1.72 | 1.41 |
| $S_{1D}$ (m) | 3.02 | 3.82 | 2.21 | 2.42 | 2.28 | 1.71 | 1.18 |

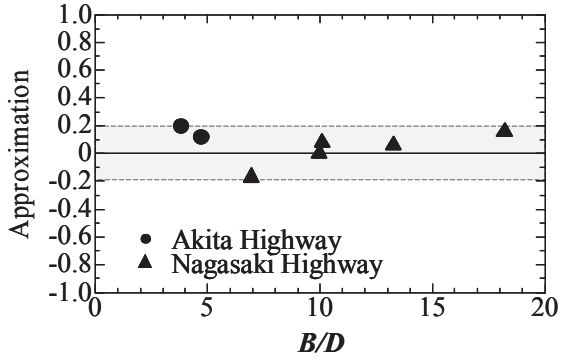


Figure 11: *B/D* and Approximation

The correlation between *B/D* and Approximation is shown in Figure 11.

Overall, if the maximum error about 20% (the gray area in the Figure 11) is admissible for the construction sites, the prediction computed by two-dimensional analysis in any shape of embankment and bedrock can be replaced by the prediction computed by one-dimensional analysis.

## 6. Conclusion

The conclusions acquired in this paper are summarized as follows:

1) The applicability of one-dimensional soil/water coupled analysis in consolidation settlement prediction of embankment is presented.

2) According to the comparisons between the settlements, in the case of Akita highway of which *B/D* is low, two-dimensional analysis can simulate the settlement behavior well, but one-dimensional analysis cannot, and in the case of Nagasaki Highway of which *B/D* is high, both the one-dimensional and two-dimensional analysis can simulate the settlement behavior well.

3) In this study, when the maximum error about 20% is admissible for the construction sites, the prediction computed by two-dimensional analysis in any shape of embankment and bedrock can be replaced by the prediction computed by one-dimensional analysis.

## References

[1] Iizuka, A. and Ohta, H. : A determination procedure of input parameters in elasto-viscoplastic finite element analysis, Soil and Foundations, Vol.27, No.3, pp.71-87, 1987

[2] Terzaghi, K. and Peck, R. : Soil Mechanics in Engineering Practice, 2nd Ed., John Wiley & Sons, 1967

[3] Takeyama, T.: Some problem affected on reliability of solution in soil/water coupled finite element method and its theoretical resolution methods, 2007 (in Japanese)

[4] Sekiguchi, H. and Ohta, H. : Induced anisotropy and time dependency of clay, *Proc.Specialty Session 9th ICSMFE*, pp.229-239, 1977

# Experimental study on adhesion behavior between rough surfaces of solid bodies

Student Number: 07M18190 Name: LEI Lei Supervisor: TAKAHASHI Kunio

# 表面粗さを持つ固体間における凝着現象の実験的検討

雷磊

正弦波状表面粗さを持つアルミニムブロックと平面シリコンゴムを用いて, 実験的に外圧と凝着幅との関係を調べた. 外圧と凝着幅のヒステリシス関係が観察された. それは試験サンプル表面の sub-roughness の影響だと考えられる. エネルギー損失率 $\alpha$ という概念を面凝着理論に導入することで, ヒステリシスを予測することができた. また, 面凝着理論に基づき, 部分接触凝着を表面粗さ, 凝着仕事, 及び弾性率で表すことができ, 理論と検証実験を通して, 弾性率可変材料の使用により, 把持及び離脱の可能性を示唆した.

## 1 Introduction

The effect of adhesion on elastic contact is significant in joining technology as well as micro- and nano-scale applications (e.g. micro-/nano-electromechanical systems (MEMS/NEMS) components). The adhesion contact between an infinite elastic body and a rigid body with single-sinusoidal surface roughness has been solved theoretically by Rachmat[1]. The hysteresis of the contact is assumed as an energy dissipation and a simple treatment for the dissipation is proposed by Johnson[2]. The mechanism of the dissipation energy by the surface sub-roughness was theoretically and experimentally investigated by Guduru[3][4], although the investigation is only for the point contact. In case of point contact, the adhesion force is only dependent on the surface shape (curvature) and the work of adhesion. However, in case of area contact, the adhesion force not only depends on the work of adhesion and surface shape, but also depends on the elastic constant. Using the elastic constant dependency property, it is possible to design a mechanism to control grip and release.

The present study is based on Rachmat's theory[1]. The mechanism of hysteresis and the possibility of grip and release by varying elastic constant are investigated experimentally.

## 2 Theory

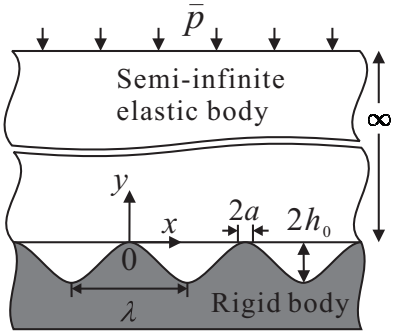


Fig. 1 Model of adhesional contact between a semi-infinite elastic body and a rigid body having sinusoidal surface roughness.

Figure 1 shows the schematic illustration of the adhesion between a semi-infinite elastic body with flat surface and a rigid body with sinusoidal surface roughness under external pressure. The relation between the external pressure $\bar{p}$ and the contact width $2a$ can be expressed by Eq. (1).

$$\begin{aligned} \bar{p}^* &= \sin^2(\pi a/\lambda) \\ &\quad -\left(\Delta\bar{\gamma}\sqrt{1+(2\pi h_0/\lambda)^2\sin^2(2\pi a/\lambda)}\tan(\pi a/\lambda)\right)^{1/2} \\ \bar{p}^* &= \bar{p}/(E^*\pi h_0/\lambda), \qquad \Delta\bar{\gamma} = \Delta\gamma/(E^* h_0^2\pi^2/(2\lambda)), \\ E^* &= E/(1-\nu^2) \end{aligned} \tag{1}$$

The solid line in Fig.2 shows the plot of Eq.(1). As shown in Fig.2, at the initial contact of the two bodies without external pressure, the contact width increases from A to B where the energy is at its local minimum. After that, if we give a pressure between D and C, the contact width changes along the solid line. If we give a pressure larger than C, the contact will snap to the perfect contact. If we give a pressure less than D, the contact will be separated.

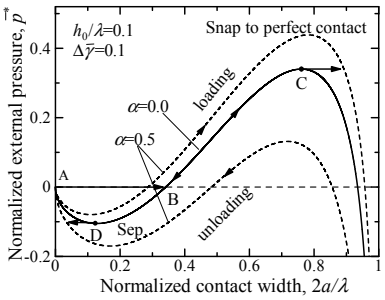


Fig. 2 The relation between the normalized external pressure and the normalized contact width for $h_0/\lambda$=0.1, $\Delta\bar{\gamma}$ = 0.1

### 2.1 Sub-roughness model

In Rachmat's theory[1], the roughness is assumed to be single-sinusoidal. However, the actual surfaces have another sub-roughness on the sinusoidal roughness. The effect of the sub-roughness on the adhesion could be explained in the same manner as the work done by

Guduru(2007)[3], which shows the effect of the sub-roughness on point contacts. But the contact in the present study is area contact.

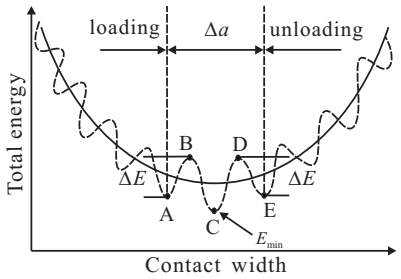


Fig. 3 schematic illustration of the relation between the total energy and the contact width.

Figure 3 shows a schematic illustration of the relation between the total energy and the contact width. The existence of the sub-roughness is supposed to change the energy curve from the solid line to the broken line. The most stable state is point C. However it might stop at a locally stable point A, due to the existence of the sub-roughness. In the same manner, in case of unloading, the contact width might stop at E. Therefore we can observe the hysteresis loop between the loading and unloading process. Since Guduru'theory[3] is for point contact, it can not be applied to the present case. However, the effect of the sub-roughness can be quantitatively discussed using the concept of this theory[3]. Furthermore, the effect can be approximately explained using the theory of Johnson[2]. In the same manner as the theory[2], we can assume that excess energy is required both in loading and unloading processes, to overcome the energy gap $\Delta E$ in Fig3, respectively. Since the energy release rate $G$ is expressed by

$$G = \Delta\gamma \tag{2}$$

in case of no sub-roughness, we have to add some excess energy corresponding to the energy gaps. So, during loading, the energy release rate must be changed to $-G = -\Delta\gamma + \alpha G$, and during unloading, $G = \Delta\gamma + \alpha G$. Therefore, the hysteresis can be expressed by replacing the $\Delta\gamma$ in Rachmat's theory[1] by

$$G = \Delta\gamma/(1 + \alpha) \tag{3}$$

$$G = \Delta\gamma/(1 - \alpha) \tag{4}$$

An example of the loading and unloading processes is plotted in Fig.2 with dashed lines, using $\alpha = 0.5$.

## 2.2 Grip and release by varying elastic constant

The pressure at point (D) and point (C) in Fig.2 are dependent on $\Delta\overline{\gamma}$. Their relations are shown in the plot in Fig.4. In this figure, curve $OQ_3$ shows the separation point (D). Curve $Q_1Q_3$ shows point (C) approaches a state of perfect contact. After normalizing the curve $OQ_3$ in Fig.4 by the following methods (Eq.5～6), the relation between the pressure required to separate the partially contacted interface and the elastic constant can be obtained, as shown in Fig.5.

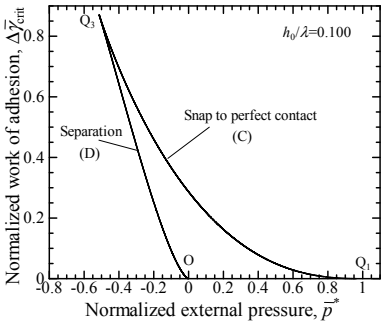


Fig. 4 The relations between the work of adhesion and the external pressure for $h_0/\lambda = 0.1$.

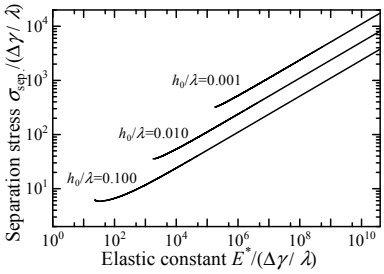


Fig. 5 The relation between the elastic constant and the external pressure required to separate the interface, partially contacted.

$$\breve{\sigma}_{sep.} = \sigma_{sep.}/(\Delta\gamma/\lambda) \tag{5}$$

$$\breve{E} = E^*/(\Delta\gamma/\lambda) \tag{6}$$

Figure 5 suggests that three-figure of change in elastic constant is required to make one-figure of change in adhesional force.

# 3 Experiment system and procedures

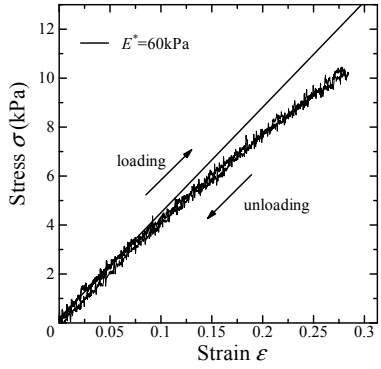


Fig. 6 The stress-strain curve for silicon rubber.

A transparent silicon rubber (FUSOUGOMU) of 15 mm ($z$) × 38 mm ($x$) × 10 mm ($y$) is used as the elastic body. The elastic constant is measured as shown in Fig.6, and $E^* = 60$ is obtained. Aluminum alloy blocks (purity 99.95%, 30 mm ($z$) × 37.5 mm ($x$) × 3 mm ($y$) are used as the rigid body. Their surface are processed to have sinusoidal roughness of two different amplitudes, such as, $h_0/\lambda$=0.04,$h_0/\lambda$=0.02,$\lambda$=5 mm, by using a wire-cutting

machine. The surfaces are then polished carefully using alumina particles (Baikalox, 0.1CR).

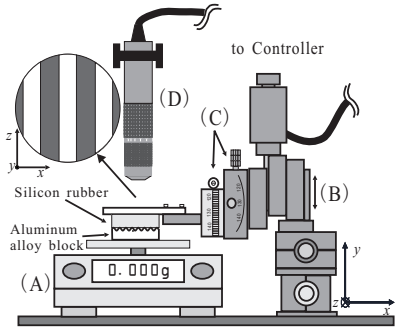


Fig. 7 Illustration of the experiment system used.

Figure 7 shows the experimental system, which consists of (A) an electronic balance (Sartorius, TE153S) to measure the external pressure, (B), (C) automated precise stages, crossed roller stage and goniometer Stage (Suruga Seiki, K701-20LMS, B43-38N, B54-60UNR) to adjust the vertical position and the angle of the elastic body, and (D) an optical microscope (KEYENCE, VH-7000) to observe the contact width through the transparent rubbers. The experiment is done in an acrylic box to avoid the effect of dusts and moisture. The samples are cleaned in an ultrasonic bath with alcohol and set on the system as shown in Fig.7. The horizontal angles of the elastic body are adjusted by the stages (C) and the samples are driven by automated stage (B). The contact width at the center of the sample is observed.In each measurement of the force, it takes 3 to 10 (min) to obtain stable width.

# 4 Results and discussion

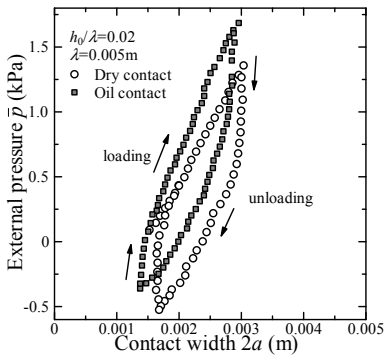


Fig. 8 The hysteresis measured under a dry condition and an oily condition for $h_0/\lambda$=0.02.

Figure 8 shows the hysteresis measured under dry condition and oily condition using a fatty alcohol (Linear AlkylbenzeneSulfonate). Fig.9 shows the hysteresis loops both in lower stress region and higher stress region. As shown in these figures, the comparable hysteresis is observed even in the oily condition as well as in dry condition and the hysteresis seems independent of the stress. These results suggest that the hysteresis is not mainly due to the surface friction. Since no hysteresis is observed in the measurement of elastic body as shown in Fig.6, the

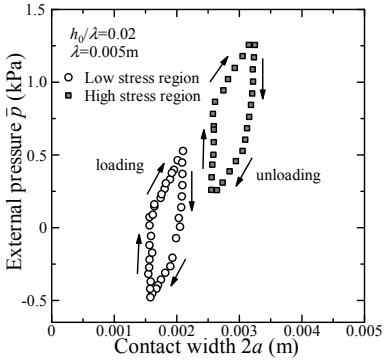


Fig. 9 The hysteresis measured in a lower stress region and a higher stress for $h_0/\lambda$=0.02.

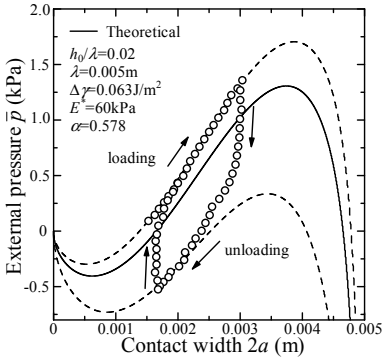


Fig. 10 Comparison between theoretical and experimental result for $h_0/\lambda$=0.02.

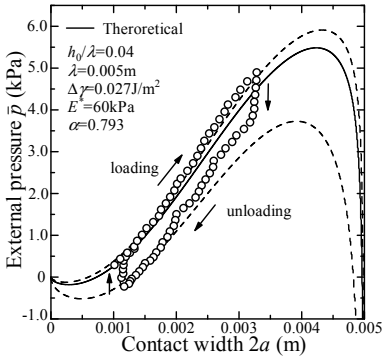


Fig. 11 Comparison between theoretical and experimental result for $h_0/\lambda$=0.04.

mechanism of the hysteresis is considered to be due to the energy gaps caused by the surface sub-roughness.

The Eq.(1) is fitted to the experimental results as shown in Fig.10 and 11. As the results, $\Delta\gamma$ = 0.063J/m$^2$ and $\alpha$ = 0.578 are obtained for the sample shown in Fig.10), and $\Delta\gamma$ = 0.027J/m$^2$, $\alpha$ = 0.793 are obtained for the sample shown in Fig.11. Consequently, adhesion is very sensitive to the surface condition. So, the fitting resulte of the work of adhesion is different between Fig.10 and Fig.11. The experimental results show a good agreement with the theory in the loading processes. On the other hand, in the unloading process, the measurement results does not agree well with the in loading process. Furthermore, the unloading process of Fig.10 and 11 shows the same tendency. The mechanism of the ten-

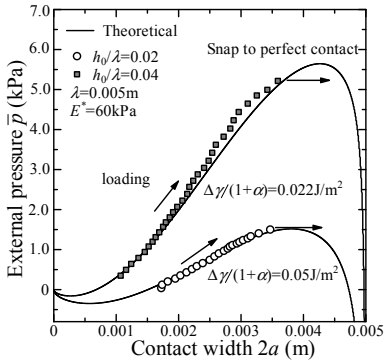


Fig. 12 Comparison between theoretical and experimental result for $h_0/\lambda$=0.02, $h_0/\lambda$=0.04. (loading process)

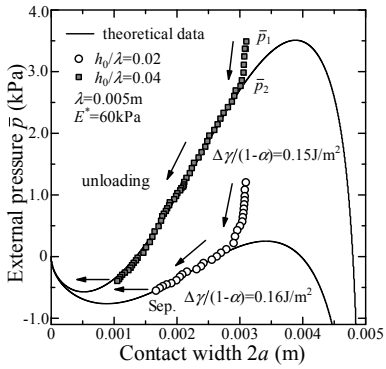


Fig. 13 Comparison between theoretical and experimental result for $h_0/\lambda$=0.02, $h_0/\lambda$=0.04. (unloading process)

dency is still unclear. However the sub-roughness assumption used in the present study can be treated as a good approximation for the hysteresis loop.

Figure 12 shows the pressure which lead to snap to the perfect contact. In case of $h_0/\lambda$ = 0.02, the expeimental result shows good agreement with theoretical one. But in case of $h_0/\lambda$ = 0.04 the measurement slightly differs from the theory at the region of $\bar{p}$ > 2.0 kPa. The external pressure $\bar{p}$ of this region, by considering the stress at the contact region, corresponds to the stress $\sigma$ > 4 kPa in Fig.6. As show in Fig.6 at this stress the elastic constant slightly decreases. This explains the reason why the pressure required to snap to perfect contact decreases, as shown in Fig.12.

Figure 13 shows the experimental results for separation process. The pressure is decreased from the contact width $2a \approx 3.10$ mm. As for the sample $h_0/\lambda$ = 0.02, during the pressure decreases from $\bar{p}_1 \approx 3.4$ kPa to $\bar{p}_2 \approx 2.8$ kPa, the change of the contact width is very small and different from the theoretical prediction. On the other hand, at the region $\bar{p}_2 < 2.8$ kPa, the mesurement results are in good argreement with the theory with $\Delta\gamma/(1-\alpha) = 0.15$ J/m$^2$. Similar tendency is also observed for the sample of $h_0/\lambda$=0.02. However, the separation stresses for both samples seem to be smaller than the theoretical prediction. Just before the separation, separated area expands from the sample edge of $z$-direction and the separation occurs, meanwhile the theory assumes the infinite width of the sample. Since the difference is due to the edge effect, the difference would decrease for larger samples or larger applictions.

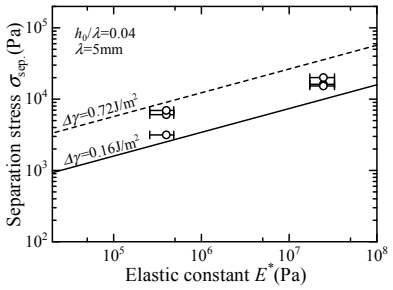


Fig. 14 Comparison between theoretical and experimental result for $h_0/\lambda$=0.04.

Figure 14 shows experimental results of the separation stress as an function of the elastic constant. A shape memory gel prepared by professor Gong is used. The elastic constant of the shape memory gel is $2 \times 10^5 \sim 5 \times 10^5$ Pa above 50 ℃, and $10^7 \sim 3 \times 10^7$ Pa below 30 ℃. The theory suggests the work of adhesion $\Delta\gamma$ to be $0.16 \sim 0.72$ J/m$^2$, which is well acceptable from the view point of material science. The dispersion of the measurements seems larger than that at the lower temperature. It could be due to the stability of temperature and the alignment process, which is easier at the lower temperature than that at higer temperature. Since the elasticity dependence of the separation stress is well expressed by the theory, it can be used for the design of grip-and-release devices.

# 5 Conclusion

The adhesion contact between the silicon rubber and the Aluminum alloy block having sinusoidal roughness is investigated using Rachmat's theory [1] considering the surface sub-roughness. Based on the sub-roughness model, the work of adhesion and the parameter $\alpha$ can be obtained from the measurements. The pressure required to snap to perfect contact and to separate the contact can be well predicted using the work of adhesion and the parameter $\alpha$.

Based on Rachmat's theroy[1], the possibility of grip and release by varying elastic constant is considered. The experimental results, by using shape memory gel, was in good agreement with the theoretical prediction.

# References

[1] R. Rachmat A. Sriwijaya: Adhesion of a semi-infinite elastic body in contact with a sinusoidal rigid surface, Doctoral thesis (Tokyo Institute of Technology , 2007)

[2] K. L. Johnson: Mechanics of adhesion, Tribology Int. 31 413

[3] P. R Guduru, C. Bull: Detachment of a rigid solid from an elastic wavy surface: Theory, Journal of the Mechanics and Physics of Solids 55 (2007) 445-472

[4] P. R Guduru, C. Bull: Detachment of a rigid solid from an elastic wavy surface: Experiments, Journal of the Mechanics and Physics of Solids 55 (2007) 473-488

# Phenols-polluted Water Treatment Using Enzyme and Recovery of Free Enzyme

Student ID: 07M18208 Name: He LI Supervisor: Prof. Sachio HIROSE,
Associate Prof. Naoya ABE

# フェノール系排水の酵素的処理とその遊離酵素の回収に関する研究

李 賀

Abstract
本研究では、高価な酵素を有効利用するため、添加剤により酵素反応を促進させ、かつ、遊離酵素を回収・再利用するフェノール系排水の酵素的処理法を検討する。添加剤として温度応答性を有するキトサン誘導体を利用し、酵素反応プロセスにおける酵素再利用条件を明らかにする。併せて、フェノール系排水として、カテコール、クレゾール、塩素系フェノールなどを含む混合系排水について酵素的処理の可能性を検討する。

*Key words: Phenolic compounds, wastewater, Enzyme treatment, Temperature-responsive polymer, enzyme recycle*

## 1. Introduction

Phenolic compounds are discharged in the wastewater streams of various industries such as coal conversion, wood preservation, olive oil factory, metal casting, pulp, paper manufacturing and so on. Most of these compounds are toxic and have been classified as hazardous pollutants. Phenols in water have special adverse effects since as little as 0.005mg/L of phenol will cause objectionable tastes and odors when it combines with chlorine to form chlorophenols.

There are many advantages of an enzyme-based treatment over conventional biological and chemical/physical treatment which have been discussed by Nicell *et al.* (1993) [1]. In most instances, physicochemical treatment processes are not very selective in condition that the number of pollutants removed during treatment; therefore, such processes are more economically feasible for the treatment for dilute wastewater. Chemical oxidation, for example, can become very expensive for high strength wastes, although the targeted pollutants might have a low concentration. Activated sludge is commonly used to reduce organic compound in municipal and industrial wastewater; however it has difficulty in removing toxic pollutants to low levels (Aitken, 1993) [2].

Enzymes have a major appeal in chemical processes as 'green chemistry' reagents, which will allow future sustainable development. Biological technologies dealing with the use of oxidoreductive enzymes, for instance, laccases, peroxidases and tyrosinases, may represent an efficient, alternative way to address the clean up of phenol-polluted wastewater. And they show many attractive properties for bio-transformation, such as wide specificity, high stability in solution, and easy availability from plant materials.

In enzyme-based treatment method, various enzymes such as Horseradish peroxidase (HRP), Coprinus macrorhizus peroxidase (CMP), Arthromyces ramosus peroxidase (ARP), and Soybean peroxdase (SBP) have proven to be effective in removing phenolic compounds from water (Al-Kassim *et al.*, 1993, Mceldoon *et al.*, 1995)[3-4]. Among these enzymes, HRP is the most widely used due to the stability and its advantage in production. However, there were only few studies that focused on the mixture wastewater and high cost of enzyme still remains as a challenging in enzyme treatment. Thus, the recycle of enzyme could be a way for practical application.

In this study, the type of enzyme was selected at the first. Catalytic activity, economic and quantity of production of enzyme were appraised. HRP was selected finally. And tyrosinase was also used to contrast. Therefore, the objectives of this study are to: (1) investigate removal rate of phenolic compounds using HRP and tyrosinase; (2) investigate the effect of the chemical additives

including hydroxybutyl chitosan(HBC), carboxymethylcellulose(CMC) and chiosan on the efficiency of the catalytic transformation of phenols; and (3) investigate the recovery rate of free enzyme after treatment using HBC or κ-Carrageenan.

## 2. Materials and Methods

*2.1 Materials*

HRP was purchased from Biozyme Laborates (South Wales, UK). Tyrosinase (5370Units/mg, solid) was purchased from Sigma Chemical Company. And all other chemicals were the highest purity available and purchased from Wako Pure Chemicals Co., Japan.

*2.2 Phenolic compounds polymerizing reaction*

Each of the phenolic compounds polymerizing reaction was carried out at 37℃ using phosphate buffer (pH 6.5). The initial concentration of phenol was 500mg/l. After treatment, the supernatants were filtered through 0.45μm filters and analyzed for phenols concentration by 3-dimensional high-performance liquid chromatography (3D-HPLC). The concentration of phenolic compounds in mixture wastewater (phenol; catechol and substituted phenols) were also analyzed as same procedure.

*2.3 Effect of the additives*

Each additive (0.5g/l) was added into the treatment. After the treatment, phenol concentration of the samples were analyzed by HPLC. And phenol concentration were analyzed when HBC(0.5～20g/l) or CMC(0.96～2.02wt%) was added.

*2.4 Recovery rate of the free enzyme*

After the phenols polymerizing reaction, HBC(20～30g/l) or κ-Carrageenan(10g/l) was used to recover the free enzyme. The treatment system using HBC was shown in Fig. 1. The recovered enzyme activity was analyzed by UV-1800.

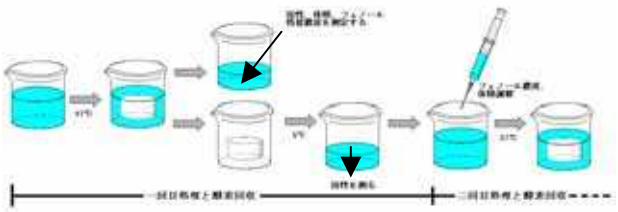

Figure 1. Treatment System

*2.5 3D-HPLC analysis*

The 3D-HPLC analysis was performed with a Hitachi instrument equipment (LaChrom Elite L-2455). A wakoshi ¢ (4.6mm×10mm column) was used. Isocratic solution was performed at a flow rate 1ml/min mobile phase composed of water, and acetnitorile (60:40%; v/v),T=30℃, P*max*=20MPa.

*2.6 HRP activity assay*

A modified assay was employed to measure the HRP enzyme activity using phenol, 4-amonoantipyrine (4-AAP) and hydrogen peroxide as substrates. The approach provided all components except enzyme near saturation concentration so that the initial rate of reaction became directly proportional to the amount of enzyme present. The assay mixture contained 250μl of 48mM 4-AAP, 2500μl of 20mM phenol, 1250μl of 0.1M phosphate buffer (pH 6.5) and 1000μl of enzyme solution. The rate of reaction was measured by monitoring the rate of formation of a non-precipitated product which absorbed light at a peak wavelength of 450nm (UV-1800, Simadzu).

## 3. Results and Discussion

*3.1 Phenolic compounds polymerizing reaction without additives*

The enzymatic activity of HRP and tyrosinase is dependent on pH with a broad optimum over the pH range of 6 to 9. In previous paper[5-6], the optimum conditions of the activity of HRP is 37℃ and pH6.5. Table 1 shows that phenolic compounds removal efficiency when each enzyme 4U/ml was added. It can be seen that enzymatic activity of HRP is greater than tyrosinase. And the reaction rate of HRP is also higher than that of tyrosinase.

In actuality, there are some different phenolic compounds in a wastewater. Two models wastewater of phenolic compound mixtures were investigated in this study. For instances group (Ⅰ) includes phenol, catechol, and chloro-derivatives. Group (Ⅱ) includes phenol, catechol, and p-substituted phenols. Table 2 shows removal efficiency of phenolic compounds in two groups. Although each polymerizing reaction reacts at the same time, the transformation is different. The exceptional behaviour of p-nitrophenol in group (Ⅱ) shows that no enzymatic reaction occurred completely. Because the reaction ability of each phenolic compounds is different.

It can be seen that the total quantity of transformation is similar between two groups, because catalytic ability of HRP was not changed.

**TABLE 1**

Treatment of Phenols by Enzyme in a Batch Reactor

| *Enzyme* | *Compounds* | *Removal (%)* |
|---|---|---|
| HRP | Phenol | 29 |
| | Catechol | 65 |
| | p-chlorophenol | 49 |
| | 2,4-dichlorophenol | 88 |
| | 2,4,6-trichlorophenol | 100 |
| | p-nitrophenol | 23 |
| | p-cresol | 64 |
| Tyrosinase | Phenol | 7 |
| | Catechol | 43 |
| | p-chlorophenol | 54 |
| | 2,4-dichlorophenol | 13 |
| | 2,4,6-trichlorophenol | 31 |
| | p-nitrophenol | 0 |
| | p-cresol | 25 |

**TABLE 2**

Transformation of Phenols in Mixture Model Wastewater

| | *Compounds* | *Removal (%)* | *Quantity (mmol)* |
|---|---|---|---|
| Ⅰ. | Phenol | 16.0 | 3.4 |
| | Catechol | 43.7 | 11.90 |
| | p-chlorophenol | 8.0 | 1.24 |
| | 2,4-dichlorophenol | 18.5 | 2.27 |
| | 2,4,6-trichlorophenol | 71.0 | 7.19 |
| | **Total** | | 26.00 |
| Ⅱ. | Phenol | 9.0 | 1.91 |
| | Catechol | 47.0 | 12.81 |
| | p-chlorophenol | 9.5 | 1.48 |
| | p-nitrophenol | 0 | 0 |
| | p-cresol | 58.0 | 10.73 |
| | **Total** | | 26.93 |

*3.2 Phenolic compounds polymerizing reaction using additives*

Fig. 2 shows transformation of phenols in polymerizing reaction using additives. It observed that, the removal efficiency is improved definitively than before, when HBC, HPC, PEG, or gelatin was added. Addition of chitosan or κ - Carrageenan remarkably improved the removal efficiency. But, insoluble polymer did not precipitate very well, when κ - Carrageenan was added(Fig. 3).

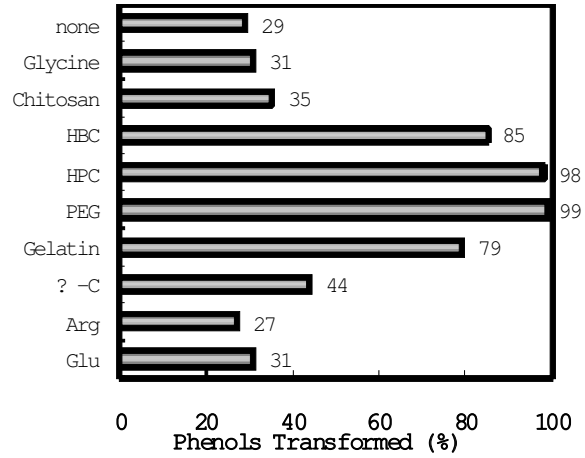


Figure 2. Phenol Removal Efficiency Using Additives


Figure 3. Insoluble Precipitates in Polymerizing Reaction

Fig. 4 shows the effect of additives on other phenols removal at 500mg/l initial phenol concentration. The highest removal efficiency is observed when using HBC. When HBC or CMC is added, the viscosity of solution increased. Fig. 5 indicates that the polymerizing reaction would be disrupted if the viscosity of CMC is too high.

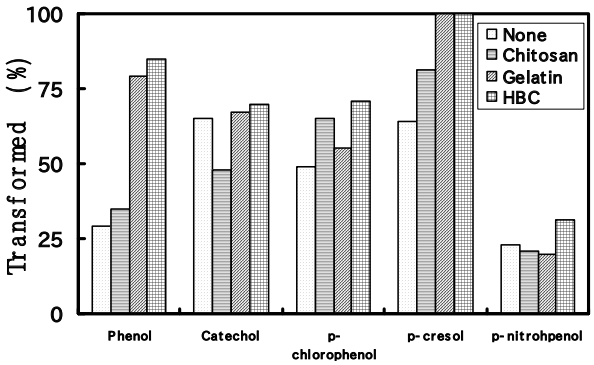


Figure 4. Effect of Additives on Treatment

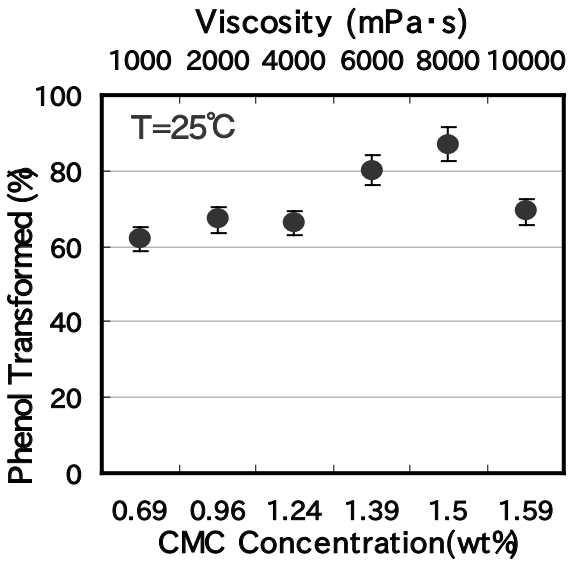


Figure 5. Effect of Viscosity on Treatment

*3.3 Recovery rate of the free enzyme*

Temperature-responsive of polymer, HBC or κ - Carrageenan was used to recover the free enzyme(Fig. 1). About 38% HRP can be recovered by HBC; and 23% by κ - Carrageenan (Fig. 6). The recovery rate is lower than that be expected, because HRP is inactivated by $H_2O_2$ (Fig. 7). Use of HBC can recover 79% activated HRP at 40min after the beginning of the treatment.

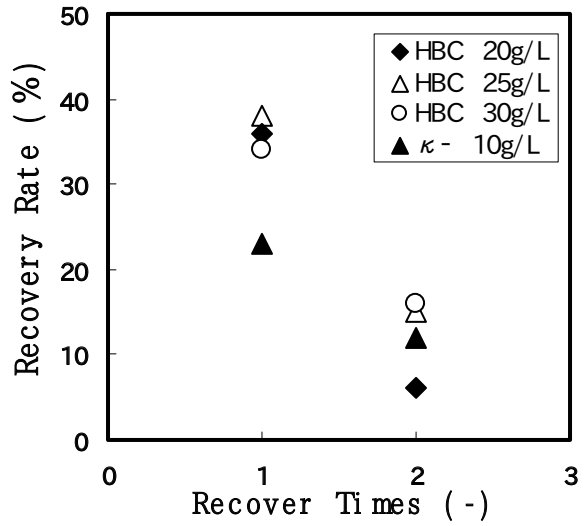


Figure 6. Recovery Rate of the Free Enzyme

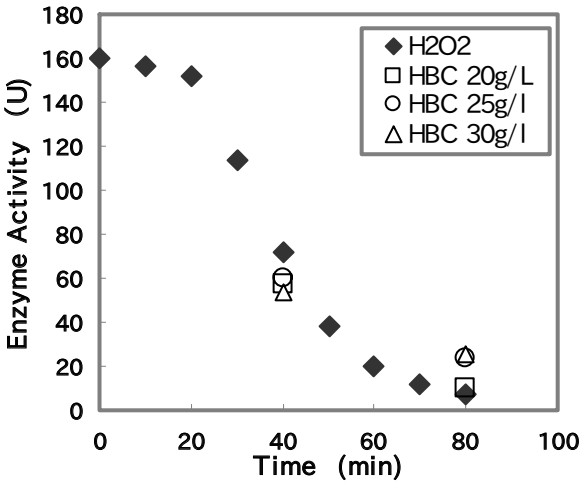


Figure 7. Enzyme Activity in Treatment

## 4. Conclusion

The enzymatic method successfully removed phenolic compounds from model wastewater. Using additives such as HBC is an option to improve the enzymatic method in economic perspective. Further improvement of the enzymatic method may be achieved by retaining HRP in additives polymer if the enzyme inactivation is sufficiently suppressed. The recover enzyme system using HBC seems to be more economic and potential for practical use.

## Reference

[1] J.A.Nicell, et al., Bioceterioration Abstracts, Vol 7, pp1-8 (1993)

[2] Aitken M.D: Waste treatment applications of enzyme: opportunities and obstacle. *Chem.Eng.J, Vol* 52, B49-B58 (1993)

[3] Al-Kassim L, et al., Evaluation of the removal of aromatic and halogenated unsaturated hydrocarbons from synthetic wastewater by enzyme catalyzed polymerization. In 48th Purdue Industrial Waste Conference Proceedings, pp413-420 (1993)

[4] McEldoon J. P, et al., Enzyme Microb. Technol. Vol 17, pp359-365 (1995)

[5] Shuichi KAWATOKO, Enzymatic treatment of phenol wastewater with thermo -responsive chitosan, Master thesis of Tokyo Tech (2006)

[6] LI He: Removal of Phenol in high concentration condition using Chitosan derivative and Enzyme, Bachelor thesis in Tokyo Tech, (2007)